Optical Control of Josephson Coupling in Striped $La_{2-x}Ba_xCuO_4$

Dissertation

zur Erlangung des Doktorgrades an der Fakultät für Mathematik, Informatik und Naturwissenschaften

Fachbereich Physik der Universität Hamburg

Vorgelegt von

Dawei Fu

Hamburg

2021

Gutachter/innnen der Dissertation:	Prof. Dr. Andrea Cavalleri Prof. Dr. Ludwig Mathey
Zusammensetzung der Prüfungskommission:	Prof. Dr. Andrea Cavalleri Prof. Dr. Franz Kärtner Prof. Dr. Ludwig Mathey PD Dr. Guido Meier Prof. Dr. Peter Schmelcher
Vorsitzende/r der Prüfungskommission:	Prof. Dr. Peter Schmelcher
Datum der Disputation:	23.03.2022
Vorsitzender Fach-Promotionsausschusses PHYSIK:	Prof. Dr. Wolfgang Hansen
Leiter des Fachbereichs PHYSIK:	Prof. Dr. Günter H. W. Sigl
Dekan der Fakultät MIN:	Prof. Dr. Heinrich Graener

Eidesstattliche Versicherung / Declaration on oath

Hiermit versichere ich an Eides statt, die vorliegende Dissertationsschrift selbst verfasst und keine anderen als die angegebenen Hilfsmittel und Quellen benutzt zu haben.

Die eingereichte schriftliche Fassung entspricht der auf dem elektronischen Speichermedium.

Die Dissertation wurde in der vorgelegten oder einer ähnlichen Form nicht schon einmal in einem früheren Promotionsverfahren angenommen oder als ungenügend beurteilt.

I hereby declare, on oath, that I have written the present dissertation on my own and have not used other than the mentioned resources and aids.

The submitted written version is identical to the version on the electronic storage medium.

This work has never been presented to other persons or evaluation panels in the context of an examination.

Hamburg, den 30.11.2021

_____

Dawei Fu

致 我的家人

Abstract

High-T_C cuprate superconductors display a rich phase diagram at low temperatures with coexisting and competing orders such as structural distortions of the crystal lattice, periodic charge- and spin-ordering, and superconductivity. The nature of interaction between these ordered phases (most of which are determined by strong electronic correlations) has been an intriguing area of research, as many believe it holds valuable insights into the mechanism behind the unusually high transition temperature of superconductivity in these materials, compared to those of conventional superconductors.

The stripe order, a periodic ordering of charges and spins into one-dimensional stripes in the CuO_2 planes, is commonly found in hole-doped compounds of the La-214 family, such as $La_{2-x}(Ba, Sr)_xCuO_4$. This thesis is focused on investigating the relationship between the stripe order and superconductivity in the La-214 compounds using ultrashort laser pulses, with the aim of probing and potentially optimizing and stabilizing pre-existing superconducting fluctuations in the striped normal state.

Earlier NIR pump - THz probe experiments found that photo-excitation induces a transient state with optical signatures of superconductivity in $La_{2-x}Ba_xCuO_4$. These tantalising observations were interpreted as a result of photo-excitation melting away the stripe order which competes with superconductivity at equilibrium. The first experiment of the present thesis benchmarks this interpretation by performing NIR pump-THz probe measurements on $La_{2-x}Ba_xCuO_4$ in externally applied magnetic fields to finely control the delicate balance between the stripe order and the equilibrium superconducting phase, and maps out the dependence of the transiently enhanced/induced superconducting properties on the external magnetic field. Surprisingly, we found a significant increase in the lifetime of the transient superconducting response with increasing magnetic fields. These results were interpreted as an indication that the light-induced state originates not from simple optical melting of stripes, but rather emerges from activated tunnelling between optically excited superconducting stripes (the so-called Pair Density Wave) in adjacent planes.

The second experiment of this thesis explores a different path towards understanding the relationship between the stripe order and superconductivity. In light of recent discovery of third harmonic generation of THz radiation by nonlinear Josephson tunnelling currents in the stripe phase of the same compound, numerical simulation predicts that more characteristic signatures of nonlinear Josephson tunnelling can be found after excitation by large-amplitude THz driving pulses. Electric Field Induced Second Harmonic (EFISH) is employed as an ultrafast voltmeter to monitor the voltage drop across the Josephson coupled CuO_2 planes in $La_{2-x}Ba_xCuO_4$. It is found that voltage anomalies associated with 2π phase slips are detected not only in the superconducting state but also in the normal, striped phase.

The results presented in this thesis produce further evidence for pre-existing Josephson coupling in the stripe phase which can be activated by optical excitation or in a highly nonlinear driving regime.

Zusammenfassung

Hochtemperatursupraleiter zeigen bei tiefen Temperaturen ein reichhaltiges Phasendiagramm, mit vielen nebeneinander bestehenden und konkurrierenden Ordnungen auf, wie z. B. strukturelle Verzerrungen des Kristallgitters, periodische Ladungs- und Spin-Ordnung und Supraleitfähigkeit. Die Art der Wechselwirkung zwischen diesen geordneten Phasen, von denen die meisten durch starke elektronische Korrelationen bestimmt werden, ist ein faszinierendes Forschungsgebiet, da es wertvolle Einblicke in den Mechanismus der hohen Übergangstemperatur der Supraleitung in diesen Materialien zu erlangen ermöglicht.

Die Streifenordnung, eine periodische Anordnung von Ladungen und Spins in eindimensionalen Streifen in den CuO_2-Ebenen, findet sich häufig in hochdotierten Verbindungen der La-214-Familie, wie $La_{2-x}(Ba, Sr)_xCuO_4$. In dieser Arbeit wird die Beziehung zwischen dieser Streifenanordnung und der Supraleitung in den La-214-Verbindungen mit ultrakurzen Laserpulsen untersucht, um die bereits vorhandenen supraleitenden Fluktuationen im streifenförmigen Normalzustand zu charakterisieren und möglicherweise zu optimieren und stabilisieren.

Frühere NIR-Pump- und THz-Probe Experimente zeigen, dass die Photoanregung einen vorübergehenden Zustand mit optischen Signaturen der Supraleitung in $La_{2-x}Ba_xCuO_4$ hervorruft. Diese Beobachtungen wurden als Resultat der Photoanregung interpretiert, die die Streifenordnung schmilzt, die mit der Supraleitung im Gleichgewicht konkurriert. Das erste Experiment der vorliegenden Arbeit überprüft diese Interpretation, mittels NIR-Pump-THz-Probe Experimenten an $La_{2-x}Ba_xCuO_4$ in extern angelegten Magnetfeldern. Es wurde dabei versucht, dass empfindliche Gleichgewicht zwischen der Streifenordnung und der supraleitenden Gleichgewichtsphase zu verändern, und die Abhängigkeit der vorübergehend verstärkten/induzierten supraleitenden Eigenschaften vom externen Magnetfeld aufzuzeigen. Es stellte sich heraus, dass sich die Lebensdauer des vorübergehenden supraleitenden Zustandes mit zunehmenden Magnetfeldern signifikant erhöht. Diese Ergebnisse werden als Hinweis darauf interpretiert, dass der lichtinduzierte Zustand nicht durch einfaches optisches Schmelzen der Streifen entsteht, sondern vielmehr durch aktiviertes Tunneln zwischen optisch

angeregten supraleitenden Streifen (die so genannte Pair Density Wave) in benachbarten Ebenen.

Das zweite Experiment dieser Arbeit hat einen anderen Ansatz um das Verständnis der Beziehung zwischen der Streifenordnung und der Supraleitung zu untersuchen. Ausgehend von der Entdeckung der Existenz einer dritten Harmonischen der THz-Strahlung, welche durch nichtlineare Josephson-Tunnelströme in der Streifenphase erzeugt werden, sagen numerische Simulationen voraus, dass durch die Anregung der Probe mittels eines THz-Pump Pulses große Amplituden eines nichtlinearen Josephson-Tunnelns gefunden werden können. Die dabei durch elektrische Felder induzierte zweite Harmonische (EFISH) wird als ultraschnelles Voltmeter eingesetzt, um den Spannungsabfall über die durch den Josephson Effekt gekoppelten CuO_2-Ebenen in $La_{2-x}Ba_xCuO_4$ zu überwachen. Es zeigt sich, dass Spannungsanomalien, die mit 2π-Phasenverschiebungen verbunden sind, nicht nur im supraleitenden Zustand, sondern auch in der normalen, gestreiften Phase nachgewiesen werden können.

Die Ergebnisse in dieser Arbeit vorgestellten liefern weitere Beweise für eine bereits existierende Josephson-Kopplung in der Streifenphase, die durch optische Anregung oder in einem hochgradig nichtlinearen Antriebsregime aktiviert werden kann.

Table of Contents

1. Introduction

In certain materials, notably many elemental metals and certain alloys, when the temperature is cooled below the so-called critical temperature T_C, the sample undergoes a dramatic transition from a metal into a state characterised mainly by two physical properties: zero electrical DC resistance and the Meissner effect. The former, as the name suggests, is when the electrical resistance, as measured by placing the sample in a circuit with an external constant current source and measuring the resulting voltage drop across the sample, drops to zero. Figure 1-1 (a) shows the result of Heike Kamerlingh Onnes' first observation of a sharp drop in resistivity across a narrow transition in mercury. The latter is when a sample is placed in a weak magnetic field, non-dissipative supercurrents form inside the sample and screen the external magnetic field, which decays exponentially over a characteristic depth, known as the London penetration depth, to zero within the bulk of the material (Meissner and Ochsenfeld 1933). Figure 1-1 (b) illustrates the effect of expulsion of the magnetic field when T_C is crossed. Taken together, the phenomenon underlying these two characteristics is known as superconductivity (Tinkham 2004).

Superconductivity was discovered in the year 1911 by H. K. Onnes in Leiden, the Netherlands, soon after his success in liquifying helium in 1908 (Onnes 1911). As a result of

(a) (b)

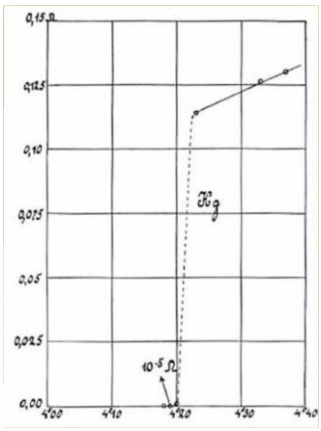

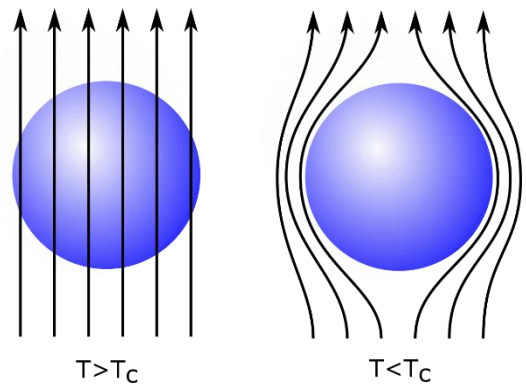

Figure 1-1: (a) Zero resistance (Onnes 1911) and (b) Meissner effect in a superconductor below the critical transition temperature T_C

the disappearance of electrical resistance, H. K. Onnes subsequently demonstrated persistent currents in a coil of lead wire, immersed in liquid helium cooled to 1.8 K, in absence of any external source. Excitement spread quickly after the discovery, but it was not until more than four decades later a satisfactory microscopic theory of this phenomenon was produced by John Bardeen, Leon Cooper, and Robert Schrieffer (BCS) (Van Delft and Kes 2010).

In the 1950s, a series of important developments on possible attractive interactions between electrons mediated by phonons came into being (Fröhlich 1950, Bardeen and Pines 1955). Later, Cooper showed that this arbitrarily small attraction can in fact lead to the formation of bound pairs of electrons, dubbed Cooper pairs (Cooper 1956). Finally in 1957, Bardeen, Cooper, and Schrieffer assembled the pieces together and published the first microscopic theory of superconductivity, which predicts, at sufficiently low temperature, an instability of the Fermi sea and the condensation of electrons into a new ground state through Cooper pairing (Bardeen, Cooper et al. 1957). The paired electrons acting as the lossless charge carriers occupy states of equal and opposite momenta and spin, and a Cooper pair has a spatial extension on the order of the coherence length, a quantity related to the Fermi velocity and the critical temperature of superconducting transition of the material, usually in the range from tens of nanometres to a micrometre. The theory further predicts a macroscopic wavefunction for the entirety of all the condensed electron pairs as well as the existence of a characteristic energy gap between the bound state and the excited state where a Cooper pair is broken up into quasiparticles (Kittel 1976). Bardeen, Cooper, and Schrieffer were jointly awarded the Nobel prize in physics in 1972 for this milestone achievement in understanding superconductivity.

Despite the tremendous success of the BCS theory in describing superconductivity in metals and alloys, J. Georg Bednorz and K. Alex Mueller discovered, in the year 1986, superconductivity in lanthanum barium copper oxide ($La_{2-x}Ba_xCuO_4$, also known as LBCO), a lanthanum-based cuprate perovskite material, which has a surprisingly high critical temperature of 35 K. This was the first time a T_C exceeding 30 K was measured, an upper limit set by the BCS pairing mechanism and the Debye frequency. Subsequently, many other layered materials with similar structures, primarily in the cuprate families, were discovered to have T_C well over 100 K, hence dubbed High-Temperature Superconductors (HTS). The BCS theory is unable to explain such high critical temperatures, and the lack of isotope effect (see Chapter 2) in cuprates alludes to a “glue” different from the BCS pairing mechanism that

supports such high T_C. What makes the new discoveries particularly significant is the fact that transition temperatures above 77 K, the boiling point of nitrogen, have profound implications in practical applications of superconductivity. Liquid nitrogen as a cryogen is much cheaper to produce than liquid helium, and has significantly less strict requirements on storage and transport. The broader range of applications enabled by the high T_C failed to materialise, however, partly because these materials turned out to be technically difficult to manufacture in useful forms like wires (Tinkham 2004).

As illustrated in Figure 1-2, over the years after the discovery of LBCO as the first HTS, new families of compounds with high T_C have regularly been discovered, such as iron-based and organic superconductors. Applying very high pressure (>150 gigapascals) was found to give rise to T_C in excess of 200 K in hydrogen sulphide (Drozdov, Eremets et al. 2015). Recently, room-temperature superconductivity has been shown to be possible under extremely high pressure (>250 GPa) in carbonaceous sulphur hydride (Snider, Dasenbrock-Gammon et al. 2020).

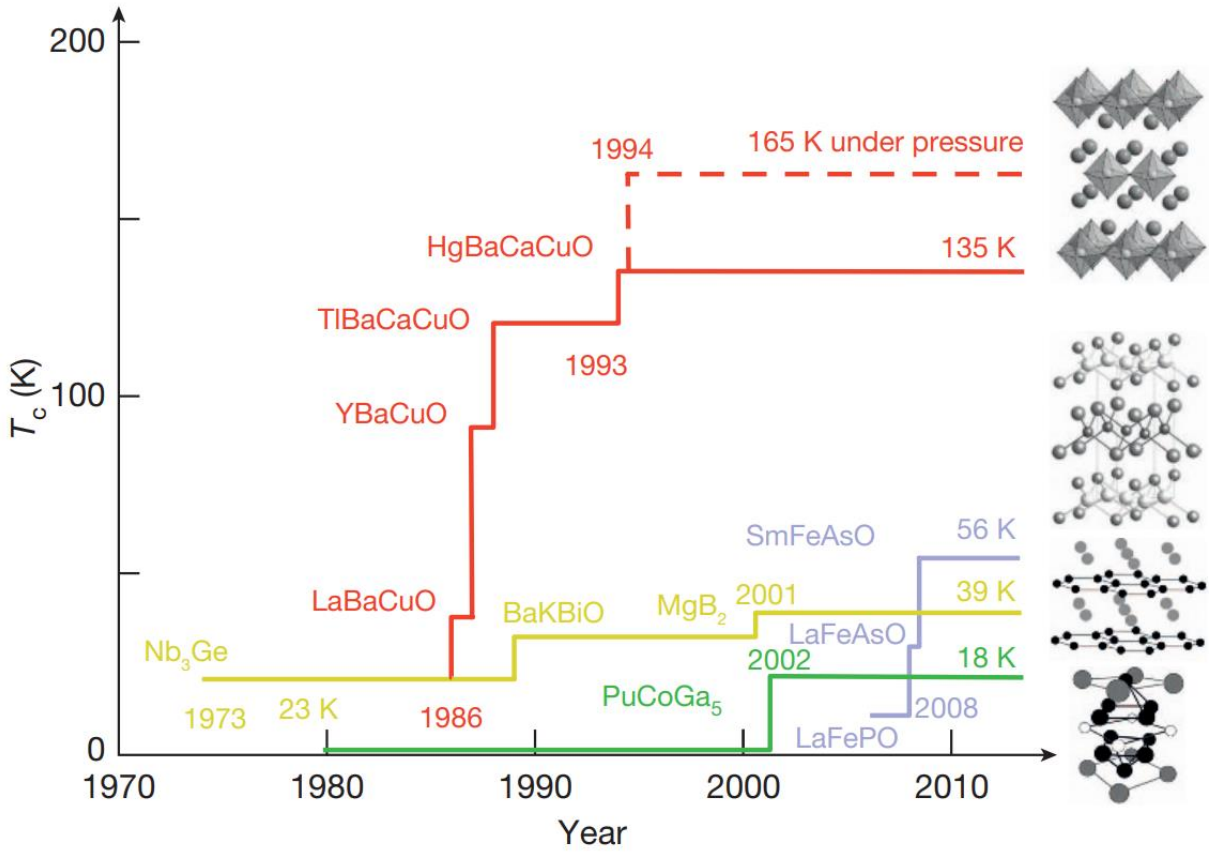

Figure 1-2: Superconducting transition temperatures versus year of discovery for various classes of superconductors with illustrations of the respective crystal structures on the right. Reprinted by permission from Springer Nature: (Keimer, Kivelson et al. 2015).

Another novel avenue towards superconductivity at higher temperatures has been revealed through the phenomenon known as light-induced superconductivity, where, upon photoexcitation tuned to certain resonances in the material, transient states displaying characteristic properties consistent with a superconducting-like behaviour over a short period of time at temperatures far above the equilibrium T_C (Cavalleri 2018), up to one nanosecond in an alkali-fulleride K_3C_{60} (Budden, Gebert et al. 2021). Among them, one specific family of cuprates, LBCO, has been of particular interest. LBCO has a layered structure common to many cuprates, where superconducting copper oxide planes are separated by insulating regions containing La, Ba ions as a charge reservoir, doping holes into the CuO_2 planes, and Josephson tunnelling of Cooper pairs between the planes lead to three-dimensional superconductivity. In this compound, the coexistence of a so-called "stripe" phase, in which doped holes form one-dimensional chains within two-dimensional CuO_2 planes, with superconductivity presents a unique playground for investigating the interaction between different macroscopic orders. It has been found previously that high-energy photoexcitation above T_C in the stripe phase at certain dopings leads to transient emergence of superconducting behaviour (Nicoletti, Casandruc et al. 2014).

In particular, the observation in LBCO reveals an interesting connection to the theoretical postulation and experimental evidence for a kind of spatially modulated superfluid condensate, known as the pair density wave (PDW, see Chapter 2 for detail). The stripes have been shown to decouple the copper oxide planes and hence frustrate interlayer Josephson tunnelling, causing a suppressed T_C at dopings where they are stabilised and robust (Berg, Fradkin et al. 2007, Berg, Fradkin et al. 2009). However, more recent findings point to possible pre-existing formation of Cooper pairs at temperature far above T_C and behaviour consistent with the PDW picture (Rajasekaran, Okamoto et al. 2018). Therefore, a key question to be asked is, whether the light induced state is merely a result of the optical melting of the stripes to relieve the frustration, or whether the stripes are indeed a form of the PDW that can be excited through strong perturbation to the system. These are the questions this thesis sets out to investigate.

The main approach of both experiments presented in this thesis is to make use of ultrafast terahertz (THz) techniques to study out-of-equilibrium response of the LBCO cuprate superconductor. In the first experiment, the dynamic response after strong excitation is carefully mapped out as a function of an externally applied magnetic field, essentially

introducing a third dimension to the typical temperature-doping phase diagram of the material. Here, the main focus is on using the magnetic field as a tuning knob to finely control the delicate balance between different orders in the ground state. The magnetic field plays an important role, because of its strong influence on the strength of the stripes (Berg, Fradkin et al. 2009, Hücker, v. Zimmermann et al. 2013), by creating alternative starting points from which the light induced transient state emerges, which are inaccessible through cooling or chemical doping alone. The results reveal new evidence consistent with the PDW interpretation.

The second experiment follows a similar path to that of (Rajasekaran, Casandruc et al. 2016) and combines strong field THz excitation with a novel probe in search of more convincing signatures of local Josephson tunnelling in the stripe phase of LBCO, the structure of which can be approximated as a stack of Josephson junctions (Kleiner, Aigner et al. 1994). Here, a special kind of optical probe based on Electric Field Induced Second Harmonic (EFISH) is able to sensitively measure the instantaneous voltage drop between copper oxide planes (von Hoegen, Fechner et al. 2019), which is a direct function of the Josephson phase excursion. Here, the Josephson phase is driven to amplitudes by the THz electric field so large that it "slips" to a neighbouring minimum instead of returning to its original equilibrium position after the driving field is gone. Such phase slips can be readily reproduced by simulating the response of a long Josephson junction under the influence of a "non-perturbative" force, i.e. one exceeding the common regime of nonlinear perturbation. It was found that signatures of phase slips can be detected also above T_C, all the way up to the charge-order transition temperature. This is taken as a strong indication of Josephson coupling in the normal, striped phase, the response of which is visible only under strongly nonlinear excitation. The experimental data agrees with the simulation and yields further evidence supporting the PDW picture for the stripe phase. Taken together, these experiments provide compelling insights in the nature of interaction between superconductivity and other macroscopic orders such as the stripes, and serve to point future investigations in potential directions of intriguing findings.

To this date, a comprehensive understanding of the underlying mechanism to explain the unconventionally high transition temperatures of these HTS is still lacking, thus making fabrication of new compounds with T_C close to room temperature under atmospheric pressure a journey in the dark. Nevertheless, it is the goal of this thesis to advance the current

understanding of HTS and explore new functionalities out of equilibrium on ultrafast timescales at temperatures far above the equilibrium T_C.

This thesis is structured as follows. Chapter 2 introduces in detail the fundamentals of conventional and high-T_C superconductivity as well as highlighting the complex landscape of competing quantum orders at low temperatures in several cuprate superconductors with an emphasis on LBCO. In Chapter 3, a quick review of several experimental studies is given as examples of utilising ultrafast photoexcitation to control the superconducting order in cuprates. Chapter 4 explores extensively the Josephson effect and its application to LBCO's c-axis dynamics through the use of numerical simulation and relevant experimental confirmations. Chapter 5 presents the first main experiment of this thesis in which I studied carefully the interplay between the light-induced transient superconductivity in LBCO and an externally applied magnetic field, where observations contradict the conventional wisdom that strong magnetic fields tend to impair superconducting robustness. In the following Chapter 6, I report the second experiment of this thesis in which more convincing evidence for the existence of pre-formed pairs of superconducting carriers above the critical temperature is reported in the same material, again through the use of ultrafast pump-probe techniques involving THz light. Finally, the thesis concludes with a summary and an outlook in Chapter 7.

2. Superconductivity and competing orders in high-T_C cuprates

2.1 Introduction to conventional superconductivity

2.1.1 General properties and the London equations

After the initial discovery of superconductivity in mercury at the temperature of 4.19 K by Onnes in 1911, a number of other materials have been found to display similar electrical characteristics at low temperatures. This is the case for many elemental metals such as lead at 7 K, niobium at 9.2 K, as well as compounds like niobium nitride with T_C = 16 K. This novel state, where all electrical resistance seemed to vanish turned out to possess yet another property, as discovered by the German physicists Walther Meissner and Robert Ochsenfeld in 1933, where a weak magnetic field initially penetrating a sample in the normal state gets expelled completely once it is cooled below the critical transition temperature T_C, which became known as the Meissner Effect. This suggests that the superconducting state is fundamentally different from a perfectly conducting metal, because, in the case of the latter, magnetic flux would be expected to remain trapped inside rather than being expelled.

These two characteristics, perfect DC conductivity and perfect diamagnetism, became the defining criteria of a superconductor. In 1935, the brothers Fritz and Heinz London proposed two equations to explain the phenomenology of superconductivity (London and London 1935). Later known as the London equations, they describe the microscopic electric and magnetic fields inside a superconductor as

$$E = \frac{m}{n_s e^2}\frac{\partial J_s}{\partial t}$$

$$B = -\frac{m}{n_s e^2} \nabla \times J_s$$

where J_s is the superconducting current density, *e* the electron charge, *m* the electron mass, and n_s a phenomenological parameter associated with the number density of superconducting carriers, which varies continuously from 0 at T_C to an asymptotic value of a small fraction of *n*, the total number of conducting carriers in the system, as the temperature approaches zero.

The first equation describes perfect conductivity. An applied electric field induces an accelerating current, rather than simply sustaining a constant one as Ohm's law would imply in a normal conductor, because there is no electrical resistance to oppose the motion of charges. The second equation, when combined with Ampere's Law $\nabla \times B = \frac{4\pi}{c} J$, yields

$$\nabla^2 B = \frac{1}{\lambda_L^2} B$$

where $\lambda_L = \sqrt{\frac{mc^2}{4\pi n_s e^2}}$ is the London penetration depth, and *c* the speed of light. In this form, the Meissner effect is an obvious solution, where a non-zero magnetic field gets screened exponentially in the interior of a superconductor over a characteristic length scale as $B(x) = B(0)e^{-\frac{x}{\lambda_L}}$, where *x* is assumed to be the distance from the sample surface, as illustrated in Figure 2-1. The screening is a result of the formation of persistent supercurrents which generate a counteracting magnetic field but do not decay over time due to zero electrical resistance.

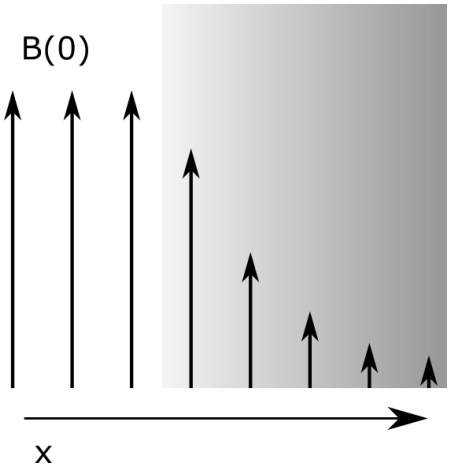

Figure 2-1: Illustration of the screening of the magnetic field from the surface, where B(0) is the field in vacuum, and inside the material the field decays as $B(x) = B(0)\,exp(-x\,/\,\lambda_L)$. The London penetration depth λ_L denotes the distance over which the field amplitude is reduced to $1/e$ of the value at the surface.

2.1.2 The Ginzburg-Landau theory

In 1950, the Ginzburg-Landau (GL) theory achieved another important milestone in developing a phenomenological description of macroscopic superconductivity. Vitaly Ginzburg and Lev Landau proposed a complex pseudo-wavefunction ψ as an order parameter within Landau's general theory of second order phase transitions, and a free energy *F* as a function of not only the order parameter itself but also its gradient (Ginzburg and Landau 1950).

The wavefunction ψ gives the local density of superconducting electrons as $n_s(\vec{r}) = |\psi(\vec{r})|^2$, where n_s is the superfluid density as defined in the London equations in Section 2.1.1. This quantity acts as the order parameter because it goes to zero in the normal state and is nonzero below the phase transition to the superconducting state. Then, it is argued that the free energy of a superconducting condensate can be expressed by the variational principle and a series expansion in powers of ψ and $\nabla\psi$ with coefficients α and β, and minimising the free energy with respect to ψ and vector potential *A* yields the following equations

$$\alpha(T)\psi + \beta(T)|\psi|^2\psi + \frac{1}{2m^*}\left(-i\hbar\nabla - \frac{e^*\boldsymbol{A}}{c}\right)^2\psi = 0$$

$$\boldsymbol{J_s} = -\frac{ie^*\hbar}{2m^*}(\psi^*\nabla\psi - \psi\nabla\psi^*) - \frac{e^{*2}}{m^*c}|\psi|^2\boldsymbol{A}$$

where m^* is the effective mass and e^* the charge of the superfluid carrier in a magnetic field with vector potential *A*.

The first equation describes an order parameter ψ dependent on the vector potential *A* in a form analogous to the nonlinear Schrödinger equation for a free particle. The second equation gives the superconducting current density in a form analogous to the probability current of a wavefunction. Together, these two equations address two features beyond the scope of the London theory: the spatial variation of n_s and nonlinear effects in presence of magnetic field exceeding certain critical thresholds, commonly denoted as H_C. These are relevant in an intermediate state of the superconductor in which normal and superconducting regions coexist.

In addition to rewriting the London penetration depth now in terms of the order parameter ψ as

$$\lambda = \sqrt{\frac{m^* c^2}{4\pi|\psi|^2 e^{*2}}}$$

the next crucial insight by the GL theory is the introduction of a characteristic length scale now called the GL coherence length,

$$\xi(T) = \frac{\hbar}{\sqrt{|2m^*\alpha(T)|}} = \frac{\Phi_0}{2\sqrt{2}\pi H_c \lambda}$$

where Φ_0 is the magnetic flux quantum. The GL coherence length defines the distance over which the wavefunction ψ can change without undue energy increase, i.e. without destroying the superconducting state.

Furthermore, the ratio of these two length scales can be defined as

$$\kappa = \frac{\lambda}{\xi}$$

the so-called GL parameter. For conventional elemental superconductors, the coherence length is much larger than the penetration length, hence $\kappa \ll 1$; these materials are also called the Type I superconductors, and displays almost perfect diamagnetism until the critical field H_c is reached.

However, in 1957, Alexei Abrikosov published results showing a different kind of behaviour in magnetic fields (Abrikosov 1957). Rather than a discontinuous breakdown of superconductivity at H_c, continuous penetration of magnetic flux into the superconductor is

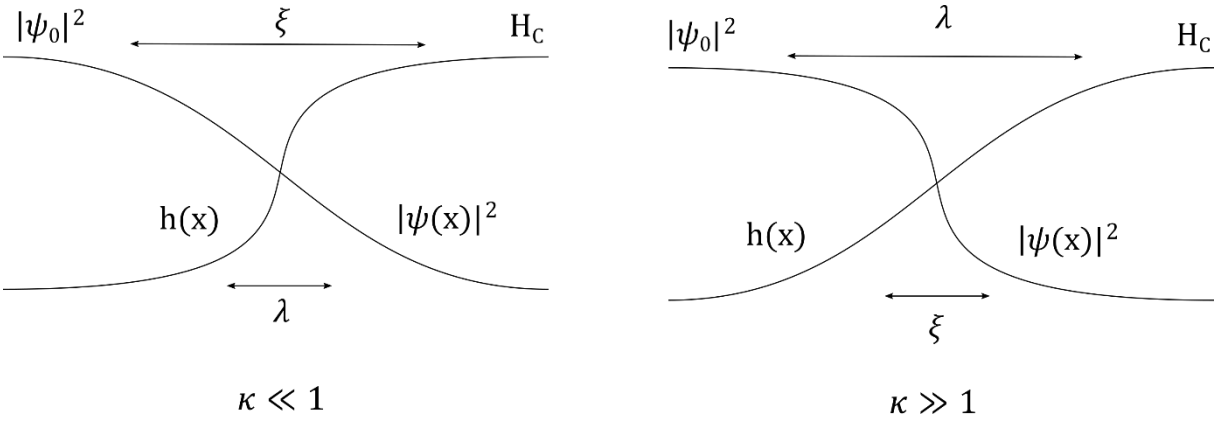

Figure 2-2: The order parameter magnitude $|\psi(x)|^2$ and local magnetic field $h(x)$ as a function of position close to the interface between superconducting and normal domains, where $|\psi_0|^2$ and H_c are the maximum values, respectively. In a Type I superconductor (left), the superfluid density varies over a longer distance than magnetic field. In a Type II superconductor (right), the opposite is true.

observed, when the applied field is greater than a lower threshold H_{c1} but not exceeding a higher limit H_{c2}. Beyond H_{c2}, superconductivity is destroyed completely. This is now known as the Type II superconductor. The difference between the two types is illustrated in Figure 2-2.

2.1.3 The BCS theory

It was not until half a century later since Onnes' initial discovery, in 1957, a first satisfactory microscopic theory of superconductivity was developed by J. Bardeen, L. N. Cooper and J. R. Schrieffer (BCS), but a few other crucial discoveries in the 1950s laid the foundation for the final formulation of the BCS theory. The first of them is the isotope effect. Discovered independently by Emanuel Maxwell (Maxwell 1950) and C. A. Reynolds et al. (Reynolds, Serin et al. 1950), a proportionality relation was observed among isotopes of Hg where the T_C scales as the inverse square root of the isotopic mass M, i.e. $T_c \propto M^{-0.5}$. The isotope effect was subsequently measured in other superconductors like Sn, Pb, and Tl (de Launay 1954) with similar values for the power of mass, and motivated the reasoning that superconductivity depends on factors other than the electrons and potentially lattice vibrations also play a role.

The next major advance was developed by Herbert Fröhlich (Fröhlich 1950) and later by John Bardeen and David Pines (Bardeen and Pines 1955). It was postulated that an attractive force between electrons can be mediated by phonons via electron-phonon coupling.

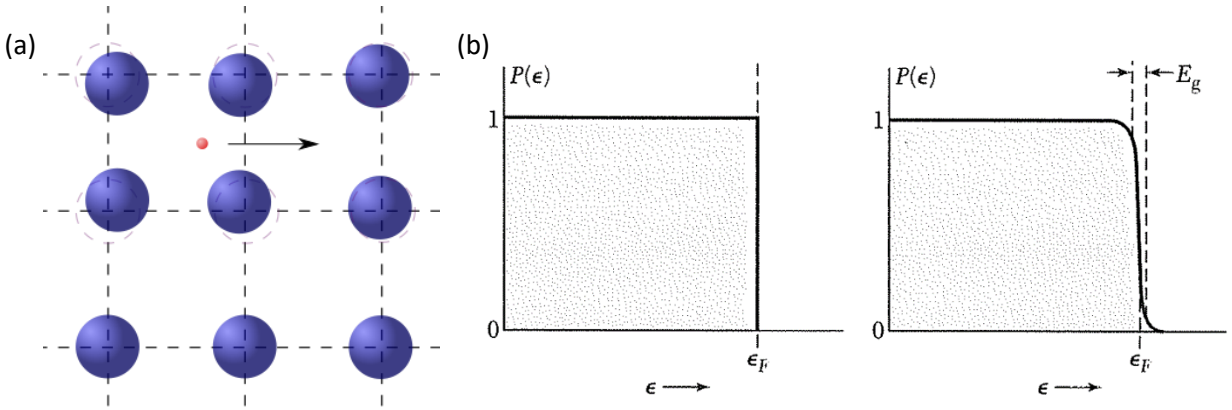

Figure 2-3: (a) Attractive interaction between electrons mediated by the lattice (phonons). (b) Left: occupation of states in the ground state of a non-interacting Fermi gas; Right: the BCS ground state with a gap of width $E_g = 2\Delta$ near the Fermi level. Reprinted by permission from John Wiley and Sons: (Kittel 1976).

An intuitive picture is illustrated in Figure 2-3 (a). When an electron passes through the lattice, it attracts the positive ions from their equilibrium positions and creates a polarisation. Along its trail, the electron leaves behind a lattice distortion. If a second electron enters this neighbourhood before the ions relax back to their original positions, the local dipole moment will lead to lowered energy for the electron because the Coulomb repulsion from the first one is screened by the ions. In essence, this mechanism results in an attractive interaction between the two electrons.

In 1956, Leon Cooper showed that an arbitrarily weak attraction can lead to pairing of electrons with equal and opposite momenta and spins into a bound state, i.e. the Cooper pairs, arguing that the Fermi sea is unstable against the formation of at least one bound pair (Cooper 1956). This is the last missing piece of the puzzle from which the complete formulation of the BCS theory finally resulted. Given Cooper's postulate, it can be shown that Cooper pairs would condense until some kind of equilibrium is reached, which occurs when the state of the system has changed dramatically from the original Fermi sea and the binding energy gained from additional pair formation has gone to zero. Subsequently, in 1957, the BCS theory proposed a macroscopic wavefunction in which all the electrons form pairs, and a new ground state can be found which lowers the total energy by having a fraction of the paired electrons close to the Fermi level condense, and an energy gap opens up at the Fermi level (see Figure 2-3 (b)).

The concept of a coherence length is also central to the BCS theory. Denoted by ξ, similar to the GL theory, the coherence length describes the spatial dimension of a Cooper pair. The centre-of-mass coordinates of many interacting pairs lie within a sphere of diameter ξ. The entire superfluid condensate can be thought of as consisting of a large number of overlapping pairs with phases locked. The theory also predicts that a minimum energy is required to break such a pair to produce two quasi-particle excitations. As illustrated in Figure 2-4 (a), this minimum energy, $E_g = 2\Delta(T)$, is predicted to scale with temperature as

$$\frac{\Delta(T)}{\Delta(0)} \approx 1.74\left(1-\frac{T}{T_c}\right)^{\frac{1}{2}}$$

increasing from zero at T_C to a limiting value

$$E_g(0) = 2\Delta(0) = 3.528 k_B T_C$$

as $T \to 0$, where k_B is the Boltzmann constant.

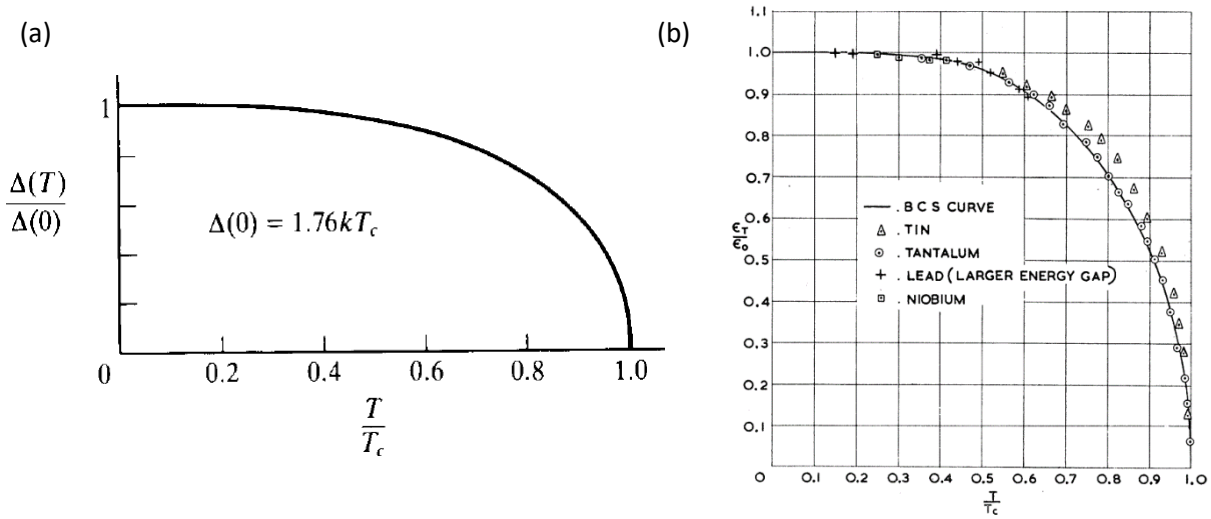

Figure 2-4: (a) A typical temperature dependence of the superconducting energy gap predicted by the BCS theory. Figure taken from (Tinkham 2004). (b) Experimental measurements of the gap in Nb, Ta, Sn, and Pb plotted on top of the BCS prediction. Reprinted with permission from (Townsend and Sutton 1962) Copyright 2022 by the American Physical Society.

Since its initial publication, the validity of the BCS theory has been supported by numerous experiments. Electron tunnelling has been shown to confirm the density of excited states above the gap as well as the quantitative correctness of the electron-phonon coupling mechanism (Tinkham 2004). As shown in Figure 2-4 (b), experimental data of the temperature-dependent energy gap in Nb, Ta, Sn, and Pb is found to be in good agreement with the theory (Townsend and Sutton 1962). The isotope effect is also accounted for in the BCS theory, although non-elemental-metallic superconductors seem to deviate from the prediction (Bill, Kresin et al. 1998).

Despite its ground-breaking success in providing the first comprehensive framework to describe the pairing mechanism and accurately predicting many thermodynamic quantities for elemental superconductors, the BCS theory did not anticipate materials with critical temperatures much higher than the record at that time, i.e. Nb_3Ge with T_C = 23 K. Consequently, the discovery of unconventional superconductivity with T_C exceeding 100 K in the 1980s caused the next upheaval in the field.

2.2 High temperature superconductivity

2.2.1 Cuprate superconductors

The BCS theory failed to account for the anomalously high critical temperatures of a family of ceramic materials discovered in 1986 by J.G. Bednorz and K.A. Müller, later known as the cuprates (Bednorz and Müller 1986). The discovery opened up a new path in the race towards higher critical temperatures that had been seeing somewhat slow progress for decades, and a new term was coined to describe these materials, namely High Temperature Superconductors (HTSC), generally meaning ones with T_C above 30 K, differentiating from the "conventional" superconductors. The very first among them was the lanthanum barium copper oxide ($La_{2-x}Ba_xCuO_4$), or LBCO, with T_C up to around 35 K (see Figure 2-5). Soon after, a number of new entrants such as $YBa_2Cu_3O_{7-x}$ (YBCO) and $Bi_2Sr_2CaCu_2O_{8+x}$ (BSCCO) were found to have T_C in excess of 100 K. This discovery was of profoundly significant because the boiling point of nitrogen is 77 K. Having a T_C above this threshold allows the use of liquid nitrogen as the cooling agent, which is much cheaper and easier to produce than liquid helium, expanding the practical applications of these superconductors greatly.

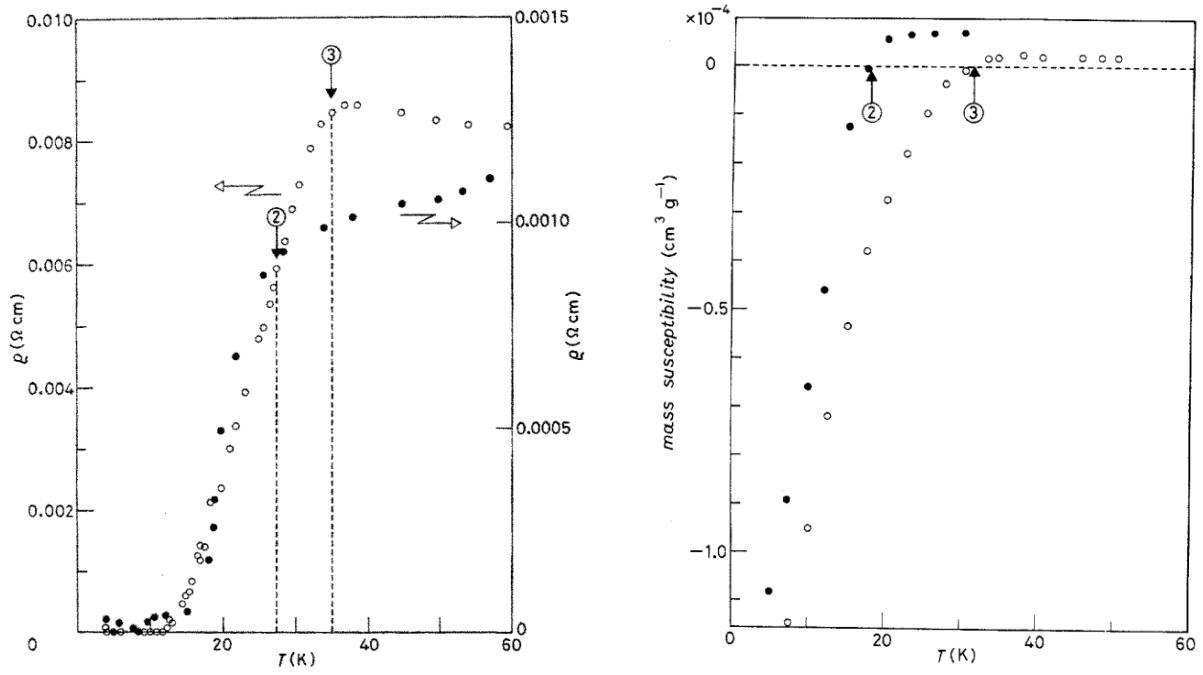

Figure 2-5: (Left) Resistivity measurements showing superconducting transition onset around 35 K; (Right) Magnetic susceptibility measurements showing onset around 35 K. From (Bednorz, Takashige et al. 1987).

One commonality among the high- T_C cuprate superconductors is the layered structure of superconducting copper oxide planes separated by insulating regions of ions such as lanthanum and barium (see Figure 2-6). The ions serve as the charge reservoir, doping holes into the CuO_2 planes. The structure is closely related to the perovskite structure. The CuO_2 planes are superconducting below T_C, but are only weakly coupled through the Josephson effect (see Chapter 5 for detail). Hence the material properties in many ways are close to that of a two-dimensional superconductor, with a large anisotropy in the electric and magnetic properties, also observed above T_C, e.g. a ratio between resistivities in the out-of-plane and in-plane directions (perpendicular or parallel to copper oxide planes) $\rho_c \,/\, \rho_{ab}$ as high as 10^5 (Tinkham 2004). Under strong magnetic fields (~8 T for $La_{2-x}Sr_xCuO_4$, see Section 2.3.2), the superconducting planes even behave as a stack of decoupled, two-dimensional films.

Another important feature of high- T_C superconductors including cuprates is that, they are all Type-II superconductors. As opposed to type-I superconductors such as most elemental metals, which has a single critical magnetic field H_C above which superconductivity is destroyed in the bulk, type-II superconductors have an intermediate phase between two critical field values, H_{C1} and H_{C2}, in which the magnetic field penetrates into the bulk in the form of vortices, where a loop of supercurrent encircles a normal-state core containing one

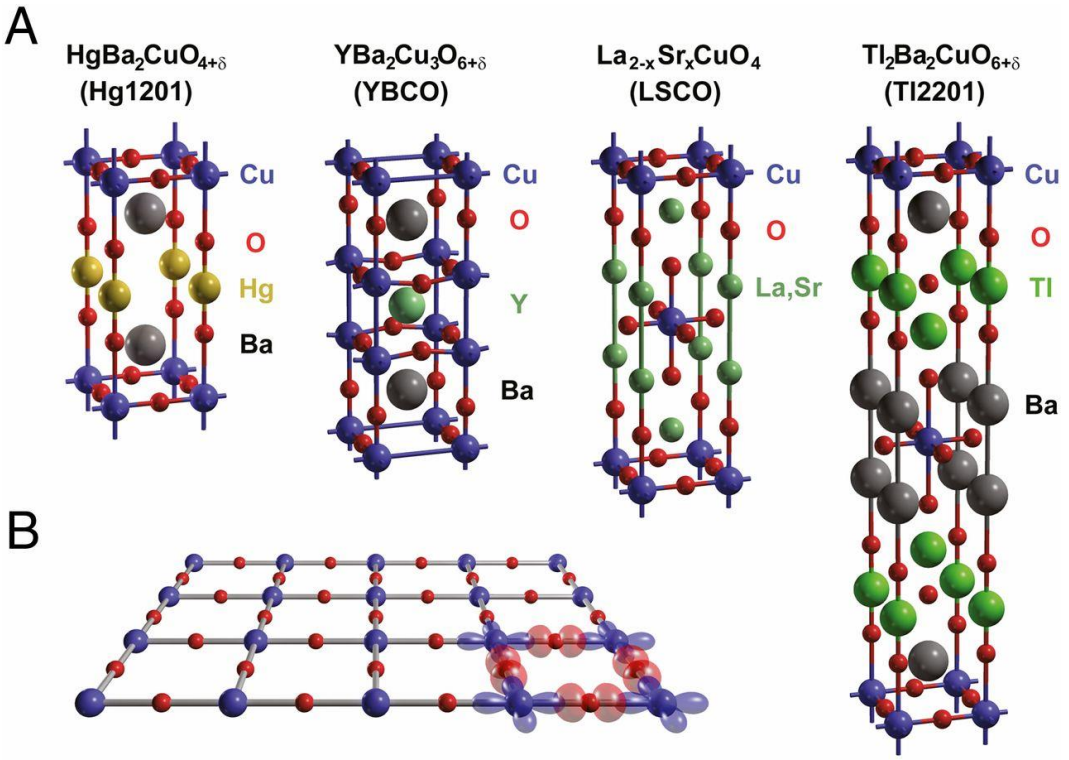

Figure 2-6: Crystal structures of four cuprates: (A) the unit cells and (B) the copper oxide plane. From (Barišić, Chan et al. 2013).

quantum of magnetic flux. Above H_{C2}, superconductivity breaks down as in type-I materials. if a piece of cuprate superconductor is cooled in an external field between H_{C1} and H_{C2}, magnetic flux can become trapped inside, a phenomenon known as flux pinning, which enables the sample to be suspended over a magnet, with many practical applications such as frictionless joints and transportation.

A convenient way to model this kind of layered structure in a superconductor is the Lawrence and Doniach (LD) formalism, proposed by W. E. Lawrence and S. Doniach (Lawrence and Doniach 1970). Here, the layered superconductor is modelled as a stack of two-dimensional superconducting sheets, each having its own GL order parameter $\psi_n(x,y)$, coupled together by Josephson tunnelling between neighbouring layers. The anisotropy is accounted for by setting different masses m_{ab} and m_c to reflect the different modes of transport in the in-plane and out-of-plane directions, while ignoring the relatively small anisotropy in the *ab* plane. As a result, the coherence length is also highly anisotropic, as

$$\xi_i(T) = \frac{\hbar}{\sqrt{|2m_i\alpha(T)|}}$$

where *i* corresponds to a particular crystallographic axis. In the case of weak interlayer coupling, $m_{ab} \ll m_c$, and hence $\xi_{ab} \gg \xi_c$.

Similarly, anisotropy for the penetration depth λ_i is the inverse of ξ_i, because

$$2\sqrt{2}\pi H_c(T)\xi_i(T)\lambda_i(T) = \Phi_0$$

Note that here λ_i defines the screening by supercurrents flowing along the *i*-th axis, not the screening of a magnetic field along the *i*-th axis. Furthermore, the anisotropy of the critical magnetic fields can be derived by considering $H_{c1} \sim 1 / \lambda^2$ and

$$H_{C2\|c} = \frac{\Phi_0}{2\pi\xi_{ab}^2}$$

$$H_{C2\|ab} = \frac{\Phi_0}{2\pi\xi_{ab}\xi_c}$$

and it can be shown that $H_{c1\|ab} \ll H_{c1\|c}$ and $H_{c2\|ab} \gg H_{c2\|c}$. For convenience, a dimensionless anisotropy parameter *γ* links all these quantities together as

$$\gamma = \left(\frac{m_c}{m_{ab}}\right)^{\frac{1}{2}} = \frac{\lambda_c}{\lambda_{ab}} = \frac{\xi_{ab}}{\xi_c} = \frac{H_{c1\|c}}{H_{c1\|ab}} = \frac{H_{c2\|ab}}{H_{c2\|c}}$$

Values for γ can vary between ~7 for YBCO and ≥150 for BSCCO (Tinkham 2004).

At the time of this writing, there is no comprehensive theory commanding a consensus on the precise pairing mechanism nor on the high T_C in these materials. It is still debated how different the microscopic mechanism causing high temperature superconductivity is from that found in conventional superconductors described by the BCS theory. Although evidence still points to Cooper pairs of electrons with zero net momentum as the superconducting carriers (Tinkham 2004), including the usual AC Josephson effect frequency $2eV / h$ (Estève, Martinis

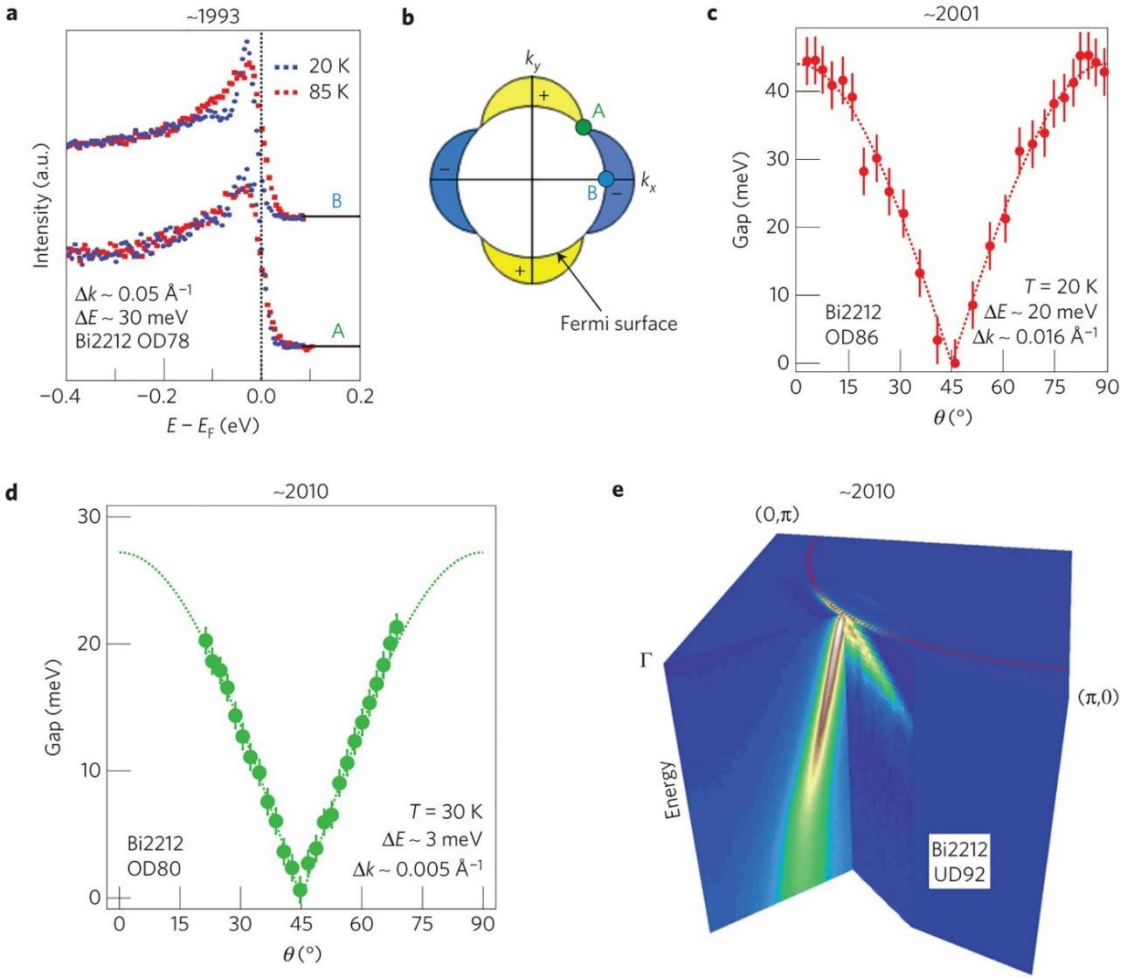

Figure 2-7: (a) Superconducting gap anisotropy first observed in 1993 [reproduced from (Shen, Dessau et al. 1993)]. The lower spectra (A) are taken at the node and the upper spectra (B) at the antinode. (b) Schematic of a d-wave order parameter on a circular Fermi surface. Gap is zero at the node where the superconducting gap changes sign (A) and maximum at the antinode (B). (c) Typical synchrotron gap measurement a decade ago as a function of the Fermi angle ϑ. Error bars indicate uncertainty of determining E_F (±0.5 meV), error from the fitting procedure and an additional 100% margin. (d) Near-nodal gaps measured by a modern laser-based ARPES system with superior resolution and high photon flux. Error bars reflect 3σ error in the fitting procedure and an additional 100% margin. (e) Three-dimensional ARPES data set, showing the quasi-particle dispersions both perpendicular and parallel to the Fermi surface near the node, reproduced from (Vishik, Lee et al. 2010). Reprinted by permission from Springer Nature: (Hashimoto, Vishik et al. 2014).

et al. 1987), the usual size of the flux quantum $hc / 2e$ (Gammel, Bishop et al. 1987, Gough, Colclough et al. 1987, Koch, Umbach et al. 1987), and Andreev reflection along time-reversed trajectories as with conventional superconductors (Hoevers, Van Bentum et al. 1988), d-wave pairing, i.e. a superconducting gap with d-wave-like symmetry as opposed to s-wave symmetry in a conventional BCS superconductor, has been proposed as one possible distinction (Schrieffer, Wen et al. 1989, Monthoux, Balatsky et al. 1991, Monthoux, Balatsky et al. 1992, Monthoux and Pines 1994, Monthoux and Scalapino 1994). Indeed, increasing experimental confirmation of d-wave symmetry of the energy gap has been provided by angle-resolved photoemission spectroscopy (ARPES) measurements (Wells, Shen et al. 1992, Shen, Dessau et al. 1993, Ding, Norman et al. 1996). Figure 2.7 shows a few examples of such measurements. In this thesis, one specific family of cuprate is focused on, namely $La_{2-x}Ba_xCuO_4$. The next few sections will introduce the material in more detail.

2.2.2 The La-214 family compounds

The first high-T_C superconductor discovered, $La_{2-x}Ba_xCuO_4$ belongs to the so-called La-214 family, because its undoped parent compound is La_2CuO_4. As is common to all cuprate superconductors, La_2CuO_4 also has a layered structure. As shown in Figure 2-8 (b), each copper oxide block contains a single CuO_2 plane, and adjacent CuO_2 planes are separated by two layers of LaO. While CuO_2 planes are conducting, LaO layers are insulating. The LaO blocks also act as a charge reservoir, allowing impurity atoms to dope electrons or holes into the CuO_2 planes. The crystallographic unit cell contains two formula units, with equivalent axes *a* and *b* along the planes and *c* perpendicular to them. The crystal structure belongs to the space group I4/mmm (Wesche 2015).

There is now general agreement that La_2CuO_4 is an insulator. It should be metallic based on the tight-binding model, but the insulating behaviour can be explained by the Hubbard model. Here, strong electron-electron repulsion makes charges localised and unable to freely move around carrying electrical currents. In this case, the band is half-filled, which

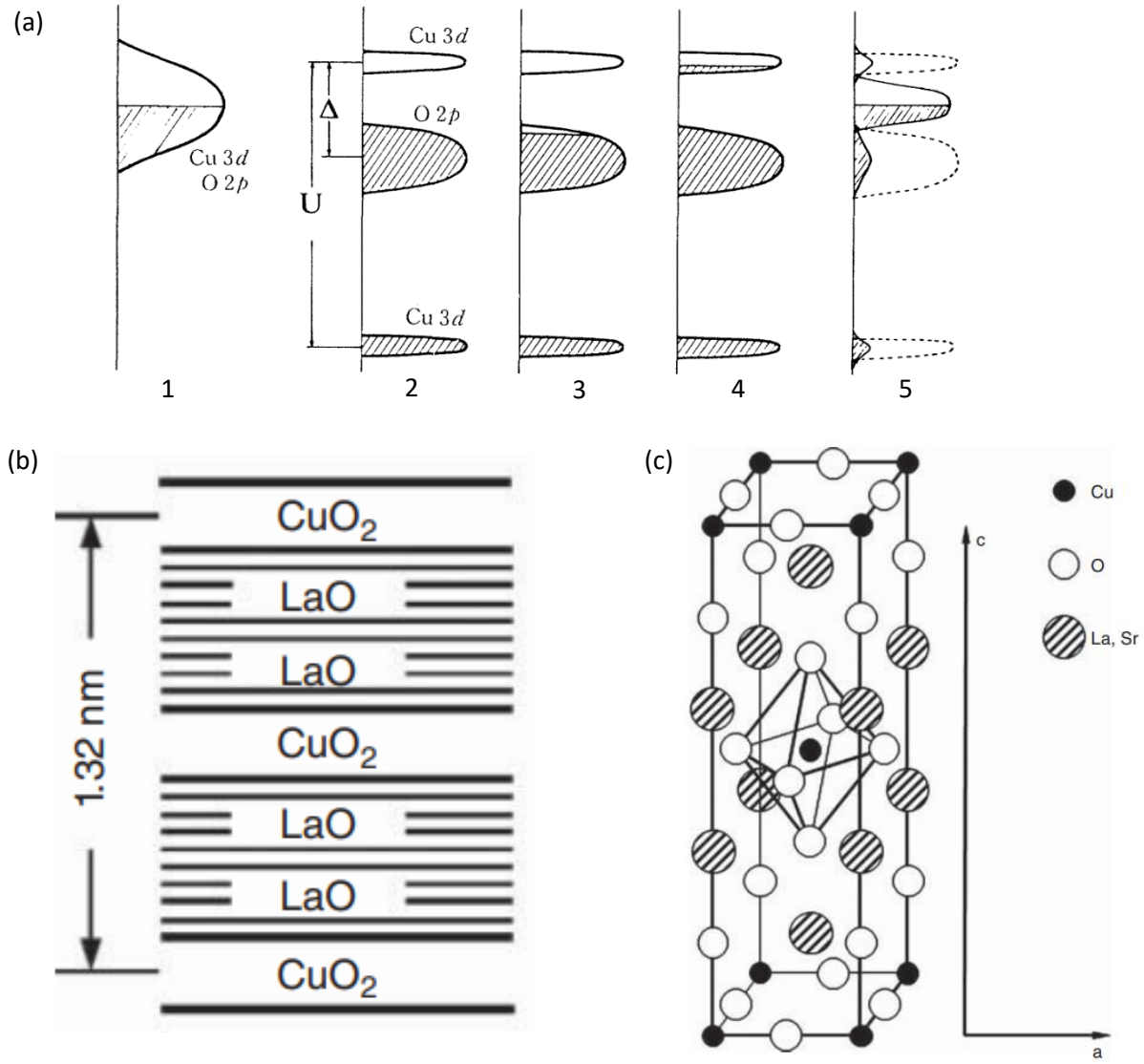

Figure 2-8: (a) Schematic energy diagrams for doped and undoped CuO_2 planes. 1. Band picture for a half-filled (undoped) CuO_2 plane (Fermi liquid). 2. Charge-transfer (CT) insulating state of the undoped CuO_2 plane with split Cu 3d bands due to on-site Coulomb repulsive interaction U. The O 2p band is separated by a charge-transfer energy Δ from the upper Cu 3d band. 3. and 4. show rigid CT energy bands doped with holes and electrons, respectively. 5. An image of the doped CuO_2 plane inferred from experimental measurements. Reprinted with permission from (Uchida, Ido et al. 1991). Copyright 2022 by the American Physical Society. (b) Layering scheme of La_2CuO_4. (c) Schematic of the crystal structure of $La_{2-x}(Ba, Sr)_xCuO_4$. Panels (b) and (c) reprinted by permission from John Wiley and Sons: (Wesche 2015).

would have suggested metallic behaviour, but a strong repulsive energy cost *U* resulting from putting two electrons on the same site dominates over the hopping energy *t*, the charges are essentially bound to their individual ion and are no longer mobile, rendering the ground state an insulator. As a result, the half-filled band splits into two, separated by *U* with the lower Hubbard band being completely filled and the upper Hubbard band empty [see Figure 2-8 (a) 1 and 2]. This also leads to antiferromagnetism (AF) because oppositely aligned spins between neighbouring sites can gain an extra energy $4t^2 / U$ through virtual hopping, also known as

the exchange energy *J (Lee, Nagaosa et al. 2006)*. However, it has been shown that, in fact, a more accurate description of La_2CuO_4 is a so-called charge-transfer (CT) insulator (Zaanen, Sawatzky et al. 1985). Here, the gap corresponds to between the O *2p* and the split Cu *3d* upper Hubbard band, separated by *Δ* rather than *U*.

In the parent compound La_2CuO_4, the oxidation state of lanthanum ions is +3 and that of the copper ions +2. The four O^{2-} ions take up the eight electrons provided by the two lanthanum plus one copper ions. When partial substitution of La^{3+} by Ba^{2+} or Sr^{2+} causes a reduced number of electrons, one Cu^{2+} can become Cu^{3+} in order to maintain charge neutrality, because copper ions can take +1, +2, or +3 oxidation states. A schematic of the structure with substituted ions is shown in Figure 2-8 (c). This is called hole doping. In usual semiconductors, the effect of hole/electron doping on the electronic structure involves the valence band becomes occupied by holes/electrons or impurity states are formed within the gap [see Figure 2-8 (a) 3 and 4], but in La_2CuO_4 it's not the whole picture. In fact, a redistribution of states that fills up the CT gap is found as a result of hole doping by transferring states from both the conduction band and the valence band of the undoped parent insulator [see Figure 2-8 (a) 5] (Uchida, Ido et al. 1991).

Hole doping corresponds to the right half of generic phase diagram shown in Figure 2-9, where the parent compound sits in the middle at $x = 0$ with a high AF ordering temperature. The AF order is quickly suppressed and disappears by a 3-5% hole concentration, and almost immediately after the suppression of AF, superconductivity emerges for a wide range of dopings, from ~6% to ~25%. On the left half of the diagram, corresponding to electron doping, the AF order is more robust and survives up to x = 14%, beyond which superconductivity also appears *(Lee, Nagaosa et al. 2006)*.

Taking $La_{2-x}Sr_xCuO_4$ (LSCO) as an example, the superconducting dome has a peak for x = 16%, with T_C = 36 K. This is known as the optimal doping level. The region to the left of the optimal doping the phase diagram on the hole doping side is the underdoped region, whereas to the right of it is the overdoped region. The region above the superconducting T_C in the underdoped side has been of a hot topic of study (Emery and Kivelson 1995, Varma 1999, Chakravarty, Laughlin et al. 2001), known as the pseudogap phase, where a partial gap opens up in some parts of the Fermi surface while others retain their conducting properties (Timusk and Statt 1999). The pseudogap phase has a transition temperature T^* which decreases

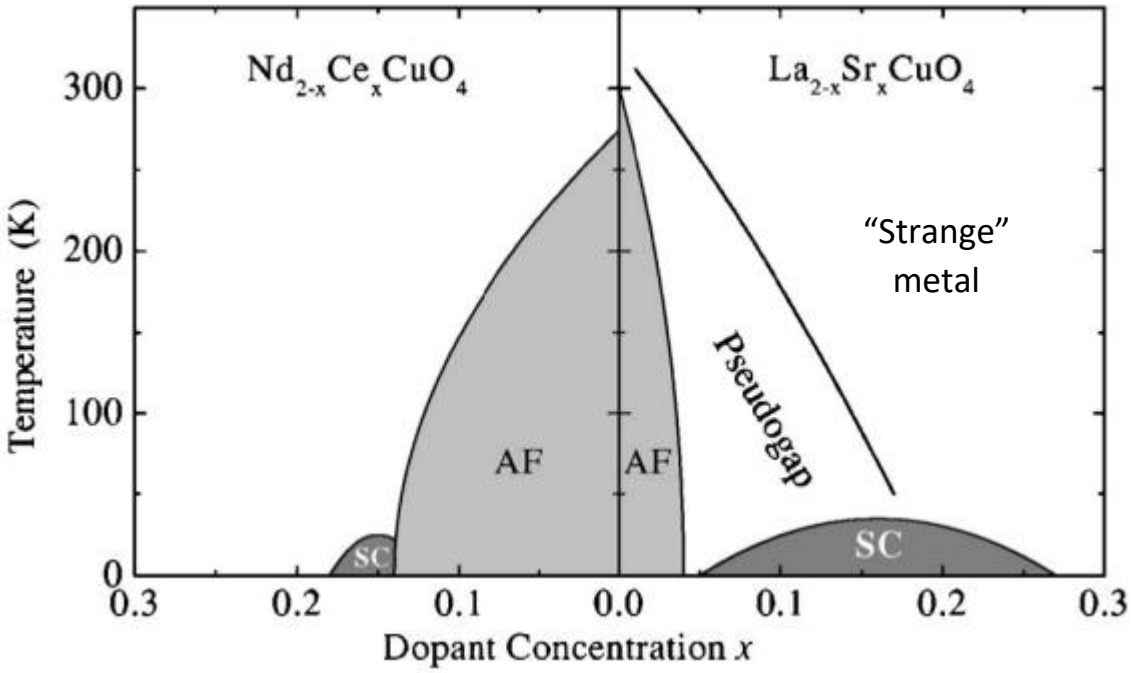

Figure 2-9: A generic phase diagram of electron- or hole-doped cuprate superconductor, showing superconductivity (SC), antiferromagnetism (AF), pseudogap, and "strange" metal regions. Reprinted with permission from (Damascelli, Hussain et al. 2003). Copyright 2022 by the American Physical Society.

monotonically with increasing hole concentration (Doiron-Leyraud, Cyr-Choinière et al. 2017), although it's still debated whether this is a real phase transition. Some evidence suggests possible existence of preformed Cooper pairs in the pseudogap phase at temperatures far above the superconducting T_C, e.g. measurements with ARPES (Kanigel, Chatterjee et al. 2008, Yang, Rameau et al. 2008, Nakayama, Sato et al. 2009), angular magnetoresistivity (Sandu, Cimpoiasu et al. 2004), and Nernst effect (Xu, Ong et al. 2000), but the precise nature of the pseudogap remains a hotly debated topic in research (Wesche 2015). Beyond optimal doping, the region above superconducting T_C behaves more like a normal metal, but has unconventional transport properties such as a resistivity scaling linearly with temperature over a wide range of temperatures, as opposed to a typical second power relation in normal metals, hence dubbed the "strange metal" phase (Greene, Mandal et al. 2020).

The strong interactions between electrons in cuprates lead to a zoo of various structural and electronic phase transitions in these cuprates at temperatures below 100 K, e.g. the low-temperature tetragonal (LTT) transition and the formation of stripe orders in $La_{2-x}Ba_xCuO_4$ and $La_{2-x}Sr_xCuO_4$. Complex interplay among coexisting and sometimes competing ground states introduce further complications to efforts to understand the origin of high-T_C superconductivity, but also creates a rich playground to explore how such interplay can be

exploited in pursuit of even higher T_C. Section 2.3 introduces some of these orders of particular relevance to this thesis.

2.2.3 C-axis optical properties of $La_{2-x}Ba_xCuO_4$

In addition to resistivity and magnetic susceptibility measurements such as in Figure 2-5, cuprate superconductors below T_C also display characteristic signatures in optical response functions, particularly when the light electric field is polarised along the direction perpendicular to the CuO_2 planes. As an example, shown in Figure 2-10 is the out-of-plane reflectivity R, of $La_{2-x}Ba_xCuO_4$, x = 9.5%, for the superconducting state, with a zoomed in focus on the low THz frequency range where characteristic signatures of the superconducting order are the most pronounced.

One of the most noticeable features of coherent superconducting transport to emphasise is a sharp edge in the reflectivity, a result of the Josephson plasma resonance, located at 0.5 THz in the 9.5% doping. This corresponds to the collective mode of plasma

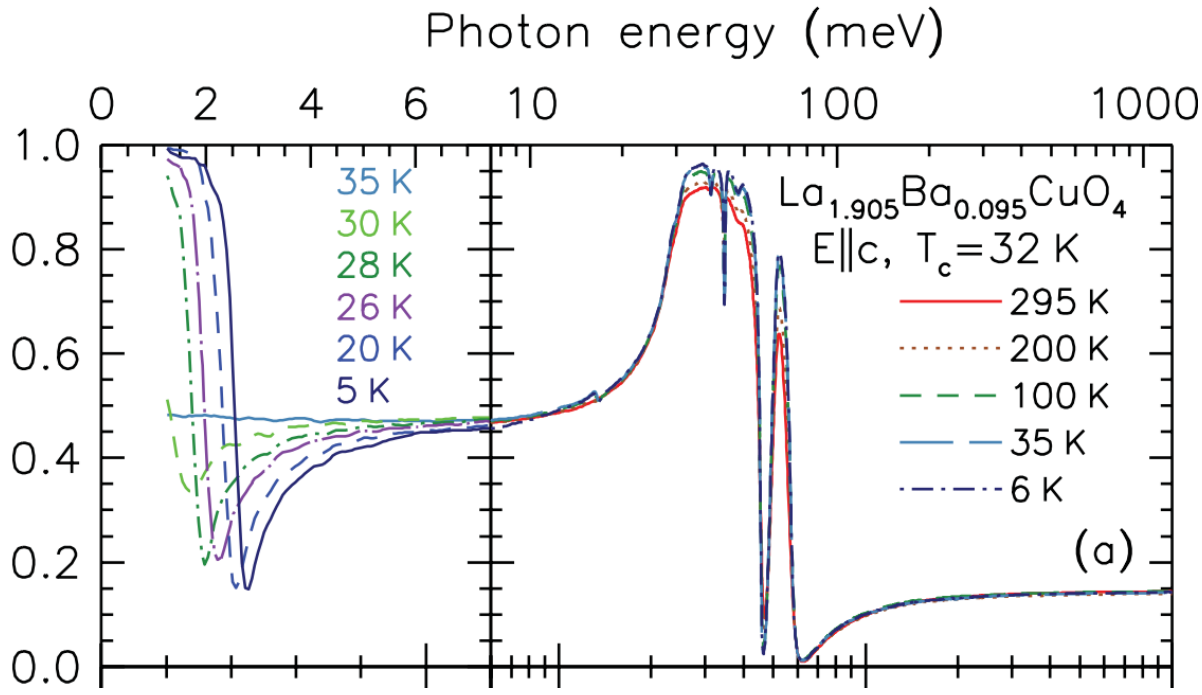

Figure 2-10: Temperature dependence of reflectance of LBCO 9.5% for light polarised along the c-axis. Reprinted with permission from (Homes, Hücker et al. 2012). Copyright 2022 by the American Physical Society.

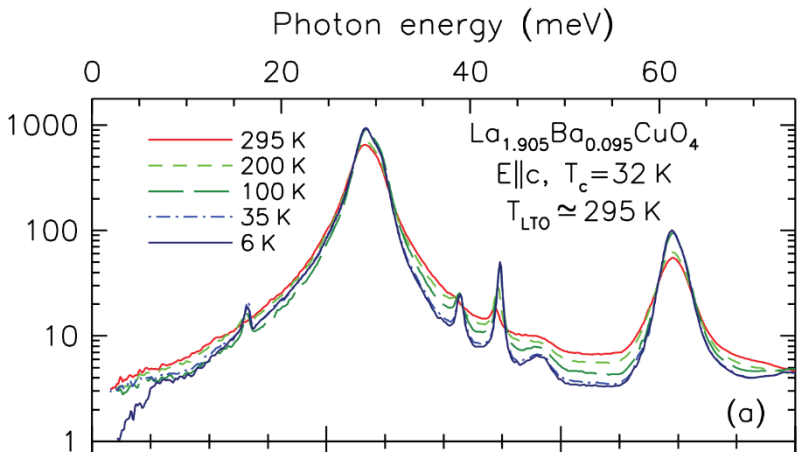

Figure 2-11: The temperature dependence of the real part of the optical conductivity of $La_{2-x}Ba_xCuO_4$ 9.5% for light polarized along the poorly conducting c axis. Reprinted with permission from (Homes, Hücker et al. 2012). Copyright 2022 by the American Physical Society.

oscillation of superconducting carriers between the copper oxide planes (see Chapter 4 for detail), and is commonly used as a measure of the strength of interlayer tunnelling of the supercurrent. As shown in Figure 2-10, this plasma edge in reflectivity shows a monotonic red shift with increasing temperature, and disappears completely when crossing T_C. In addition, when the superconducting order finds itself in stiff competition with other ordered phases such as the stripe order and is strongly suppressed, as is the case in the 11.5% doping, the frequency of the plasma edge tends to be significantly lower, at 0.15 THz, compared to 0.5 THz in the 9.5% doping where the stripes are relatively weak (see Section 2.3 for detail).

The real part of conductivity is suggestive of something close to a zero-resistance response at low frequency in the superconducting state below T_C, and is supposed to display a delta function in the DC limit, which, however, is not accessible with traditional optical techniques (see Figure 2-11). The imaginary part, on the other hand, shows a divergent behaviour as frequency approaches zero. This is indicative of the perfect-inductor aspect of a superconductor, where the application of a DC electric field induces an accelerating supercurrent in the opposite direction of the applied field. A divergent σ_2 towards zero frequency is also commonly employed as a key signature of superconducting order (see Chapter 4).

The dielectric function is closely related to the conductivity (see Appendix A), with interchanged behaviour between the real and imaginary parts. One useful feature is the zero crossing in the real part of $\tilde{\varepsilon}(\omega)$ at precisely the plasma frequency. This results from the fact

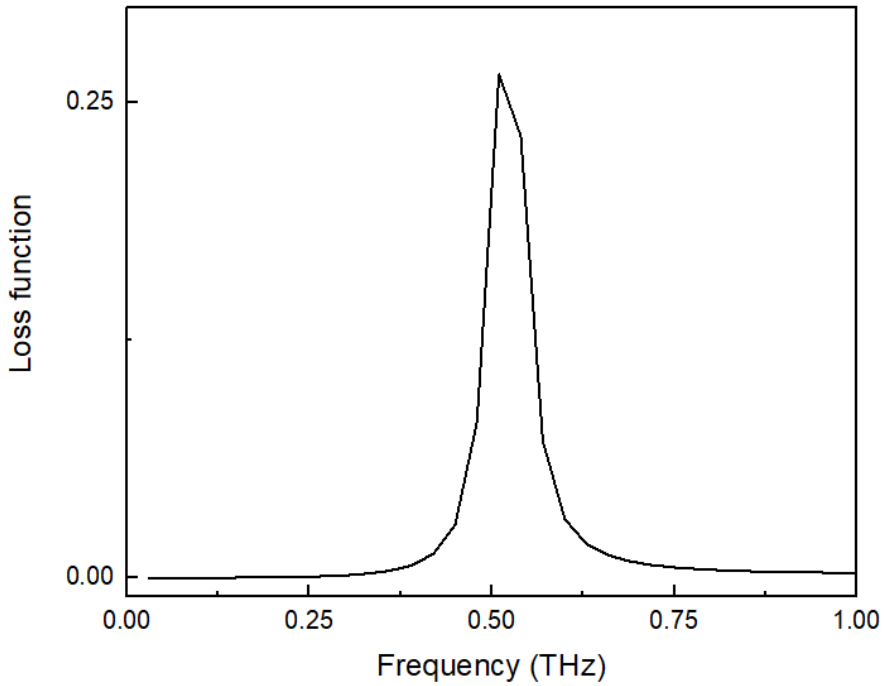

Figure 2-12: Loss function of LBCO 9.5%

that, when driven on resonance, the plasma displacement is completely out of phase with the driving field, hence giving zero in-phase response, which is what ε_1 measures. An often-plotted quantity closely related to this is the energy loss function, a basic parameter measured by electron loss spectroscopy, defined as

$$\Delta E = Im\left(-\frac{1}{\tilde{\varepsilon}(\omega)}\right)$$

The loss function displays a peak at the plasma frequency, as shown in Figure 2-12.

2.3 Other ordered phases and their interplay with superconductivity

2.3.1 The stripe order

In $La_{2-x}Ba_xCuO_4$, hole doping, as discussed in Section 2.2.2, introduces extra charges which need to arrange themselves in a way that minimises the total energy. Three main contributions are at play in this competition: the kinetic energy is lowered if the electrons are delocalised; the interaction energy due to spins prefers anti-alignment between neighbouring sites as in an antiferromagnet; and the Coulomb repulsion energy is minimised when electrons are far apart. As a compromise among these competing factors, the end result is the formation of one-dimensional chains, also known as stripes, creating a spatial modulation of carrier concentration. The stripes also act as phase boundaries between intermediate spins with local antiferromagnetic correlations.

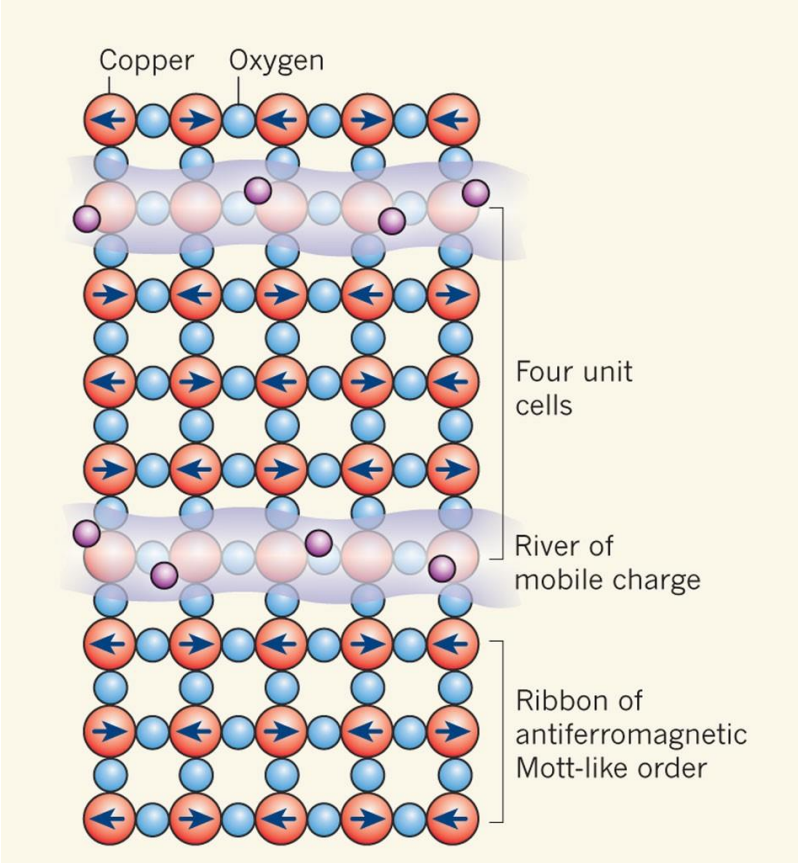

Figure 2-13: Stripe-like pattern forms within the copper oxide planes: regions of antiferromagnetic Mott-like order are separated by "rivers" of doped, mobile charges. Reprinted by permission from Springer Nature: (Moler 2010).

Such stripes are the strongest at x = 1/8 doping, i.e. every eighth electron is removed from the system. The hole density is directly related to the number of ions substituted. Taking LSCO as an example, the La ion is 3+ whereas Sr is 2+, so for every La substituted by Sr, an extra electron is pulled out of the copper oxide layer and put into its valence band. Here, the charges concentrate within narrow stripes parallel to the copper-oxygen bonds, forming a periodic pattern which repeats itself every four lattice unit cells (see Figure 2-13). At exactly 1/8 doping, the stripes are commensurate with the lattice and almost quasi-static, while deviating from 1/8 makes them fluctuate dynamically.

The first experimental evidence for the stripe order was found in a nickelate $La_2NiO_{4.125}$ (Tranquada, Buttrey et al. 1994), where the stripes are aligned diagonally, as shown in Figure 2-14 (a). Not long after, the stripe order was also identified in a cuprate, $La_{1.48}Nd_{0.4}Sr_{0.12}CuO_4$ (Tranquada, Sternlieb et al. 1995), where the alignment runs parallel to the Cu-O bonds, illustrated in Figure 2-14 (b). In $La_{2-x}Ba_xCuO_4$ (LBCO), evidence for the existence of the stripe

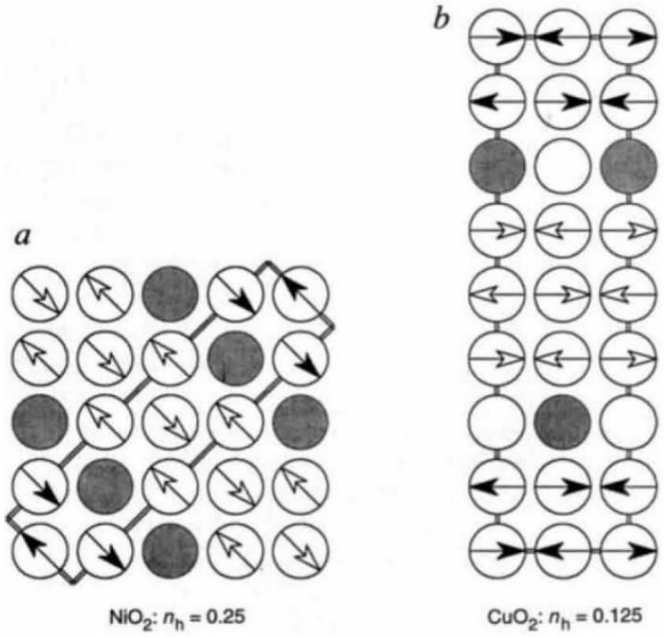

Figure 2-14: A schematic of the stripe pattern in (a) a NiO_2 plane observed in hole-doped La_2NiO_4 with a hole density of n_h = 1/4 and (b) a CuO_2 plane of hole-doped La_2CuO_4 with n_h = 1/8. In both, only the metal atoms are represented; the oxygen atoms, which surround the metal sites in a square planar array, have been omitted. Arrows indicate the orientation of magnetic moments on metal atoms, which are locally antiparallel; the spin direction rotates by 180° (relative to a simple antiferromagnetic structure) on crossing a domain wall, as emphasized by the change in filling of the arrow heads. The solid lines outline the magnetic unit cell in each case. Holes are located at the anti-phase domain boundaries, which are indicated by the rows of circles without arrows. A filled circle denotes the presence of one hole, centred on a metal site. Reprinted by permission from Springer Nature: (Tranquada, Sternlieb et al. 1995).

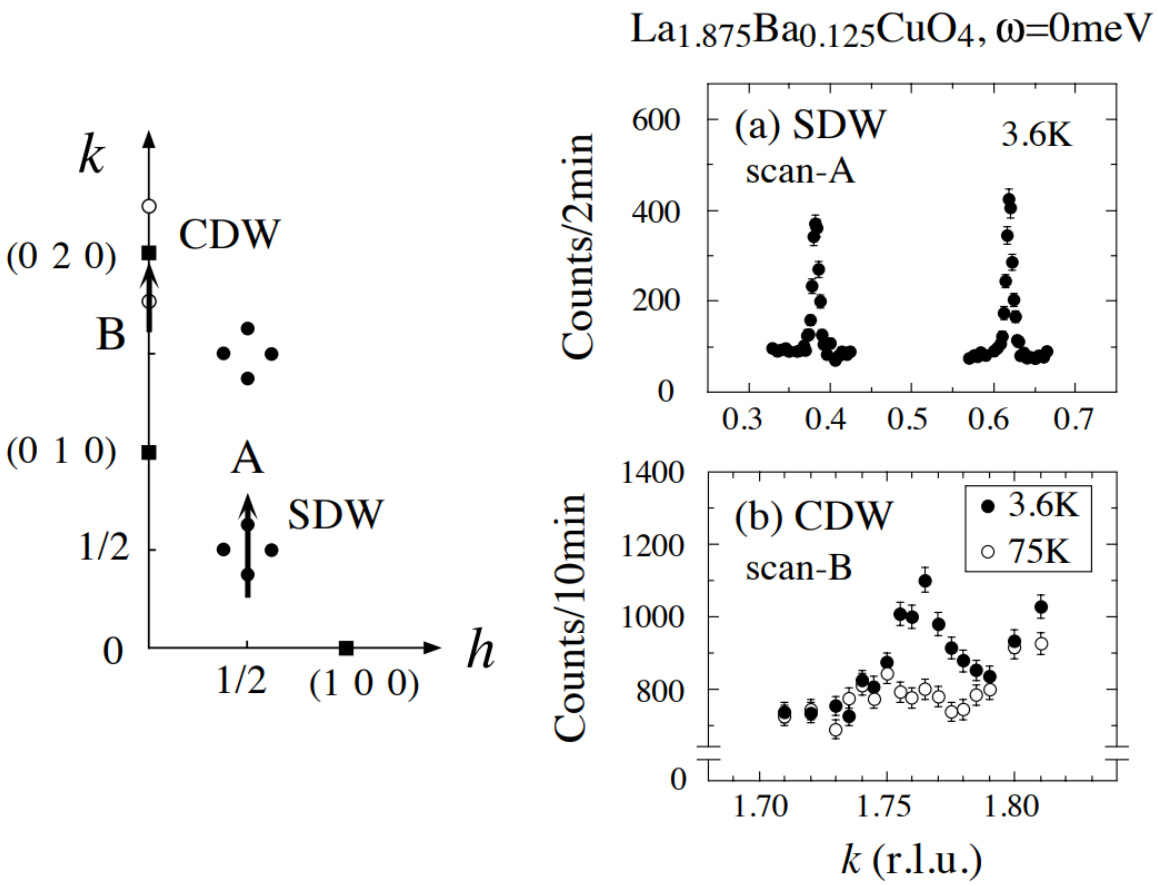

Figure 2-15: (Left) Reciprocal space map indicating locations of superlattice peaks, with arrows indicating paths of neutron diffraction scans A and B. (Right) (a) Magnetic superlattice peaks measured along scan A in LBCO with x = 0.125 at T = 3.6 K. (b) Charge-order superlattice peak measured along scan B at 3.6 K (filled circles), with background measured at 75 K (open circles). Reprinted with permission from (Fujita, Goka et al. 2004). Copyright 2022 by the American Physical Society.

order was also found via neutron (Fujita, Goka et al. 2004, Dunsiger, Zhao et al. 2008, Tranquada, Gu et al. 2008) and X-ray scattering (Abbamonte, Rusydi et al. 2005, Kim, Gu et al. 2008, Tranquada, Gu et al. 2008) experiments. An example of the neutron scattering data is shown in Figure 2-15.

In recent years, increasing evidence has surfaced that these charge and spin stripes populate the phase diagrams of cuprates (Lee, Birgeneau et al. 1999, Hirota 2001, Fujita, Yamada et al. 2002, Fink, Schierle et al. 2009). However, the interplay between the stripes and the superconducting order remains a hotly debated topic. One thing that baffled many since the discovery of LBCO as the first high T_C superconductor was that, a surprising, so-called 1/8 anomaly in its phase diagram was observed (Moodenbaugh, Xu et al. 1988). The superconducting dome created by hole doping displayed a sharp dip around the doping x = 1/8, as shown in Figure 2-16. This suppression of T_C alludes to the presence of a competing

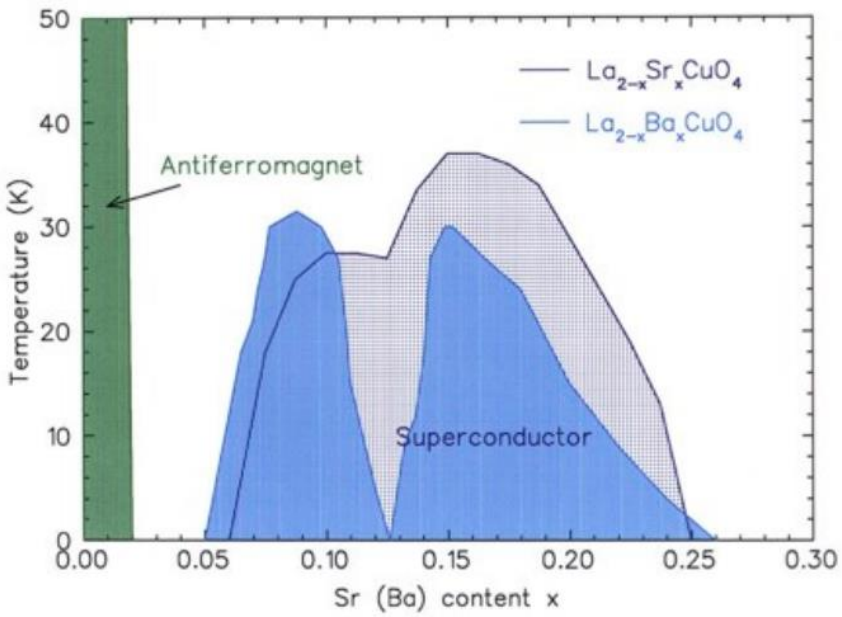

Figure 2-16: Superconducting T_C versus hole doping level x in LBCO and LSCO, illustrating the 1/8 anomaly. Reprinted from (Tranquada 2013), with the permission of AIP Publishing.

order of some sort. The fact that the stripes are also the most pronounced at this doping is very suggestive of a connection between the stripes and superconductivity. However, in LSCO, a fairly similar compound from the same parent material La_2CuO_4, only a slight kink on the superconducting T_C versus doping curve was observed around 1/8 doping.

The reason for this discrepancy lies in the crystal structure of LBCO (Axe, Moudden et al. 1989). At high temperature, the CuO_6 octahedra, which make up the copper oxide planes, have no average tilt, giving the CuO_2 planes four-fold rotational symmetry. With decreasing temperature, LBCO goes through a structural transition from the high-temperature tetragonal (HTT) phase to the low-temperature orthorhombic (LTO) phase, where the octahedra rotate around the [110] axis. Note that the tilt axis is in the diagonal direction of the CuO_2 square lattice, and neighbouring octahedra sharing a corner would tilt in opposite directions. Upon further cooling, a second structural transition occurs from the LTO phase to the low-temperature tetragonal (LTT) phase, where the tilt axis becomes parallel to the Cu-O bonds. Hence, orthogonal Cu-O bonds become inequivalent; in one direction, the bonds are straight while those perpendicular to them become bent. In addition, the tilt axis rotates 90 degrees, i.e. alternates between [100] and [010], between adjacent copper oxide planes along the c-axis (see Figure 2-17). It is believed that this anisotropy introduced by the LTT transition plays a key role in the pinning of the stripes, and each CuO_2 plane pins the stripes to a unique direction based on the LTT distortion axis (Hücker, v. Zimmermann et al. 2011). Furthermore,

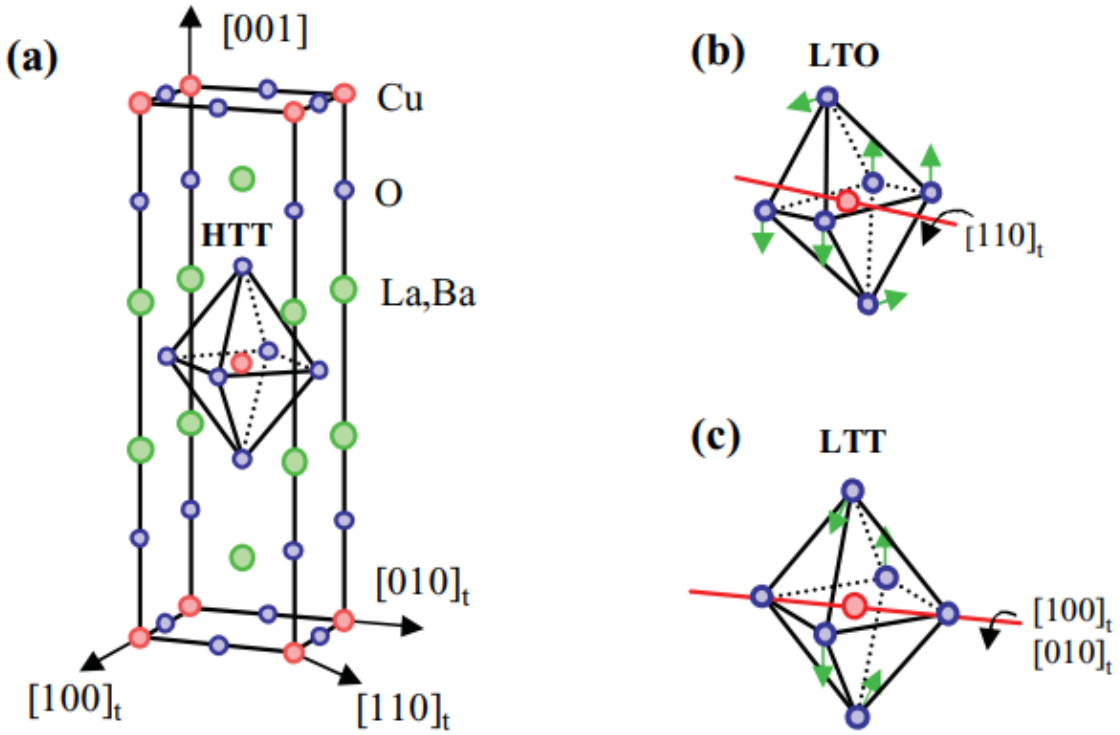

Figure 2-17: Crystal structure and reciprocal lattice of LBCO. (a) the unit cell in the HTT phase; tilt directions of the CuO_6 octahedra in (b) the LTO phase and (c) the LTT phase. Reprinted with permission from (Hücker, v. Zimmermann et al. 2011). Copyright 2022 by the American Physical Society.

originally a chemical unit cell consists of two CuO_2 layers, but an alternating arrangement between equivalent layers doubles the size of a unit cell along the c-axis.

While both have an LTO phase, the LTT transition is present only in LBCO and not in LSCO, which was found to be the key to the occurrence of strong stripe order. The doping with strongest stripes coincides with the suppression of superconducting T_C in both compounds, hence pointing to the competition between the stripes and bulk superconductivity (Tranquada 2013). However, angle-resolved photoemission spectroscopy measurements have detected a gapped Fermi surface in LBCO, similar to that found in the bulk superconducting state in LSCO, with a doping dependence that peaks around x = 1/8 doping (Valla, Fedorov et al. 2006), consistent with one interpretation that static stripe order does not suppress superconducting pair formation but rather disrupts phase coherence, causing the CuO_2 planes to become decoupled and the 3D superconducting coherence destroyed, while a form of fluctuating 2D superconductivity survives (Li, Hücker et al. 2007). Extra evidence from X-ray and neutron diffraction data combined with static magnetisation measurements further shows that the amplitudes of charge and spin orders are unaffected by the onset of bulk 3D superconducting

coherence, nor does the onset of spin order and weak in-plane 2D superconductivity have any effect on the charge order itself (Hücker, v. Zimmermann et al. 2011).

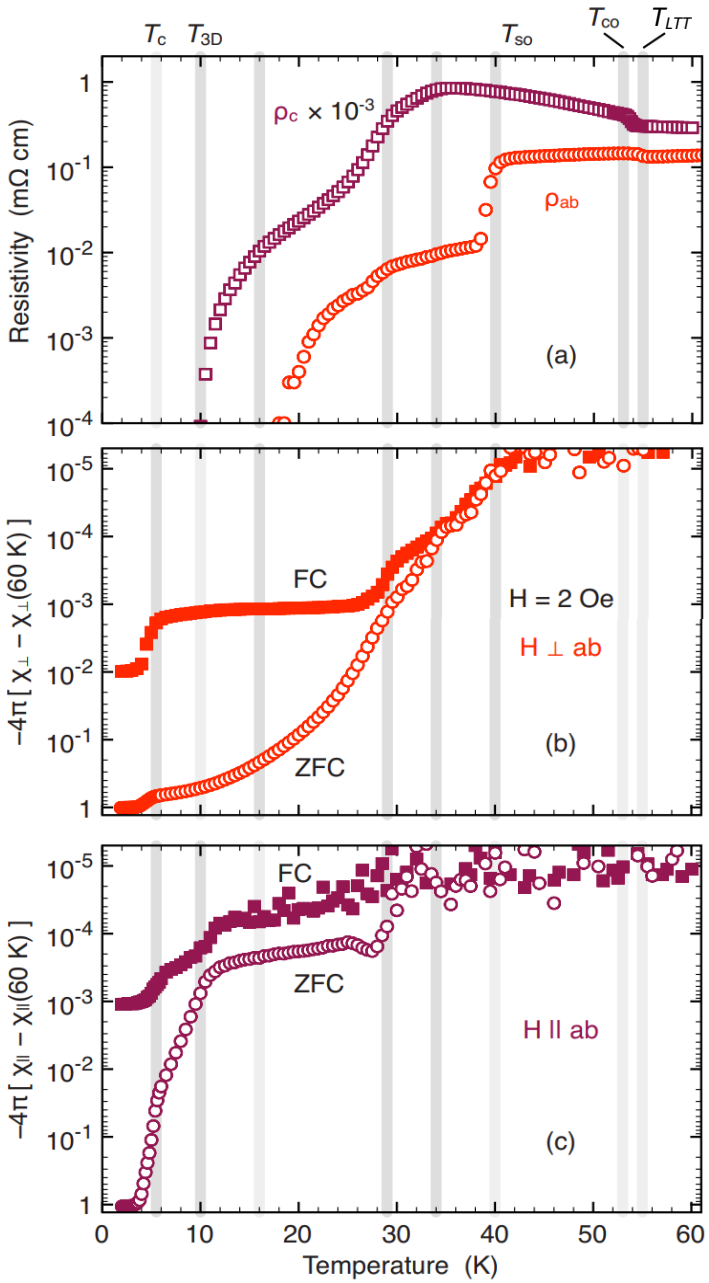

Figure 2-18: Temperature-dependent measurements on single crystals of LBCO x = 1/8 (a) In-plane resistivity, ρ_{ab} (circles), and resistivity perpendicular to the planes, ρ_c, divided by 10^3 (squares). (b) Magnetic susceptibility measured with the field perpendicular to the planes and (c) parallel to the planes for an applied field of 2 Oe. χ has been corrected for shape anisotropy and the offsets (to allow plotting on a logarithmic scale) are $4\pi\chi_\perp(60\ K) = 4.2 \times 10^{-4}$ and $4\pi\chi_\parallel(60\ K) = 1.6 \times 10^{-5}$. Vertical gray lines denote relevant temperatures, with labels at the top. T_C is the bulk superconducting transition temperature, T_{3D} where ρ_c goes to zero, T_{SO} the spin order transition temperature, T_{CO} the charge order transition temperature, and T_{LTT} the LTO-LTT transition temperature. Reprinted with permission from (Tranquada, Gu et al. 2008). Copyright 2022 by the American Physical Society.

In fact, it was found that 2D superconducting correlations onset at roughly the same temperature as the spin order, where upon cooling, the in-plane resistivity drops by an order of magnitude and weak diamagnetism develops, while the c-axis resistivity remains high, as shown in Figure 2-18 (Tranquada, Gu et al. 2008). In particular, in the temperature range of 10 K to 16 K, the in-plane resistivity has become immeasurably small, yet the c-axis resistivity remains on the order of 0.1 mΩ cm. Furthermore, while ARPES measurements point to a gap formation at temperatures in excess of 40 K (Valla, Fedorov et al. 2006), bulk superconductivity showing the Meissner effect and zero DC resistance in all directions does not occur until below T_C = 4 K. To understand the anomalous decoupling of 2D and 3D superconducting transitions, it is worth looking at what changes occur that frustrates 3D superconducting coherence along the c-axis.

2.3.2 Pair density wave

Josephson coupling between neighbouring CuO_2 layers is responsible for 3D superconducting coherence in cuprates. The suppression of 3D superconducting order while 2D correlations are unaffected suggests frustration of Josephson coupling to be the cause. To explain this, a novel type of superconducting order within the stripes, the so-called Pair Density Wave (PDW) was proposed (Berg, Fradkin et al. 2007, Berg, Fradkin et al. 2009). The PDW is a superconducting state in which the order parameter varies periodically as a function of position such that its spatial average vanishes. In cuprates, they are believed to coexist with the unidirectional stripe order, where the spatially dependent wavefunction of the PDW oscillates between positive and negative going from one stripe to another. As illustrated in Figure 2-19 (a), the pair wave function has a large amplitude in each charge stripe, and changes sign between neighbouring stripes, crossing zero in the antiferromagnetic stripe. The period is the same as the spin order. Since the stripes are aligned perpendicular to those in adjacent planes, the net interlayer Josephson coupling average out to zero [see Figure 2-19 (b)] (Tranquada 2013).

The original proposal for the PDW state was in response to the observation of a sharp decrease in interlayer coupling in $La_{1.85-y}Nd_ySr_{0.15}CuO_4$ across an LTO to LTT transition due to increasing Nd doping (Tajima, Noda et al. 2001, Himeda, Kato et al. 2002). The early ARPES

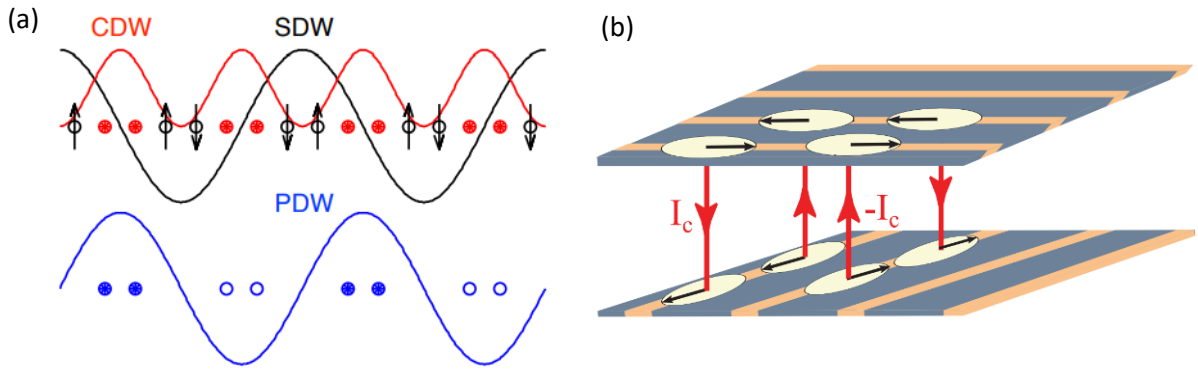

Figure 2-19: (a) Schematic of CDW, SDW, and PDW orders, illustrating the relations among the phases of the modulations. Figure taken from (Fujita, Hiraka et al. 2011). (b) Out-of-phase arrangement of the order parameter between adjacent planes results in cancellation of the Josephson tunnelling current, hence suppressing 3D superconductivity. From (Rajasekaran, Okamoto et al. 2018). Reprinted with permission from AAAS.

study of PDW in $La_{1.48}Nd_{0.4}Sr_{0.12}CuO_4$ at T = 15 K, more than twice higher than T_C in this material, finds a gapless nodal arc of states extending to about one third of the nominal Fermi surface and a gap in the antinodal region of up to 30 meV (Chang, Sassa et al. 2008). In the following year, ARPES measurements on LBCO with x = 0.125 also reveal, for temperatures higher than the spin-order transition, a gapless nodal arc of states and a substantial antinodal gap (He, Tanaka et al. 2009). These observations are consistent with the notion that cuprates with stripes exhibit local PDW order (Berg, Fradkin et al. 2009).

To provide further evidence for the existence of this novel 2D superconducting order, a way to exert finer control the strength of stripe order than hole doping is desired. It was found that in LSCO, a modest magnetic field up to 8 tesla, well below the upper critical field $H_{c2}(T)$, applied along the c-axis is able to suppress signatures of the Josephson plasma resonance, a sensitive probe of interlayer phase coherence, in far-infrared reflectance measurements, yet only a slight reduction in the in-plane superfluid density is detected, suggesting the CuO_2 planes become essentially decoupled, as shown in Figure 2-20. One explanation given for the unexpectedly low decoupling magnetic fields which cause phase decoherence is a field-induced antiferromagnetic order, giving rise to a form of 2D superconductivity bearing strong resemblance to that found in 1/8-doped LBCO in presence of existing static stripe order (Schafgans, LaForge et al. 2010). More recently, similar results have also been found in other cuprates of the La-214 family, such as $La_{1.7}Eu_{0.2}Sr_{0.1}CuO_4$ and $La_{1.48}Nd_{0.4}Sr_{0.12}CuO_4$ (Shi, Baity et al. 2019, Shi, Baity et al. 2020).

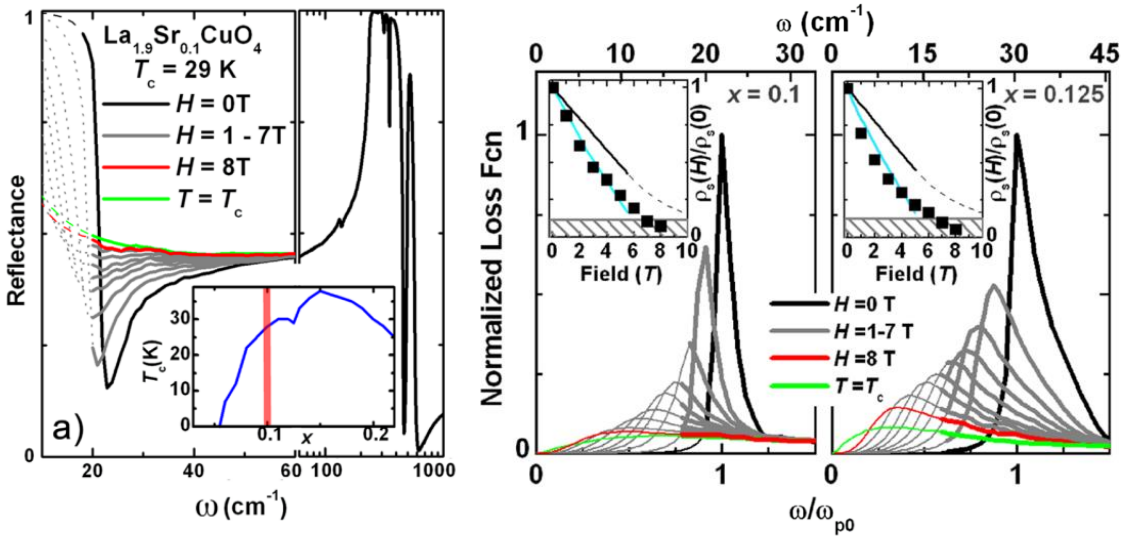

Figure 2-20: (Left) Far-infrared reflectance of LSCO x = 0.1 showing the evolution of the JPR at T = 8 K in magnetic field. Inset: the superconducting phase diagram of LSCO for various Sr content. (Right) Loss function at T = 8 K for two dopings. Thick lines are range of extrapolation independent results. Insets: Normalized superfluid density $\rho_s(H,T)$ / $\rho_{s0}(H,T)$ vs applied field at T = 8 K. Reprinted with permission from (Schafgans, LaForge et al. 2010). Copyright 2022 by the American Physical Society.

The conventional understanding for the destruction of superconducting order in layered systems like cuprates by magnetic fields perpendicular to CuO_2 planes involves misalignment of vortices, reducing Josephson coupling between the planes, and predicts that the in-plane and out-of-plane resistivity, $\rho_{\parallel}$ and $\rho_{\perp}$ respectively, should become finite at the same time. However, motivated by the results on LSCO, resistivity measurements carried out

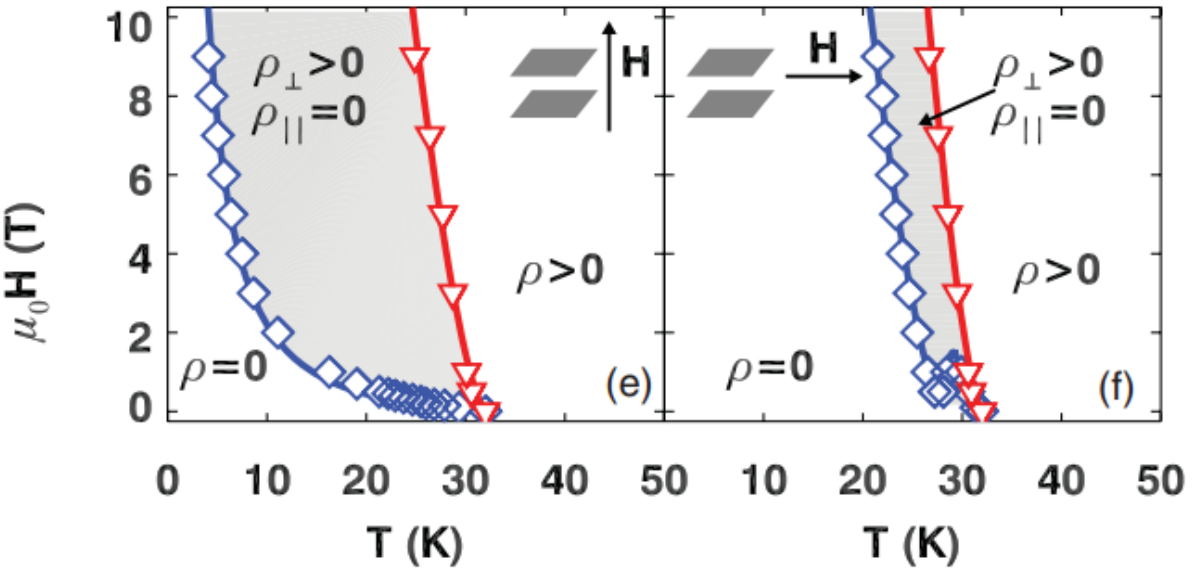

Figure 2-21: Magnetic field-temperature Phase diagram for in-plane and out-of-plane resistivities for magnetic fields applied in either direction, indicating anisotropic boundaries for the onset of finite resistivity. Reprinted with permission from (Wen, Jie et al. 2012). Copyright 2022 by the American Physical Society.

on LBCO with x = 0.095 under magnetic fields, applied in both the in-plane and out-of-plane directions, produced results contradicting the prediction above.

This doping of LBCO has a higher T_C of 32K and weaker stripe order than the x = 1/8 doping. In zero field, resistivity in both directions indeed approach zero at the same temperature. When an out-of-plane magnetic field up to 8 T is applied, however, $\rho_\perp$ was found to drop towards zero at a much lower temperature than $\rho_\parallel$ does (see Figure 2-21). With applied field parallel to the planes, the effect is smaller. In addition, it was shown that the

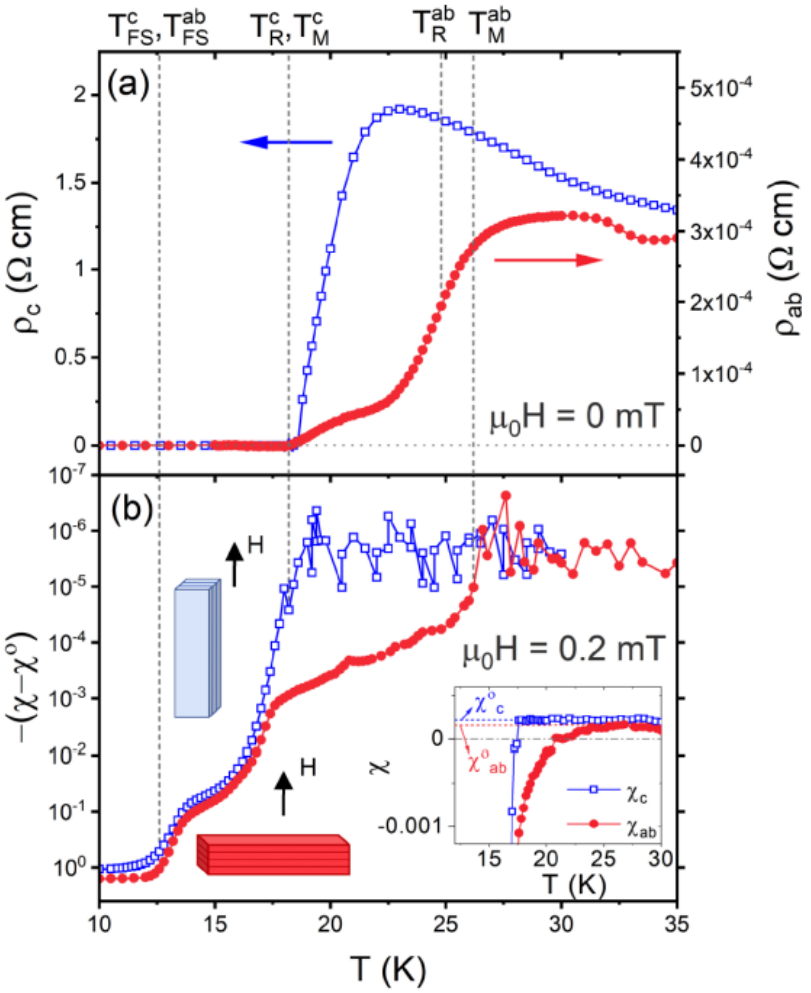

Figure 2-22: (a) Temperature dependence of the resistivity (in zero applied magnetic field) for current along the c*-axis (blue squares) and parallel to the* ab *planes (red circles). (b) Temperature dependence of the volume magnetic susceptibility with a field of μ_0H = 0.2 mT applied parallel to the planes, χ_c (blue squares), and perpendicular to the planes, χ_{ab} (red circles). The inset shows the susceptibilities on a linear scale near the initial transitions; linear fits to the normal state, and extrapolated to low T, are indicated by dashed lines. Subtraction of these fits enables the logarithmic-scale plots of the main panel. Characteristic temperatures are labelled by their subscripts (FS: full shielding, R: resistivity, M: susceptibility) and superscripts (ab: in-plane, c: out-of-plane). Reprinted with permission from (Lozano, Gu et al. 2021). Copyright 2022 by the American Physical Society.*

stripes are enhanced by a strong field applied out of plane, resulting in a condition qualitatively similar to that found in x = 1/8 doping in zero field (Wen, Jie et al. 2012).

This kind of decoupled behaviour is not limited to measurements in magnetic fields. Zn substitution has been known to suppress superconductivity (Fukuzumi, Mizuhashi et al. 1996), and has been found to reduce superfluid density comparable to a magnetic vortex core (Nachumi, Keren et al. 1996). It was postulated that Zn substitution into LBCO should result in 2D superconductivity in absence of external magnetic fields. In addition to early work showing reduced T_C for 3D coherence after substitution (Wen, Xu et al. 2012), it was found that 1% Zn substituted for Cu in LBCO x = 9.5% causes initial onset of 2D superconductivity at roughly 25 K (T_R^{ab} in Figure 2-22), as measured by the in-plane resistivity ρ_{ab} displaying a substantial drop as well as the onset of weak diamagnetism for magnetic fields along the out-of-plane direction (T_M^{ab} in Figure 2-22). By contrast, ρ_c and the corresponding susceptibility only show a transition below 18 K ($T_{R,M}^{c}$ in Figure 2-22). Full bulk superconductivity does not occur until below 12 K (T_R^{ab} in Figure 2-22). The results are consistent with Zn doping inducing 2D superconductivity at temperatures much higher than the bulk T_C and Zn impurities pinning PDW order locally (Lozano, Gu et al. 2021).

On the other hand, unlike the magnetic field decoupling CuO_2 planes and suppressing interlayer tunnelling, high pressure has been shown to raise T_C by supressing the low-temperature LTT structural distortion (Katano, Funahashi et al. 1993, Ido, Kudo et al. 1996, Hücker, v. Zimmermann et al. 2010). It was postulated that, if bond-aligned charge-stripe order, which correlates with the anomalous suppression of T_C near optimal doping in LBCO as discussed in Section 2.3.1, can only occur in the LTT phase, then a large jump in T_C should be expected when the LTT phase is suppressed. It has been shown that, by applying hydrostatic pressure up to 14.7 GPa on LBCO samples, the x = 12.5% doping sees its T_C reach up to 18 K, from below 4 K at ambient pressure [see Figure 2-23 (a)]. At the same time, while the LTT structural transition is also totally suppressed at 1.85 GPa, it is found that the charge-stripe order continues to exist beyond 1.85 GPa, as shown by X-ray diffraction measurements. It should be pointed out that, despite the significantly increased T_C at x = 12.5% doping, it is still far below that of the other dopings away from 12.5% up to over 30 K [see Figure 2-23 (b)]. Hence, it is concluded that the reduced symmetry during the LTT structural transition alone is not strongly correlated with the existence of the stripe order, and is indeed consistent with

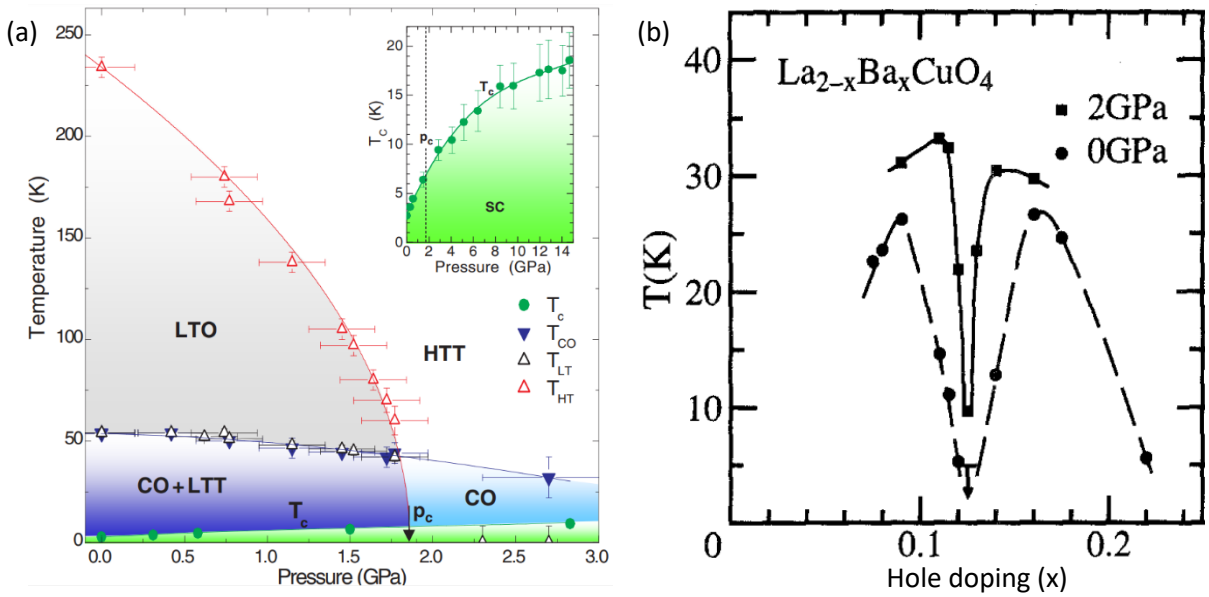

Figure 2-23: (a) Observed temperature versus pressure phase diagram of $La1_{.875}Ba_{0.125}CuO_4$. Indicated are the transition temperatures of the structural phases high-temperature tetragonal (HTT), low-temperature orthorhombic (LTO), and low-temperature tetragonal (LTT), the charge-stripe phase (CO), and bulk superconductivity (SC). At ambient pressure, T_{HT} = 235 K, T_{LT} = 54 K, T_{CO} = 54 K, and T_C = 3 K, respectively. The line separating LTO from HTT describes $T_{HT}(p)$ as a function of pressure p using $T_{HT}(0)[(p_c - p) / p_c]^{0.5}$ with a critical pressure of p_c = 1.85. Inset: T_C for pressures up to 14.7 GPa. Reprinted with permission from (Hücker, v. Zimmermann et al. 2010). Copyright 2022 by the American Physical Society. (b) T_C for LBCO near the x = 0.125 doping. Reprinted by permission from Springer Nature: (Ido, Kudo et al. 1996).

the picture in which the striped superconductor (e.g. a PDW phase) is responsible for the suppression of bulk superconductivity (Hücker, v. Zimmermann et al. 2010).

Given the richness of exotic ordered phases found in the phase diagram of many cuprate superconductors at low temperature, and in particular LBCO (see Figure 2-24), investigating the interplay between them is crucial to developing a comprehensive understanding of the mechanism behind high T_C superconductivity. Among the many coexisting ground states, abundant signs of competition have been identified by experiments discussed in this chapter. Tuning the relative strengths of each of them provides further insights into potential ways to engineer new materials with more desirable properties. In addition to magnetic fields and pressure, intense radiation in the form of laser pulses is also highly useful for precise and selective coupling to excitation of certain ground states, such as the Josephson plasma resonance. Furthermore, out-of-equilibrium dynamics can shed additional light on nonlinear behaviour when the system is coherently driven far away from

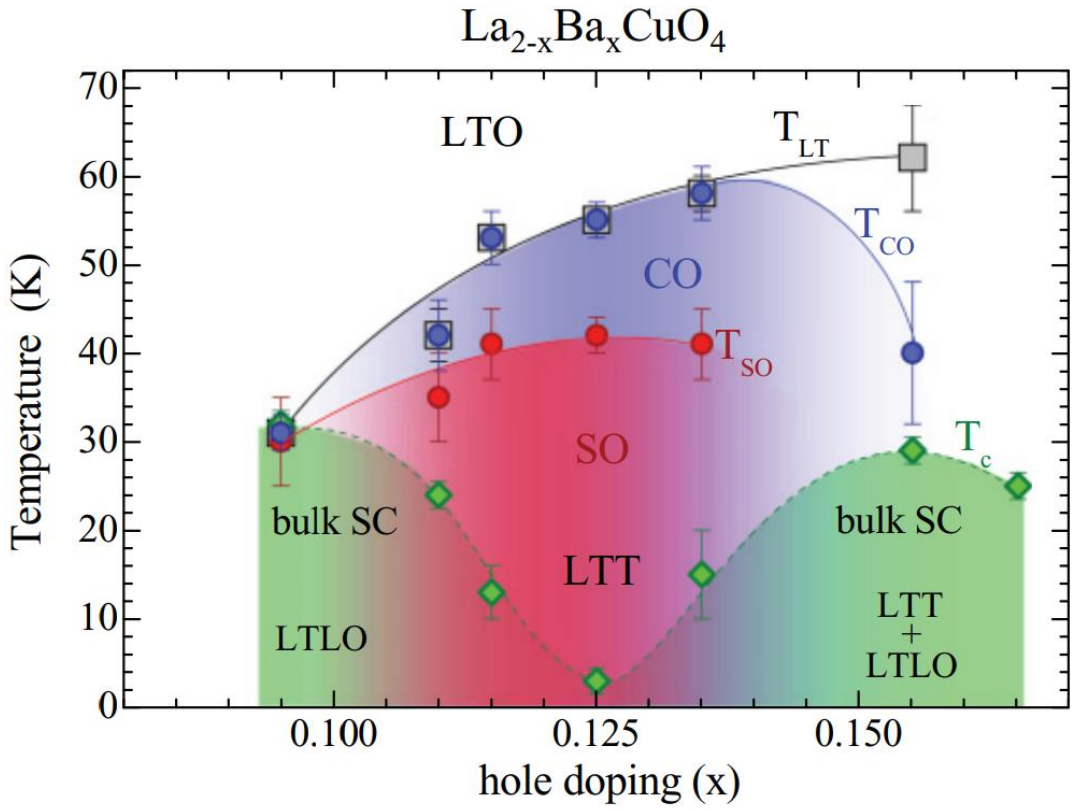

Figure 2-24: Temperature versus hole-doping phase diagram of LBCO, populated by many ordered phases and transition including the charge order (CO), spin order (SO), bulk superconductivity (SC), low-temperature orthorhombic (LTO), low-temperature tetragonal (LTT), low-temperature less-orthorhombic (LTLO) transitions. Reprinted with permission from (Hücker, v. Zimmermann et al. 2011). Copyright 2022 by the American Physical Society.

equilibrium, revealing hidden states on the same phase diagram but invisible to linear and in-equilibrium methods of measurement.

Traditional tools focused on measurements of electronic transport and magnetism properties are useful for studying the equilibrium response. On the other hand, dynamics upon perturbing the system tends to take place on time scales, ranging from femtoseconds (fs) to nanoseconds (ns), too fast to probe with these techniques. Therefore, it is natural to employ light pulses both as a way to set off various dynamics and as a method to take "snapshots" of the material response with high temporal resolution, with the additional advantage of a wide range of frequency components to choose from for focusing on various spectral segments of material parameters, which become available thanks to developments in nonlinear optical techniques and table top ultrafast high intensity laser sources. In particular, terahertz (THz) radiation provides a convenient way of coupling to low-energy excitations (e.g. the JPR) without causing undesirable noise such as quasiparticle excitation that could mask the interesting dynamics.

Following this line of reasoning, in the next chapter, several examples of optical control of superconductivity in cuprate superconductors are discussed, and in Chapter 5, the first experiment of this thesis brings together the magnetic field as a tuning knob of different ground states in LBCO and pump-probe THz spectroscopy to provide new and surprising evidence for the existence of the PDW state.

3. Optical control of superconducting order

Control of material properties with light on strongly correlated solids has seen popular use in recent decades (Cavalleri, Rini et al. 2005, Polli, Rini et al. 2007, Basov, Averitt et al. 2011, Ehrke, Tobey et al. 2011). In particular, laser pulses at mid-infrared (MIR) and terahertz (THz) frequencies have become readily available for resonant excitation of many low-energy modes, such as vibrational modes of the crystal lattice (phonons) and superconducting gaps, as well as studying the coherent, nonlinear dynamics of the materials, if the electric field strengths are strong enough.

In this chapter, several examples of optical control of superconductivities in cuprates are reviewed. These studies shed light on the delicate balance between different coexisting or competing orders at low temperatures and possible revival of superconductivity through optical stimulation of phonon modes in the normal state on an ultrafast time scale (Fausti, Tobey et al. 2011, Först, Tobey et al. 2014, Hu, Kaiser et al. 2014, Mankowsky, Subedi et al. 2014, Nicoletti, Casandruc et al. 2014, Casandruc, Nicoletti et al. 2015).

3.1 Single layer cuprates

3.1.1 Stripe melting and light induced superconductivity in $La_{1.8-x}Eu_{0.2}Sr_xCuO_4$

Hole doped $La_{1.8-x}Eu_{0.2}Sr_xCuO_4$ (LESCO) shares the same parent compound La-214 with previously discussed LBCO (see Sections 2.2 and 2.3), as well as many of the same features in its phase diagram at low temperature, i.e. superconductivity emerging from

antiferromagnetic Mott insulator through chemical doping, a stripe order enhanced by the low-temperature tetragonal (LTT) structural transition, and the suppression of superconducting transition T_c for all doping levels below $x = 0.2$ but most strongly near $x = 1/8$, where superconductivity is completely suppressed in LESCO. See Figure 3-1 (a) for a schematic of the crystal structure and (b) for a phase diagram of this material.

In the experiment by (Fausti, Tobey et al. 2011), a non-superconducting sample of LESCO with $x = 1/8$ was illuminated with intense MIR radiation with 15 um wavelength, which is resonant with a phonon mode corresponding to the Cu-O stretch motion in the CuO_2 planes. Through time-domain THz spectroscopy measurements, a transient superconducting state was observed.

In equilibrium, the Josephson plasma resonance (JPR) in c-axis reflectivity is often used as a key signature of superconductivity in cuprates, a result of Josephson tunnelling of charge carriers between adjacent CuO_2 planes. The reflectivity spectra of $La_{1.84}Sr_{0.16}CuO_4$, a very similar compound, are shown in Figure 3-2 (a), where the JPR as an edge appears close to 60

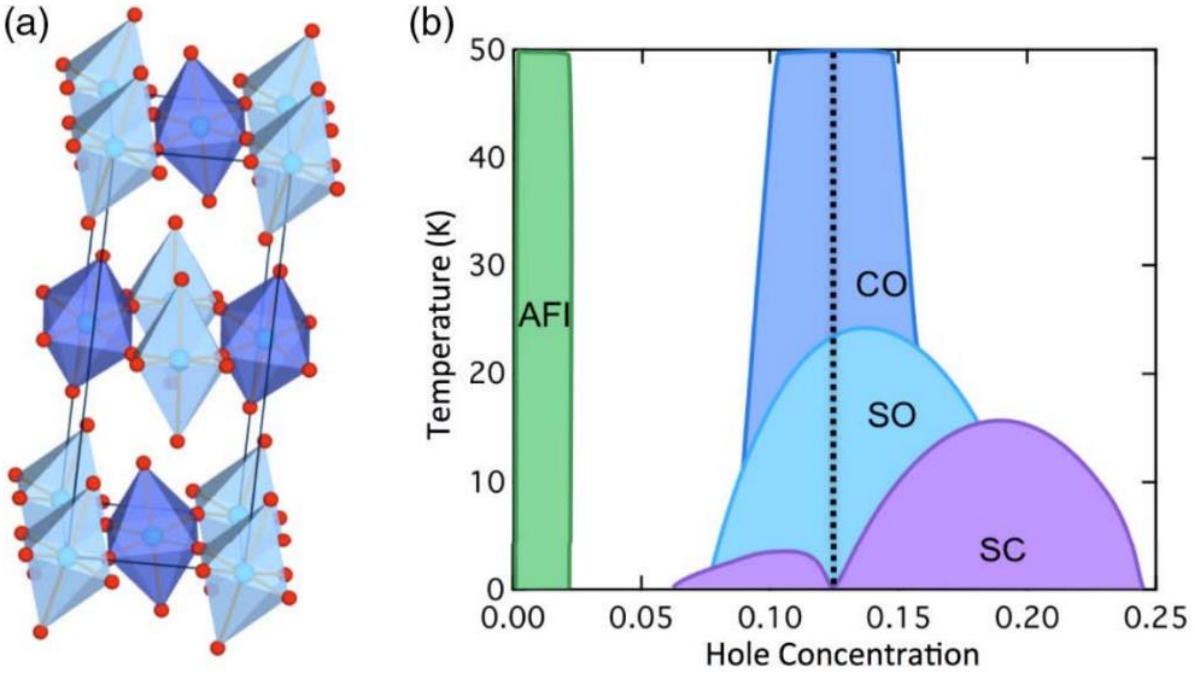

Figure 3-1: (a) Schematic crystal structure and (b) phase diagram $La_{1.8-x}Eu_{0.2}Sr_xCuO_4$. This compound is an antiferromagnetic insulator at x = 0. A low-temperature structural distortion (LTT), associated with buckling of the CuO_2 planes, quenches superconductivity at all doping levels below x = 1/8 (vertical dashed line). At this doping, a one-dimensional modulation of charges (CO) and spins (SO), the stripe state, emerges in the planes. At x > 1/8, the compound is superconducting. Adapted from (Mankowsky, Först et al. 2016).

cm^{-1} (~2 THz) below T_C while the spectrum is featureless above T_C. In LESCO, the reflectivity at 10 K is also a flat line, as shown in Figure 3-2 (b).

5 ps after photoexcitation with the MIR pulses, however, a clear edge develops at the same 2 THz frequency as in $La_{1.84}Sr_{0.16}CuO_4$ in equilibrium, as shown in Figure 3-2 (c). This is suggestive of possible superconducting transport induced by the MIR radiation. Furthermore, the quantity $\lim_{\omega\to 0} \omega\sigma_2(\omega)$ is proportional to the superfluid density and can be dynamically traced by measuring low-frequency transient imaginary conductivity. As plotted in Figure 3-2 (d) and (e) as a function of time delay τ, a finite superfluid density appears promptly after photoexcitation, before relaxing into a plateau over several ps, where a metastable superconducting state has possibly formed. In Figure 3-2 (f), the pump-wavelength dependence of the inverse threshold for light-induced superconductivity is shown as a

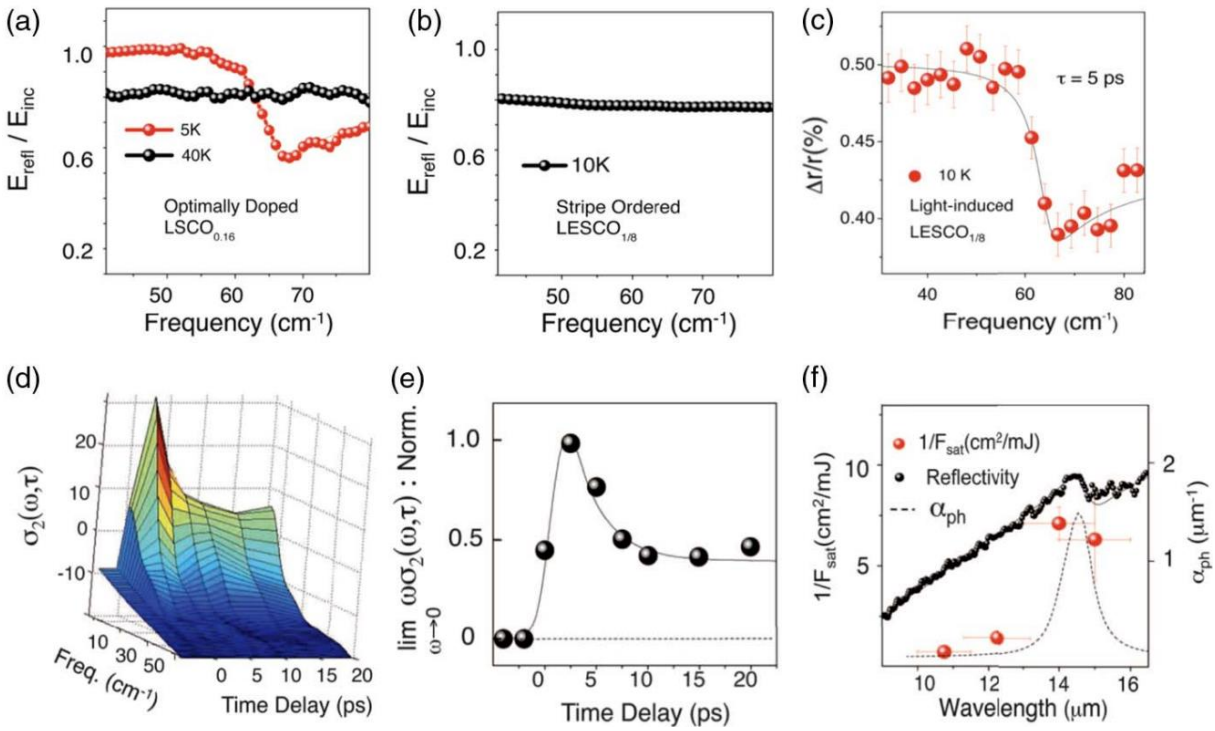

Figure 3-2: (a) Equilibrium c-axis reflectivity of $La_{1.84}Sr_{0.16}CuO_4$ (T_C = 35 K). In the superconducting state, the appearance of a JPR reflects coherent interlayer transport. Above T_C, incoherent ohmic transport is identified by a flat and featureless spectrum. (b) Equilibrium c-axis reflectivity of $La_{1.675}Eu_{0.2}Sr_{0.125}CuO_4$ at 10 K, showing the response of a non-superconducting compound. (c) Reflectivity changes induced in $La_{1.675}Eu_{0.2}Sr_{0.125}CuO_4$ by MIR excitation at 10 K, displaying a light-induced JPR. (d) Corresponding frequency- and time-delay-dependent imaginary conductivity (showing a $1/\omega$-like divergence) and (e) extracted superfluid density. (f) Inverse threshold (photo-susceptibility) as a function of pump wavelength (red dots), tuned in the spectral region of the Cu–O stretching mode. Data are shown along with the equilibrium ab-plane reflectivity and absorption coefficient (dashed) of $La_{1.675}Eu_{0.2}Sr_{0.125}CuO_4$. From {Fausti, 2011 #18}. Reprinted with permission from AAAS.

measure of photo-susceptibility, plotted in comparison with the equilibrium absorption coefficient α (dashed line). An observed resonance at the frequency of the driven phonon suggests a connection between the direct excitation by the light pulses and the formation of transient superconductivity.

The later work by (Hunt, Nicoletti et al. 2015) shed more light on the temperature dependence and relaxation dynamics of the transient state. In this experiment, which uses the same MIR excitation as in (Fausti, Tobey et al. 2011), improved signal-to-noise yielded observation of light-induced superconductivity up to a temperature of ~ 80 K, which corresponds to the charge order transition temperature T_{CO} in LESCO, while in the previous experiment a signal above noise was seen only up to ~15 K. The results are shown in Figure 3-3 (a), where a light-induced reflectivity edge survives up to $T_{CO} \cong 80$ K. interestingly, a discontinuous drop is seen when crossing the spin order temperature $T_{SO} \cong 25$ K.

Additionally, the temporal evolution of the light-induced state can be fit with a double exponential decay with good agreement. The two decay time constants τ_1 and τ_2 are plotted as a function of temperature in Figure 3-3 (b). Two distinct kinetic regimes can be identified: the life-time stays almost independent of temperature up to T_{SO} but decreases exponentially with increasing temperature above T_{SO} and up to T_{CO}. One explanation for the behaviour in the

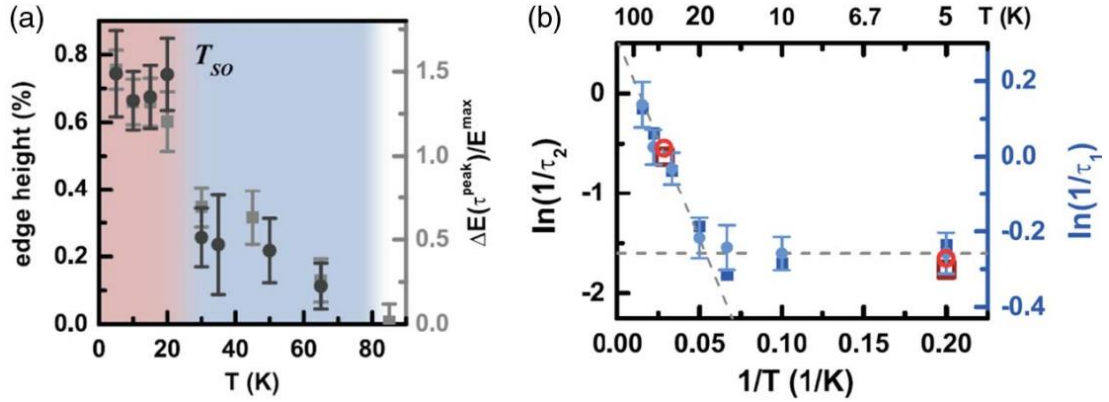

Figure 3-3: (a) Pump-induced change in the THz field amplitude and corresponding size of the Josephson plasma edge measured in $La_{1.675}Eu_{0.2}Sr_{0.125}CuO_4$ at 1.8 ps time delay after MIR excitation, at different base temperatures. The JPR size remains approximately constant below the spin-order transition temperature T_{SO}, but drops rapidly between T_{SO} and T_{CO} (dark gray circles). (b) Arrhenius plot of the relaxation rate as a function of temperature. The fast component τ_1 (dark blue squares) and the slow component τ_2 (light blue circles) track the decay of the coherence length of the transient plasma. The lifetime of the transient state remains temperature independent (horizontal gray dashed line) below the spin-order transition temperature, $T_{SO} \simeq 25$ K. Above this transition, the lifetime exhibits an exponential temperature dependence, with an energy scale of 4 meV for τ_2 and 0.8 meV for τ_1 (gray dashed line). Reprinted with permission from {Hunt, 2015 #154}. Copyright 2022 by the American Physical Society.

$T_{SO} < T < T_{CO}$ range is the expectation of a transition between two different thermodynamic phases separated by a free energy barrier. Based on the transition temperature, the extracted energy scale on the order of meV corresponds to that of spin fluctuations found in other single-layer cuprates (Petit, Moudden et al. 1997, Lee, Yamada et al. 2003, Kofu, Lee et al. 2009), suggestive of the regulating role played by spin rearrangements in the transition between the two phases. This is consistent with previous observations that strong spin fluctuations can develop in the range $T_{SO} < T < T_{CO}$ (Tranquada, Gu et al. 2008, Grafe, Curro et al. 2010).

The fact that below T_{SO} a departure from this behaviour is observed could be related to the freezing out of such spin fluctuations, which is compatible with quantum coherent tunnelling between two states such as between superconductivity and a pair density wave at constant carrier density. In this picture, Cooper pairing would already exist in the CuO_2 planes and are superimposed or intertwined with the stripe phase (Hayward Lauren, Hawthorn David et al. 2014, Lee 2014, Fradkin, Kivelson et al. 2015). Hence, the dynamic destruction of the stripes gives rise to transient 3D superconductivity by allowing Josephson tunnelling along the c-axis to re-establish.

The question of the fate of the stripe order and the LTT distortion in the context of the light-induced superconducting state is further explored by the experiment of (Först, Tobey et al. 2014) through the use of femtosecond resonant soft X-ray diffraction in the closely related

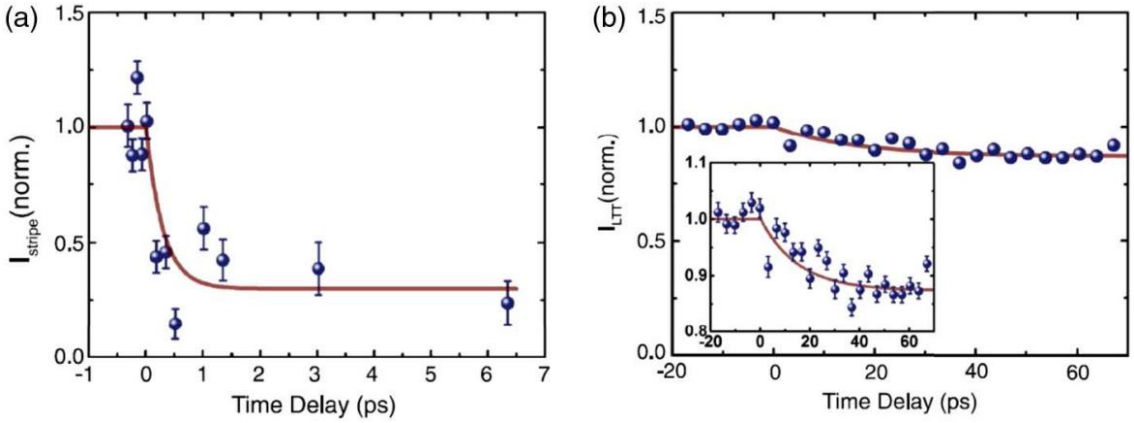

Figure 3-4: (a) Transient intensity of the charge stripe order diffraction peak in $La_{1.875}Ba_{0.125}CuO_4$ measured at the (0.24 0 0.5) wave vector. MIR excitation results in a prompt sub-picosecond decrease of the scattered intensity. The red solid line is an exponential fit with a time constant of 300 fs, i.e., the resolution of the experiment. (b) Corresponding changes in the intensity of the (001) diffraction peak (reflecting the LTT distortion) in the same crystal under the same excitation conditions. The red solid line is an exponential fit yielding a time constant of 15 ps. Reprinted with permission from {Först, 2014 #146}. Copyright 2022 by the American Physical Society.

compound $La_{1.875}Ba_{0.125}CuO_4$ (LBCO). The stripe order is tracked by the (0.24 0 0.5) wave vector while the LTT distortion is measured by the (001) diffraction peak. Again, MIR pulses at a similar fluence are used to excite the in-plane Cu-O stretching phonon mode in LBCO at 15 K.

The integrated scattering intensity of the stripe order diffraction peak is plotted against time delay after photoexcitation in Figure 3-4 (a). A prompt reduction of 70% is seen within 1 ps after the pump pulse hits the sample, which is a similar time scale over which transient superconductivity onsets in LESCO as found by (Fausti, Tobey et al. 2011), further supporting an intimate connection between the two. By contrast, the LTT distortion follows a distinct time scale. As shown in Figure 3-4 (b), the integrated scattered intensity is reduced by only 12% with a much larger time constant of ∼15 ps.

Taken together, these results demonstrate a picture in which phonon excitation by MIR pulses causes the melting of stripes and leads to a transient, non-equilibrium state with superconducting signatures, while leaving the LTT structural distortion mostly unaffected. This works through the removal of suppression on Josephson tunnelling between the planes by the stripes, hence re-establishing coherent interlayer coupling on sub-picosecond time scales. It is worth noting that the role of the LTT distortion is a minor one, as other studies on LBCO with non-resonant excitation at near-infrared and optical frequencies also observe light-induced superconductivity (Nicoletti, Casandruc et al. 2014, Casandruc, Nicoletti et al. 2015). This topic is discussed in more detail in the following Section 3.1.2.

3.1.2 Charge-transfer excitation in $La_{2-x}Ba_xCuO_4$

Ultrafast optical excitation of the in-plane Cu-O bond stretching mode in $La_{1.675}Eu_{0.2}Sr_{0.125}CuO_4$ (LESCO 12.5%), a doping where a robust stripe order strengthened by the LTT distortion completely suppresses superconductivity, has demonstrated re-establishment of coherent interlayer tunnelling, which can be understood in terms of ultrafast removal of frustration of interlayer coherence (Fausti, Tobey et al. 2011). Femtosecond resonant X-ray diffraction revealed decoupling of the stripe and lattice orders on ultrafast time scales in LBCO 12.5% - a closely related compound with many similar structural features - further supports the view that the stripes are responsible for preventing interlayer coupling

in equilibrium (Först, Tobey et al. 2014). Therefore, it is sensible to seek alternative means of removal of the stripe order in LBCO.

Unlike the mid-infrared radiation for excitation of lattice vibration modes demonstrated in Section 3.1.1, 800 nm is not a wavelength in resonance with any such normal modes. Rather, in LBCO, it is located on the shoulder of a peak in conductivity which corresponds to an electronic interband transition. Due to the high photon energy at 1.5 eV, this kind of near-infrared (NIR) excitation has been used for melting charge density wave order on an ultrafast time scale in a range of materials (Eichberger, Schäfer et al. 2010, Petersen, Kaiser et al. 2011, Rohwer, Hellmann et al. 2011, Liu, Gierz et al. 2013). Given plentiful evidence discussed in Chapter 2 for stripes of spatially modulated charge and spin ordering found in hole-doped LBCO at low temperature coexisting and competing with superconductivity, it is sensible to make use of such high energy excitation to perturb the stripe order and observe the ensuing dynamics of the superconducting condensate to help shed light on the entangled nature of interactions between these ordered states.

In the study by (Nicoletti, Casandruc et al. 2014), 800 nm-wavelength laser pulses with ~100 fs duration are shone onto LBCO samples, with polarisation of the electric field set to be parallel to the out-of-plane direction of the single crystal. Then a single-cycle broadband THz pulse is reflected off the sample surface, also polarised along the c-axis, and optical response

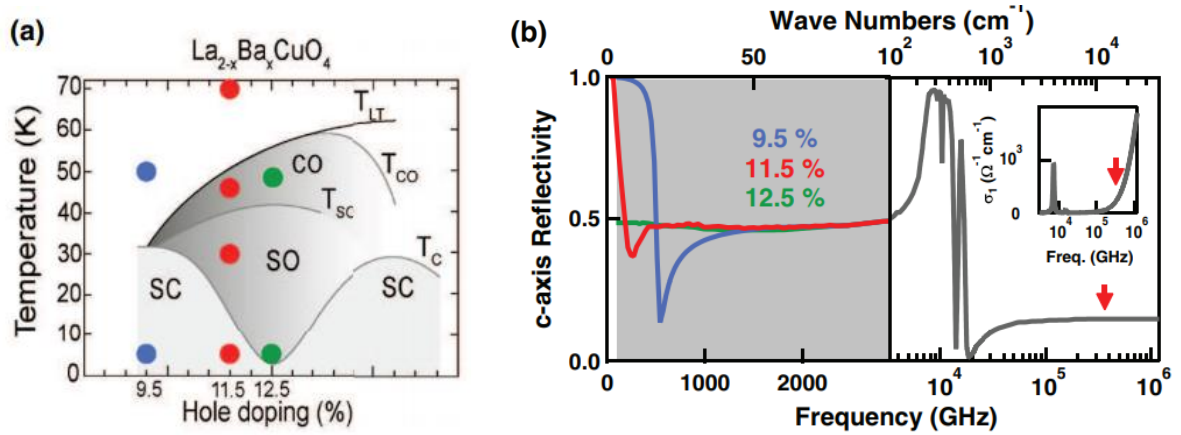

Figure 3-5: (a) Temperature-doping phase diagram of LBCO, as determined in (Hücker, v. Zimmermann et al. 2011). T_C, T_{CO}, T_{SO}, and T_{LT} indicate the superconducting, charge-order, spin-order, and structural transition temperatures, respectively. Colored circles indicate the different dopings and temperatures for which data are reported here. (b) Equilibrium c-axis optical properties of LBCO. Left panel: THz reflectivity of the three samples at T = 5 K. The region investigated in this experiment is shaded in gray. Right panel and inset: broadband c-axis reflectivity and optical conductivity of LBCO from (Homes, Hücker et al. 2012). Red arrows indicate the pump photon energy. Reprinted with permission from (Nicoletti, Casandruc et al. 2014). Copyright 2022 by the American Physical Society.

functions including reflectivity, conductivity, and energy loss function are retrieved as a function of time delay between the NIR pump pulse and the THz probe pulse. Three nominal doping levels were studied, with x = 9.5%, 11.5%, and 12.5%, covering the underdoped region of the phase diagram as well as the important 1/8 doping where the stripes are the strongest. A phase diagram of the compounds measured is shown in Figure 3-5 (a).

At equilibrium, a clear edge in measured c-axis reflectivity corresponding to the Josephson plasma resonance can be seen for the 9.5% and 11.5% dopings in the superconducting state, at ~500 GHz for x = 9.5% and ~200 GHz for x = 11.5%, whereas the

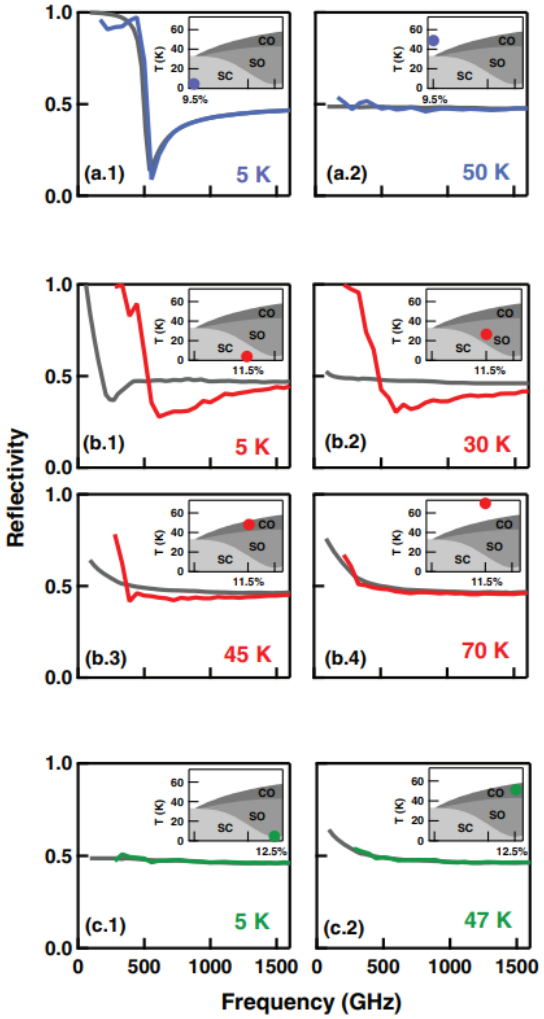

Figure 3-6: (Color online) THz reflectivity of LBCO displayed at different doping values and temperatures at equilibrium (gray) and 1.5 ps after excitation (colored). Data in panels (a) and (b) have been taken with a pump fluence of ~2 mJ/cm^2 (a saturation in the fluence dependence of the pump-induced changes was found above ~1 mJ/cm^2). Those in panels (c) were taken instead with ~3 mJ/cm^2. All spectra are shown in the region below 1600 GHz to highlight the pump-induced changes. The low-frequency cutoff is due to sample-size effects. Transient spectra cover a narrower range, due to the higher noise of the pump-probe measurement. Reprinted with permission from (Nicoletti, Casandruc et al. 2014). Copyright 2022 by the American Physical Society.

transition T_C for 12.5% sample (<2.4K) is too low to be achieved, and hence the normal state reflectivity is featureless in this frequency range, as shown in Figure 3-5 (b).

In the pump-probe measurements, 800 nm pump pulses with fluence up to 2 mJ/cm^2 are focused onto the samples. The retrieved transient response from all measured dopings are shown in Figure 3-6. 1.5 ps after strong photoexcitation with, however, distinct behaviours emerge depending on the doping level. In the lowest doping x = 9.5%, a very small blue shift of the plasma edge in reflectivity is seen in the superconducting state [panel (a.1)], possibly as a result of enhanced interlayer tunnelling; in the normal state, not much seems to have happened [panel (a.2)].

Far more striking is the response of the x = 11.5% sample. In the superconducting state below T_C [panel (b.1)], a dramatic blue shift is observed, from ~200 GHz at equilibrium to 600 GHz. Furthermore, in the stripe phase above T_C [panel (b.2)], a reflectivity edge develops when there is none at equilibrium. This light induced edge survives up to the charge order transition temperature T_{CO} [panel (b.3)], and is no longer detectable above that point [panel (b.4)]. Perhaps a bit surprisingly, on the x = 12.5% sample, no light-induced changes are seen at all measured temperatures and time delays [panels (c)]. It is postulated that this could be the result of the fact that the photo-susceptibility is much higher because the stripes are static and commensurate in this doping.

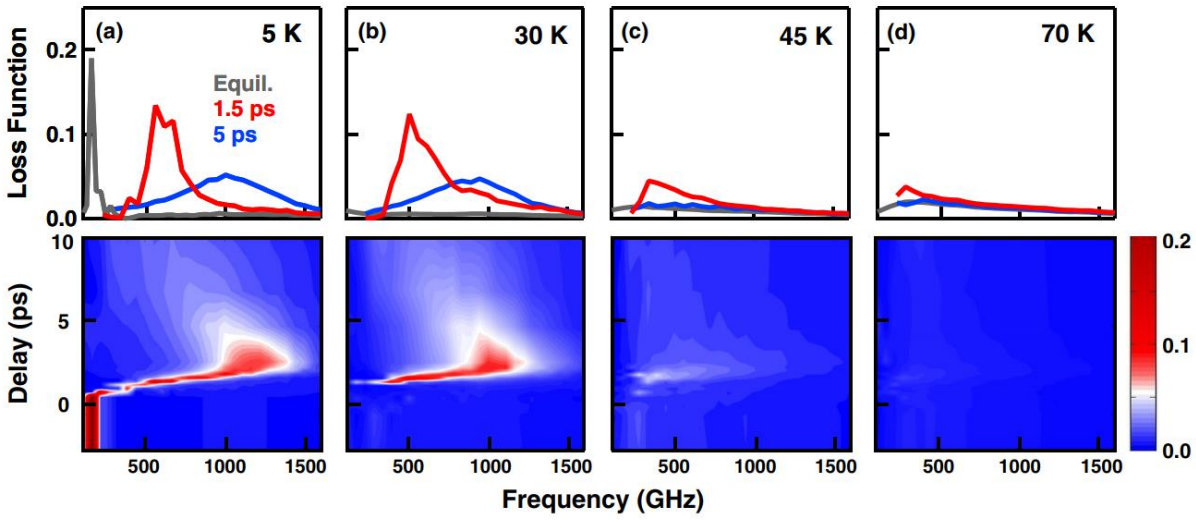

Figure 3-7: (Color online) Energy loss function $Im\left(-\frac{1}{\tilde{\varepsilon}(\omega)}\right)$ of $La_{1.885}Ba_{0.115}CuO_4$ as a function of temperature and pump-probe delay. The lower panels show its evolution throughout the light-induced dynamics. The upper panels show selected line cuts at negative (gray), +1.5 ps (red), and +5 ps (blue) time delay. All data have been taken using a pump fluence of 2 mJ/cm^2. Reprinted with permission from (Nicoletti, Casandruc et al. 2014). Copyright 2022 by the American Physical Society.

A more direct way to track the evolution of the plasma edge is to plot the energy loss function $Im\left(-\frac{1}{\tilde{\varepsilon}(\omega)}\right)$, which displays a peak at the plasma frequency, as shown in Figure 3-7. Focusing on the x = 11.5% doping where the light-induced effect is the strongest, a continuous blue shift of the loss function peak takes place after the NIR pulse strikes, shifting up to ~1200 GHz at ~2.5 ps delay, a six-fold increase, before relaxation starts [panels (a)]. A similar behaviour is observed in the stripe phase at $T_C < T = 30\ K < T_{SO}$ [panels (a)], and progressively weakens as temperature increases [panels (c)], until disappearing completely above T_{CO} [panels (d)].

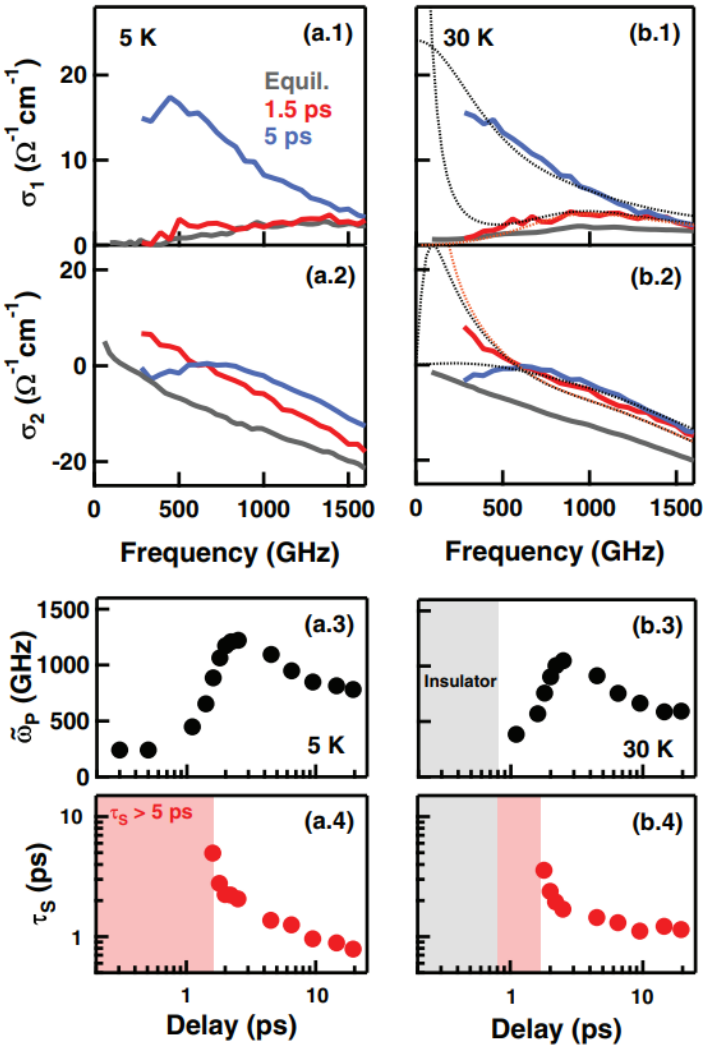

Figure 3-8: [Panels (a.1), (a.2), (b.1), (b.2)] Complex optical conductivity of $La_{1.885}Ba_{0.115}CuO_4$ at 5 and 30 K, shown at different pump-probe delays, for a fluence of 2 mJ/cm^2. In panels (b.1) and (b.2) examples of fits with a Drude model (black dots) and with a perfect-conductor model (red dots) are displayed. [Panels (a.3), (a.4), (b.3), (b.4)] Parameters extracted from the Drude fits as a function of pump-probe delay. The gray shaded region indicates the insulating regime (no Drude fit possible). The red shaded area refers to the highly coherent state. Reprinted with permission from (Nicoletti, Casandruc et al. 2014). Copyright 2022 by the American Physical Society.

Also instructive is to look at the conductivity $\sigma_1(\omega) + i\sigma_2(\omega)$, shown in Figure 3-8. At equilibrium, a superconducting response include a fully gapped σ_1 and a σ_2 that turns positive at low frequency and keeps on increasing towards zero frequency, plotted as grey curves in panels (a.1) and (a.2). Again, features of enhanced coherent transport, in the superconducting state [panels (a.1) and (a.2)], or induced, in the stripe phase [panels (b.1) and (b.2)], interlayer tunnelling are detected at about 1.5 ps after photo-excitation (red curves), where the σ_2 is enhanced significantly or induced while σ_1 retains the gap-like region at low frequency. The complex conductivities point to an increase in the interlayer coupling and is incompatible with a charge excitation scenario. It is worth noting that the light-induced response saturates at ~1 mJ/cm^2 fluence and is different from what would be expected from above-gap incoherent plasma excitation in a semiconductor. At later delays (τ = 5 ps, blue curves), the response approaches that of a more incoherent state.

The transient conductivities can be fit with a Drude model as,

$$\sigma_1(\omega) + i\sigma_2(\omega) = \frac{\omega_p^2}{4\pi}\frac{\tau_s}{1 - i\omega\tau_s}$$

where ω_p is the plasma frequency and τ_s the carrier scattering time. The model produces good agreement with the data at all temperatures and time delays. High-frequency Lorentz oscillators are added to reproduce the background in the optical spectra and are kept constant during fitting. Such fits are plotted in Figure 3-8 (b.1) and (b.2) as black dots, in good agreement with the experimental data at all temperatures and delays. Then, the screened plasma frequency $\tilde{\omega}_p = \omega_P / \sqrt{\varepsilon_{FIR}}$ (where $\varepsilon_{FIR} \cong 30$) and the scattering time τ_s can be extracted from the fits, as shown in Figure 3-8 (a.3)(a.4)(b.3)(b.4).

Below T_C [panels (a.3) and (a.4)] and at delays $\tau \leq 1.5$ ps, the Drude model captures the measured transient data well, with $\tau_s > 5$ ps or with the spectrum of a superconductor with $\tau_s \to \infty$ as

$$\sigma_1(\omega) + i\sigma_2(\omega) = \frac{\omega_p^2}{8}\delta[\omega = 0] + \frac{\omega_p^2}{4\pi}\frac{i}{\omega}$$

At 30 K [panels (b.3) and (b.4), the extracted parameters also show a state with high-mobility carriers being induced and optical properties compatible with a transient superconductor.

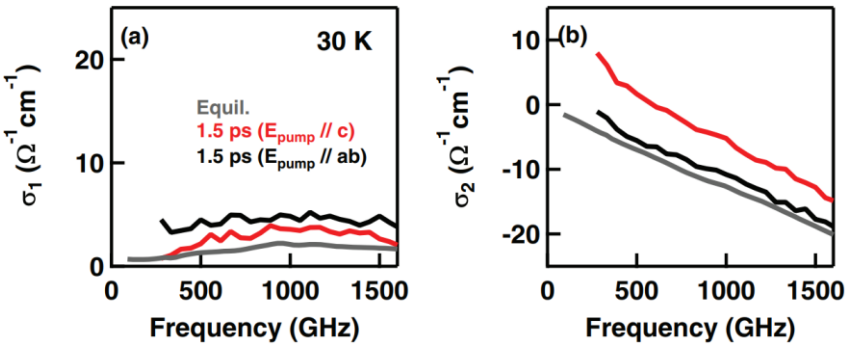

Figure 3-9: Complex optical conductivity of $La_{1.885}Ba_{0.115}CuO_4$ at 30 K, 1.5 ps after optical excitation with light polarized perpendicular (red) or parallel (black) to the CuO_2 planes. Data are taken with the same pump fluence of 2 mJ/cm^2. Reprinted with permission from (Nicoletti, Casandruc et al. 2014). Copyright 2022 by the American Physical Society.

At longer time delays ($\tau \geq 2$ ps), it is observed that the system relaxes into a state of reduced coherence. The data can be fit with a scattering time of $\tau_s \sim 5$ ps, which reduces to ~1 ps at even later delays. Meanwhile, $\widetilde{\omega}_p$ keeps increasing up to more than 1 THz at 2.5 ps delay before relaxing back to roughly 500 GHz. The scattering time is still considered anomalously high for conventional incoherent transport, and could even be interpreted as indicative of a coherent state where fluctuations play a big role. This is analogous to the interpretation of equilibrium response of LSCO both below and above T_C presented by (Bilbro, Aguilar et al. 2011).

As shown in Figure 3-9, where the transient conductivities from Figure 3-8 (b) at 30 K (red) are compared with those observed with pump polarisation rotated to be parallel to the CuO_2 planes. It was also found that, pump field polarised in-planes generates a much weaker effect than out-of-plane. Not only is the induced interlayer coupling much stronger as demonstrated by the low-frequency uptick in σ_2 when the pump is polarised out-of-plane, but also the quasiparticle response is weaker in σ_1 than in-plane excitation. One explanation could be a combination of the weak coupling to quasiparticle excitation in two-dimensional superconductors by out-of-plane polarisation, and effective melting of stripe order over many layers allowing for more coherent Josephson tunnelling. However, based on the THz measurements alone, it is not fully clear how much of the photoinduced response stripe melting is responsible for. Hence, two subsequent studies aim to address this question.

The first follow-up experiment by (Casandruc, Nicoletti et al. 2015) explores the question of the efficiency of coupling to the stripe order by optical excitation, where several different wavelengths of light are examined in the context of the transient superconducting state. The measurements focus exclusively on LBCO x = 11.5% because of its most pronounced

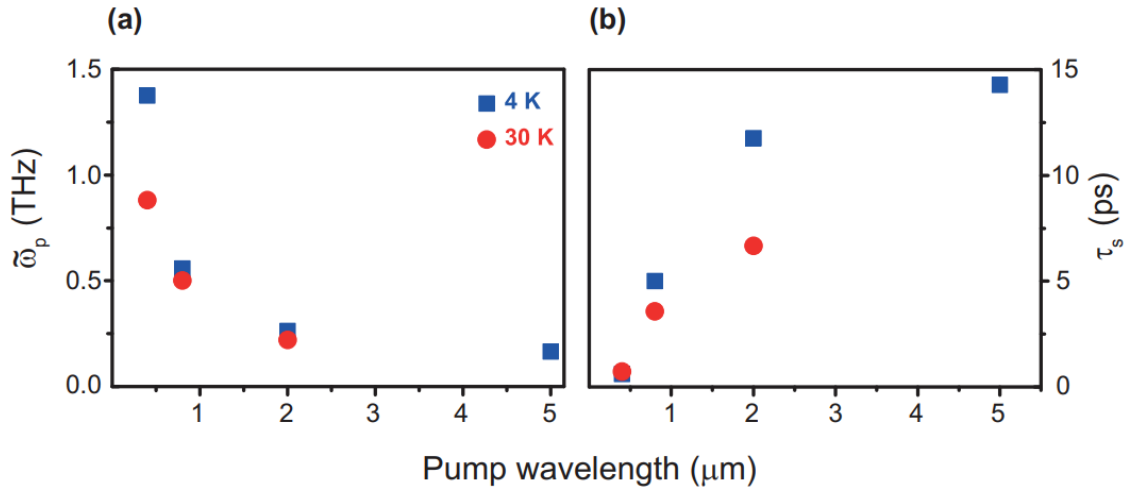

Figure 3-10: (a) Screened plasma frequency and (b) scattering time of the transient state displayed as a function of pump wavelength for temperatures below (blue) and above (red) TC. All values have been extracted via Drude fits to the spectra measured at τ = 1.5 ps with a pump fluence corresponding to ~2 × 10^{20} photons/cm^3. Estimates of $\tilde{\omega}_p$ and τ_s were also obtained directly from the loss function peak frequency and inverse width, in perfect agreement with those extracted from the fits. Reprinted with permission from (Casandruc, Nicoletti et al. 2015). Copyright 2022 by the American Physical Society.

and intriguing transient responses among all dopings studied in the previous experiment. Following a similar procedure of fitting the transient optical conductivities at all temperatures and pump-probe delays for four different excitation wavelengths – 400 nm, 800 nm, 2 μm, and 5 μm – the screened plasma frequency $\tilde{\omega}_p$ and scattering time τ_s are extracted.

These two quantities at 1.5 ps time delay are plotted in Figure 3-10 for all four excitation wavelengths. The main message from the plot is the following: interlayer tunnelling is most effectively enhanced at shorter pump wavelengths, but incoherent processes set in sooner and the transient phase relaxes faster after excitation with higher photon energies. The explanation proposed for this result is that strong electronic correlations are dominant in stabilising charge order in the first place. As opposed to conventional understanding that competing orders like the charge density wave and superconductivity interact on energy scales close to the ordering temperatures ($\sim$10 meV), the condition of experiment is suggestive of the notion that interactions on a high energy scale can also compete and cooperate to provide order at far lower energies.

Another experiment studying the same sample by (Khanna, Mankowsky et al. 2016) focuses on disentangling the roles played by optical stripe melting and lattice structural changes by direct comparison of the time scales of these dynamics. Time-resolved resonant soft X-ray diffraction (TR-RSXD) and THz time domain spectroscopy are employed to

demonstrate the dominant correlation between disruption of the stripe order and enhanced superconducting coupling caused by near-IR excitation at 800 nm, with the major difference from the experiment by (Nicoletti, Casandruc et al. 2014) in the polarisation now along the in-plane direction. Again, measuring exclusively the x = 11.5% doping of LBCO, the experiment tracks the stripe order using a charge-density wave with incommensurate wave vector (0.23 0 0.65), while the LTT structural distortion involving a buckling of the Cu-O-Cu bonds in the CuO_2 planes and a tilting of the CuO_6 octahedra is monitored via the (0 0 1) reflection. Together, these two diffraction peaks provide a direct probe of the extent of stripe ordering and LTT distortion.

As shown in the left panel of Figure 3-11, the change in diffraction peak intensities $\Delta I_\tau / I_0$ as a function of pump-probe delay τ is plotted. Both peak intensities are observed to decrease by ~40%, however the time constant from fitting the decays (black and red curves) differs dramatically. For the stripe order (0.23 0 0.65) peak, a value of 10 ± 3 ps is found, indicating a prompt response within a few hundred femtoseconds after photoexcitation. By contrast, the LTT (0 0 1) peak decreases over a much longer time scale with 77 ± 7 ps time constant. This demonstrates that the 800 nm photoexcitation creates a charge transfer

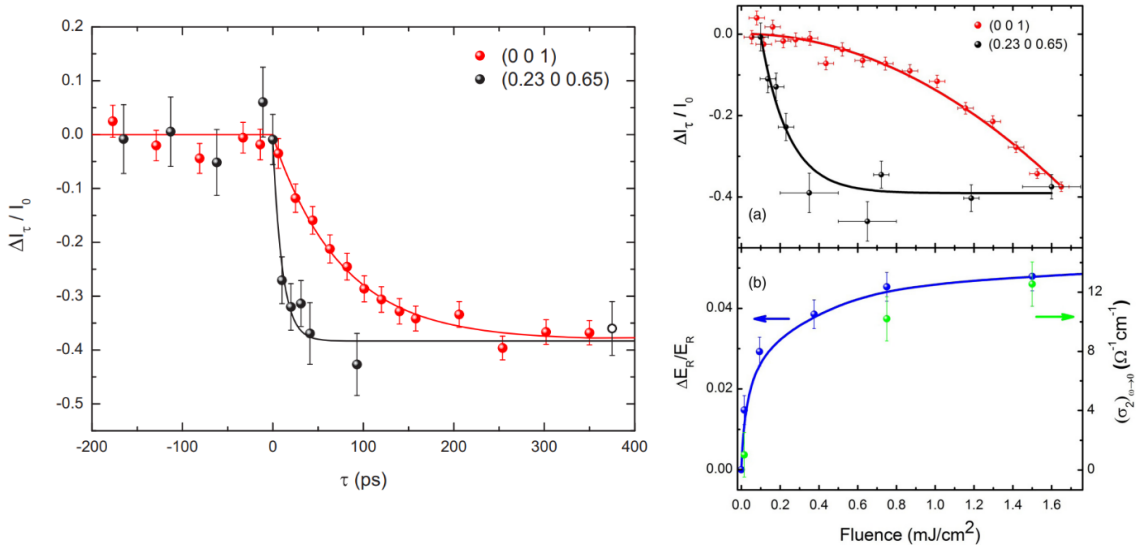

Figure 3-11: (Left) Intensity changes in the (0.23 0 0.65) charge-ordering diffraction peak (solid black circles) and (0 0 1) LTT distortion diffraction peak (solid red circles) following near-infrared photoexcitation using a pump fluence of 1.6 mJ/cm^2. (Right) (a) Fluence dependence of the (0.23 0 0.65) charge-ordering diffraction peak (solid black circles) and (0 0 1) LTT distortion diffraction peak (solid red circles) intensity after photoexcitation with τ = 350 ps. The red line shows a quadratic fit whereas the black line shows an exponential fit to the data. (b) Changes in the electric field, $\Delta E_R / E_R$ (solid blue circles) and $(\sigma_2)_{\omega \to 0}$ (solid green circles) as a function of fluence (frequency = 0.2 THz, τ = 1.5 ps). The blue line shows a fit using an exponential function. Reprinted with permission from (Khanna, Mankowsky et al. 2016). Copyright 2022 by the American Physical Society.

nonequilibrium phase in which the stripe order is strongly suppressed while the LTT distortion remains largely unaffected, similar to the effect of phonon excitation in (Först, Tobey et al. 2014).

The THz time-domain reflectivity measurements produce results qualitatively similar to those first reported by (Nicoletti, Casandruc et al. 2014). A transient state of enhanced interlayer coupling evidenced by the blueshift of the reflectivity edge and enhancement of σ_2 towards low frequencies at 1.5 ps time delay, is followed by reduced coherence shown by a broadened edge in reflectivity and a σ_2 no longer diverging at 2.5 ps.

Taken under the same near-IR excitation condition, the TR-RSXD and THz results allow direct comparison of the time scales of the light-induced changes. The enhancement of interlayer coupling develops in $\sim$1 ps after photoexcitation, which is consistent with the observed collapse of the stripe order. On the other hand, the LTT lattice distortion reacts on a significantly longer time scale ($>$10 ps).

A fluence dependence measurement further supports this distinction. Shown in the right panel of Figure 3-11 is the same two diffraction peak intensities as a function of pump fluence at a fixed time delay $\tau = 350$ ps. At $\sim$0.5 mJ/cm^2, the stripe melting saturates while the LTT distortion remains mostly intact. For comparison, the transient changes in the low-frequency limit of $(\sigma_2)_{\omega\to 0}$ and reflected electric field $\Delta E_R \,/\, E_R$ at the peak of the response ($\tau =$1.5 ps) are plotted below. The fact that both the THz response and the stripe order melting show a saturation at $\sim$0.5 mJ/cm^2, while the structural peak does not, reinforces the connection between the stripe melting and enhanced superconductivity.

3.2 Bi-layer cuprates

3.2.1 Optical control of superconductivity in $YBa_2Cu_3O_{6+\delta}$

In addition to LESCO and LBCO, optical control of superconductivity has also been applied to $YBa_2Cu_3O_{6+\delta}$, a bilayer cuprate (Hu, Kaiser et al. 2014, Kaiser, Hunt et al. 2014). The crystal structure is orthorhombic, consisting of bilayers of CuO_2 planes separated by insulating yttrium layers. The bilayers are further spaced by Cu-O chains determining the hole concentration within the planes. See Figure 3-12 (a) for an illustration of the structure.

Analogous to the single-layer compounds discussed in Section 3.1, a reflectivity edge corresponding to the JPR can be seen in the c-axis THz response, a result of inter-bilayer Josephson tunnelling of superconducting carriers. Figure 3-12 (b) shows the reflectivity for several dopings of YBCO. They are all situated in the underdoped region of the phase diagram.

The MIR excitation is now tuned to resonantly drive the so-called apical oxygen phonon mode, which involves oscillation of oxygen atoms between the bilayers, because their static

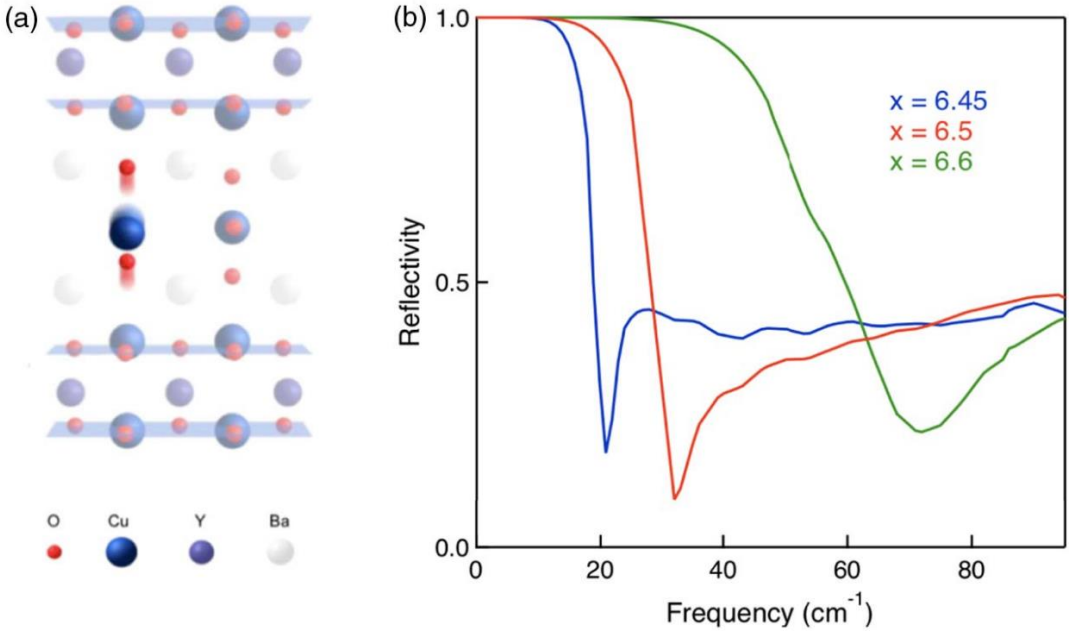

Figure 3-12: (a) Crystal structure of orthorhombic $YBa_2Cu_3O_{6.5}$ and sketch of the resonantly excited B_{1u}-symmetry IR-active phonon mode, comprising c-axis motions of the apical oxygen atoms between bilayers. Reprinted with permission from (Först, Mankowsky et al. 2015). Copyright 2022 American Chemical Society. (b) Equilibrium reflectivity spectra of $YBa_2Cu_3O_{6.45}$, $YBa_2Cu_3O_{6.5}$, $YBa_2Cu_3O_{6.6}$ measured along the c-axis, showing clear edges at the JPR frequencies. Adapted with permission from (Kaiser, Hunt et al. 2014). Copyright 2022 by the American Physical Society.

positions have been shown to affect the in-plane band structure and correlate strongly with maximum T_C in each cuprate family (Pavarini, Dasgupta et al. 2001). Therefore, one might expect that oscillations of the atoms driven to large amplitude by resonant MIR pulses could also result in changes in the superconducting behaviour in YBCO.

The light induced response in the superconducting state is shown in Figure 3-13 (a)-(c). For all three dopings, optical excitation results in an increase in the imaginary conductivity σ_2, which points to an enhancement of inter-bilayer Josephson coupling. In reflectivity, this corresponds to the appearance of a new JPR with higher stiffness than, and at the expense of, that in equilibrium. At 100 K, above the highest equilibrium T_C in the YBCO family, a light-induced reflectivity edge is seen at ~1 ps time delay after photoexcitation, as shown in Figure 3-13 (g)-(i), analogous to observations in LESCO as discussed in Section 3.1.1. At the same time,

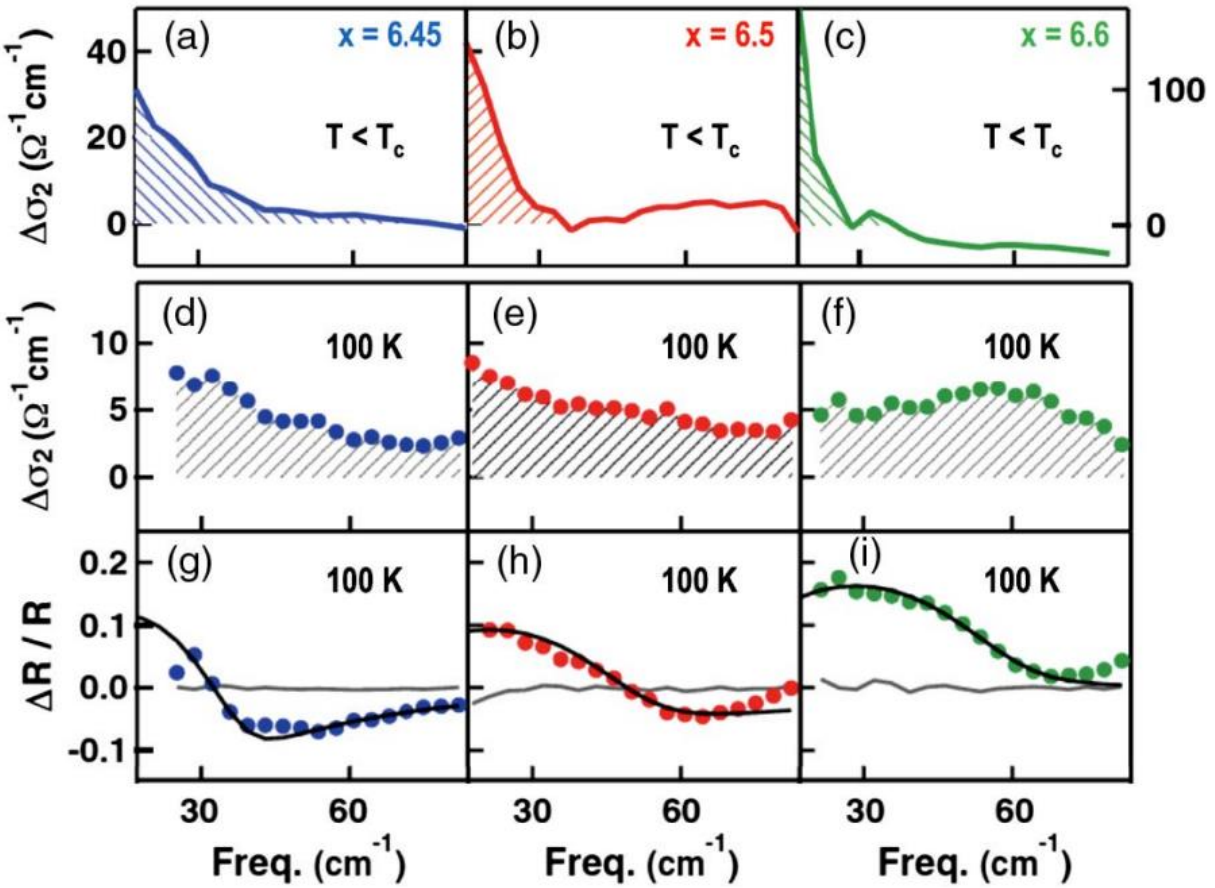

Figure 3-13: (a)–(c) Transient changes in the c-axis imaginary conductivity of $YBa_2Cu_3O_{6.45}$, $YBa_2Cu_3O_{6.5}$, and $YBa_2Cu_3O_{6.6}$ measured below T_C (i.e., in the superconducting state), 1 ps after MIR phonon excitation. Data in (a) and (b) refer to the right σ_2 scale, while those in (c) to that on the left. (d)–(f) Light-induced imaginary conductivity changes measured in the same samples, under the same excitation conditions, and at the same time delay as in (a)–(c), at a base temperature of 100 K (above T_C). (g)–(i) Light-induced reflectivity changes corresponding to the conductivity curves in (d)–(f). Adapted with permission from (Kaiser, Hunt et al. 2014). Copyright 2022 by the American Physical Society.

an increase in σ_2 is also observed [see Figure 3-13 (d)-(f)], compatible with a transient superconducting state induced above the equilibrium T_C.

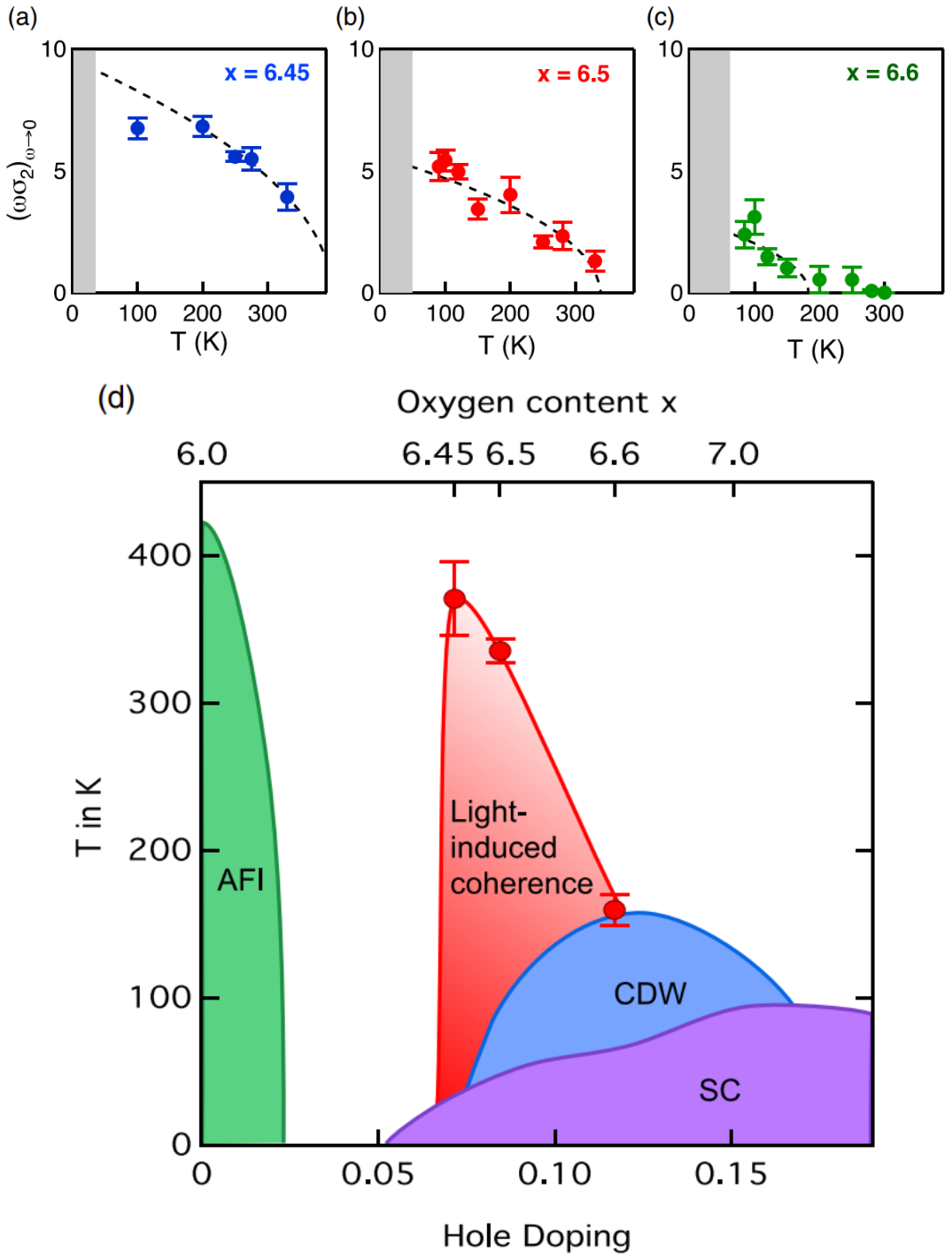

Figure 3-14: (a)–(c) Strength of the light-induced inter-bilayer coupling measured in $YBa_2Cu_3O_{6.45}$, $YBa_2Cu_3O_{6.5}$, $YBa_2Cu_3O_{6.6}$ at ~1 ps pump-probe delay as a function of base temperature and quantified by the zero-frequency extrapolation of the enhancement in imaginary conductivity. Gray shaded regions refer to the equilibrium superconducting state. (d) Phase diagram of $YBa_2Cu_3O_x$. AFI, CDW, and SC refer to the equilibrium antiferromagnetic insulating, charge-density-wave, and superconducting phase, respectively. The red circles, estimated from the data in (a)–(c), delimit the region where signatures of possible light-induced superconductivity were measured. Reprinted with permission from (Nicoletti and Cavalleri 2016) ©The Optical Society.

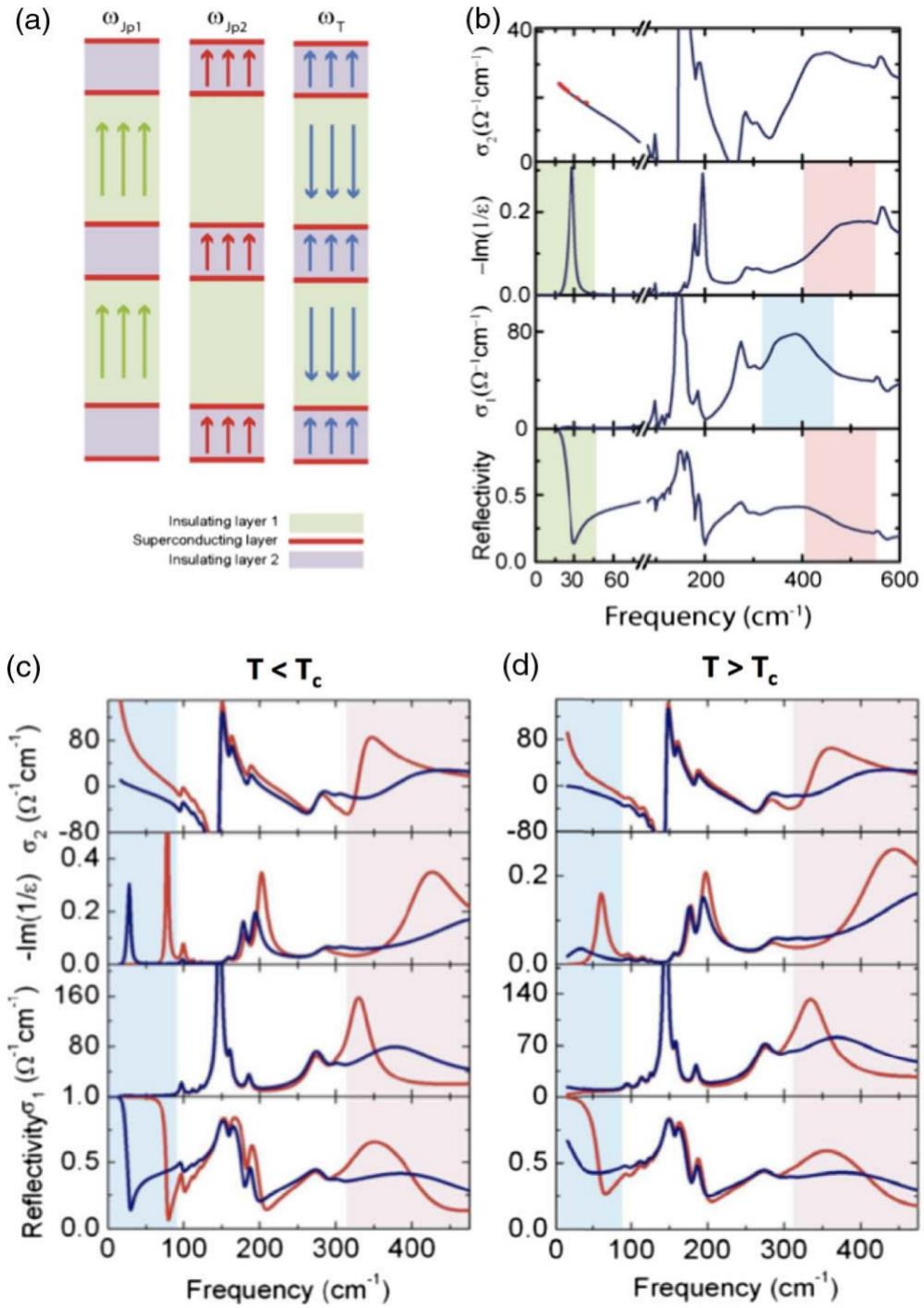

Figure 3-15: (a) In the superconducting state, the structure of $YBa_2Cu_3O_{6.5}$ can be viewed as two Josephson junctions in series, giving rise to two longitudinal modes (ω_{JP1}, ω_{JP2}) and a transverse mode (ω_T) (arrows indicate the direction of the current). (b) Equilibrium c-axis optical properties of $YBa_2Cu_3O_{6.5}$. Superconductivity is evidenced by the $1/\omega$ divergence (red dashed) in the imaginary conductivity. Both longitudinal JPRs appear as peaks in the loss function and edges in reflectivity (green and red shaded). The transverse JPR appears as a peak in σ_1 (blue shaded). (c), (d) Effective medium fits used to reproduce the transient broadband optical response after MIR excitation. Blue curves refer to the unperturbed component ($\gtrsim 80\%$) (equilibrium superconductor below Tc and normal insulator above T_C). Red curves indicate the photo-susceptible component ($\lesssim 20\%$), which has a stiffer inter-bilayer JPR and red-shifted high-frequency plasmons. Reprinted by permission from Springer Nature: (Hu, Kaiser et al. 2014).

The relaxation dynamics of the light-induced reflectivity edge follows a similar double exponential decay to that found in LESCO. The time scales here, however, are much faster with $\tau_1 \cong 0.5$ ps and $\tau_2 \cong 5$ ps, and the ground state recovers within ~10 ps, suggesting that the excitation mechanism might be different from that in LESCO.

The measurements were repeated at higher temperatures to identify a temperature scale *T'* where light-induced superconductivity disappears for different dopings [see Figure 3-14 (a)-(c)]. *T'* is found to increase with decreasing hole concentration and exceed room temperature at *x* = 6.45 doping, tracking the pseudogap transition *T** (Timusk and Statt 1999), as shown in the phase diagram in Figure 3-14 (d). Here, the pseudogap phase is characterised by anomalous electronic properties and possible presence of pre-formed Cooper pairs without phase coherence (Emery and Kivelson 1995, Corson, Mallozzi et al. 1999, Gomes, Pasupathy et al. 2007). The experimental data is suggestive of a transfer of phase coherence from the phonon excitation to the pre-formed pairs, resulting in a transient superconductor.

Further insight into the driving mechanism of light-induced superconductivity in YBCO is provided by a closer look into the dynamics of another Josephson plasmon under identical excitation conditions, the so-called intra-bilayer plasma mode at ~15 THz, corresponding to the Josephson tunnelling within the bilayer units of YBCO (van der Marel and Tsvetkov 1996, van der Marel and Tsvetkov 2001) [see Figure 3-15 (a)]. Similar to the lower-frequency JPR, this plasmon is also seen as an edge in reflectivity and a peak in the loss function. Another so-called transverse plasmon related to the mixing of these two modes shows up as a peak in real conductivity σ_1 [see Figure 3-15 (b)].

In equilibrium, the intra-bilayer plasmon can be seen up to 150 K, which is much higher than T_C, and this is used to define the pseudogap phase in YBCO with precursors of superconductivity in the normal state by coherent tunnelling of pre-formed Cooper pairs within the bilayer units (Dubroka, Rössle et al. 2011, Uykur, Tanaka et al. 2014).

In this experiment by (Hu, Kaiser et al. 2014), time-resolved ultrabroadband spectroscopy is used to map out the dynamics after MIR excitation on the single doping *x* = 6.5. The measurements found that the transient optical properties can be fit at all temperatures and time delays with good agreement by assuming an effective medium with two components – one ($\geq$ 80%) not significantly affected by MIR excitation and the other ($\leq$ 20%) photo-susceptible and displaying a stiffened low-frequency JPR below T_C and a light-

induced JPR above T_C. Concomitantly, a redshift of the intra-bilayer plasmon is also observed. Representative examples of the fits are shown in Figure 3-15 (c) and (d).

Results from the two experiments together describe a scenario where inter-bilayer Josephson coupling is either enhanced or induced at the expense of intra-bilayer tunnelling, while the total number of Cooper pairs is conserved. This redistribution of coherent coupling is observed only in $\lesssim 20\%$ of the sample throughout the pseudogap phase. Intrinsic inhomogeneity existing already in equilibrium in this region of the phase diagram of high-T_C cuprates (Vershinin, Misra et al. 2004) may also play a role explaining the observations here.

Unlike the single-layer cuprates in which light-induced superconductivity is compatible with the vibrationally driven melting of the competing stripe phase, as discussed in Section 3.1, the case of YBCO is more complicated. A charge density wave phase found in the underdoped region of the phase diagram of bilayer cuprates (Wu, Mayaffre et al. 2011, Ghiringhelli, Le Tacon et al. 2012) offers a possibility that the phonon excitation could be removing the CDW phase and allowing superconductivity to re-establish at higher temperatures than in equilibrium.

Similar to the case of single-layer cuprates, an X-ray diffraction study by (Först, Frano et al. 2014) sought to quantify the extent to which the light induced changes of the CDW order

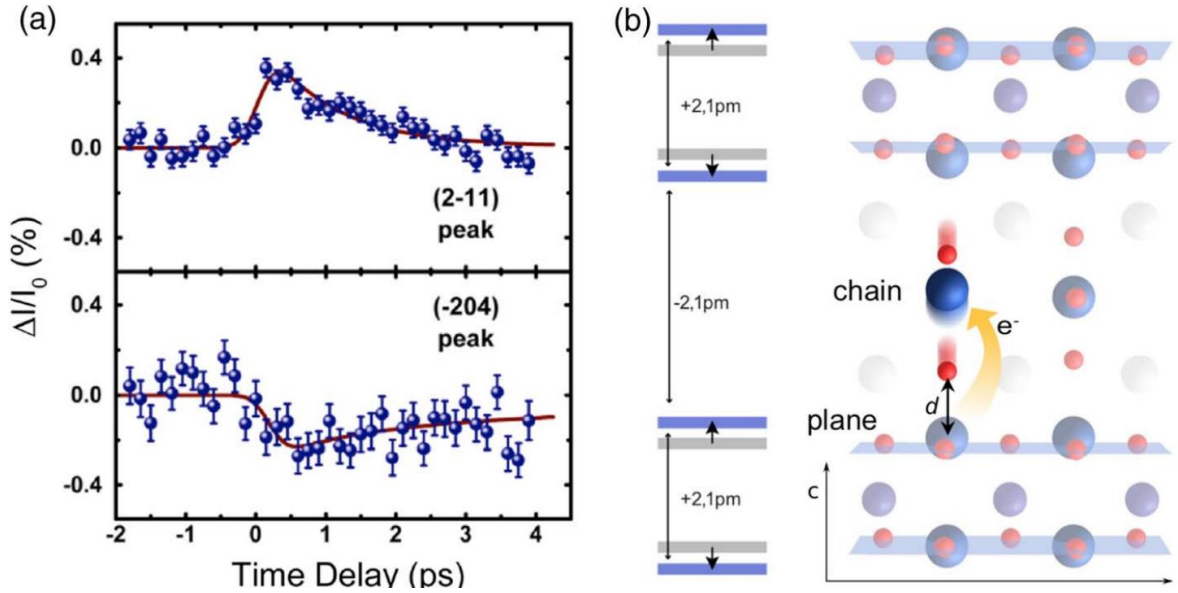

Figure 3-16: Relative changes in diffracted intensity of the (–2 –1 1) and the (–2 0 4) Bragg peaks measured in $YBa_2Cu_3O_{6.5}$ after MIR excitation at 100 K. Results of simultaneous fits to all data are shown as red lines. (b) Sketch of the reconstructed transient crystal structure at the peak signal. The atomic displacements from the equilibrium structure involve a decrease in inter-bilayer distance, accompanied by an increase in intra-bilayer distance. Reprinted with permission from (Först, Mankowsky et al. 2015). Copyright 2022 American Chemical Society.

are correlated with the emergent transient superconductivity. The experiment found that, under the same MIR excitation conditions as in (Hu, Kaiser et al. 2014, Kaiser, Hunt et al. 2014), at least 50% of the in-plane CDW order is melted. While this result is suggestive of the competing nature of the interaction between charge ordering and superconductivity in YBCO up to the CDW transition temperature ($\sim$150 K), enhanced coherence of inter-bilayer transport up to 300 K and above at the x = 6.45 doping where no CDW exists in equilibrium indicates that additional mechanism is at work behind the observation of light-induced superconductivity in YBCO.

One such option points out that, atomic positions in the displaced crystal structure created by the photoexcitation (Först, Mankowsky et al. 2015, Mankowsky, Först et al. 2016) might favour high-T_C superconductivity (Pavarini, Dasgupta et al. 2001, Slezak, Lee et al. 2008, Weber, Haule et al. 2010). The principle behind lattice displacement involves nonlinear phononics, where strong, resonant driving of an IR-active phonon mode allows coupling to other modes and creates a shift in the potential energy minimum, resulting in a unidirectional force on certain atoms and motion of them lasting several picoseconds. The experiment by (Mankowsky, Subedi et al. 2014) focuses on this question through the use of femtosecond hard X-ray diffraction, again under the same MIR excitation conditions.

The data demonstrating the lattice dynamics occurring in the transient superconducting state is summarised in Figure 3-16 (a). At 100 K, a prompt change in intensity of two representative diffraction peaks is observed corresponding to the rearrangement of the atoms in the unit cell. The decay dynamics follows a similar time scale as light-induced superconductivity (Hu, Kaiser et al. 2014, Kaiser, Hunt et al. 2014), suggestive of a close link between the two.

Figure 3-16 (b) illustrates the reconstructed transient structure. The in-plane O-Cu-O bond buckling is found to increase, and the distance from apical oxygen to planar copper decrease. Moreover, the intra-bilayer distance increases while CuO_2 planes within the bilayer units move closer to each other, leading to enhanced inter-bilayer coupling. Intuitively, this result is consistent with the THz measurements by (Hu, Kaiser et al. 2014).

Density functional theory calculations based on the transient crystal structure also predicts a charge transfer from the CuO_2 planes to the Cu-O chains, resulting in an effective increase of hole doping of the planes. This kind of self-doping effect has been shown to

accompany the temperature-driven superconducting transition at equilibrium in YBCO and could play a big role in explaining the formation of the superconducting phase (Magnuson, Schmitt et al. 2014).

3.2.2 Parametrically amplified phase-incoherent superconductivity in $YBa_2Cu_3O_{6+\delta}$

More recently, a study by (von Hoegen, Fechner et al. 2019) has made new progress in uncovering the underlying mechanism for light-induced superconductivity in YBCO. In this experiment, time- and scattering-angle-resolved second harmonic generation (SHG) was measured under the same MIR excitation conditions as in the studies on YBCO discussed in

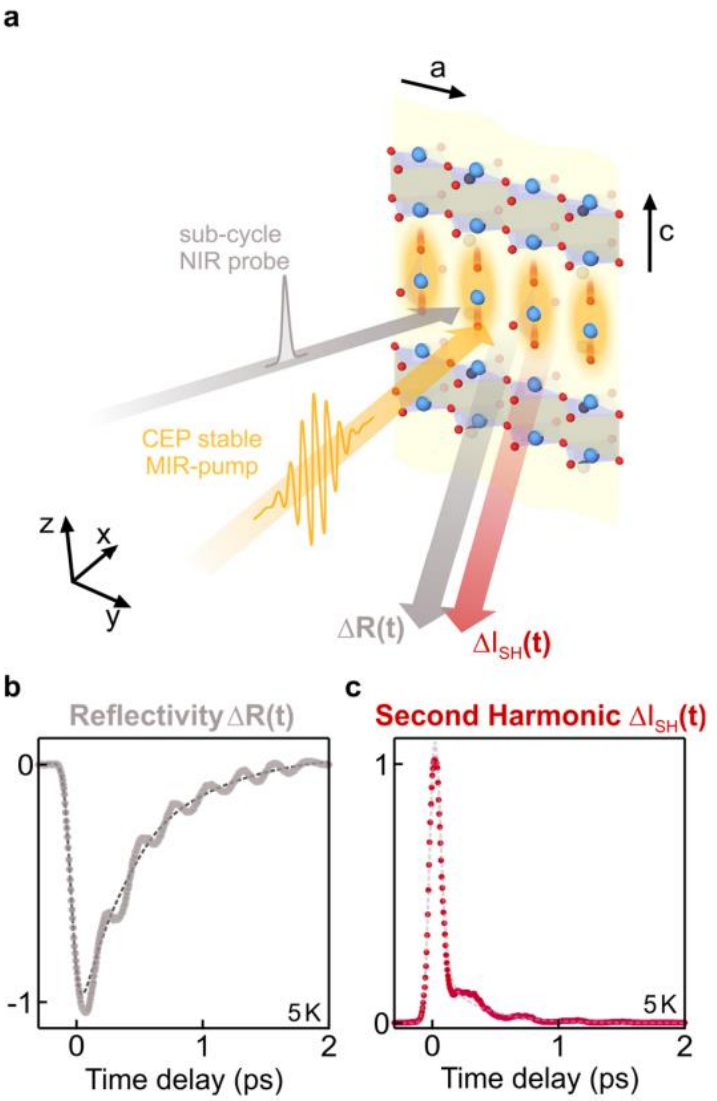

Figure 3-17: (a) Schematic of the probe geometry. The 800-nm near-IR probe (grey) and mid-IR pump (yellow) pulses were polarized along the $YBa_2Cu_3O_{6.48}$ crystals c-axis and perpendicular to the CuO_2-planes. The resonantly excited apical oxygen vibrations are shaded in yellow. Light at the fundamental (grey arrow) and second harmonic (red arrow) frequency is reflected from the sample. (b) Time-resolved polarization rotation of the linear reflectivity at 800 nm wavelength, showing coherent modulations due to fully symmetric Raman phonon modes. (c) Time resolved second harmonic intensity at 400 nm wavelength (red circles) and a numerical fit to the non-oscillatory component of the signal (dashed line). The data in (b) and (c) are shown for 5 K base temperature. Figure taken from (von Hoegen, Fechner et al. 2019).

Section 3.2.1. Here, 800-nm wavelength NIR pulses polarized along the c-axis of $YBa_2Cu_3O_{6.48}$ and $YBa_2Cu_3O_{6.65}$ serve as the probe [see Figure 3-17 (a)], and the time-dependent linear reflectivity $\Delta R(t)$ and time-dependent 400-nm second harmonic intensity $\Delta I_{SH}(t)$ were recorded [see Figure 3-17 (b) and (c)]. Both signals display a prompt change after the pump and the probe overlap in time, before decaying smoothly with super-imposed coherent oscillations.

This measurement is based on a mechanism different from the common SHG technique used in nonlinear optics. Here, the process behind the generation of the second harmonic signal, known as Stimulated Hyperraman Scattering (SHS), is four-wave mixing, mediated by a third-order susceptibility $\chi^3(\omega_{IR}, \omega_{IR}, \omega_{THz})$, where ω_{IR} denotes the frequency of the probe pulse and ω_{THz} the frequency of the excited modes. Hence, the modulated signal is centred at the optical frequency $2\omega_{IR}$. More intuitively, this can be understood to behave as a time-dependent effective second-order susceptibility $\chi^2_{eff}(\omega_{IR}, \omega_{IR}, t)$, where t is time, resulting from the inversion symmetry breaking by the oscillating mode in a centrosymmetric medium.

While the reflectivity change corresponds to the nonlinear excitation of Raman-active phonon modes and is well understood (Först, Manzoni et al. 2011, Mankowsky, Först et al. 2015), the SHG response is more interesting. Shown in Figure 3-18 are representative data taken at a range of pump electric fields from 300 kV/cm to 7 MV/cm on $YBa_2Cu_3O_{6.48}$. After extracting the oscillatory part of the time-resolved second harmonic intensity, the time traces and the corresponding Fourier transforms show a number of frequency components. In Figure 3-18 (a) and (b), the frequencies of the two resonantly driven modes at 17 THz and 20 THz are dominant (shaded in yellow). The higher field data in Figure 3-18 (c)(d) and (e)(f) reflect a nonlinear response where nonlinearly coupled modes are also excited by the directly driven ones. The most striking one is the 2.5 THz oscillation (shaded in red), present at 500 kV/cm but more pronounced at 7 MV/cm. The amplitude of this mode increases nearly 100-fold between the fields used in (c)(d) and (e)(f), alluding to an unusual regime of amplification. Similar results are also seen in $YBa_2Cu_3O_{6.65}$, in which the low-frequency amplified mode oscillates at 2.8 THz instead of 2.5 THz.

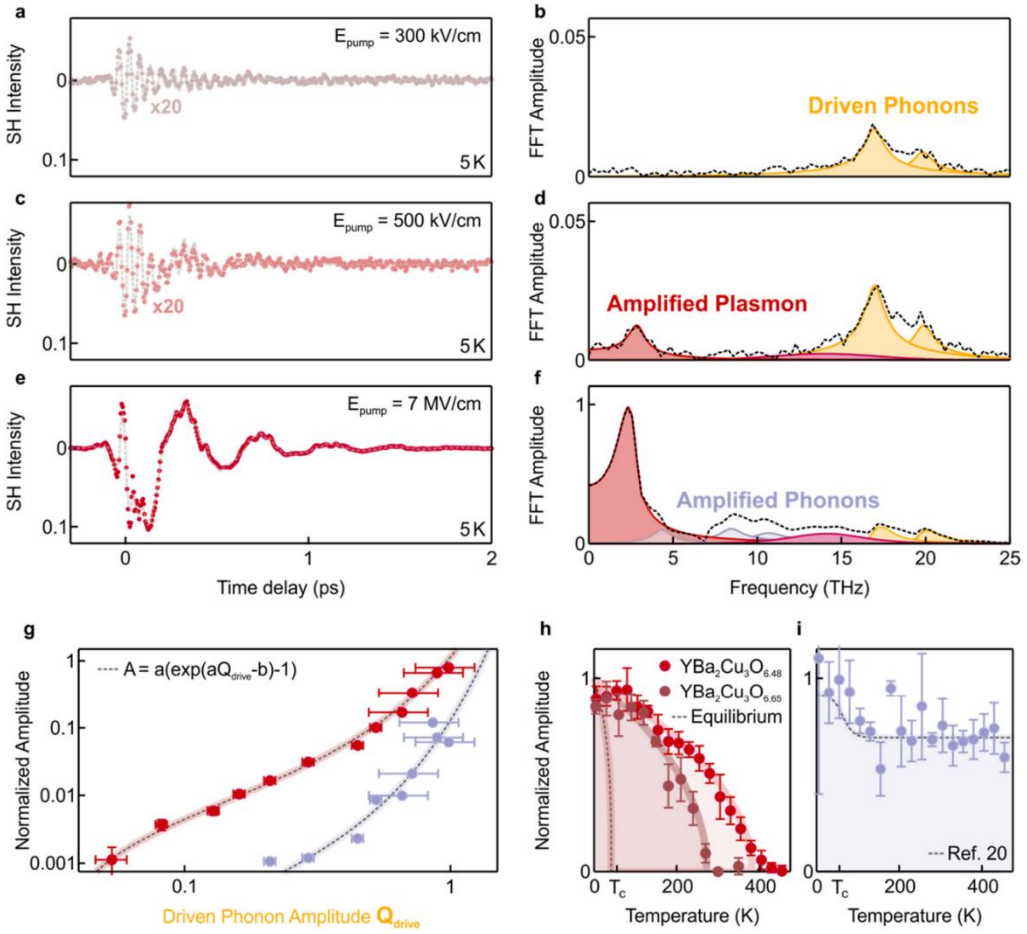

Figure 3-18: (a) and (b) Coherent SHS signal at the lowest excitation field (E = 0.3 MV/cm) and the corresponding Fourier amplitude spectrum at T = 5 K, well below the critical temperature T_C = 48 K. The high frequency oscillations at 17 and 19.5 THz (yellow peaks) are coherent symmetry breaking apical oxygen vibrations, resonantly driven by the excitation pulse. (c) and (d) Coherent SHS response at higher excitations fields (E = 0.5 MV/cm) at the same temperature. The peaks at ν_1 = 2.5 THz and ν_2 = 14 THz (red and magenta) are ascribed to coherent oscillations of Josephson Plasma modes. (e) and (f) The coherent SHS response at significantly stronger excitations (E = 7 MV/cm) show the same coherences of panel (c) and (b), with additional modes drawn as grey peaks. These additional peaks are dominated by those at 8.6 and 10.5 THz and label additional phonons nonlinearly coupled to the resonantly driven lattice modes. (g) Measured amplitude of the amplified low frequency Josephson Plasmon J_P and the amplified phonon amplitude $Q_{amplified}$ plotted as a function of the driven apical oxygen vibration amplitude Q_{drive}. The dashed line is an exponential fit $A(Q) = a\left(e^{\alpha Q_{drive}-\beta} - 1\right)$ to the data. Error bars represent the standard deviation σ of the amplitudes extracted by numerical fits. (h) Full temperature dependence of the Josephson plasmon peaks in panel (d) (shaded area) for $YBa_2Cu_3O_{6.48}$ (red) and $YBa_2Cu_3O_{6.65}$ (dark red). The lines are fits to the data with a mean-field approach. The dashed line is the temperature dependence of the equilibrium low-frequency Josephson plasma resonance in $YBa_2Cu_3O_{6.5}$, which disappears at T_C. (i) Temperature dependence of the amplitude of the nonlinearly coupled infrared active phonons at 8.5 and 10 THz. Their temperature dependence from equilibrium infrared measurements in $YBa_2Cu_3O_{6.5}$ is shown as a dashed line. Error bars represent the standard deviation σ of the amplitudes obtained by repeating the experiment under equivalent conditions. Figure taken from (von Hoegen, Fechner et al. 2019).

By fitting the oscillations with a sum of different frequencies, the amplitudes for the 2.5 THz mode $J_1 \propto \Delta I_{SH}(t)_{\omega=2.5\,THz}$ and 8.6 THz mode $Q_{amplified} \propto \Delta I_{SH}(t)_{\omega=8.6\,THz}$ can be extracted. Then, the growth of the amplified modes can be quantified as a fraction of the drive $Q_{drive} \propto \Delta I_{SH}(t)_{\omega=17\,THz}$, as shown in Figure 3-18 (g). A threshold can be identified above which each nonlinearly coupled mode grows exponentially and is amplified by at least three orders of magnitude.

Figure 3-18 (h) and (i) show the temperature dependence of $J_1(Q_{drive}, T)$ for the two measured dopings as well as $Q_{amplified}(Q_{drive})$. The low-frequency mode, at 2.5 THz in $YBa_2Cu_3O_{6.48}$ and 2.8 THz in $YBa_2Cu_3O_{6.65}$, is found to follow the temperature dependence of neither of the equilibrium modes, such as the 1 THz JPR as measured by THz reflectivity in equilibrium, which disappears at T_C [dashed curve in Figure 3-18 (h)], nor the phonon resonances, which remain large above T_C [dashed curve in Figure 3-18 (i)]. By contrast, $J_1(T)$ decays only at a characteristic temperature scale T', which can be extracted from an empirical fit function proportional to $\sqrt{1 - T/T'}$, yielding $T' \approx$ 380 K and 280 K for $YBa_2Cu_3O_{6.48}$ and $YBa_2Cu_3O_{6.65}$, respectively. These values are in good agreement with the corresponding pseudogap temperature T^* in each compound. The distinction between the temperature dependence of J_1 and of the amplified phonon should be underscored, the latter of which is consistent with the corresponding equilibrium phonon modes and remains constant for all temperatures above T_C.

In addition, the symmetry of the 2.5 THz mode is found to be distinct from that of phonons, indicative of a lower symmetry for which at least two mirrors of the equilibrium YBCO structure are lost (*Pm* or lower, whereas the equilibrium structure is *Pmmm* and the driven and amplified phonons are *Pmm2*). Furthermore, the scattering angle dependence of the 2.5 THz mode displays a spatial distribution deviating from that of the driven and amplified phonons.

Given all the evidence strongly suggesting the nature of low-frequency oscillation to be unlike the phonons, a theoretical explanation is proposed to describe the observation and origin of the mode claimed to be an amplified Josephson plasmon. In YBCO, there are two Josephson Plasmon Polaritons (JPP) in the superconducting state, which are dispersive c-axis modes consisting of interlayer tunnelling currents and propagating along CuO_2 planes. At zero momentum, the two modes are dominated by currents flowing between the bilayers and

within the bilayers, corresponding to the lower-frequency and higher-frequency modes, respectively. At non-zero momentum, however, in-plane superflow is also involved in addition to the c-axis currents, with a dispersion relation determined by the inductive response of the planes. In Figure 3-19 (a) and (b), such a computed equilibrium dispersion curve is shown.

Then, relations between the supercurrents and electromagnetic fields can be obtained by considering the kinetic energies of the interlayer tunnelling and in-plane superflow. Intuitively, the c-axis currents J_1 and J_2 are driven by the lattice excitation because the changes in the in-plane kinetic energy also perturb the in-plane gradients of the order parameter phase $\nabla_{x,y}\theta_n(x,y,t)$, where $\theta_n(x,y,t)$ is the order parameter in layer n. This

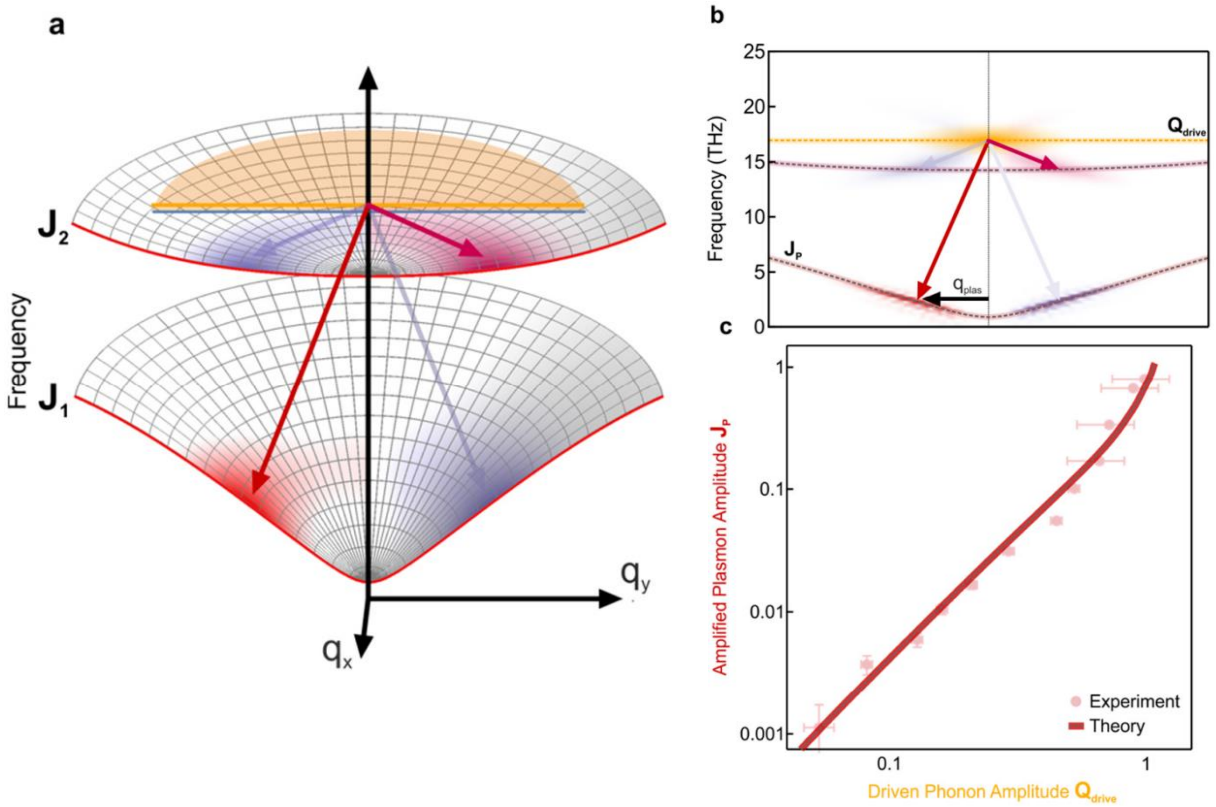

Figure 3-19: (a) Dispersion of the inter (J_1) and intra-bilayer (J_2) Josephson plasma modes along the in-plane momenta q_x and q_y in $YBa_2Cu_3O_{6.5}$. The red lines are a cut through the $q_x = 0$ plane. The apical oxygen phonon mode at 17 THz (yellow) does not disperse along either direction. The three-wave scattering process is sketched as red and blue arrows and results from a numerical simulation in response to the resonant drive of the apical oxygen phonon at $q = 0$ are shaded in the same colors. The response vanishes along q_x, parallel to the light propagation direction. (b) Detailed insight into the simulation results along q_y for $q_x = 0$. The driven phonon with zero momentum excites a pair of Josephson Plasmon Polaritons, J_1 and J_2, with opposite wavevectors q_y and frequencies that add up to the phonon frequency. The two processes for mirrored momentum transfer are shown as red and blue arrows, respectively. (c) Simulated excitation strength dependence (dashed line) of the low frequency 2.5 THz oscillations, together with the experimental data (dots) from Figure 3-18 (g). Figure taken from (von Hoegen, Fechner et al. 2019).

phase gradient, through the second Josephson equation $J_{n,n+1} = J_C\, sin(\Delta\theta_{n,n+1})$, makes the c-axis tunnelling dependent on the in-plane spatial coordinate. Hence, the equations of motion for the JPPs can be written as

$$\ddot{J_1} + 2\gamma_{J_1}\dot{J_1} + \omega_{J_1}^2(q_{x1}, q_{y1})J_1 = -aq^2 Q_{drive}(t)J_2$$

$$\ddot{J_2} + 2\gamma_{J_2}\dot{J_2} + \omega_{J_2}^2(q_{x2}, q_{y2})J_2 = -aq^2 Q_{drive}(t)J_1$$

where $\omega_{J_i}^2(q_{xi}, q_{yi})$ describe the in-plane equilibrium dispersion. These equations predict three-wave mixing between the apical oxygen phonons Q_{drive} and the upper and lower JPPs, leading to the excitation of damped harmonic oscillations for J_1 and J_2 at finite momenta along the two-dimensional dispersion curves in Figure 3-19 (a). Furthermore, pairs of JPPs with frequencies satisfying $\omega_1 + \omega_2 = \omega_{drive}$ and opposite in-plane momenta ($q_{x1} = -q_{x2}$ and $q_{y1} = -q_{y2}$) are predicted to be excited by the phonon. A numerical solution is displayed in the colour-coded dispersion of Figure 3-19 (a) and (b). Based on this, the calculated momentum at which the excitations of J_1 and J_2 are expected is found to be in good agreement with experimental data.

Moreover, the theoretically predicted energy and momentum matching is consistent with the experimentally determined frequency resonances ($\omega_{drive}\sim$ 17 THz, $\omega_1\sim$ 2.5 THz, and $\omega_2\sim$ 14.5 THz). The exponential amplification of the JPP [Figure 3-19 (c)] also resembles the experimental results in Figure 3-18 (g). Finally, the predicted symmetry of the finite-momentum modes also agrees with the measured data.

This theory goes on to explain the transient reflectivity edges reported in the previous THz measurements discussed in Section 3.2.1. The three-wave mixing excitation results in two counter-propagating JPPs with opposite momenta, which interfere to produce a standing wave pattern of the order parameter phase along the sample surface y direction. Then, the theory shows that this leads to a zero-momentum modulation of the superfluid density, which amplifies parametrically another plasma wave as demonstrated by a separate study [(Rajasekaran, Casandruc et al. 2016), see Chapter 4 for detail]. From this, transient THz reflectivity can be computed both below and above T_C. In Figure 3-20, a comparison between the calculation and the experimental data from (Kaiser, Hunt et al. 2014) is shown. Below T_C [see Figure 3-20 (a) and (b)], an additional plasma edge is predicted at frequency ~2 THz, above the equilibrium JPR at ~1 THz, in agreement with experimental measurements [see

Figure 3-20 (e) and (f)]. Above T_C [see Figure 3-20 (c) and (d)], the featureless reflectivity is reproduced by assuming the same interlayer coupling strength as in the superconducting state but with a sizeable increase in de-phasing, making the Josephson plasmon overdamped. After photoexcitation, the plasma edge is predicted to reappear at ~2 THz, again blue shifted with respect to the below-T_C equilibrium JPR. Compared to experimental data [see Figure 3-20 (g) and (h)], good agreement is found.

In addition to various cuprates, such optical techniques have shown to produce similar response from organic materials, such as alkali-fulleride K_3C_{60}, that carry signatures of superconductivity even in the normal state above T_C. Again, selective excitation of certain lattice vibration modes seems to effectively generate a long-lived state lasting into the nanosecond regime. However, so far there is no wide consensus on the underlying mechanism behind light-induced superconductivity in either cuprates or organic compounds (Cavalleri 2018).

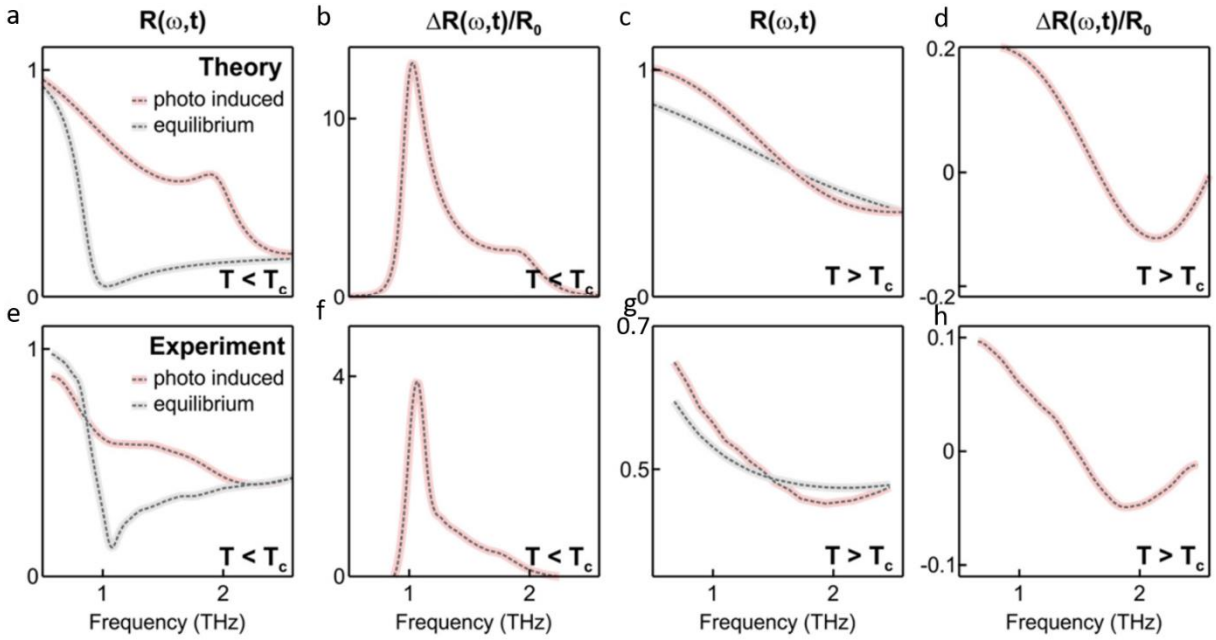

Figure 3-20: (a) and (b) Calculated photo-induced (red) and equilibrium (grey) THz reflectivity below T_C and the normalized reflectivity changes $\Delta R(\omega, t) / R_0$, respectively. The finite-momentum Josephson Plasmon Polariton induces a second plasma edge at a frequency close to 2 THz and overall enhancement of the reflectivity above the equilibrium plasma edge. (c) and (d) Calculated photo-induced (red) and equilibrium (grey) THz reflectivity above T_C and the normalized reflectivity changes $\Delta R(\omega, t) / R_0$, respectively. Excitation of the apical oxygen vibration leads to the appearance of a plasma edge at a frequency close to 2 THz, which is clearly visible in the normalized reflectivity changes $\Delta R(\omega, t) / R_0$. (e), (f), (g), and (h) show the same features, observed experimentally in time-resolved THz reflectivity measurements after resonant excitation of apical oxygen oscillations (Kaiser, Hunt et al. 2014). Figure taken from (von Hoegen, Fechner et al. 2019).

In Chapter 5, the focus will be returned to the original high-T_C superconductor LBCO, building on the studies introduced in Section 3.1.2 on transient revival of superconducting coherence in the stripe phase with non-resonant near-IR excitation. Then an experiment is presented which utilises a strong magnetic field as a tuning knob to investigate the connection between the stripe order and light-induced superconductivity. But before that, a closer look at Josephson physics is in order in Chapter 4.

4. Nonlinear Josephson phase dynamics

4.1 Modelling a Josephson junction

In the year 1962, the British physicist Brian David Josephson predicted the mathematical relationships for a form of supercurrent, one that flows continuously without any voltage applied between two superconducting electrodes separated by a thin insulating barrier, known as a Josephson junction. Named after him, the DC Josephson effect describes the supercurrent I as a function of the difference in phase of the macroscopic wavefunction of the superconducting order parameter in the two electrodes as

$$I = I_c \, sin(\Delta\varphi)$$

where the critical current I_c is the maximum supercurrent the junction can support. In addition, he predicted that if a voltage difference *V* were maintained across the junction, the phase difference $\Delta\varphi$ would evolve over time according to the relation, known as the AC Josephson effect, as

$$\frac{d\Delta\varphi}{dt} = \frac{2eV}{\hbar}$$

where *e* is the electron charge and $\hbar$ the Planck constant. The supercurrent would essentially oscillate sinusoidally with amplitude I_c and frequency $\nu = 2eV/h$. Here, the quantum energy $h\nu = 2eV$ can be understood as the energy carried by a Cooper pair tunneling through the junction (Josephson 1962, Josephson 1964).

Given the two relations above, one can calculate the Josephson coupling energy stored in the junction by integrating the electrical work done by a current source in changing the phase as

$$\int IV\,dt = \int I\frac{\hbar}{2e}d(\Delta\varphi) = -E_J\cos(\Delta\varphi) + const.$$

where $E_J = \hbar I_c\,/\,2e$ is a characteristic parameter of the Josephson junction. The coupling energy has a minimum when the two phases are equal, so that $\Delta\varphi = 0$. The critical current I_c depends on the thickness of the barrier between the electrodes as well as its material, and is a measure of the strength of the coupling.

Another useful quantity can be derived from the two Josephson equations, by first differentiating the Josephson current relation with respect to time and then substituting the Josephson voltage relation, as

$$\frac{\partial I}{\partial t} = I_c\cos(\Delta\varphi)\frac{\partial\varphi}{\partial t} = I_c\cos(\Delta\varphi)\frac{2eV}{\hbar}$$

Rearranging to have

$$V = \frac{\hbar}{2eI_c\cos(\Delta\varphi)}\frac{\partial I}{\partial t} = L(\varphi)\frac{\partial I}{\partial t}$$

where $L(\varphi)$ acts as a kinetic inductance as a function of the Josephson phase difference as

$$L(\varphi) = \frac{\hbar}{2eI_c\cos(\Delta\varphi)} = \frac{L_J}{\cos(\Delta\varphi)}$$

and $L_J = L(0) = \frac{\hbar}{2eI_c}$ is a characteristic parameter of the Josephson junction, named the Josephson inductance. It is related to the Josephson energy by $E_J = L_J I_c^2$.

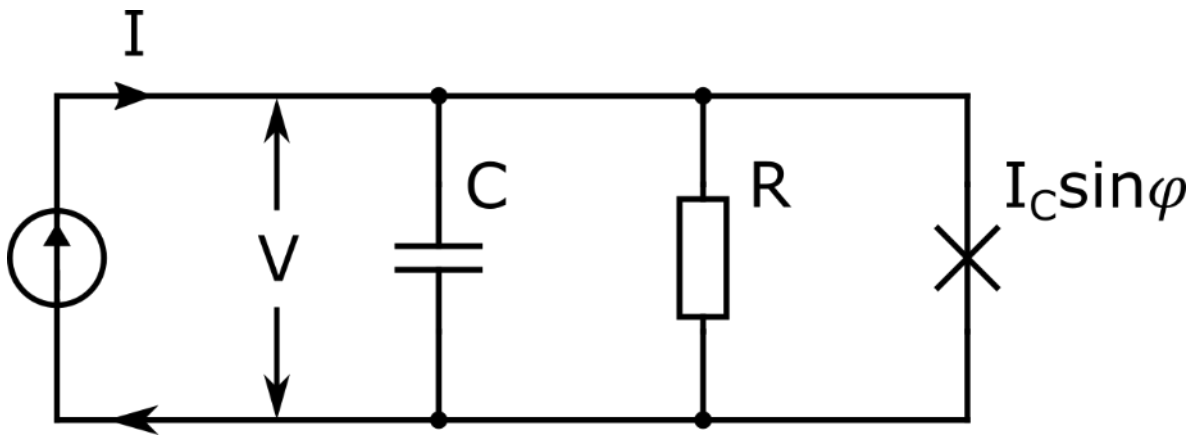

Figure 4-1: The Resistively and Capacitively Shunted Junction (RCSJ) equivalent circuit to a Josephson junction.

4.2 The equivalent circuit model for a short junction

The first Josephson equation describes the response of the junction in the dc regime; for a finite voltage situation involving the ac Josephson effect, however, the dissipation of resistive flow is not captured. Hence, an equivalent circuit known as the Resistively and Capacitively Shunted Junction (RCSJ) model is commonly used to fully characterise the behaviour of a short junction with negligible spatial dimensions in the lateral directions. Here, the junction is modelled as a nonlinear inductive element, as derived above, shunted by a resistance *R* and a capacitance *C*, which reflect the dissipative quasiparticle transport and geometric shunting between the two electrodes of the junction, respectively (see Figure 4-1).

Within the RCSJ model, an external bias current is applied to the parallel circuit, and a time dependent Josephson phase $\Delta\varphi$ develops (hereafter simplified as φ). The temporal evolution can be described by the equation of motion relating the bias current I_{ext} to the individual currents flowing through each component as

$$I_{ext} = C\frac{dV}{dt} + \frac{V}{R} + I_c \sin\varphi$$

Making use of the Josephson voltage relation, because the voltage drop across all three components is identical, the equation of motion can be rewritten in terms of the Josephson phase φ, eliminating the voltage, as

$$I_{ext} = \frac{\hbar C}{2e}\frac{d^2\varphi}{dt^2} + \frac{\hbar}{2eR}\frac{d\varphi}{dt} + I_c \sin\varphi$$

Cleaning up the pre-factors, one arrives at a form intuitively interpretable as a driven oscillator under a viscous force

$$I_{ext} = M\frac{d^2\varphi}{dt^2} + D\frac{d\varphi}{dt} + I_c \sin\varphi$$

where $M = \frac{\hbar C}{2e}$ and $D = \frac{\hbar}{2eR}$ taking up the roles of inertia and damping coefficient. From this, it is possible to calculate a potential energy landscape in which the driven oscillator finds itself in

$$U(\varphi) = -\int (I_{ext} - I_c \sin\varphi)\, d\varphi = -I_{ext}\varphi - I_c \cos\varphi + const.$$

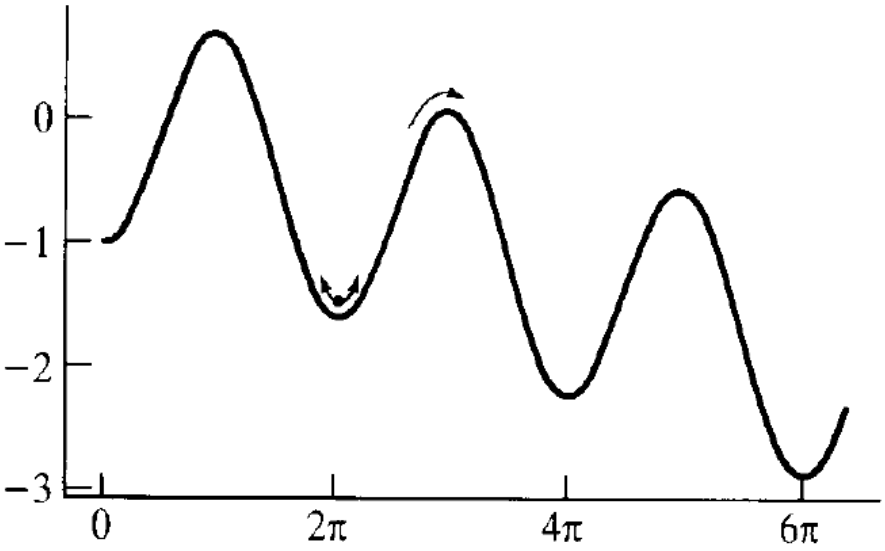

Figure 4-2: The "tilted washboard" potential. The phase can be visualised as a ball moving within the potential landscape. Figure taken from (Tinkham 2004).

As depicted in Figure 4-2, this is commonly known as the "tilted washboard" potential.

In fact, a mechanical analogue can provide useful insights into the dynamic response of such a system under an external driving force under different conditions. Consider a familiar simple pendulum with moment arm I_c, moment of inertia *M*, damping coefficient *D*, phase angle φ, and subject to an external torque I_{ext}. Such a pendulum is illustrated in Figure 4-3, with *M* provided by a flywheel and *D* by a paddle-wheel arrangement. If an equation of motion is to be derived from Newton's Law for this system, it would have the exact same form as the equation above for the circuit model.

Furthermore, it can be readily seen that clear analogies exist between the torques and the electrical currents, the angular velocity and the voltage (with a certain proportionality factor), the kinetic energy and the electrostatic energy stored in the capacitor, and the gravitational energy and the Josephson coupling energy.

It can be instructive to consider a few examples that illustrate the analogous behaviour in both systems. Firstly, if a small dc bias current $I_{ext} \ll I_c$ is applied, the Josephson element shorts the resistor and capacitor, and the voltage remains zero. In the mechanical system, this corresponds to a small constant torque causes the pendulum to deviate slightly from the equilibrium vertical position, and holds it at an angle. The angular velocity is zero because it is sitting still, agreeing with the zero voltage drop in the circuit model.

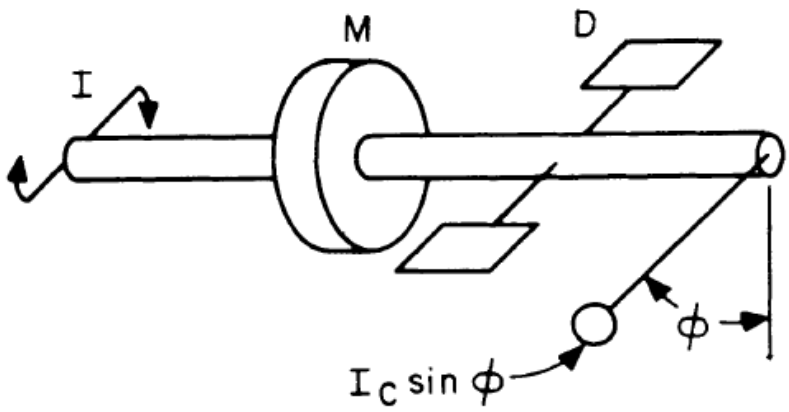

Figure 4-3: A mechanical analogue of the equivalent circuit. The system consists of a simple pendulum with moment arm I_c, moment of inertia M, damping coefficient D, phase angle φ, and subject to an external torque I_{ext}, with M provided by a flywheel and D by a paddle-wheel arrangement. Figure taken from (Schwartz 2013).

For all $I_{ext} \leq I_c$, the circuit remains in the zero-voltage state. Intuitively this makes sense, because I_c corresponds to the pendulum being held at the horizontal position where the torque by gravity is at maximum. As soon as I_{ext} exceeds I_c, the pendulum will be pushed beyond the vertically up position and fall down on the side, completing a full 2π rotation and keeping on rotating at a frequency dependent on the applied torque and damping. In the circuit model, the external driving current exceeds the maximum current the Josephson element can support, and the Josephson phase starts advancing with time, creating a time-dependent voltage drop (see Figure 4-4). This can also be understood by considering the washboard potential as plotted in Figure 4-2. Since the tilting of the cosine potential is directly

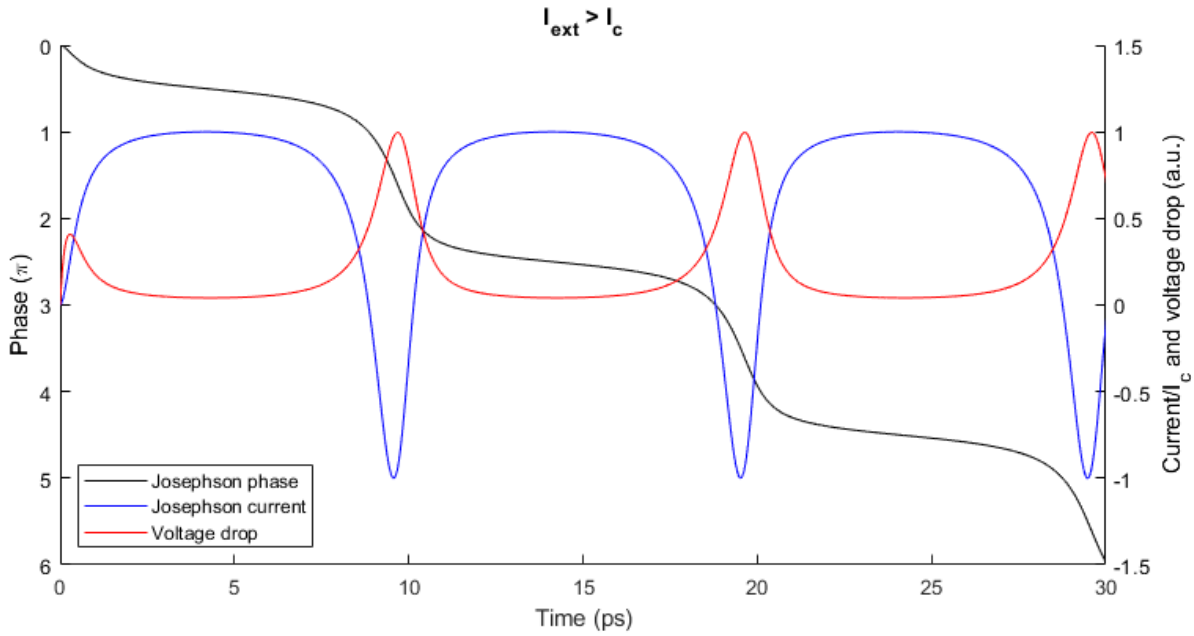

Figure 4-4: Phase, current, and voltage evolution over time for a driving current I_{ext} greater than the critical current I_C.

proportional to the bias current, at $I_{ext} = I_c$ the barrier between two adjacent minima becomes only horizontal inflection points in the otherwise continually downward slope, and no stable equilibrium point exists for all $I_{ext} \geq I_c$.

4.3 Dynamics of a long Josephson junction

In order to expand the discussion to the more general case of a long Josephson junction with extended spatial dimensions, without loss of generality, the coordinate system can be chosen to have the surface of the electrodes A and B lying in the *xy*-plane, a magnetic field H applied along the *y* direction, while the tunnelling current flows in the *z* direction (see Figure 4-5). If the electrodes are thick compared to λ, the London penetration depth of the material of which they are composed, and separated by an insulating barrier of thickness *d*, then the magnetic flux Φ enclosed by a contour as depicted in Figure 4-5, including two tunnelling paths separated by a distance Δx perpendicular to the field direction, can be found by using Faraday's Law,

$$\Phi = H(2\lambda + d)\Delta x$$

It is then possible to show that the magnetic field induces a spatial gradient in the Josephson phase as

$$\frac{\partial \varphi}{\partial x} = \frac{2\pi}{\Phi_0}(2\lambda + d)H \quad \text{and} \quad \frac{\partial \varphi}{\partial y} = 0$$

where $\Phi_0 = \frac{\hbar}{2e}$ is the magnetic flux quantum. Combining the Maxwell's equation in absence of a time-dependent electric field, $\frac{\partial H}{\partial x} = \frac{4\pi}{c}J$, and the Josephson current relation, $J = J_c \sin(\varphi)$, yields

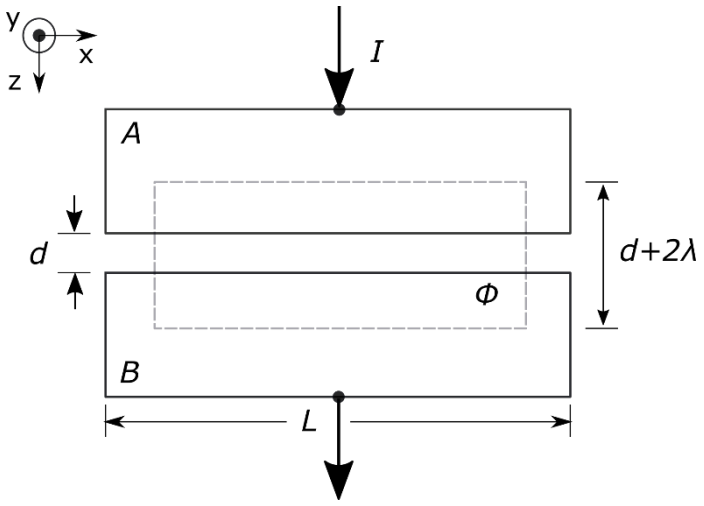

Figure 4-5: Schematic diagram of a long Josephson junction.

$$\frac{\partial H}{\partial x} = \frac{4\pi J_c}{c} sin(\varphi)$$

Differentiating the previous equation and substituting the one above into the right-hand side produces a second-order differential equation

$$\frac{\partial^2 \varphi}{\partial x^2} = \frac{1}{\lambda_J^2} sin(\varphi)$$

where the Josephson penetration depth is defined as

$$\lambda_J = \sqrt{\frac{c\Phi_0}{8\pi^2 J_c(2\lambda + d)}}$$

This plays the role of a penetration depth because for small φ, this equation reduces to the familiar form

$$\frac{\partial^2 \varphi}{\partial x^2} = \frac{1}{\lambda_J^2} \varphi$$

which has a solution $\varphi \sim e^{\pm x/\lambda_J}$ describing an exponential decay from the outside edge of the junction, similar to the Meissner effect found in bulk superconductors. The screening holds as long as the magnetic field is much smaller than $4\pi J_c \lambda_J / c$, analogous to the lower critical field H_{c1} of a type-II superconductor, above which the field will penetrate inside the junction in the form of Josephson vortices.

Further generalising the consideration to account for time-dependent electric and magnetic fields, it can be shown that integrating over the same contour the Maxwell's equation $\nabla \times E = -\frac{1}{c}\frac{\partial B}{\partial t}$ gives

$$\frac{\partial E_z}{\partial x} = \frac{2\lambda + d}{d} \frac{1}{c} \frac{\partial H_y}{\partial t}$$

where E_z is the electric field inside the junction barrier. Now consider the other Maxwell's equation relating the fields to the displacement current density,

$$\frac{\partial H_y}{\partial x} = \frac{4\pi}{c} J_z + \frac{\varepsilon}{c} \frac{\partial E}{\partial t}$$

where J_z is the Josephson current and ε the dielectric function of the barrier. Combining the time derivative and space derivative of the two equations above respectively yields

$$\left(\frac{\partial^2}{\partial x^2} - \frac{1}{c'^2}\frac{\partial^2}{\partial t^2}\right) V = \frac{4\pi}{c^2}(2\lambda + d)\frac{\partial J_z}{\partial t}$$

where $V = E_z d$ is the voltage drop across the barrier, and

$$c' = \frac{c}{\sqrt{\varepsilon(1 + 2\lambda \,/\, d)}}$$

is known as the Swihart velocity, which determines the maximum group velocity for a propagating plasma wave inside the junction.

It is convenient to further transform this differential equation into a form containing only the Josephson phase as the dependent variable, by making use of the Josephson current and voltage relations again followed by an integration with respect to time, resulting in

$$\left(\frac{\partial^2}{\partial x^2} - \frac{1}{c'^2}\frac{\partial^2}{\partial t^2}\right)\varphi = \frac{1}{\lambda_J^2} sin(\varphi)$$

This is commonly known as the sine-Gordon equation.

The sine-Gordon equation describes the full electrodynamics of a long Josephson junction. In this context, a junction is called *small* if its width and length are small compared to λ_J, *long* if the length $L \gg \lambda_J$ while the width $W \ll \lambda_J$, and large if both dimensions are large compared to λ_J.

An additional dissipation term proportional to $\partial\varphi \,/\, \partial t$ can be included to take into account quasiparticle tunnelling at finite temperature, as is done for the calculation done in the next chapter, but is omitted for the time being for simplicity. As a nonlinear partial differential equation, the sine-Gordon equation has no general analytic solutions discovered yet, but special cases can be analysed to provide useful insights and intuition.

In the small junction limit, the spatial variation can be neglected, and the equation reduces to

$$\frac{\partial^2 \varphi}{\partial t^2} + \omega_P^2 \, sin(\varphi) = 0$$

where $\omega_P^2 = c'^2 \,/\, \lambda_J^2$. This reproduces the equation of motion derived from the RCSJ circuit model with no damping, i.e. $R = 0$, and no bias current, $I_{ext} = 0$, and an equivalent definition

of $\omega_P^2 = 2eI_c / \hbar C$. In the limiting case of small amplitude variations for φ, the equation becomes a linear second order differential equation because $sin(\varphi) \approx \varphi$ for small φ. Hence,

$$\frac{\partial^2 \varphi}{\partial t^2} + \omega_P^2 \varphi = 0$$

and one solution is that of a familiar harmonic oscillator with the natural resonance frequency being exactly ω_p. Physically, this corresponds to the collective oscillation of Cooper pairs between the two electrodes at ω_p, which is also called the Josephson plasma frequency. This is known as a longitudinal plasma mode. Similarly, in the long junction case, a propagating wave solution exists to the linearized equation of the form $\varphi(x,t) = \varphi_0\, exp[i(kx - \omega t)]$, describing a transverse plasma wave with the dispersion relation $\omega^2 = \omega_p^2 + c'^2 k^2$.

Outside of the small amplitude limit, two additional types of analytic solutions to the sine-Gordon equation exist in the form of a single or multiple solitons. Through a change of coordinates to units of length and time in λ_J and $1/\omega_p$ respectively, it can be shown that a so-called kink or antikink mode has the form

$$\varphi(x,t) = 4\, tan^{-1}\left[exp\left(\pm\frac{x - x_0 - ut}{\sqrt{1-u^2}}\right)\right]$$

where the dimensionless velocity u can take values $0 < u < 1$ in units of c'. This describes a phase front at the value of π at a point $x = x_0 + ut$ propagating in space. The phase φ takes the values from 0 to 2π as $x - (x_0 + ut)$ goes from $-\infty$ to $+\infty$ for the upper sign in the expression above, i.e. the kink soliton, or vice versa for the lower sign, i.e. the antikink soliton [see Figure 4-6 (a)].

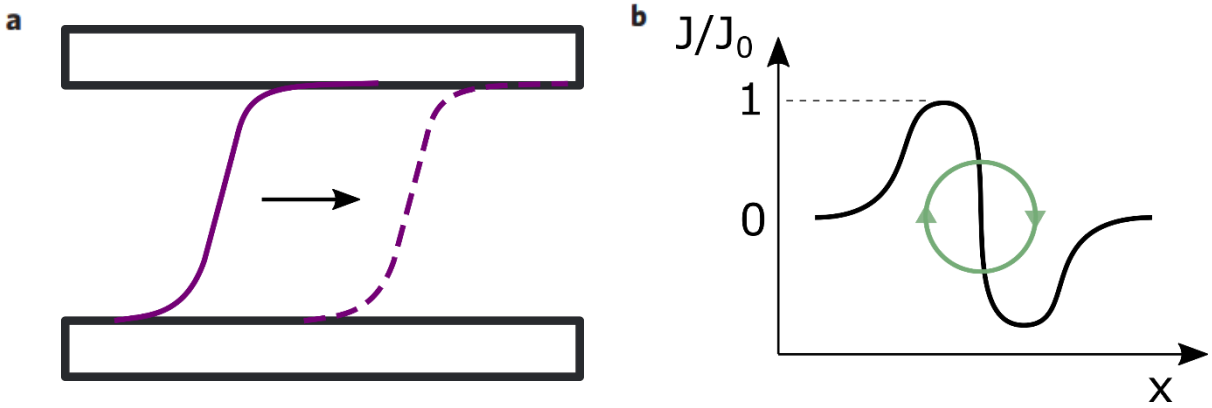

Figure 4-6: The Kink/anti-kink soliton. (a) The phase front corresponding to a 2π phase shift between the two electrodes of the junction propagates in space. (b) The normalised current flow (green curve) proportional to $sin(\varphi)$ surrounds a flux core. The kink/anti-kink soliton can also be seen as a propagating Josephson vortex.

Such a phase distribution in space gives rise to a positive Josephson current localised to a distance $\sim\lambda_J$ to the left of the point $x-(x_0+ut)$ and a negative current to the right of it. Essentially, a Josephson vortex (or anti-vortex) is formed, localised around a core that travels at velocity u, carrying one quantum of magnetic flux [see Figure 4-6 (b)]. Hence this is also known as a *fluxon* solution.

The second type of solitonic solution can be considered as a pair of kink-antikink coupled state, known as the breathers. The pair oscillate about a centre position, which can be either stationary or propagating in space, at a frequency $0<\omega_b<\omega_p$. It can be expressed as

$$\varphi(x,t)=4\,tan^{-1}\left[\frac{1}{\sqrt{\omega_b^2-1}}\sin\theta_I\,\mathrm{sech}\,\theta_R\right]$$

where

$$\theta_I=\frac{\omega_b[t-u(x_0-ut)]}{\sqrt{1-u^2}}\quad\text{and}\quad\theta_I=\frac{\sqrt{1-\omega_b}(x-x_0-ut)}{\sqrt{1-u^2}}$$

A large-amplitude breather flips the local phase between -2π and +2π, and can be understood as a vortex-antivortex pair, either stationary or in motion together, as illustrated in Figure 4-7.

In the next section, examples of past experimental evidence for nonlinear Josephson phase dynamics including soliton formation, parametric amplification, and third harmonic generation are presented, in the context of cuprate superconductors as natural stacks of coupled Josephson junctions under excitation by ultrafast laser pulses in the THz frequency.

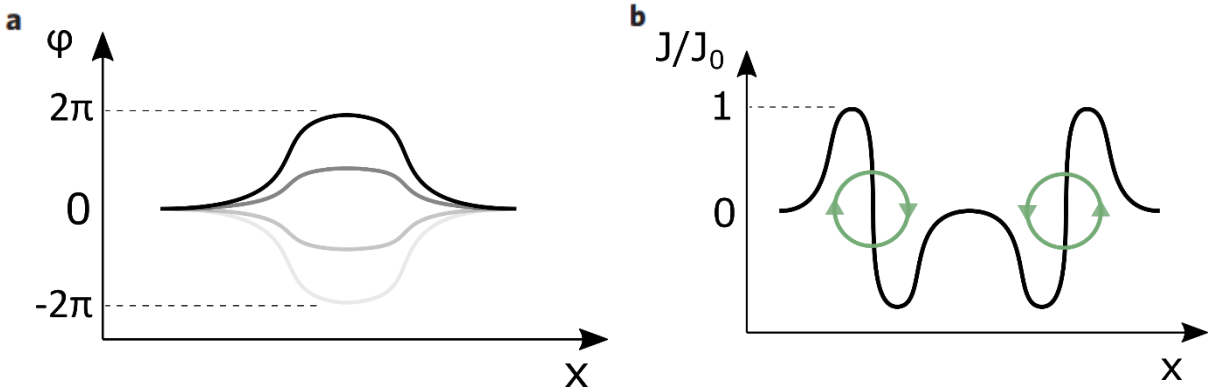

Figure 4-7: Breather soliton. (a) The phase front oscillating between 2π and -2π is shown for four different points in time. (b) A breather consists of a bound kink-anti kink pair, oscillating in space around a common centre of mass position. It can also be seen as a vortex-anti vortex pair.

In fact, the diffraction limited focus size of THz wavelengths, usually on the order of $\sim$1 mm for $<$ 1 THz, is orders of magnitude larger than the dimension of a single junction, on the order of $\sim$1 nm in LBCO for example. Hence it is reasonable to treat the system as a single junction homogeneously excited on the surface of the material. Calculations based on this approximation yield very good agreement with experimental results, as can be seen in the following sections.

4.4 Nonlinear Josephson phase dynamics in cuprates

Static control of Josephson plasma dynamics in cuprates can be achieved with DC bias currents (Kleiner, Aigner et al. 1994, Kleiner, Müller et al. 1994) or magnetic fields (Dordevic, Komiya et al. 2005, Schafgans, LaForge et al. 2010). However, this kind of excitation leads inevitably to dissipation and heating effects (Laplace and Cavalleri 2016). Strong field THz-frequency laser pulses, on the other hand, provide a way of controlling Josephson phase dynamics in a non-dissipative manner on an ultrafast time scale. In the following sections, three experiments will be discussed, providing convincing evidence for nonlinear dynamics predicted by equations governing the Josephson phase including the sine-Gordon equation as well as the original Josephson relations. One common theme among all of the experiments is the adoption of intense THz radiation for strongly perturbing the Josephson junction, due to the fact that the relatively low photon energy is less than the superconducting gap energy of the materials and hence creates few quasiparticle excitations from breaking up Cooper pairs.

4.4.1 Optical excitation of Josephson plasma solitons

In the first experiment, (Dienst, Casandruc et al. 2013) used intense narrowband radiation from a free electron laser (FEL) to generate Josephson plasma solitons (JPS) in $La_{1.84}Sr_{0.16}CuO_4$, with a superconducting transition temperature of 38 K, in the form of propagating breathers as described in Section 4.3.

Firstly, the sine-Gordon equation in one dimension was solved numerically, yielding the time- and space-dependent Josephson phase for excitations at frequencies close to the plasma resonance frequency, which sits at 2 THz at this doping, where the material is transparent. For frequency $\omega_{FEL} = 1.1\omega_{JPR}$ [see Figure 4-8 (a)], the nonlinear response is qualitatively similar to the linear regime. Hence, the nonlinear response for excitation frequencies far above the JPR is found to be small.

Closer to the resonance frequency with $\omega_{FEL} = 1.05\omega_{JPR}$ [see Figure 4-8 (b)], however, the results become sensitive to the incident field amplitude, predicting sharpened and increased phase oscillations developing as the wave propagates inside the material with

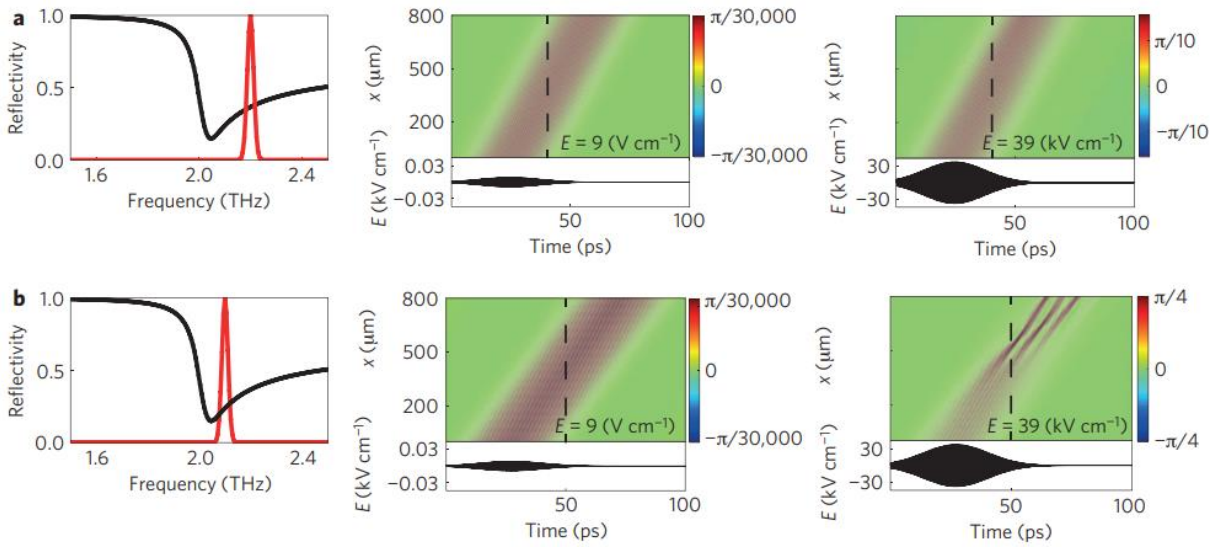

Figure 4-8: Calculated space- and time-dependent interlayer phase for $\varphi(x,t)$ for two pump wavelengths above resonance. (a) $\omega_{FEL} = 1.1\omega_{JPR}$. (b) $\omega_{FEL} = 1.05\omega_{JPR}$. In the plots on the left, the pump spectrum is shown in red superimposed on the calculated broadband linear reflectivity of the cuprate. The phase $\varphi(x,t)$ is shown in the colour plots on the left for peak field strengths of E = 9 V/cm (linear excitation). The strong-field response for E = 39 kV/cm is plotted on the right in the colour plots. Reprinted by permission from Springer Nature: (Dienst, Casandruc et al. 2013).

the pulse shape breaking up in a train, once a certain field strength threshold is crossed, in this case 39 kV/cm.

More interestingly, when the excitation pulse is tuned to immediately below the plasma frequency $\omega_{FEL} = 0.97\omega_{JPR}$ (see Figure 4-9), an evanescent wave as a result of screening in the linear regime evolves into a propagating mode when the electric field exceeds the same threshold as in the on-resonance case. A solitonic pulse of amplitude $\varphi^{peak}(x,t) \approx \pi\ /\ 4$ is observed. For even higher excitation fields, the pulse reaches higher peak amplitude of $\pi\ /\ 2$ and a train of multiple solitons is formed.

To verify the simulation results, THz time-domain pump-probe spectroscopy measurements were performed on LSCO at 6 K base temperature in the superconducting state. Here, single-cycle, broadband THz pulses polarised along the c-axis of the crystal measure the frequency-dependent complex coefficient of reflection as a function of the time delay between the probe pulse and intense, narrowband pump pulses from a THz FEL, also polarised along the c-axis. The pump frequency is tuned to cover the range from $1.1\omega_{JPR}$ to $\sim\omega_{JPR}$ with the peak electric field up to 10 kV/cm.

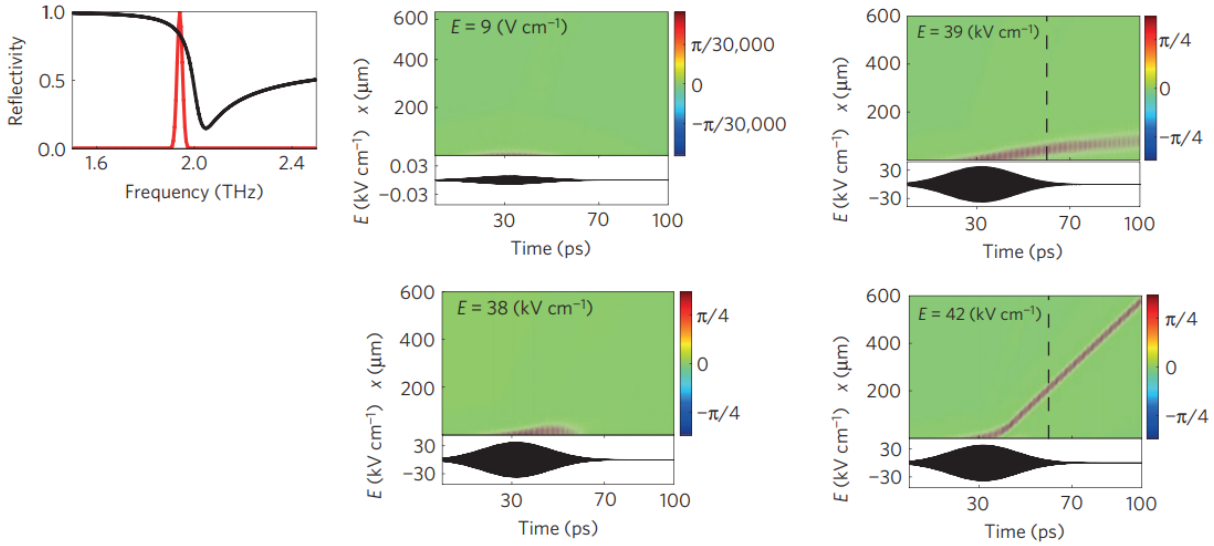

Figure 4-9: Calculated space- and time-dependent interlayer phase for $\varphi(x,t)$ for ω_{FEL} = 0.97ω_{JPR} and four pump intensities: 9 V/cm, 38 kV/cm, 39 kV/cm, 42 kV/cm. In the plot on the left, the pump spectrum is shown in red superimposed on the calculated broadband linear reflectivity of the cuprate. The linear response in the colour plot on the left is for a peak field strength of E = 9 V/cm. In the lower left graph a strong-field response is depicted for E = 38 kV/cm, where a modified evanescent wave is excited but no propagating mode ensues. Two strong-field responses are plotted on the right for E = 39 kV/cm and E = 42 kV/cm. Reprinted by permission from Springer Nature: (Dienst, Casandruc et al. 2013).

In Figure 4-10, the experimental results are compared to theory by plotting the time- and frequency dependent loss function, $Im\left(-\frac{1}{\tilde{\varepsilon}(\omega)}\right)$, which quantifies the amount of electromagnetic energy coupled into the Josephson plasma and shows a peak at the frequency of the Josephson plasma resonance. The experimental loss function is retrieved at each time delay by extracting the frequency-dependent dielectric function $\tilde{\varepsilon}^{exp}(\omega,\tau)$ from measured complex coefficient of reflection $\tilde{r}^{exp}(\omega,\tau)$ (see Appendix A). The penetration depth mismatch between the pump and probe pulses is accounted for by fitting a model of an excited layer on top of an unperturbed bulk superconductor, as discussed in previous chapters on other pump-probe experiments. The simulation results of $\varphi(x,\tau)$ are used to calculate $\tilde{r}^{calc}(\omega,\tau)$, which is then transformed into $\tilde{\varepsilon}^{calc}(\omega,\tau)$ and undergoes the same fitting procedure as for the experimental data.

There is good agreement between the theoretical and experimental loss functions for pump frequencies above the plasma resonance. A redshift of the loss function peak is predicted by the simulation during and immediately after the pump pulse, when the nonlinear propagating plasma wave traverses the volume being probed [see Figure 4-10 (a)]. No significant effect is observed after the pump wave has propagated beyond the probe

penetration depth. When the pump frequency is tuned closer to resonance with the JPR, the

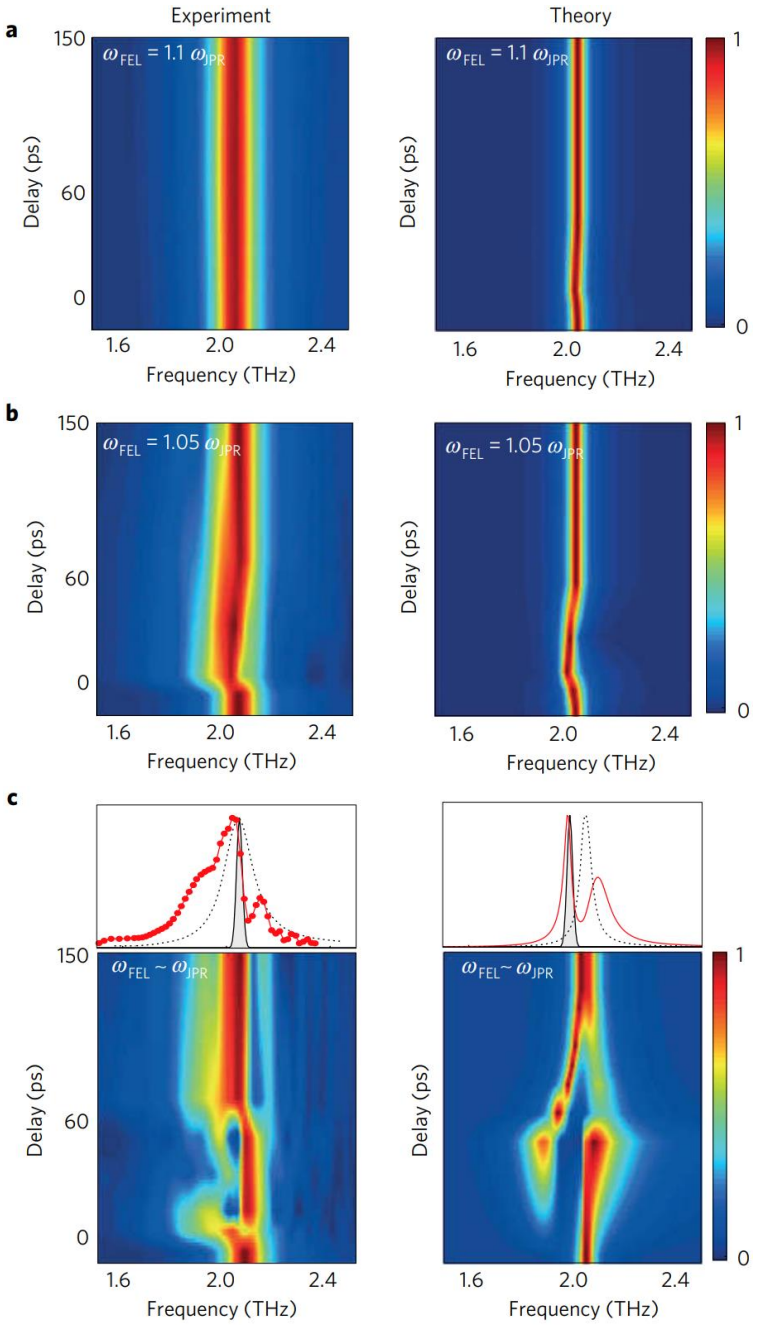

Figure 4-10: Perturbed loss functions. (a), (b) Frequency- and time-delay-dependent loss function for $\omega_{FEL} = 1.1\omega_{JPR}$ (a) and $\omega_{FEL} = 1.05\omega_{JPR}$ (b). Experimental loss functions extracted from the data are shown on the left. The theoretical loss functions, extracted from the calculated high-field phase profiles of Figure 4-8, are shown on the right. (c) $\omega_{FEL} \sim \omega_{JPR}$. The experimental loss function, extracted from the data, is shown on the left. The theoretical loss functions, extracted from the calculated high-field phase profiles of Figure 4-9, that is, for a field strength of 39 kV/cm, are shown on the right. At time delays larger than 50 ps both lineouts exhibit a splitting of the loss function. The lineouts shown in the uppermost part of the figure report the unperturbed loss function (black dotted line), the perturbed loss function at 80 ps time delay (red curve) and a Gaussian fit to the pump spectrum (black, shaded). The best fit is obtained for simulations at $\omega_{FEL} \sim 0.97\omega_{JPR}$. Reprinted by permission from Springer Nature: (Dienst, Casandruc et al. 2013).

effect becomes more pronounced [see Figure 4-10 (b)]. Due to more limited frequency resolution in the measurement than in the simulation, this redshift is clearly seen only in the $\omega_{FEL} = 1.05\omega_{JPR}$ case. The redshift results from an increase in the junction inductance when the phase is driven to large amplitudes, as $\omega_{JPR} = 2\pi / \sqrt{L(\varphi)C}$. This is taken as an experimental confirmation for the theoretically predicted self-induced transparency (Apostolov, Maizelis et al. 2010).

As shown in Figure 4-10 (c), comparing the experiment and the theory for the case of $\omega_{FEL} \sim \omega_{JPR}$, a soliton is formed during the pump pulse (<50 ps), where the loss function broadens to the red, and additionally a long-lived dip (>50 ps) in the loss function is observed, resulting in a split in the line shape of a cut at 80 ps [see upper panels of Figure 4-10 (c)]. This line split with a dip is attributed to interference of the optical response between regions in which the Josephson plasma soliton is present and regions where the phase remains close to zero.

It is noted that incoherent quasiparticle excitations cannot explain the observations here, because the sine-Gordon equation accounts for quasiparticle damping with the $2\gamma \frac{\partial \varphi(x,t)}{\partial t}$ term, where γ is the scattering time between the phase and quasiparticles. It only acts to broaden the linewidth.

Quantitative discrepancies between the simulation and the data exist, including the theory overestimating the velocity of the breather, the predicted electric field strength required to induce soliton formation, and the results with resonant nominal pump frequency best explained by below resonance calculations. Possible reasons cited for these discrepancies include disorder in the real junctions, which slow down the soliton from the ideal case, the effect of junction stacking, which may amplify nonlinearity compared to a single junction modelled by the 1D sine-Gordon equation, and inhomogeneous broadening caused by disorder.

In summary, experimental observations of propagating modes and a transparency window induced by on-resonance high field excitation are interpreted as evidence for Josephson plasma solitons predicted by theoretical calculation. This result also demonstrates how flux-carrying JPSs can be driven and detected by THz radiation, as a new way of, for example, sensing or manipulating vortices in presence of magnetic fields.

4.4.2 Parametric amplification of a superconducting plasma wave

The experiment by (Rajasekaran, Casandruc et al. 2016) explores the nonlinear Josephson phase dynamics where Josephson plasma waves can be parametrically amplified through the cubic tunnelling nonlinearity in the cuprate superconductor $La_{1.905}Ba_{0.095}CuO_4$, again modelled as a long Josephson junction where the Cu-O planes act as superconducting electrodes coupled by tunnelling currents along the c-axis. Here, it is argued that, since the plasma frequency of a Josephson junction can be written as $\omega_{Jp}^2 = \frac{1}{L(\varphi(t))C} = \omega_{JP0}^2\, cos\big(\varphi(t)\big)$, where $\omega_{JP0}^2 = 1\ /\ L_0C$ is the equilibrium value, correspondingly the oscillator strength $f \sim \omega_{JP}^2$ for the plasma oscillation is also a function of the Josephson phase and can be expressed as $f = f_0\, cos\big(\varphi(t)\big)$. For a resonant incident optical field of the form $E(t) = E_0\, sin\big(\omega_{JP0}t\big)$, the Josephson voltage relation gives the time-dependent phase as $\varphi(t) = \varphi_0\, cos\big(\omega_{JP0}t\big)$, where $\varphi_0 = \frac{2e\, dE_0}{\hbar\omega_{JP0}}$ and $d \sim 1$ nm is the interlayer distance [see Figure 4-11 (a) and (b)]. Hence, the oscillator strength $f = f_0\, cos\big(\varphi_0\, cos\big(\omega_{JP0}t\big)\big) \approx f_0\big[1 - \big(\varphi_0^2 + \varphi_0^2\, \mathrm{cos}\big(2\omega_{JP0}t\big)\big)\ /\ 4\big]$ is expected to be modulated at a frequency $2\omega_{JP0}$ if the electric field strength E_0 is high enough to drive the phase excursion φ_0 to large amplitudes [see Figure 4-11 (c) and (d)]. Consequently, this predicts that the modulation of the oscillator strength can serve as a pump for the parametric amplification of a second, weak plasma wave at frequency ω_{JP0}.

To demonstrate this phenomenon experimentally, THz pump-probe spectroscopy measurements were performed on $La_{1.905}Ba_{0.095}CuO_4$ with $\omega_{JP0} \cong 0.5$ THz. Here, the intense pump electric field up to 100 kV/cm peak amplitude resonantly drives the Josephson phase to large amplitudes, and mixes with the probe field through the nonlinearity induced. This field strength far exceeds the threshold for the nonlinear regime, which is defined by $\varphi_0 = \frac{2eE_0d}{\hbar w_{JP0}} \sim 1$ and is ~20 kV/cm in this material.

Changes in the reflected probe field as a function of pump probe delays, and the time delay dependent, spectrally integrated response, which is proportional to the plasma

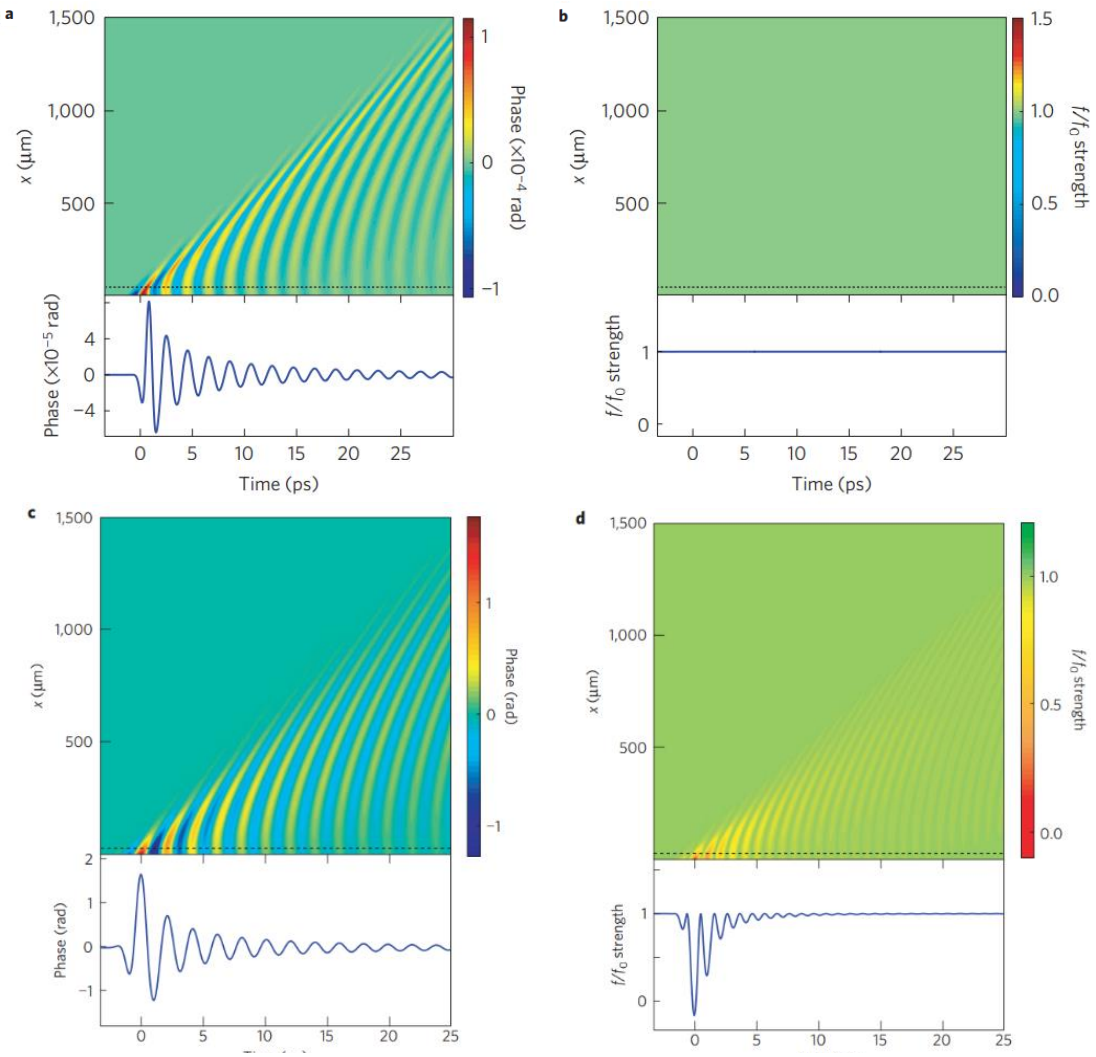

Figure 4-11: (a), (b) Simulated phase $\varphi(x,t)$ (a) and corresponding oscillator strength f (no change) (b) induced by a weak probe terahertz field. Horizontal dotted lines indicate the spatial coordinate x at which the line cuts are displayed (lower panels). (c), (d) Phase $\varphi(x,t)$ (c) and corresponding oscillator strength f (d) induced by a strong terahertz pump field, as determined by numerically solving the sine-Gordon equation in the nonlinear regime. Horizontal dotted lines indicate the spatial coordinate x at which the line cuts are displayed (lower panels). Reprinted by permission from Springer Nature: (Rajasekaran, Casandruc et al. 2016).

oscillator strength, is shown in Figure 4-12 (a) and (b). Most notably, a reduction in the integrated response is observed, accompanied by oscillations at a frequency $\sim 2\omega_{JP0}$, in agreement with the theoretical calculation. The oscillation frequency is independent of the pump field amplitude E_0 and reduces with increasing temperature at which the measurements are taken, consistent with the behaviour of the equilibrium plasma frequency ω_{JP0}. The effect is no longer observable when the temperature goes above T_C.

Time domain probe traces before and after excitation are shown for two selected pump-probe delays in Figure 4-12 (c) and (d). At specific delays, the probe field is amplified by the pump, while at other delays it is suppressed, with respect to that at equilibrium.

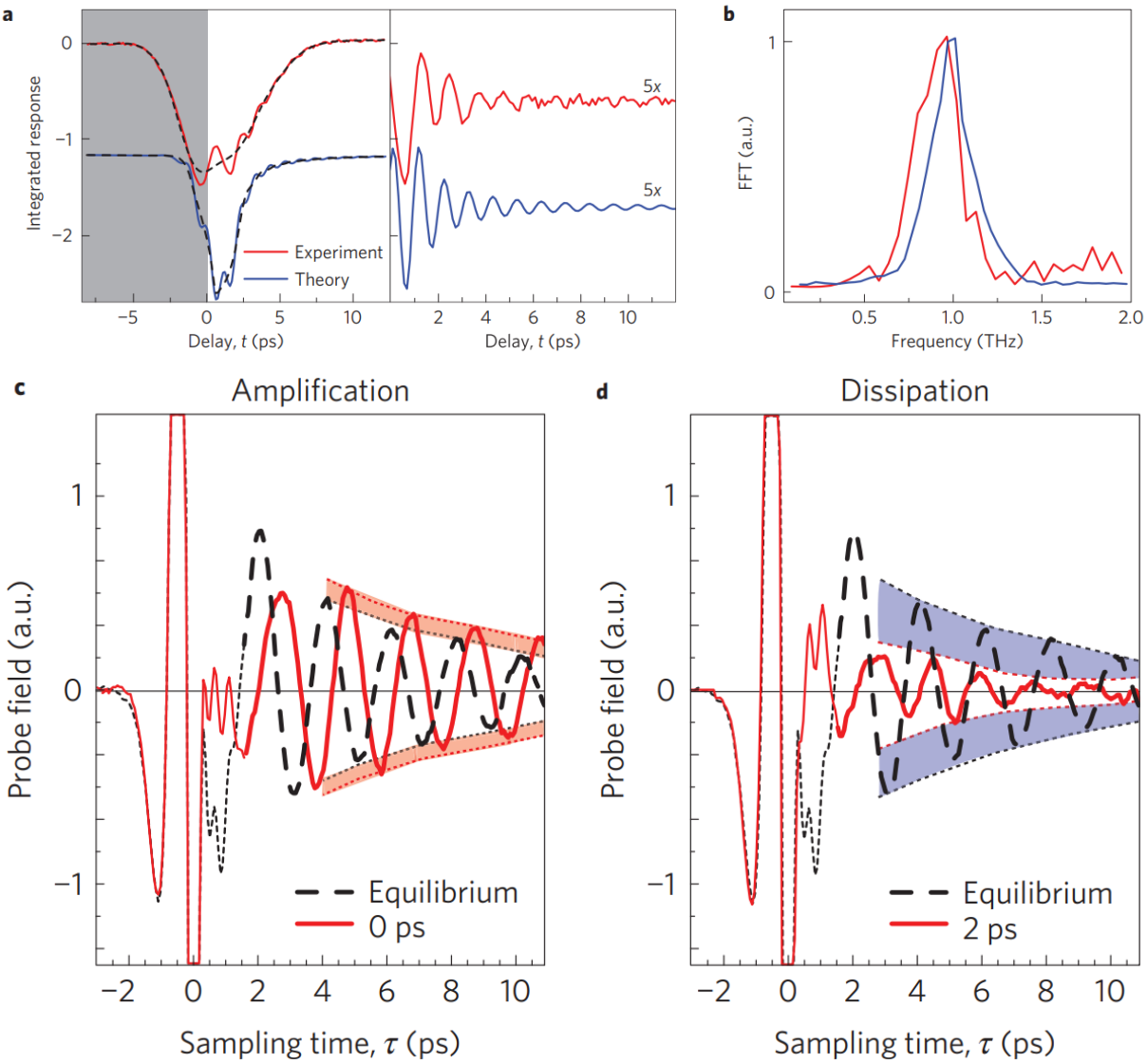

Figure 4-12: (a) Normalized spectrally integrated pump–probe response ΔE_{probe} / $E_{probe}(t, \tau_0 = 2\ ps)$. Experimental data are shown along with calculations based on the sine-Gordon equation in the nonlinear regime (displayed with a vertical offset). Dashed lines indicate an average reduction that accompanies the oscillations. The reduction was subtracted through Fourier filtering (>0.2 THz) to obtain the detail of the oscillations shown on the right. The signal buildup region affected by perturbed free induction decay is shaded in grey. (b) Fourier transform of the extracted oscillations, showing a peak at ~1 THz. (c), (d) $E_{probe}(t, \tau)$ traces measured by scanning the electro-optic sampling time τ at selected pump–probe delays t = 0 ps and t = 2 ps, respectively. Data are shown along with the same quantity measured at equilibrium (pump off). Plasma oscillations on the trailing edge of the pulses ($\tau \geq 2$ ps) are highlighted by thicker lines. Coloured shading indicates amplification (c) and suppression (d) of the JPW amplitude. Reprinted by permission from Springer Nature: (Rajasekaran, Casandruc et al. 2016).

The time delay- and frequency-dependent, loss function, $Im\left(-\frac{1}{\tilde{\varepsilon}(\omega)}\right)$, a useful quantity for tracking the plasma frequency, is plotted in Figure 4-13. For a dissipative material, it is always positive; however, as shown in the experimental data, the loss function turns

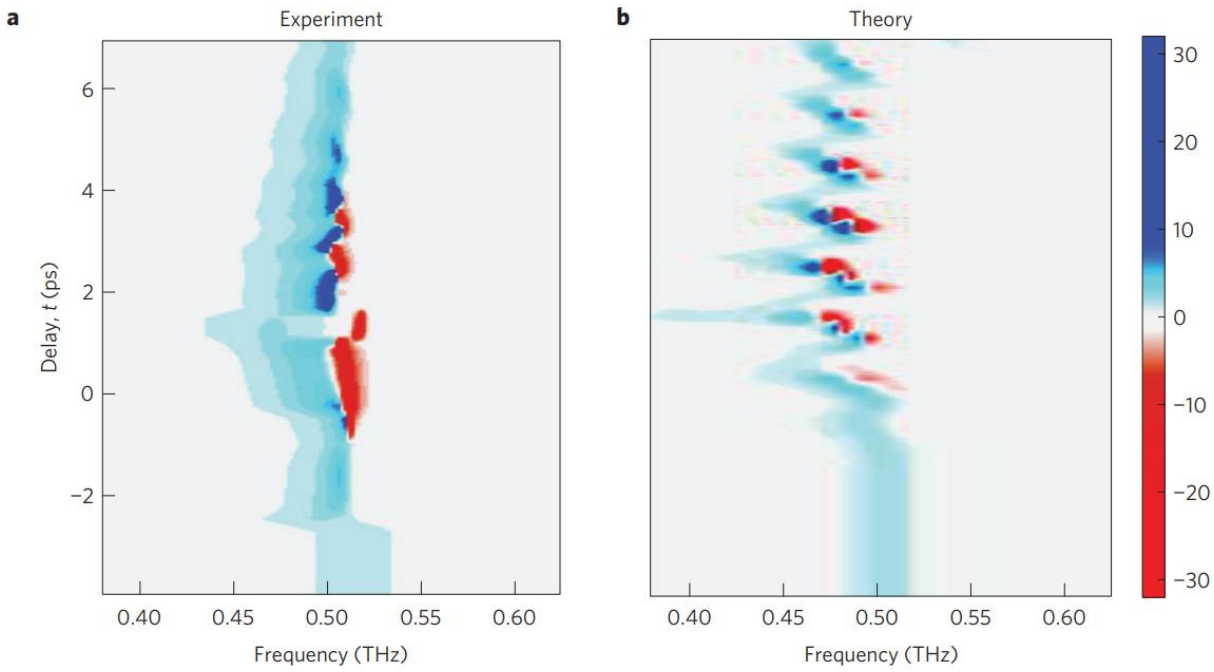

Figure 4-13: (a), (b) Time-delay-dependent and frequency-dependent loss function $L(t,\omega)$ determined experimentally (a) and by numerically solving the sine-Gordon equation in nonlinear regime (b). Note that experimental and simulated $L(\omega)$ in the region between t = −4 ps and t = −2 ps have been multiplied by a factor of five to be better visualized with the other data. Reprinted by permission from Springer Nature: (Rajasekaran, Casandruc et al. 2016).

negative for certain delay ranges after excitation (red region). This suggests that the imaginary part of the dielectric function is negative-valued and indicative of an amplification process. This effect is strong around the zero time delay, disappears after ~1 ps, and is seen again periodically with a repetition frequency of $\sim 2\omega_{JP0}$. The data is also consistent with the simulation results.

This experiment demonstrated that THz Josephson plasma waves can be parametrically amplified in a nonlinear mixing process highly sensitive to the relative phase between the pump and probe pulses, occurring at twice the frequency of the pump. This technique could directly lead to coherent control parametric control of the superfluid condensate in layered superconductors as well as a new means to manipulate or probe the properties of the materials. It is also proposed that this method could pave the way for extracting new insights into the fluctuating superconductivity over a range of temperatures above the superconducting T_C, which will be explored and presented in the next section.

4.4.3 Third harmonic generation in optically silent superfluid stripes

As the final example on nonlinear Josephson phase dynamics, the experiment by (Rajasekaran, Okamoto et al. 2018) investigates the existence of a striped superfluid state with a spatially modulated condensate in $La_{2-x}Ba_xCuO_4$, the proposed pair density wave (PDW) state. As discussed in Section 2.3 and Chapter 3, interlayer superfluid transport is suppressed by the orthogonal stripe alignment between adjacent CuO_2 layers in this material, hence rendering the stripes invisible in linear c-axis optical response [see Figure 4-14 (a)].

To overcome this, (Rajasekaran, Okamoto et al. 2018) focused on nonlinear THz frequency response in search for characteristic signatures of the superfluid stripes. THz reflectivity spectra are first measured on two different LBCO samples, with nominal doping levels x = 9.5% and 15.5% respectively, both of which exhibit homogeneous superconductivity with weak stripe order and as a result have fairly high transition temperatures $T_{co} \sim T_c = 34$ K for x = 9.5% and $T_{co} \sim 40\ K > T_c = 32$ K for x = 15.5% [see Figure 4-14 (b)]. In the superconducting state, at $T = 5K < T_c$, for low incident electric fields no more than 20 kV/cm,

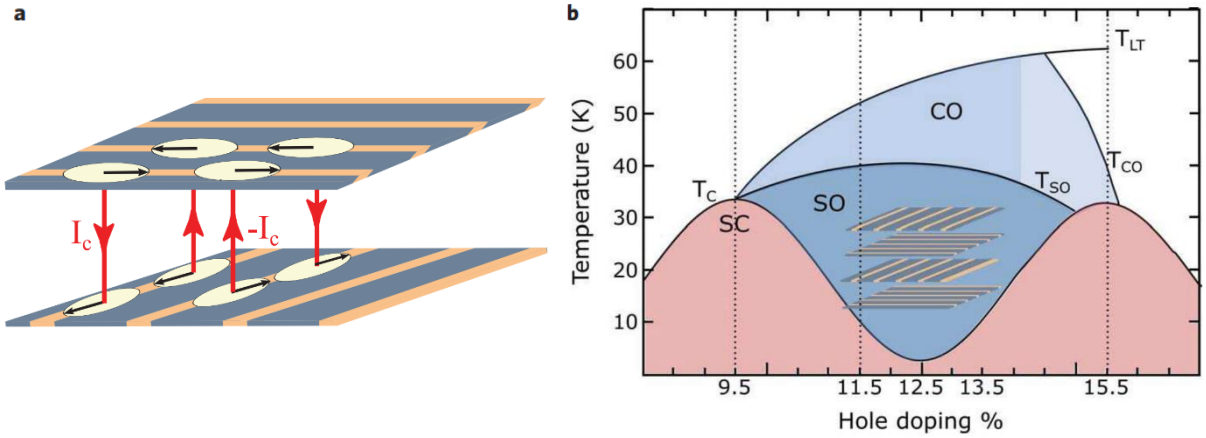

Figure 4-14: (a) Schematic of the order parameter phase in a pair density wave condensate. The black arrows represent the superconducting order parameter phase at each lattice point. Interlayer tunneling from perpendicularly aligned superfluid stripes is equivalent to a checkerboard lattice of alternating π/2 and –π/2 phase Josephson junctions. Such a lattice has tunneling currents of I_c and $-I_c$ flowing at the neighboring junctions at equilibrium (thick red lines). (b) Phase diagram for $La_{2-x}Ba_xCuO_4$. SC, SO, and CO denote the bulk superconducting, spin- and charge-ordered (striped), and charge-only–ordered phases, respectively. T_C, T_{SO}, and T_{CO} are the corresponding ordering temperatures. T_{LT} denotes the orthorhombic-to-tetragonal structural transition temperature. The samples examined in this study are x = 9.5, 11.5, and 15.5% (dotted lines). Further, a schematic stripe-ordered state is shown wherein the yellow stripes depict the charge rivers and the gray stripes depict the antiferromagnetic insulating region (inset). From (Rajasekaran, Okamoto et al. 2018). Reprinted with permission from AAAS.

Josephson plasma edges are evidently visible at the respective plasma frequencies $\omega_{JP0} = 0.5$ THz and $\omega_{JP0} = 1.4$ THz, respectively [see Figure 4-15 (A) and (C)]. However, nonlinear reflectivities measured at 80 kV/cm display two characteristic effects of nonlinear interlayer Josephson coupling: a field dependent redshift of the plasma edge and a reflectivity peak at the third harmonic of the pump frequency $\omega = 3\omega_{pump}$ [see Figure 4-15 (B) and (D)]. The amplitude of the third harmonic field $E(3\omega_{pump})$ scales with the cube of the incident driving field $E(\omega_{pump})$, and reduces with increasing temperature and disappears for $T = T_c$, following a similar dependence as superfluid density [see Figure 4-15 (E) and (F)].

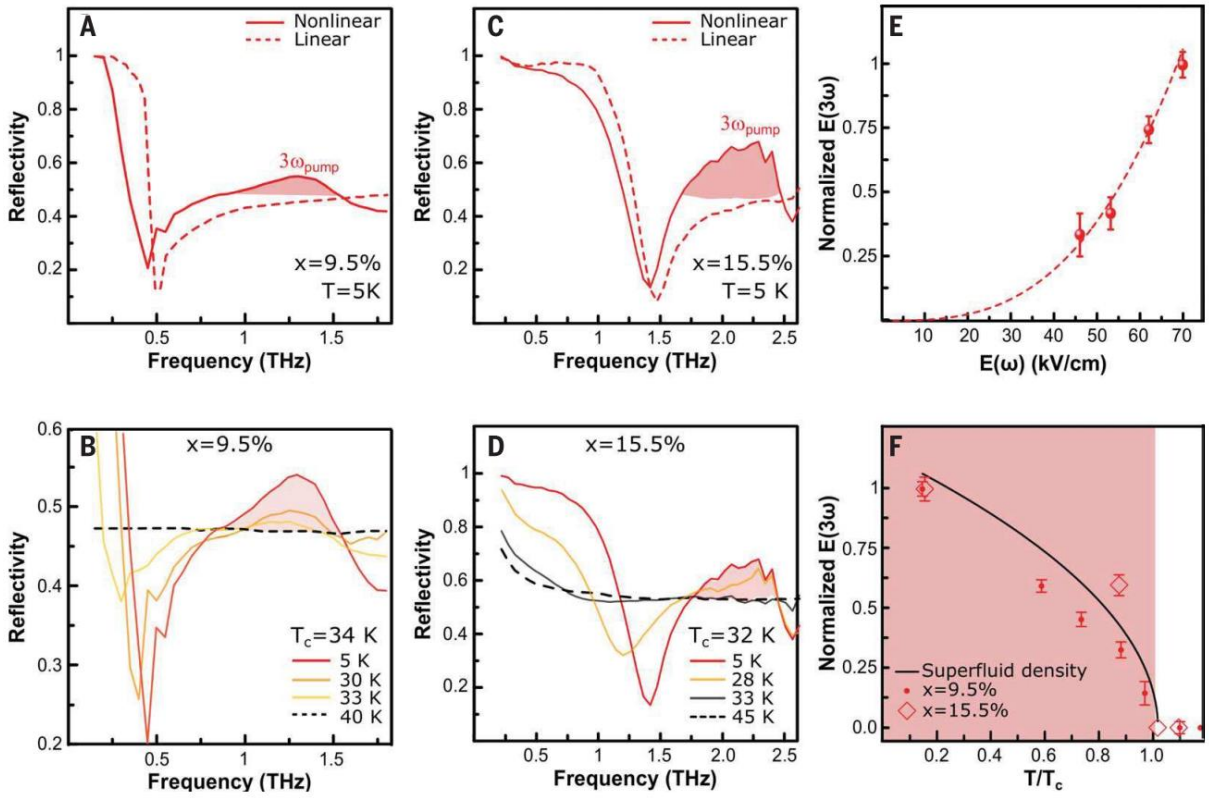

Figure 4-15: (A) Linear and nonlinear reflectivity of $La_{2-x}Ba_xCuO_4$, where x = 9.5%, measured at T = 5 K with ω_{pump} = 450 GHz. The linear reflectivity displays a Josephson plasma edge at ω_{JP0} = 500 GHz (0.5 THz), whereas the nonlinear reflectivity shows a red shift of the edge and third harmonic generation (red shading). (B) Temperature dependence of nonlinear reflectivity for x = 9.5%. The third-harmonic peak disappears above T_C = 34 K. (C) Linear and nonlinear reflectivity for x = 15.5%, measured with ω_{pump} = 700 GHz. (D) Temperature dependence of third harmonic generation in x = 15.5%. Third-harmonic generation (red shading) disappears above T_C = 32 K. (E) Third-harmonic electric field strength (normalized to the highest signal) plotted as a function of the incident electric field strength measured at T = 5 K from the x = 9.5% sample. The third-harmonic field displays a cubic dependence on the incident field strength. (F) Temperature dependence of the third-harmonic amplitude (normalized to the measurement at T = 5 K) from the x = 9.5 and 15.5% doping. The superfluid density [$\omega\sigma_2(\sigma \rightarrow 0)$] (normalized to the measurement at T = 5 K) extracted from the linear optical properties of the x = 9.5% sample is also shown. All of the quantities vanish above T_C. Red shading indicates the bulk superconducting phase. From (Rajasekaran, Okamoto et al. 2018). Reprinted with permission from AAAS.

The redshift of the plasma frequency can be explained by a similar analysis to that done for the previous experiment in Section 4.4.2. For an incident electric field polarised along the c-axis of the form $E(t) = E_0\, sin(\omega_{pump}t)$, the Josephson phase θ (note a change in choice of notation from the rest of the thesis to avoid confusion over a different concept in the original paper) can be derived from the Josephson voltage relation $\frac{\partial\theta(t)}{\partial t} = \frac{2e\,dE(t)}{\hbar}$ to get $\theta(t) \propto cos(\omega_{pump}t)$, where *e* is the electron charge, *d* the interlayer separation, and $\hbar$ the Planck constant. At the same time, the c-axis superfluid density $\rho_c \propto cos\,\theta$ and $\rho_c \propto \omega_J^2$, implying the plasma frequency depends on the Josephson phase as

$$\omega_J^2 = \omega_{JP0}^2 cos\theta = \omega_{JP0}^2 \cos[\theta_0 \cos(\omega_{pump}t)] = \omega_{JP0}^2 \left[1 - \frac{\theta_0^2}{4} - \frac{\theta_0^2 \cos(2\omega_{pump}t)}{4}\right]$$

where ω_{JP0} is the equilibrium plasma frequency and $\theta_0 = \frac{2e\,dE_0}{\hbar\omega_{pump}}$. Hence, an average red shift of the plasma frequency is expected as $\omega_{JP0}^2(1 - \frac{\theta_0^2}{4})$.

Furthermore, by the Josephson current relation, a tunnelling supercurrent is generated at the first and third harmonic frequency of the driving field as

$$I(t) = I_c\, sin[\theta_0\, cos(\omega_{pump}t)] \approx I_c \left[\theta_0 \cos(\omega_{pump}t) - \frac{\theta_0^3}{6}\cos^3(\omega_{pump}t)\right]$$

emitting third harmonic radiation.

Numerical simulations based on solving one-dimensional sine-Gordon equation, which describes the spatial and temporal evolution of the Josephson phase along the depth from the surface of the sample, produce the electric field on the surface and calculate the reflectivity for arbitrary incident fields. As shown in Figure 4-16, the simulation results reproduce the experimental data well.

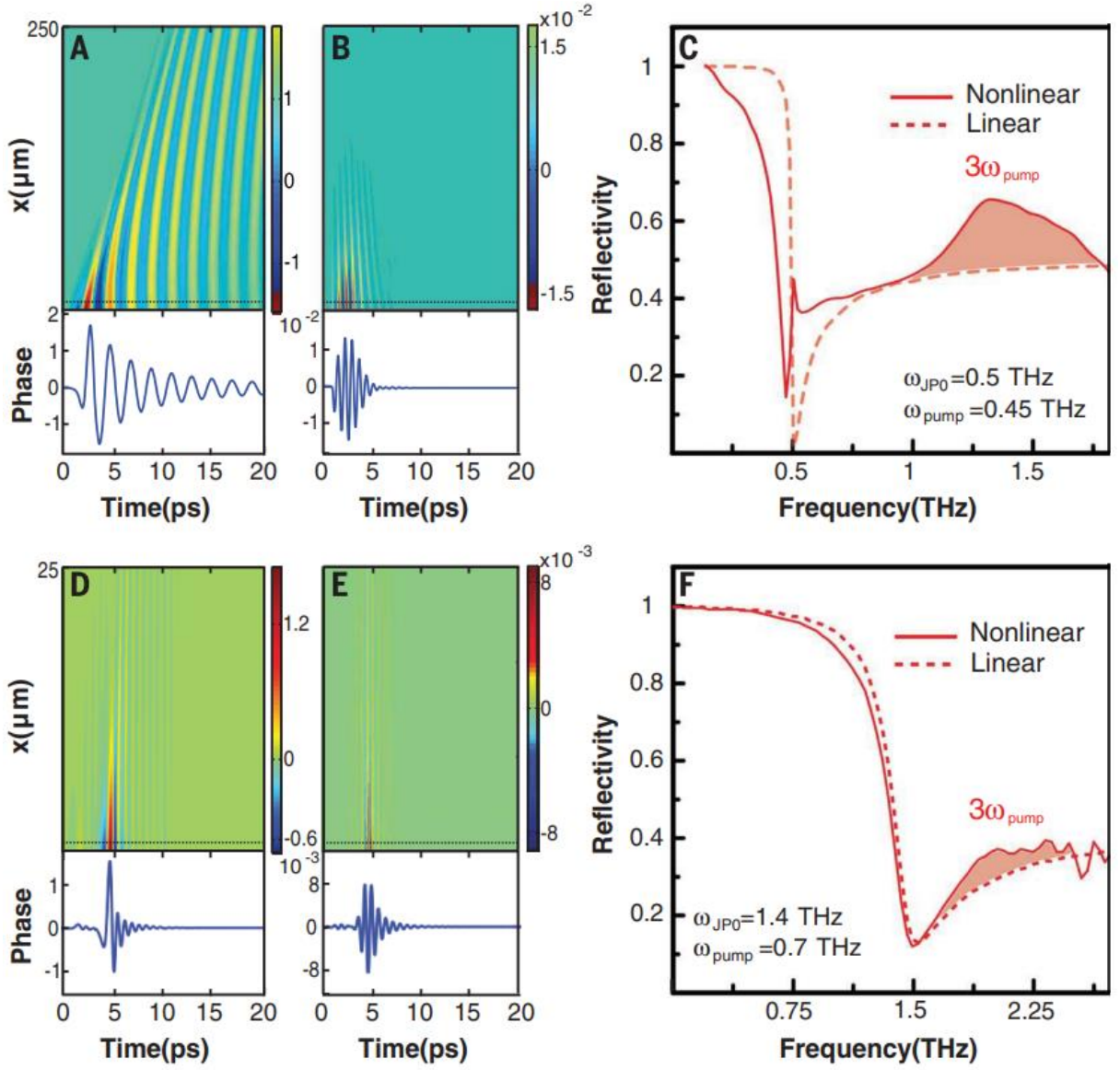

Figure 4-16: Simulated nonlinear reflectivity for homogeneous superconductivity at x = 9.5 and 15.5% doping. (A) Simulated space (x, not to be confused with the symbol for doping concentration) – and time (t) – dependent order parameter phase $[\theta(x,t)]$ obtained by numerically solving the sine-Gordon equation on x = 9.5% samples. The equation makes use of equilibrium superfluid density extracted from the linear optical properties and assumes excitation with terahertz pulses of shape and strength used in the experiment. The horizontal dotted lines indicate the spatial coordinate x at which the line cuts are displayed (lower panel). (B) Simulated order parameter phase (A) after frequency filtering centered at $3\omega_{pump}$ with its corresponding line cut (lower panel). (C) Simulated reflectivity in the linear (E = 0.1 kV/cm) and the nonlinear (E = 80 kV/cm) regime. The third-harmonic generation component is highlighted (red shading). (D to F) Same as in (A) to (C) but for x = 15.5%. From (Rajasekaran, Okamoto et al. 2018). Reprinted with permission from AAAS.

So far, the observations are well understood for dopings *x* = 9.5% and 15.5%. More strikingly, however, in the normal-state striped phase as well as the superconducting state in the doping *x* = 11.5%, a similar third harmonic signal is also detected [see Figure 4-17 (A) and (C)]. Here, despite a lack of a plasma edge in linear reflectivity for $T > T_c = 13$ K up to

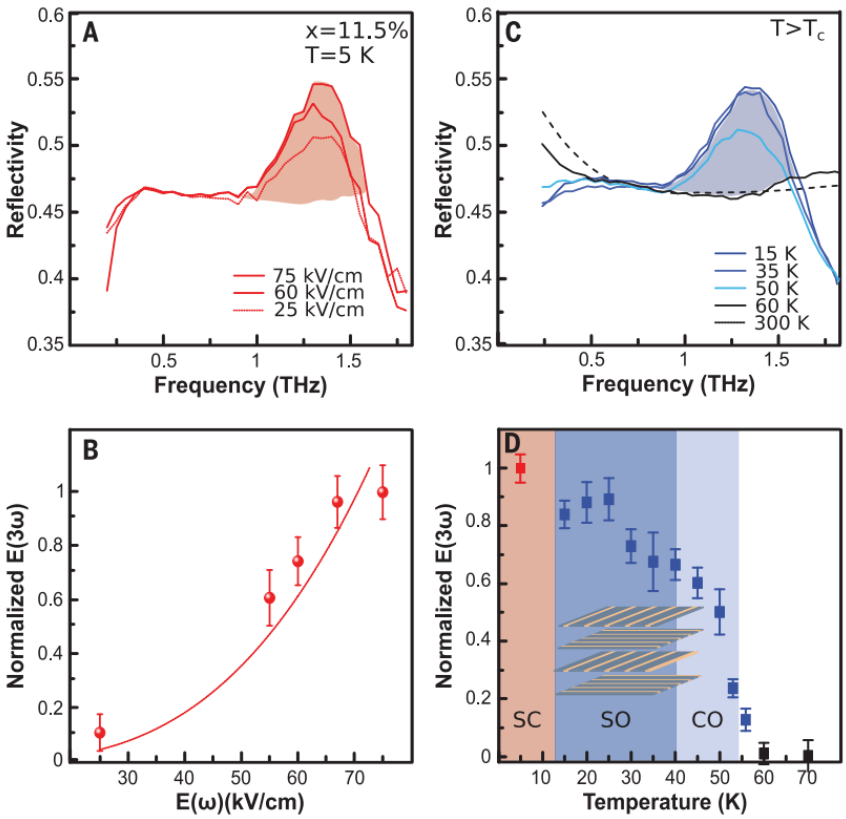

Figure 4-17: (A) Nonlinear frequency-dependent reflectivity measured in the striped x = 11.5% samples recorded for three different field strengths at T = 5 K (T_C = 13 K). (B) Electric field dependence of the third-harmonic amplitude for T = 5 K. (C) Temperature dependence of the nonlinear reflectivity for T > T_C = 13 K. (D) Temperature dependence of the third-harmonic signal (normalized to the highest field measurements at T = 5 K). From (Rajasekaran, Okamoto et al. 2018). Reprinted with permission from AAAS.

$T \sim T_{co} = 55$ K, a clear contribution of several percent of the driving field in amplitude at $\omega = 3\omega_{pump}$ is strongly suggestive of the presence of superconducting tunnelling above T_C and up to T_{CO} [see Figure 4-17 (D)].

In order to explain the third harmonic generation in the striped phase, it is argued that a pair density wave can provide large nonlinearity like that of the homogeneous condensate. Figure 4-14 (A) schematically depicts the arrangement of stripes between two neighbouring CuO_2 planes and the order parameter phase of the PDW, represented by the vector angle (black arrow), rotating by $\pi/2$ from one plane to the next, producing a checkerboard lattice of $\pi/2$ and $-\pi/2$ junctions. As a result, in equilibrium, the PDW supports a lattice of staggered tunnelling supercurrents, which average out to zero [thick red arrows in Figure 4-14 (A)].

Two normal modes contribute to the optical response, termed the φ_0 and φ_π modes. The φ_0 mode is optically active. Under the excitation of an optical field $E(t) =$

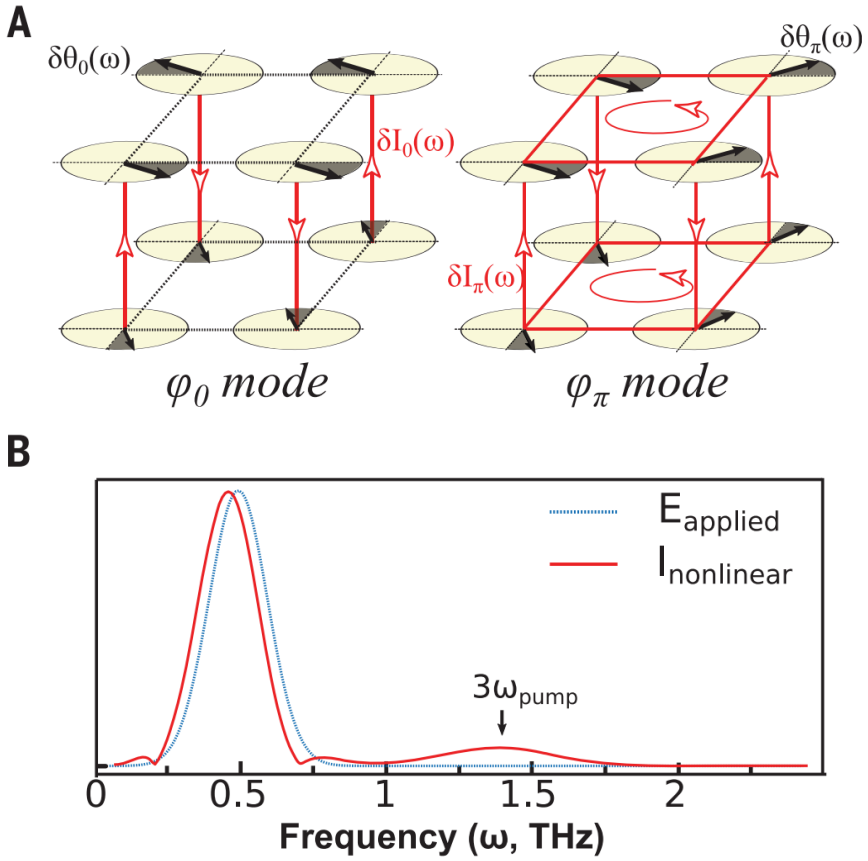

Figure 4-18: (A) Excitation modes of the PDW indicating the φ_0 and φ_π modes (see text). The shaded region under the black arrow represents the phase excursion from the equilibrium geometry ($\delta\theta_0$ and $\delta\theta_\pi$). Corresponding current fluctuations δI_0 and δI_π produced by such excitations are also depicted (thin red lines). (B) Calculated nonlinear current response for the unit cell of Figure 4-14 (A) after application of a single-cycle optical pulse centered at 500 GHz frequency. From (Rajasekaran, Okamoto et al. 2018). Reprinted with permission from AAAS.

$E_0\,sin(\omega_{pump}t)$, identical phase excursions develop $\delta\theta_0(t) = \frac{2e\,dE_0}{\hbar\omega_{pump}}\cos(\omega_{pump}t)$ at each site [shading under black arrows in Figure 4-18 (A)], giving rise to current fluctuations of equal magnitude but opposite sign at neighbouring $\pi/2$ and $-\pi/2$ junctions [red arrows in Figure 4-18 (A)], rendering this mode silent. The other φ_π mode consists of phase excursions in opposite directions at neighbouring sites and is optically inactive, as illustrated in Figure 4-18 (A).

When the nonlinear regime is accessed by strong driving fields, a non-zero optical response is expected. By considering a nonlinear expansion of the Josephson energy $U(\varphi_0, \varphi_\pi) \propto J_0\varphi_\pi^2 - J''\varphi_\pi + C\varphi_0^2\varphi_\pi$, where J_0 and J'' are the in-plane and out-of-plane Josephson energies and $C = J''/2$ is the coupling constant between the two modes, the final coupling term $\varphi_0^2\varphi_\pi$ implies indirect excitation of the φ_π mode by the φ_0 mode directly driven by the optical field.

For an electric field $E(t) = E_0\, sin(\omega_{pump} t)$, which only acts on the φ_0 mode, the equations of motion for the two modes are $\varphi_0 \approx \omega_{pump} E_0 \cos(\omega_{pump} t)$ and $\varphi_\pi \approx -2C\varphi_0^2$. Hence, the φ_0 mode oscillates at the frequency ω_{pump}, while the φ_π gets indirectly driven. Because the driving term in the equation of motion for φ_π is proportional to φ_0^2, the phase of this mode will be driven at $2\omega_{pump}$. Since the total nonlinear current $I_{tot} = \sum I_{junctions}$ contains terms of the form $2I_C\varphi_0\varphi_\pi$, the two phase coordinates $\varphi_0(\omega_{pump})$ and $\varphi_\pi(2\omega_{pump})$ mix with each other and create difference and sum frequencies ω_{pump} and $3\omega_{pump}$, leading to Josephson tunnelling currents oscillating at these frequencies [see Figure 4-18 (b)].

In summary, among other possible hypotheses for the origin of this third harmonic signal observed in the stripe ordered state of LBCO, the most plausible description is based on the existence of superconducting tunnelling and finite momentum condensation in the normal state in the form of a PDW order. In Chapter 6, the second experiment of this thesis pushes this line of research further by driving the system to even larger phase excursion to provide more convincing and unequivocal evidence for the existence of superconducting tunnelling in the stripe phase of LBCO.

5. Light-induced superconductivity in LBCO in magnetic field

5.1 Control of stripes with magnetic field

As discussed in Chapters 3 and 4, the stripe phase in LBCO shows many signs of some form of superconducting behaviour, such as revived superconducting transport through optical excitation and nonlinear THz third harmonic generation. In light of the latest results, the originally proposed picture that the stripes simply compete with the equilibrium superconducting order and suppress interlayer Josephson tunnelling no longer seems to tell the whole story. The possible existence of the novel state of spatially modulated order with superconducting fluctuations, the pair density wave (PDW), poses interesting questions about the nature of relation between the stripe order and superconductivity in many cuprates. Therefore, it is sensible to seek to manipulate the delicate balance of strengths among these coexisting ground states and observe the resulting change in the dynamics of interaction between them.

In Section 2.3, different ways of interaction with the stripe order are discussed. Among them, the magnetic field is one of the most effective tools for controlling the strength of the stripes. Studies such as (Tranquada, Gu et al. 2008) and (Wen, Jie et al. 2012) clearly demonstrate the effect of applied magnetic fields on altering the equilibrium phase diagram of LBCO. A direct measure of the charge stripe order by X-ray diffraction by (Hücker, v. Zimmermann et al. 2013) confirmed the enhancement of both in-plane and out-of-plane charge order correlations for magnetic field up to 10 T. The effect is stronger in the x = 9.5% doping (~50%) than in x = 11% (only < 10%). This is interpreted as compatible with the picture of competition between the stripes and superconductivity, because closer to the x = 1/8

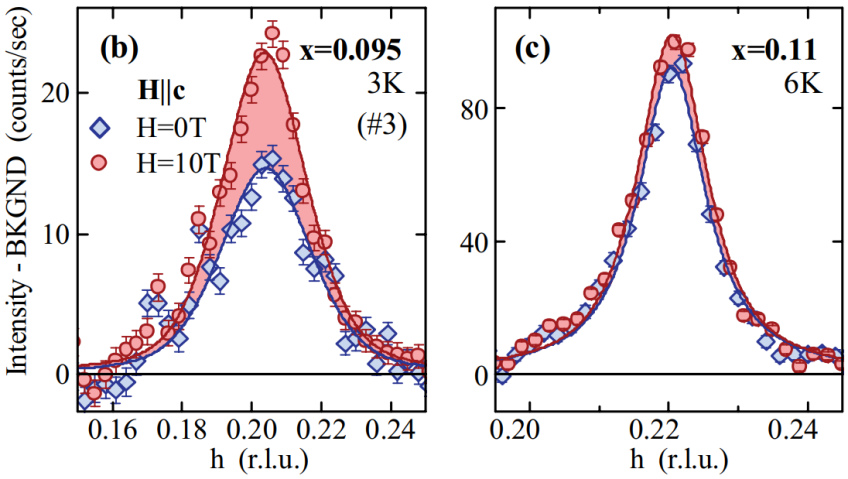

Figure 5-1: In-plane charge stripe order correlations at T ~ 3 K for LBCO x = 9.5% and 11%. Reprinted with permission from (Hücker, v. Zimmermann et al. 2013). Copyright 2022 by the American Physical Society.

doping the equilibrium is already highly suppressed and the stripes become essentially independent of the magnetic field.

Furthermore, the direction of the applied magnetic field is also of crucial importance. In (Wen, Jie et al. 2012), the resistivity measurements performed on LBCO 9.5% along the CuO_2 planes displays a stark difference in the effectiveness in suppressing the onset temperature of superconducting transition between magnetic field applied along the in-plane and out-of-plane directions. While a field of up to 8 T is capable of reducing the temperature

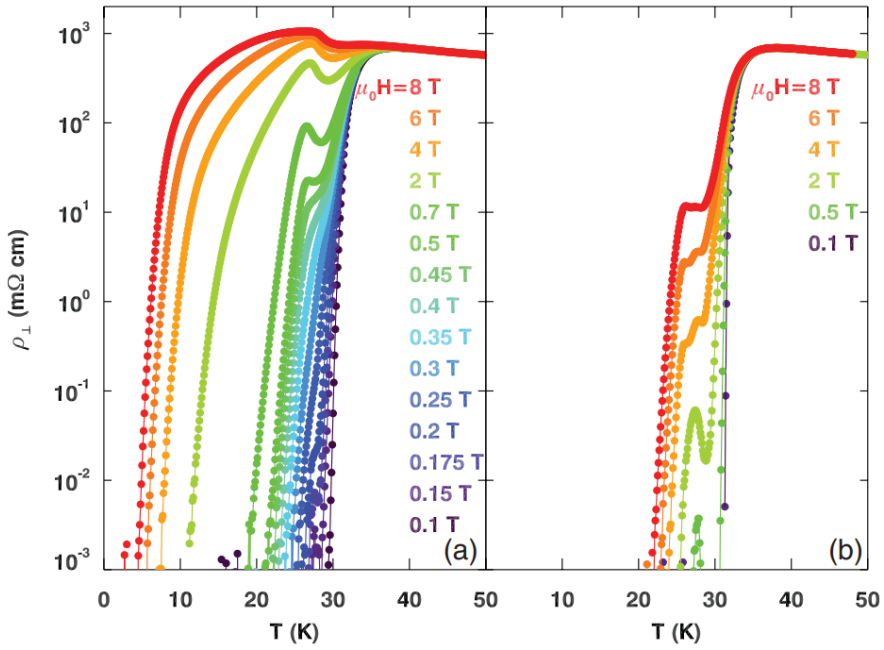

Figure 5-2: Out-of-plane resistivities vs temperature for a range of magnetic fields applied along the (a) out-of-plane and (b) in-plane directions. Reprinted with permission from (Wen, Jie et al. 2012). Copyright 2022 by the American Physical Society.

at which the out-of-plane resistivity becomes vanishingly small from ∼30 K to less than 10 K, it remains above 20 K when the magnetic field is oriented along the in-plane direction.

Therefore, in order to utilise the magnetic field as a tuning knob of the strength of the stripe order, it is most effective to apply it perpendicular to the CuO_2 planes of LBCO. In the context of optical excitation as a means of enhancing or even inducing superconducting transport, in this experiment, the interplay between the stripe order and light-induced superconductivity is investigated through the application of magnetic fields, allowing fine control over the relative strengths of equilibrium interlayer Josephson coupling and the stripes before photo-excitation and providing a range of different starting points from which non-equilibrium dynamics can be generated and studied.

5.2 Experimental realisation

For this experiment, THz time-domain spectroscopy (THz-TDS) is employed as the probing method. It utilises a broadband, single-cycle THz pulse, which reflects off the sample surface, changing amplitude and picking up a phase shift in the process, and an 800 nm gate pulse to sequentially sample the THz field with sub-picosecond resolution. This is sensitive to both the amplitude and the phase of the THz field because the THz field profile induces a transient birefringence through the Pockels effect in certain types of nonlinear crystals such as zinc telluride (ZnTe), and this results in a polarisation rotation acquired by the gate pulse. Then this change in polarisation of the gate pulse is measured through a balanced detection scheme, which converts the polarisation into change in intensity of light hitting two fast photodiodes.

The optical setup is arranged around a superconducting magnet with optical access (see Figure 5-3). Light pulses of 3.5 mJ pulse energy, 100 fs duration, 800 nm wavelength from an amplified Ti:sapphire laser are split into three parts. 80% of the total power, 2.8 mJ is the pump beam, used to photo-excite the sample and generate dynamics. 19%, or roughly 660 µJ, goes towards single-cycle, broadband THz pulse generation in a photoconductive antenna, after attenuation. The THz pulse, serving as the probe beam, is then shone onto and reflected by the sample surface. The remaining 1%, i.e. no more than 35 µJ, is reserved as the gate beam,

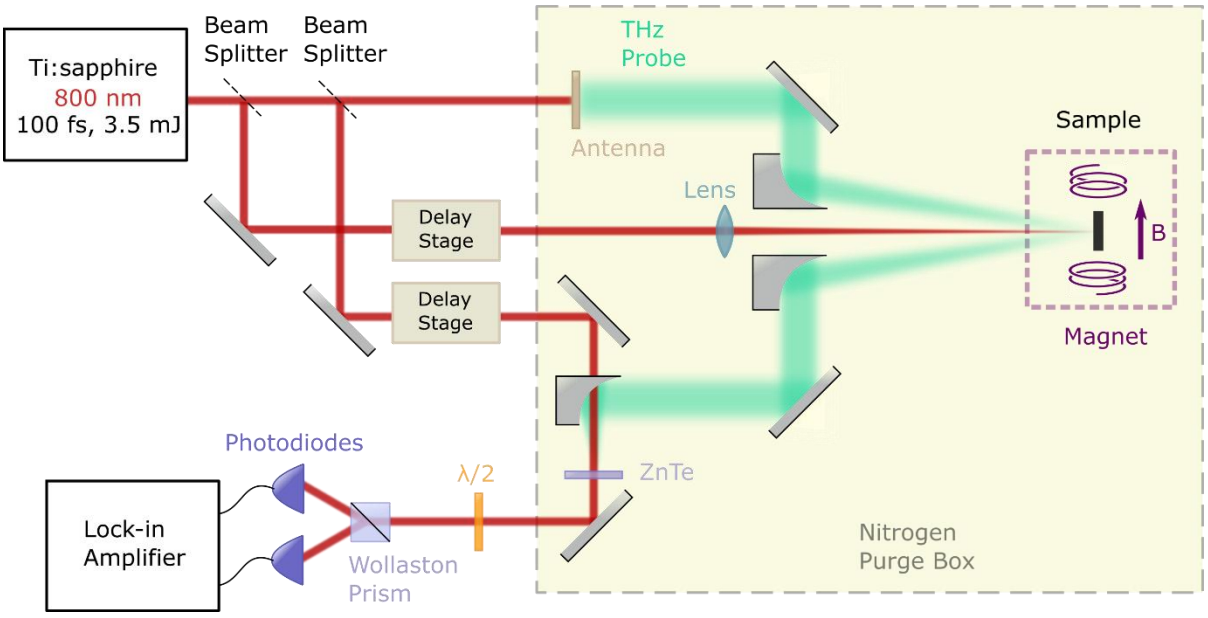

Figure 5-3: Schematic of optical setup.

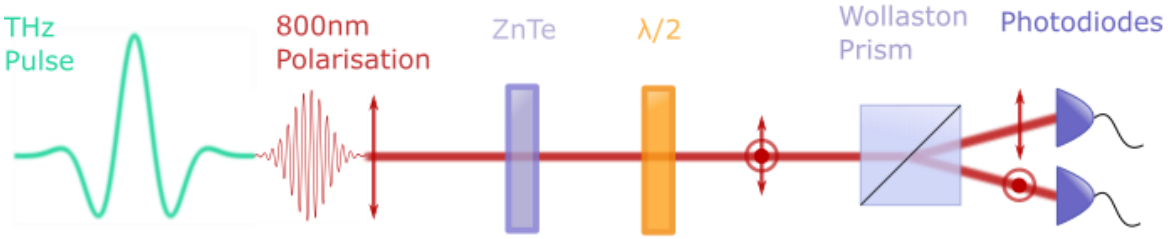

Figure 5-4: Schematic of electro-optic sampling and balanced detection

which samples the electric field of the reflected probe pulse through electro-optic sampling in a piece of ZnTe. The pump beam is at normal incidence to the sample surface, while the probe beam has a ~7° angle of incidence. Both the pump and probe beams have the electric fields polarized along the crystallographic c-axis of the LBCO sample.

In front of the two photodiodes, a half waveplate sets the polarisation of the gate beam to be linear and diagonal at first in absence of any polarisation rotation caused by the THz field, such that, when the Wollaston prism decomposes the gate beam evenly into two orthogonal components onto the two photodiodes. Because the photodiodes output a voltage signal proportional to the intensity of light received, a change in polarisation induced by the THz probe field reflected from the sample can be detected as a difference between the two photodiode outputs. By varying the delay between the probe and gate beams, the entire temporal trace of the THz field can be mapped out, and the full Fourier spectrum of the probe electric field can be retrieved.

5.3 Magnetic field tuning of light-induced superconductivity in LBCO

Two representative doping levels of LBCO are studied in presence of magnetic fields up to 7 T across the temperature range of interest. Specifically, the single crystals used were grown at nominal Ba concentrations x = 9.5% and 11.5%; both samples are superconducting with transition temperatures at T_C = 32 K and 13 K respectively. At 9.5% doping, superconductivity, charge and spin orders all appear at the same temperature, $T_{CO} = T_{SO} = T_C$ = 32 K, whereas in the 11.5% sample these transitions become decoupled, with T_{CO} = 53 K and T_{SO} = 40 K. See Figure 5-5 (a) for a phase diagram. Both samples are cut with a large crystallographic ac surface, ideal for THz reflectivity measurements [see Figure 5-5 (b)].

The optical response of the 11.5%-doped compound in the superconducting state in absence of magnetic field is plotted in Figure 5-6. The equilibrium response is shown as grey curves, and two different pump-probe delays are shown as blue dots. The $\tau = 1.4$ ps data show a response compatible with a strong, optically induced increase in interlayer tunnelling strength, as evidenced by a blueshift of the plasma edge in reflectivity from ~0.2 to ~0.6 THz [see Figure 5-6 (a)], as previously reported (Nicoletti, Casandruc et al. 2014). Correspondingly,

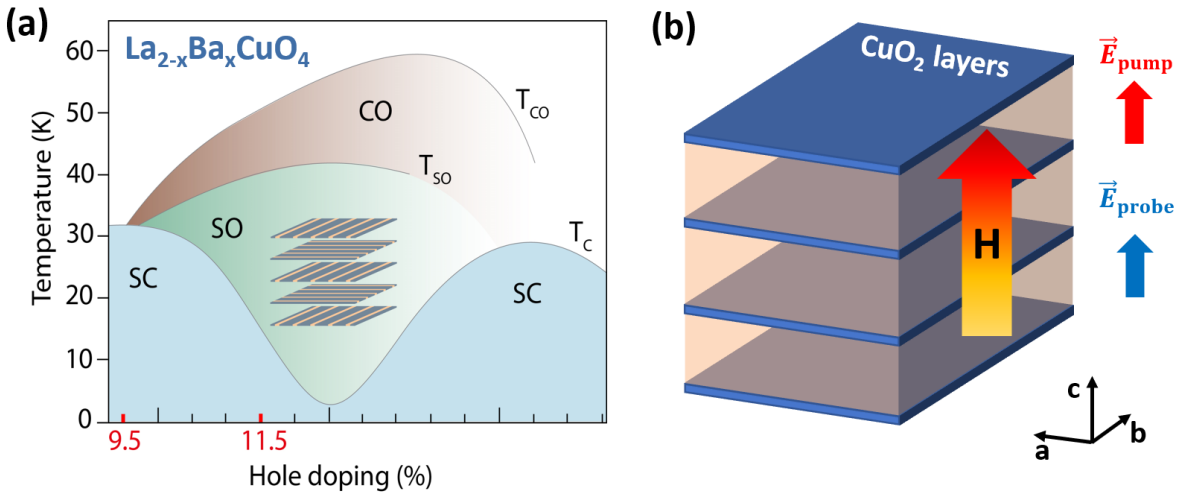

Figure 5-5: (a) Temperature-doping phase diagram of $La_{2-x}Ba_xCuO_4$, as determined in (Hücker, v. Zimmermann et al. 2011). T_C, T_{SO}, and T_{CO} indicate the superconducting, spin-order, and charge-order transition temperatures, respectively. The inset shows the 90° periodic stacking of CuO_2 planes in the stripe phase. (b) Cartoon depicting the experimental geometry. We used optical pump and THz probe pulses polarized both along the c axis. The experiment was performed in presence of magnetic fields up to 7 T, oriented along the c direction. Reprinted with permission from (Nicoletti, Fu et al. 2018). Copyright 2022 by the American Physical Society.

an enhancement in the low-frequency imaginary conductivity $\sigma_2(\omega)$ [see Figure 5-6 (c)]. These results can be well fit with a model describing the optical response of a Josephson plasma, for which the dielectric function is expressed as $\tilde{\varepsilon}(\omega) = \varepsilon_\infty\left(1 - \omega_J^2 \,/\, \omega^2\right)$, where ω_J is the plasma frequency. Fits to the transient spectra are shown as blue lines.

At longer time delay, $\tau = 2$ ps, the response evolves into that of a conductor with finite momentum relaxation rate, as evidenced by the broadening of the reflectivity edge [see Figure 5-6 (b)], and by a downturn of $\sigma_2(\omega)$ at low frequency [see Figure 5-6 (d)]. Notably, the response functions at this longer time delay can be fit with a conventional Drude model for metals, shown as blue lines. In this model, the complex dielectric function is expressed as

$$\tilde{\varepsilon}(\omega) = \varepsilon_\infty\left(1 - \frac{\omega_p^2}{\omega^2 + i\Gamma\omega}\right)$$

where ω_p is the carrier plasma frequency and Γ is the momentum relaxation time.

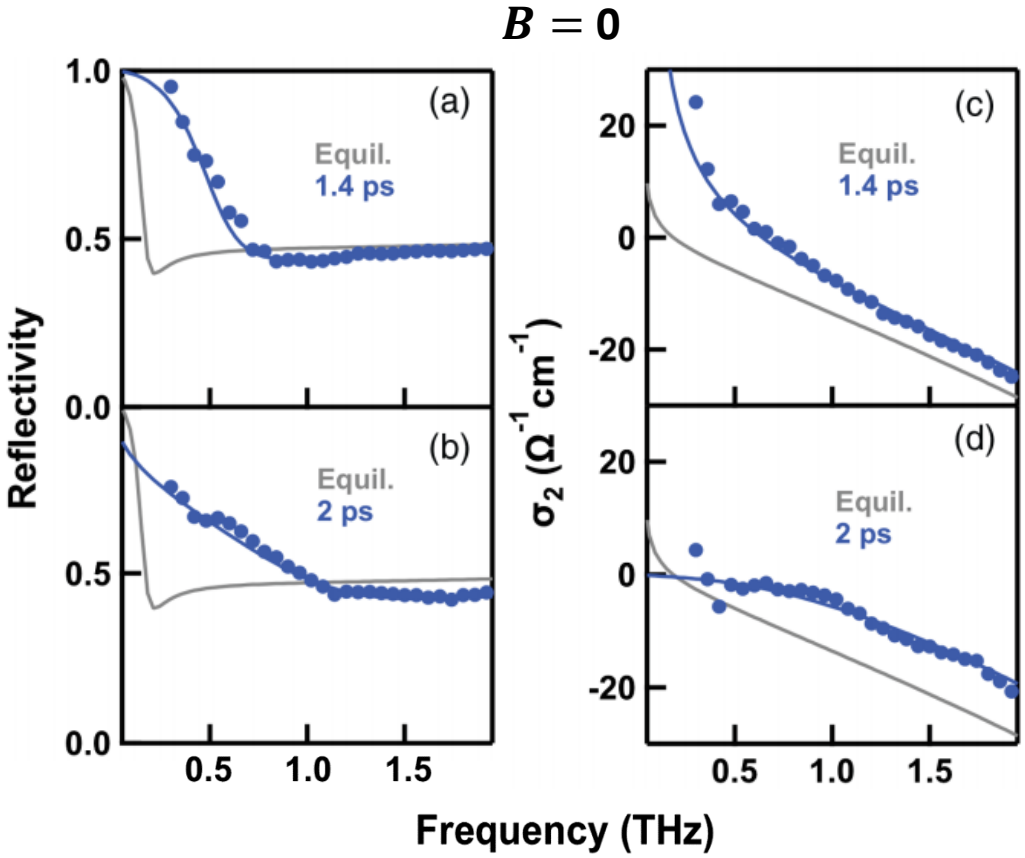

Figure 5-6: (a),(b) c-axis THz reflectivity of $La_{1.885}Ba_{0.115}CuO_4$ measured at T = 5 K (no magnetic field), at equilibrium (gray lines) and at two pump-probe time delays (τ = 1.4 and τ = 2 ps) after excitation (blue circles). Fits to the transient spectra are shown as blue lines. (c),(d) Zero-field imaginary conductivity spectra corresponding to the reflectivities shown in (a),(b). Reprinted with permission from (Nicoletti, Fu et al. 2018). Copyright 2022 by the American Physical Society.

The same measurements are repeated in presence of a 7 T magnetic field applied along the c axis direction. At equilibrium, the magnetic field induces vortices within the CuO_2 layers, stabilises charge and spin orders, and suppresses interlayer Josephson tunnelling without appreciably affecting superconducting coherence in the planes, as discussed in the earlier chapter, because $H_{c2} \gg 7$ T. The magnetic field-induced suppression of interlayer superfluid stiffness is evidenced by the redshift of equilibrium JPR, which sits at ~0.2 THz in zero field and is quenched to below the probed frequency range, i.e. < 0.15 THz, in a field of 7 T, shown as grey lines in Figures 5-6 (a) and 5-7 (a).

The light-induced response resembles that in zero field in certain ways. A clear plasma edge appears in the transient reflectivity measured 1.4 ps after photoexcitation [see Figure 5-7 (a)]. A key difference is that here the transient plasma resonance remains sharp for a longer time, displaying superconducting-like optical properties even at $\tau = 2$ ps time delay [see Figure 5-7 (b)]. This can be seen also by the diverging $\sigma_2(\omega \to 0)$ in Figure 5-7 (d). Unlike the

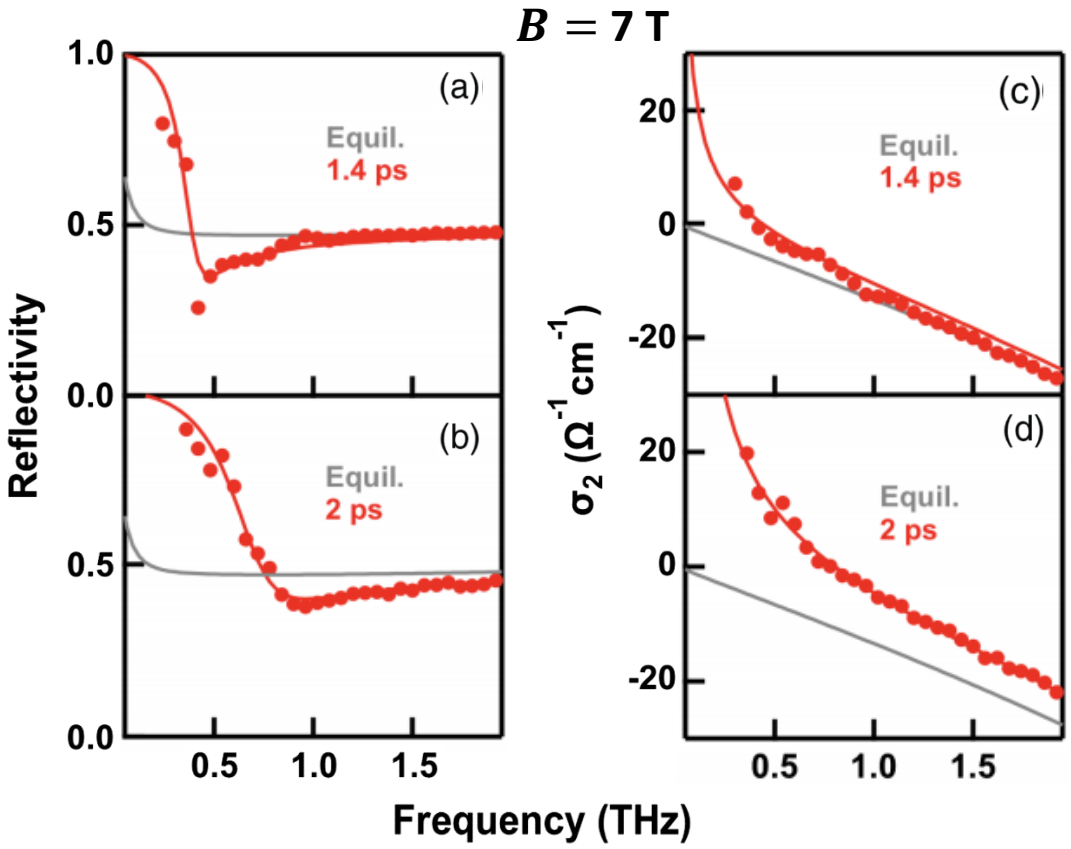

Figure 5-7: (a),(b) c-axis THz reflectivity of $La_{1.885}Ba_{0.115}CuO_4$ measured at T = 5 K and in presence of a 7 T magnetic field, at equilibrium (gray lines) and at two pump-probe time delays (τ = 1.4 and τ = 2 ps) after excitation (red circles). Fits to the transient spectra are shown as red lines. (c),(d) In-field imaginary conductivity spectra corresponding to the reflectivities shown in (a),(b). Reprinted with permission from (Nicoletti, Fu et al. 2018). Copyright 2022 by the American Physical Society.

zero-field data in Figure 5-6, the transient response measured at 7 T can be fit with the Josephson plasma formula at both time delays shown in Figure 5-7.

The coherent behaviour of this newly discovered optically enhanced superconducting state in presence of strong magnetic fields is even more evident in Figure 5-8. Here, the dynamical evolution of the interlayer phase correlation length is shown for several datasets, extracted from the Drude fits in Figure 5-7 as $\xi_c = 2\omega_p d \,/\, \Gamma$, where d is the separation between adjacent CuO_2 layers. At the earliest time delays, for which the optical properties can also be fit with the JPR model, ξ_c is at least ~20 unit cells. The upper bound is determined by the frequency resolution of our measurement and corresponds to carrier mobility larger than $\sim 10^4\ cm^2 \,/\, (V \cdot s)$. Importantly, these are extremely high values which would be unprecedented for out-of-plane transport in a highly resistive normal state oxide, and are rather strongly suggestive of a transient superconducting state.

At longer time delays, for which the response is well described by the Drude model, ξ_c becomes finite and exhibits a collapse, within a few picoseconds, down to a value close to 1-2 unit cells. This collapse becomes, not faster, when the temperature is raised to 30 K [see Figure 5-8 (a)], and it is observed to be even slower in presence of a 7 T magnetic field [see Figure 5-8 (b)]. Notably, the application of magnetic fields results in, for certain time delays ($\tau \approx$ 1-2 ps), a tenfold increase in ξ_c.

A relevant piece of information is added here by the measurement performed at $T_c < T < T_{SO}$ [Figure 5-8 (a)]. In this case, transient superconductivity emerged from the

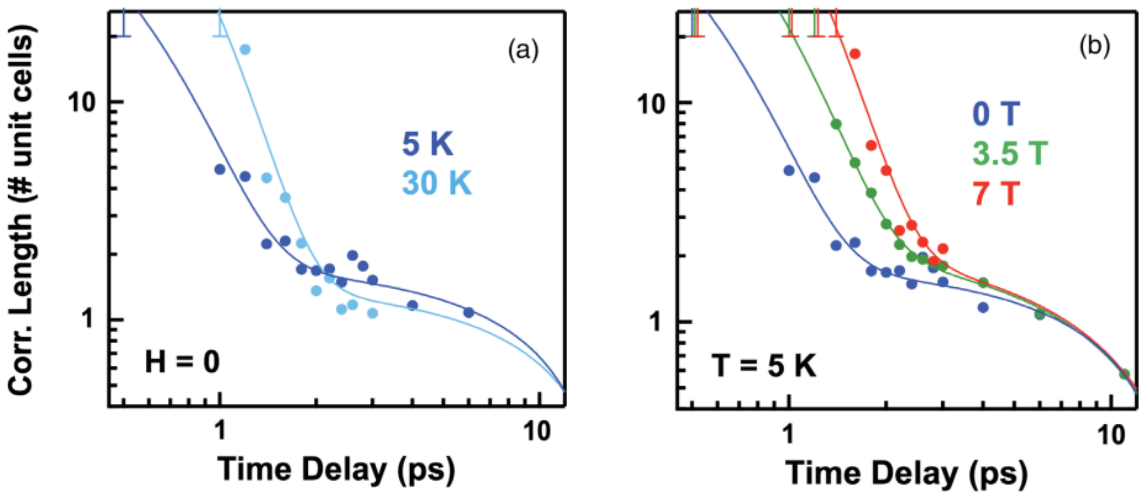

Figure 5-8: Dynamical evolution of the interlayer phase correlation length measured in $La_{1.885}Ba_{0.115}CuO_4$ for different temperatures (a) and applied magnetic fields (b). The values were extracted from the fits of Figure 5-6 and 5-7. Reprinted with permission from (Nicoletti, Fu et al. 2018). Copyright 2022 by the American Physical Society.

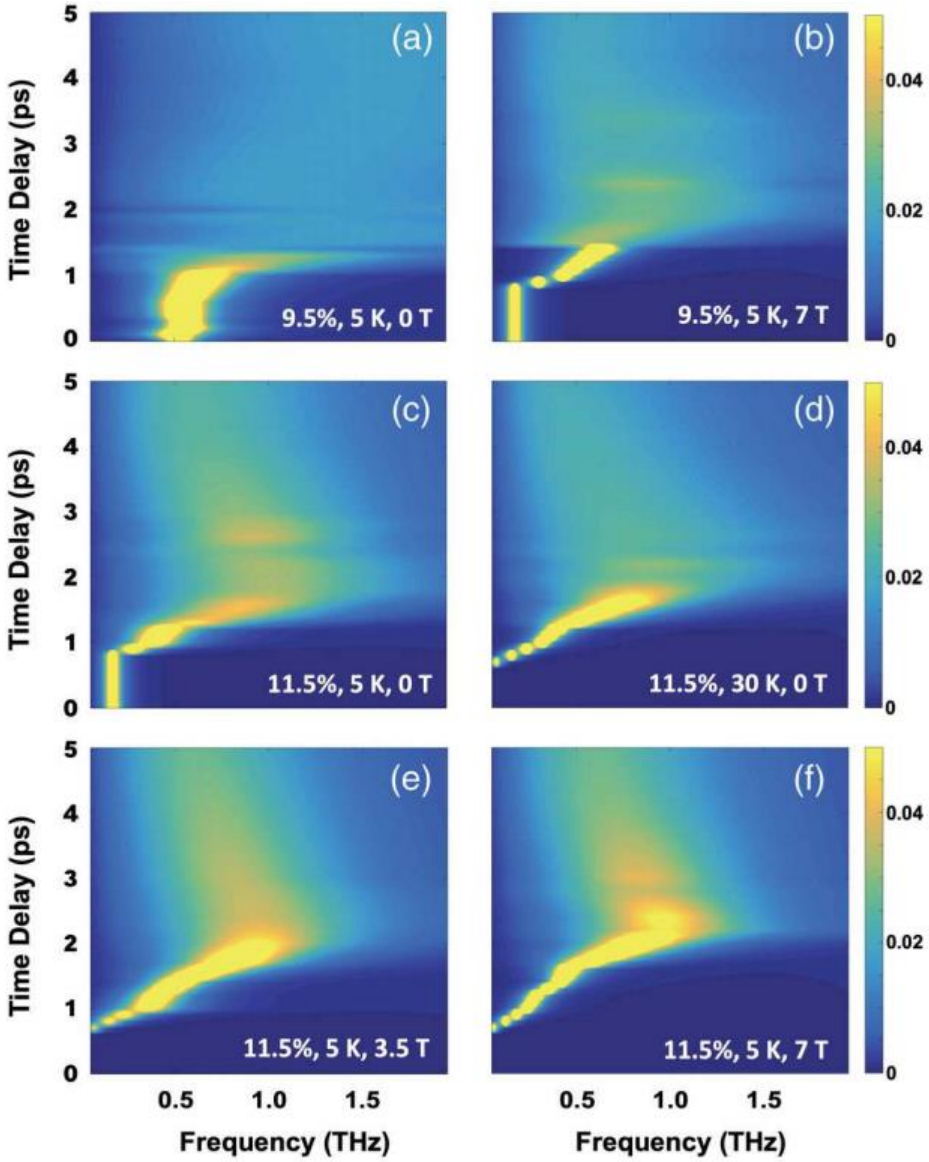

Figure 5-9: Dynamical evolution of the energy loss function of photo-stimulated LBCO under various starting conditions (different doping levels, sample temperatures, and applied magnetic field values), as extracted from fits to the data. Panels (a), (b) refer to $La_{1.905}Ba_{0.095}CuO_4$ at T = 5 K in absence (a) and in presence (b) of a 7 T magnetic field. Panels (c)–(f) show instead the response of $La_{1.885}Ba_{0.115}CuO_4$, measured at T = 5 K and H = 0 (c), T = 30 K and H = 0 (d), T = 5 K and H = 3.5 T (e), T = 5 K and H = 7 T (f). Reprinted with permission from (Nicoletti, Fu et al. 2018). Copyright 2022 by the American Physical Society.

equilibrium normal state, displaying a larger ξ_c than that found at lower temperatures. This observation suggests that, for $H = 0$, the transient superconductor induced from the normal state is "more coherent" than that induced by exciting the superconducting state at $T < T_c$.

Importantly, all data reported in Figure 5-8 display relaxation dynamics to a state with only partially reduced coherence. At $\tau > 2$ ps, the data could still be fit with momentum relaxation rates of $\Gamma \approx 1$ THz, corresponding to $\xi_c \approx$ 1-2 unit cells, values that are

anomalously low for conventional incoherent charge transport, and are instead compatible with a strongly fluctuating superconducting state.

The full dynamical response, determined for a wide range of initial conditions - including doping values, temperatures, and applied magnetic fields - is shown in Figure 5-9. Here, the frequency- and time delay-dependent energy loss function $Im\left(-\frac{1}{\tilde{\varepsilon}(\omega)}\right)$ is plotted, as extracted from fits to the optical response functions. As mentioned previously, this quantity exhibits a sharp peak at the JPR frequency, which acquires a finite width Γ as soon as momentum relaxation processes set in.

Figure 5-9 (a) shows the response of the 9.5%-doped compound below T_C at zero magnetic field, consistent with results reported by (Nicoletti, Casandruc et al. 2014). This material, for which the equilibrium superconducting phase is robust, with the JPR located at a relatively high ∼0.5 THz, and the stripe order is weak (Hücker, v. Zimmermann et al. 2011), only displays marginal enhancement of the superconducting order for $\tau \leq 1$ ps, and then, at later delays, evolves abruptly into an incoherent state, characterised by an overdamped loss function peak.

When a 7 T magnetic field is applied to the 9.5% compound [see Figure 5-9 (b)], the equilibrium interlayer superfluid stiffness is reduced, as shown by the red-shifted JPR frequency to ∼0.2 THz at $\tau \leq 0$ ps. Concomitantly, the stripe order is expected to be enhanced by ∼30% (Hücker, v. Zimmermann et al. 2013). However, here the light induced state behaves differently from that measured at $H = 0$ but rather resembles that found in the 11.5% doping. Within ∼1.5 ps after photo-excitation, a notable blue-shift of the equilibrium develops, reaching values close to 0.5 THz. This observation suggests that interlayer Josephson tunnelling, which was almost completely quenched by the magnetic field, can be transiently revived also at 9.5% doping by photo-excitation. Nevertheless, this revival occurs only over a short interval of time, and for $\tau \geq 1.5$ ps the system evolved abruptly into an incoherent state.

The middle and lower rows of Figure 5-9 [panels (c)-(f)] show the energy loss function of the 11.5% compound, for which selected optical spectra are displayed in Figure 5-7 and the extracted phase correlation lengths are reported in Figure 5-8. Note that this compound is characterised by weaker interlayer superfluid stiffness at equilibrium and a far stronger stripe order than that found at 9.5% doping, by a factor of ∼5 (Hücker, v. Zimmermann et al. 2011).

The dynamical evolution of the loss function in this compound displays, for all temperatures and applied magnetic fields, a more coherent character than that found at 9.5% doping [Figure 5-9 (a) and (b)]. In particular, the data taken at $T = 5$ K and $H = 7$ T are those showing the sharpest resonance and with the longest lifetime [Figure 5-9 (f)].

All results above clearly indicate that optically enhanced/induced superconductivity in LBCO correlates positively with the strength of the equilibrium stripe order. Indeed, the stronger the stripes, the longer the photo-induced coherence, as shown by systematically changing the doping level, sample temperature, and external magnetic field. An exception to this trend is found in the temperature dependent response of 11.5%, as seen in Figure 5-8 (a) and Figure 5-9 (c) and (d). Here, the transient lifetime is clearly enhanced in the 30 K data, despite the equilibrium charge order is reduced by $\sim$15% with respect to lower temperatures (Hücker, v. Zimmermann et al. 2011).

These observations can be interpreted by considering the role of the equilibrium, pre-existing c-axis superfluid stiffness in determining the properties of the transient state in the LBCO compounds investigated in this study. Data presented here suggest that a more robust superconductor at equilibrium adversely affects the strength and lifetime of the photo-induced interlayer coupling [Figure 5-9 (a)], while a weak or completely absent pre-existing condensate [Figure 5-9 (d)-(f)] promotes the transient superconducting state.

It can be speculated that the equilibrium and optically induced interlayer tunnelling might indeed originate from two separate entities. The former is a spatially homogeneous in-plane condensate, which contributes to the c-axis superfluid stiffness at equilibrium, and the density of which is higher for dopings away from 1/8, such as in LBCO 9.5%. The latter, within a PDW picture (Berg, Fradkin et al. 2009), may be understood as originating from superconducting stripes, the Josephson tunnelling of which is activated via photo-excitation. The strength of this latter state is also maximal close to 1/8 doping, as are the stripes themselves. The equilibrium superconductor and the photo-excited PDW may well compete rather than cooperate with each other, similar to how state charge and spin orders compete with 3D superconductivity at equilibrium.

In conclusion, the results reported above set new constraints on the overall origin of light-induced superconductivity in single-layer cuprates, which appears to emerge from the

photo-excited stripe phase and is perhaps not easily explained as simple optical melting of the stripes.

6. Measuring the nonlinear Josephson voltage in striped LBCO

6.1 Modelling voltage response in non-perturbative regime

When a Josephson junction is driven to such large phase excursion amplitudes that the phase is no longer trapped in a local potential well but is rather able to cross the barrier into neighbouring minima, exotic dynamics is expected in addition to the usual nonlinear effects discussed in the previous chapter. In order to quantitatively model the response in the so-called "non-perturbative" regime, a similar approach to that employed by (Rajasekaran, Okamoto et al. 2018) is taken.

Consider a sample consisting of a series of semi-infinite layers stacked along the z direction with the extended dimension along the x direction. The interface between the sample and free space is located at x = 0 (not to be confused with hole concentration). Translational invariance along the y direction is assumed and the spatial and temporal evolution of the Josephson phase is described by the one-dimensional sine-Gordon equation

$$\frac{\partial^2\varphi(x,t)}{\partial t^2} + 2\gamma\frac{\partial\varphi(x,t)}{\partial t} + \omega_{JPR}^2 \sin\varphi(x,t) = \frac{c^2}{\varepsilon}\frac{\partial^2\varphi(x,t)}{\partial x^2}$$

where ω_{JPR} is the plasma frequency, c the speed of light, ε the relative dielectric function, and γ a damping factor accounting for the quasiparticle tunnelling current.

Next, consider an incident THz pulse with an oscillatory electric field polarised along the z direction of the form $E(t) = E_0 e^{-t^2/\tau^2} sin(\omega_{drive} t)$, where E_0 is the amplitude, τ the pulse duration, and ω_{drive} the frequency. Propagation of the pulse in free space is not modelled,

but instead the pulse enters the calculation as a time-dependent electric field present only at $x = 0$. By the requirements of continuity of the electric and magnetic fields across the interface, namely

$$E_i + E_r = E_t$$

$$H_i + H_r = H_t$$

where the subscripts i, r, t denote the incident, reflected, and transmitted components of the fields. Combining these with the Josephson equations relating the phase gradients in space and time to the electric and magnetic fields, the following boundary condition can be derived

$$\left.\frac{\partial\varphi(x,t)}{\partial t}\right|_{x=0} - c\left.\frac{\partial\varphi(x,t)}{\partial x}\right|_{x=0} = 2\omega_{JPR}\frac{E(t)}{E_c}$$

with $E_c = \Phi_0\omega_p/(2\pi d)$, where Φ_0 is the flux quantum and d the distance between adjacent superconducting layers. Essentially, the driving field creates a gradient of the phase on the surface in time and space, which then propagates deeper into the bulk.

To numerically solve the 1D sine-Gordon equation, the finite difference method is used (implemented in MATLAB. See Appendix C). A large 2D mesh grid is created with step sizes to $\Delta x = 1$ um and $\Delta t = 4$ fs. These values have been tested to ensure numerical stability and divergence of the iterative algorithm. Figure 6-1 shows a typical response of the Josephson phase to a weak driving field, along with a line cut on the surface of the sample.

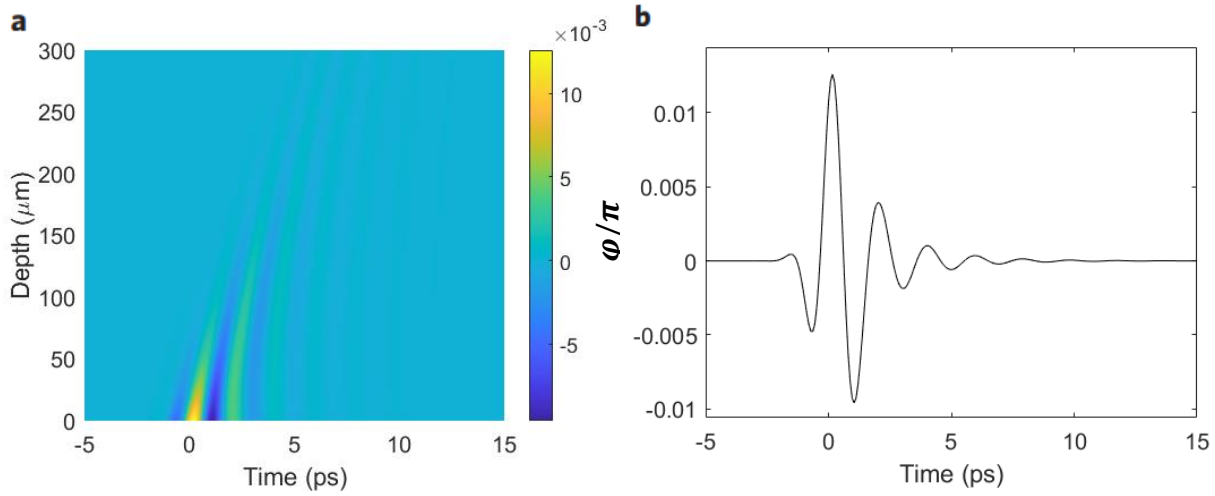

Figure 6-1: Numerical solution to the sine-Gordon equation. (a) Calculated Josephson phase $\varphi(x,t)$ as a function of time and depth in response to a small-amplitude electric field (1 kV/cm peak field) impinging on the surface. (b) Line cut of the phase on the surface $\varphi(x=0,t)$.

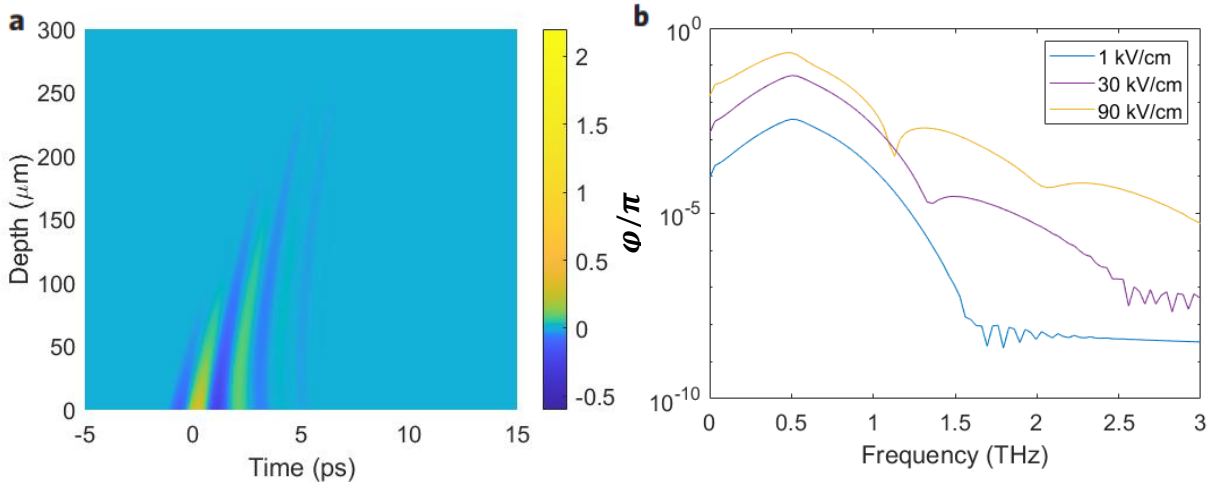

Figure 6-2: Numerical solution to the sine-Gordon equation. (a) Calculated Josephson phase $\varphi(x,t)$ as a function of time and depth in response to a medium-amplitude electric field (30 kV/cm peak field) impinging on the surface. (b) Fourier spectra of the Josephson phase for three incident field amplitudes.

In this case, the incident electric field amplitude is small, producing nothing more than a Josephson plasma wave propagating into the material, because in the linear approximation, the sine-Gordon equation reduces to a damped wave equation. It should be noted that, the phase oscillation in the aftermath of the driving field depends on damping in the sine-Gordon equation. While no direct measurement of this quantity is available, it can be estimated by the equivalent resistance and capacitance from geometric considerations. Here, the value of the damping coefficient is used as a free fitting parameter, but is found to take values on the same order of magnitude as the estimation described above.

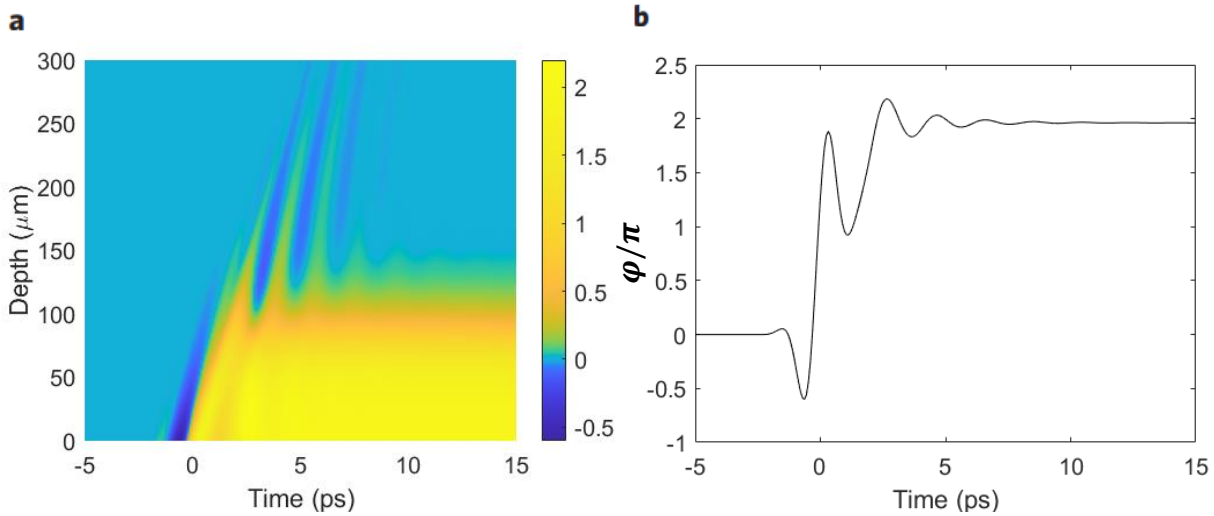

Figure 6-3: Numerical solution to the sine-Gordon equation. (a) Calculated Josephson phase $\varphi(x,t)$ as a function of time and depth in response to a high-amplitude electric field (160 kV/cm peak field) impinging on the surface. A region close to the surface of slipped phase remains after the pulse has propagated into the bulk. Line cut of the phase on the surface $\varphi(x=0,t)$.

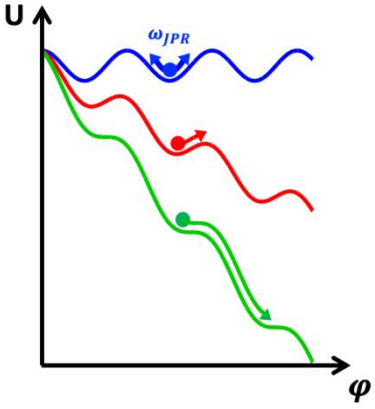

Figure 6-4: The three different regimes of excitation can be visualized in terms of a Josephson junction under the effect of a current bias, characterized by a tilted washboard potential. Each value of the electric field carried by the pulse corresponds to a certain tilting amplitude. Depending on the peak electric field, different regimes can be explored, starting from the linear one (blue), characterized by a response at the Josephson plasma frequency, ω_{JPR}, to a nonlinear perturbative regime (red), until approaching the critical current (green), a condition in which one expects to observe phase slips.

As the incident field amplitude is slowly increased, the Josephson phase is driven away from the equilibrium position at the minimum of the washboard potential, and the nonlinearity from the anharmonic potential landscape starts to manifest itself most notably in terms of high harmonic generation (see Figure 6-2). This is the result of higher order terms in the expansion of the sine term, as discussed in detail in Section 4.4.3 and experimentally verified by (Rajasekaran, Okamoto et al. 2018).

Further increasing the driving field strength, however, pushes the phase excursion into a regime less studied than before. As discussed in the previous chapter, it is possible to tilt the washboard potential landscape to such a large extent that the energy barrier between neighbouring minima no longer exists, and the phase escapes from the initial minimum and "slips" by integer multiples of 2π, before becoming trapped again when the potential landscape is restored (see Figure 6-4). This can be readily seen in Figure 6-3 below where a considerable portion of the sample has seen the phase slip to a new minimum at 2π away from the initial location at zero. The line cut at the surface also shows clearly the effect of the phase slip.

The Josephson phase, however, is not a directly measurable quantity. In order to detect the occurrence of such a phase slip, one option is to measure the instantaneous voltage drop that develops across the Josephson junction. As discussed extensively in the previous chapter, the voltage is proportional to the rate of change of the phase and could offer hints of such dramatic response.

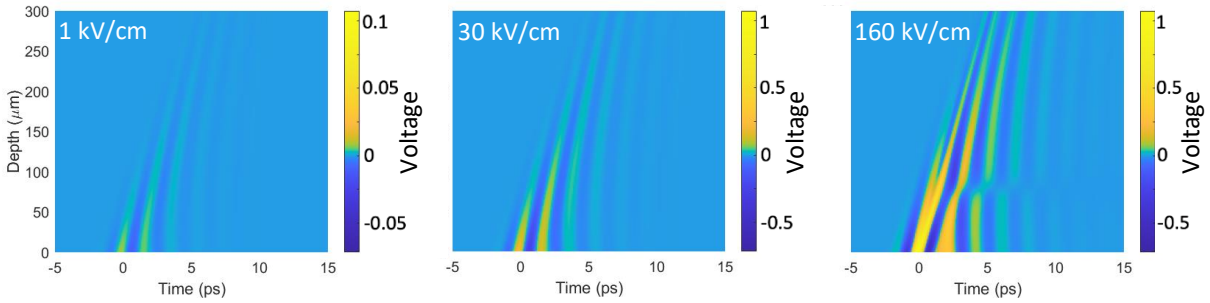

Figure 6-5: Calculated voltage drop across the Josephson junction for three amplitudes of incident electric field.

As shown in Figure 6-4, the voltage profile displays features in the phase slip scenario not seen in other regimes. This can be understood qualitatively by considering the fact that when the phase crosses over to neighbouring minima of the washboard potential, the equilibrium position shifts from 0 to 2π as a "one-way" displacement, giving rise to a large transient net voltage, while at lower driving amplitudes all the phase does is oscillating around the zero position, and the velocity of the motion is expected to scale simply as the driving field.

This discrepancy is best illustrated by looking at the frequency spectrum of the voltage profile at the surface, i.e. at x = 0. The dominant contribution is centred at 0.5 THz, the frequency of the driving field, while at intermediate fields an additional peak develops around 1.5 THz, corresponding to the third harmonic frequency of the drive. As a phase slip occurs, the amplitude of the peak at the fundamental frequency shows a dramatic jump, as shown in Figure 6-6. Qualitatively, this is expected because as the phase slips down the potential hill

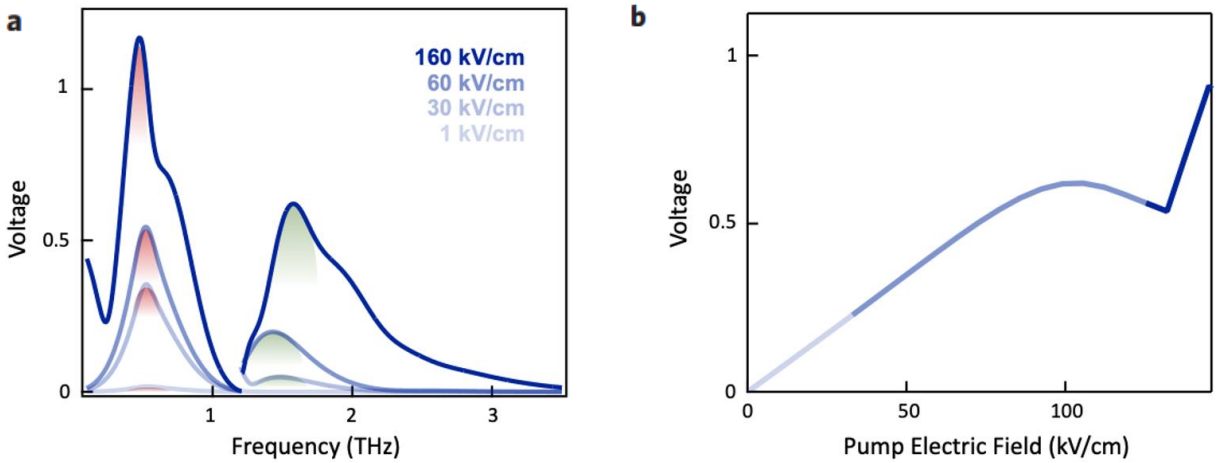

Figure 6-6: (a) Fourier transforms of the voltages in Figure 6-5, calculated at the junction boundary (x = 0) for different peak electric field values. The peaks at $\sim\omega_{drive}$ and $\sim 3\omega_{drive}$ are shaded in red and green, respectively. For a better visualization of the high harmonic components, all spectra at ω > 1.2 THz have been multiplied by 30. (b) THz electric field dependent voltage, estimated at the peak frequency in (a) by scanning peak electric field continuously. A marked jump indicative of a phase slip is apparent.

after it enters the adjacent valley, its motion contributes extra spectral weight and hence serves as a clear signature of such a phase slip.

6.2 Second harmonic generation as a probe of interlayer voltage

With the abrupt jump in voltage identified as a key signature of a Josephson phase slip, it is imperative to choose an experimental technique up to the task of detecting such an effect. In order to have temporal resolution on the order of the 100 fs, an optical probe is fitting. In particular, because LBCO is a centro-symmetric material, its second order nonlinear susceptibility tensor $\chi^{(2)}$ is zero, implying there would be no static second harmonic generation through a second order process in equilibrium. The lack of a static background second harmonic makes the Electric Field Induced Second Harmonic (EFISH) a sensible choice as the probing technique.

In conventional optics, a polarization $P(\omega)$ is induced in a material by an applied optical field $E(\omega)$ that scales linearly with the strength of the electric field, i.e. $P(\omega) \propto \chi^{(1)}E(\omega)$, where $\chi^{(1)}$ is known as the linear susceptibility. In nonlinear optics, the induced polarisation contains higher order terms and can be expressed as a power series in the electric field strength as

$$P(t) = \varepsilon_0[\chi^{(1)}E(t) + \chi^{(2)}E^2(t) + \chi^{(3)}E^3(t) + \cdots]$$

where $\chi^{(2)}$ and $\chi^{(3)}$ are the second and third order nonlinear susceptibilities, respectively. Conveniently, the polarisation can also be written as a sum of nonlinear polarisations as

$$P(t) = \varepsilon_0[P^{(1)}(t) + P^{(2)}(t) + P^{(3)}(t) + \cdots]$$

where ε_0 is the permittivity of free space, and $P^{(2)}$ and $P^{(3)}$ can be referred to as the second and third order nonlinear polarisations, respectively. In materials that display inversion symmetry, $\chi^{(2)}$ vanishes identically, such as LBCO as mentioned above. Third order nonlinear effects described by $\chi^{(3)}$, on the other hand, can occur in both centrosymmetric and non-centrosymmetric media.

For an applied field of the form $\tilde{E}(t) = Ee^{-i\omega t}$, the second order nonlinear polarisation induced can be calculated as

$$\tilde{P}(t) = \varepsilon_0\chi^{(2)}E^2(t) = 2\varepsilon_0 x^{(2)}EE^* + (\varepsilon_0 x^{(2)}E^2e^{-2i\omega t} + c.c.)$$

Here, it is obvious that the first term is a dc contribution at zero frequency, while the terms in the parentheses produce a frequency-doubled component, at the second harmonic frequency of the fundamental wave.

As mentioned above, the second order susceptibility in LBCO is forbidden by symmetry, implying the above second harmonic generation process cannot take place. However, the EFISH, a third order nonlinear process, is still possible. First proposed in the early 1960s (Terhune, Maker et al. 1962), the EFISH describes the interaction between two optical photons and a relatively low, or zero, frequency electric field, in which the induced polarisation has a frequency very close to the second harmonic of the ingoing optical field. It can be expressed as

$$\tilde{P}(2\omega_1 \pm \omega_2) \propto \chi^{(3)} E_1^2(\omega_1) E_2(\omega_2)$$

where E_1 and E_2 are the interacting electric fields with frequencies ω_1 and ω_2, respectively, and $\omega_1 \gg \omega_2$.

Here, E_2 is expected to consist of two main contributions, the pump THz field and the Josephson voltage drop, i.e. $E(t) = V(t)/d$. The pump field spans in frequency from ~0.1 THz to ~1.5 THz, and the generation technique will be discussed in detail in the next section. This effect has a weak dependence on temperature and is a dominant component in the detected SHG intensity. The Josephson voltage drop, on the other hand, comes from the strongly driven Josephson phase dynamics discussed in the previous section, and is expected to be present only below the superconducting transition temperature, because tunnelling supercurrent in the microscopic Josephson junctions requires Cooper pairs as charge carriers.

The EFISH serves as a way of sampling an instantaneous electric field with temporal resolution limited by the duration of an optical probe pulse. Because E_2 here tends to be on the picosecond time scale in this experiment (ω_2~0.1-3 THz), a probe pulse of ~100 fs duration is sufficiently short. By varying the time delay between the pump pulse and the probe pulse, the full pump-induced dynamics can be mapped out in time domain. Because the probe wavelength used in this experiment is 800 nm, with a penetration depth of ~100 nm, while the THz pump induces changes over a length scale of many μm, the probe can be approximately considered to be surveying a homogeneously excited region in the sample, eliminating the need to take into account possible penetration depth mismatch.

6.3 THz generation with the tilted pulse front technique

Conventionally, the concept of a "terahertz gap" exists because bright sources of radiation in the 0.1-10 THz range were technologically difficult to realise. Crystals with strong nonlinear optical susceptibility such as zinc telluride (ZnTe) could generate THz pulses on the order of nanojoule (nJ) energy through optical rectification, but these are inadequate for creating peak electric fields in tens of kilovolts per centimetre (kV/cm) needed to study nonlinear Josephson dynamics discussed in Section 6.1.

One alternative that has become more accessible in recent years is Free Electron Lasers (FEL). They are large-scale facilities that generate coherent, high power radiation based on spatial modulation of the motion of high-energy electrons. Narrowband, tuneable THz radiation can be produced, and is useful for selective excitation of certain modes in a material with fine spectral resolution.

In the present experiment, a table-top method is employed to generate broadband, single cycle THz pulses with energy up to several microjoule (μJ) using the so-called "tilted pulse front" technique in lithium niobate ($LiNbO_3$). Compared to other nonlinear crystals like ZnTe, lithium niobate has a much large nonlinear susceptibility coefficient, which allows for more efficient conversion of 800 nm photons into THz. A second major advantage of lithium niobate is a large band gap; the small band gap in ZnTe leads to two-photon absorption when the intensity of 800 nm pump pulses is high and limits the conversion efficiency. This is prevented in lithium niobate and hence much higher excitation power can be used.

The key to efficient generation of THz is phase matching between the 800 nm pump photon and the generated THz photon, and because of the orders of magnitude difference in frequency, this is often difficult as the refractive index differs considerably between the two frequencies; in lithium niobate, the difference in phase velocity is more than a factor of two (Hebling, Almási et al. 2002). One solution is to tilt the intensity front of the near infrared beam by a certain angle γ, such that the phase matching condition is modified and can be fulfilled easily, i.e.

$$v_{NIR}^{group} \cos\gamma = v_{THz}^{phase}$$

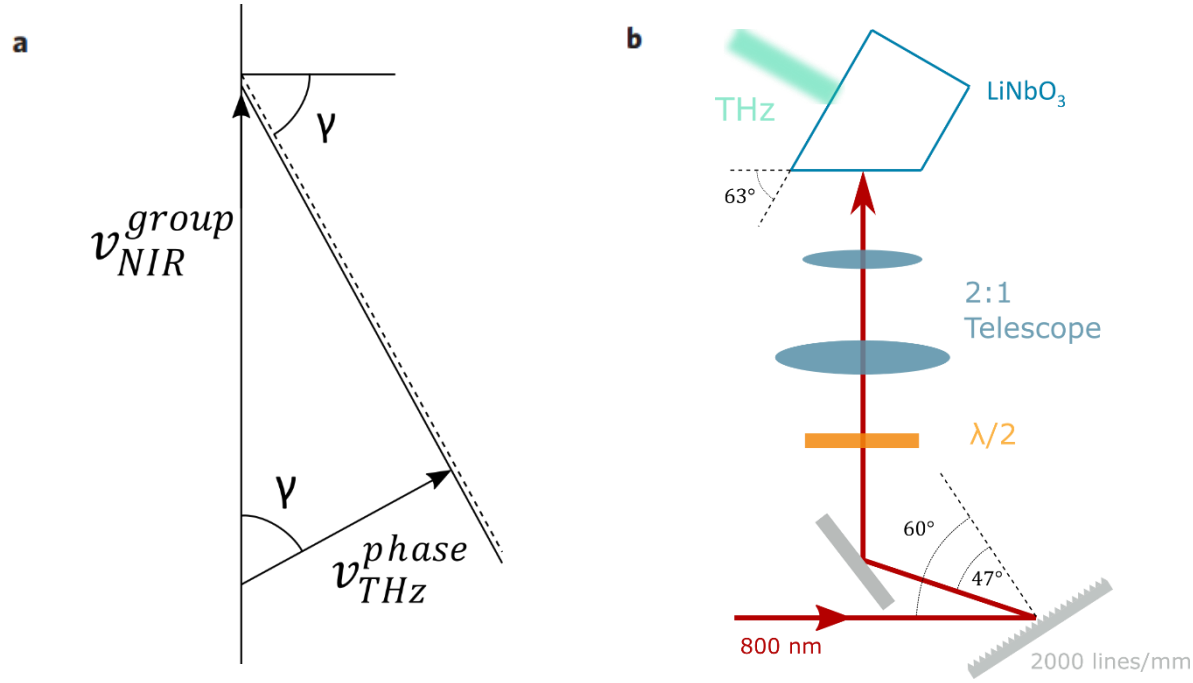

Figure 6-7: Tilted pulse front generation of THz radiation. (a) Phase matching condition for the NIR group velocity and THz phase velocity can be satisfied when the angle between the wave vectors is at angle $\gamma \sim 63°$. (b) Experimental setup for tilted pulse front generation.

For lithium niobate, the optimal angle γ is found to be ~63° [see Figure 6-7 (a)]. However, this angle is reduced when the NIR pulse enters the crystal from free space according to

$$n_{NIR} \tan\gamma = \tan\gamma'$$

where n_{NIR} is the refractive index at 800 nm in lithium niobate. Therefore, a tilt angle of $\gamma' \sim 78°$ is needed, and can be easily achieved by diffracting the beam off a grating (Bor, Racz et al. 1993). For a wavelength of 800 nm, a blazed grating with 2000 lines/cm is chosen. The beam is set to be p polarised to minimise loss at the grating, and is subsequently rotated by a half-wave plate to s polarisation before entering the crystal to make use of the highest electro-optic tensor component. Furthermore, because the grating introduces angular dispersion after diffraction, which leads to decreased pulse front tilt and lengthened pulse duration, a 2:1 telescope is included to create an image of the beam spot, which means that the transverse size of the beam is reduced by demagnification while the delay between the two sides of the beam remains that created by the grating, effectively compensating for the decrease in tilt angle (Hebling, Yeh et al. 2008).

As illustrated in Figure 6-7 (b), the 800 nm beam is directed onto the grating and diffracted, then it goes through a half-wave plate and gets imaged onto the lithium niobate

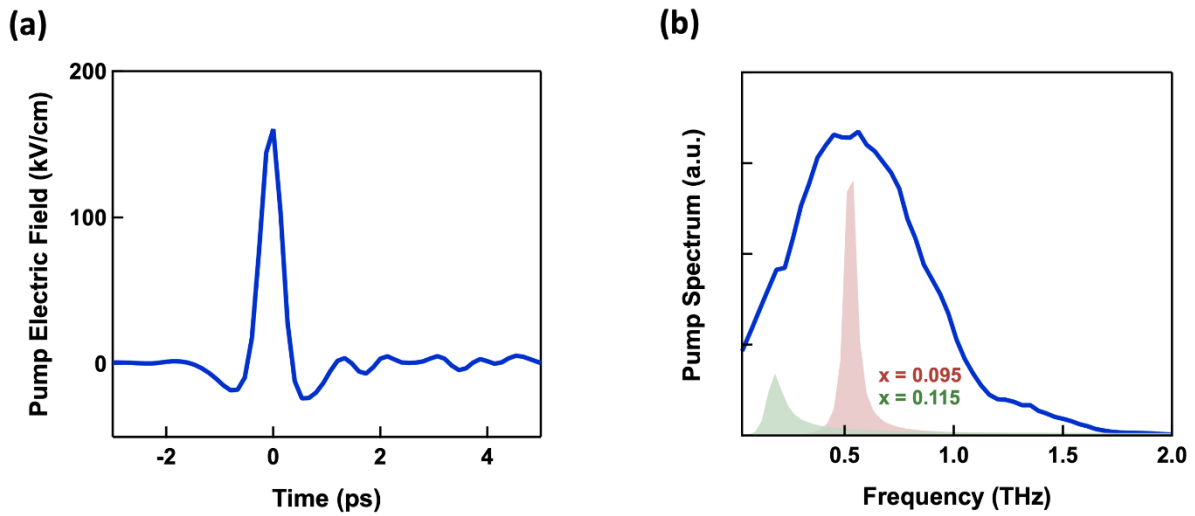

Figure 6-8: Intense THz pump pulse. (a) Time trace of THz electric field measured by electro-optic sampling. (b) Fourier transform of the THz pulse centres at 0.5 THz; equilibrium loss function in the superconducting state for two LBCO samples is superimposed for comparison (see Section 6.4 for detail).

crystal by a telescope, and finally THz radiation comes out from the side of the crystal cut at the 63° angle. A special layer of anti-reflection coating is applied on the out-coupling surface of the crystal, which serves as a buffer layer with a refractive index valued between the crystal and air at the THz frequency. The THz pulse can be measured through electro-optic sampling by another weak 800 nm gate pulse, and the time-resolved electric field as well as the frequency spectrum are shown in Figure 6-8. The ringing in the time trace beyond ~1 ps is the result of absorption and re-radiation by water vapour in air, which goes away if the environment is evacuated to below 1 mbar or purged by a constant flow of nitrogen gas.

The pulse energy of the generated THz radiation can be determined with a calibrated pyro-electric detector. Placed right at the out-coupling side of the lithium niobate crystal, the detector measures up to 6 μJ for ~3 mJ of NIR input at 1 kHz repetition rate.

The THz beam is collimated after exiting the crystal, propagated through a pair of wire grid polarisers, and focused onto the LBCO samples by a gold coated parabolic mirror. The generated THz radiation is s polarised, and the second polariser is set to ensure s polarisation. By rotating the first polariser, the THz intensity can be continuously varied. The THz beam is focused down to a spot of ~1.5 mm diameter on the sample surface, achieving a peak electric field of ~160 kV/cm.

6.4 Josephson phase slips in striped LBCO

In this experiment, again, LBCO samples of two nominal dopings are studied: x = 9.5% (LBCO 9.5%) and x = 11.5% (LBCO 11.5%). The former has weak stripe order coexisting with the equilibrium superconducting state with a relatively high T_C, coinciding with the charge- and spin-order transition temperatures $T_c \cong T_{co} \cong T_{so} \cong 32$ K. The x = 11.5% sample, being much closer to the anomalous 1/8 doping, has a much more robust stripe order with $T_{co} \cong 53$ K and $T_{so} \cong 40$ K, suppressing the superconducting transition significantly, with $T_c \cong 13$ K.

The optical setup uses an amplified Ti:sapphire laser as the source, which outputs 3.5 mJ, 100 fs pulses of 800 nm wavelength at 1 kHz repetition rate. The full beam is split into two parts of proportion 99:1, where the 99% is used for THz pump generation by the tilted pulse front technique, and the 1% serves as the probe beam for EFISH generation, the details of both of which have been discussed in Sections 6.2 and 6.3. The relative time delay between the pump and probe pulses is controlled by a delay stage. After interacting with pump on the sample, the reflected probe is directed to a photomultiplier detector, in front of which there are two 400 nm band pass filters to reduce noise from other wavelengths. The output of the photomultiplier is fed into a lock-in amplifier, which isolates the pump-induced signal by integrating away noise components at other frequencies. A schematic of the setup is shown in Figure 6-9.

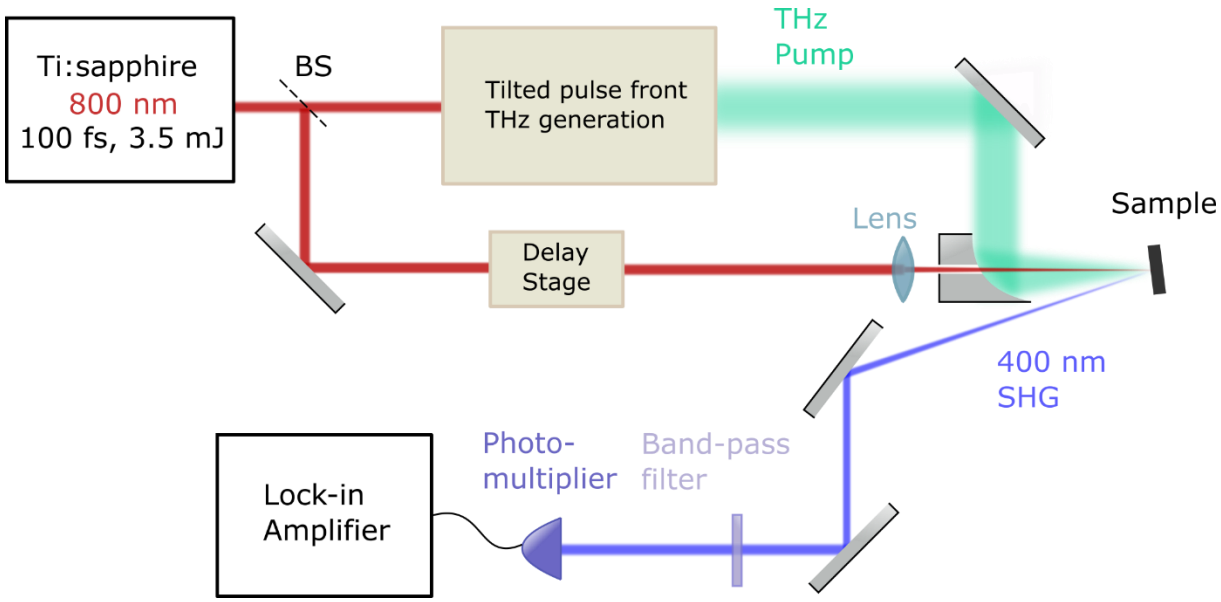

Figure 6-9: Schematic of the experimental setup.

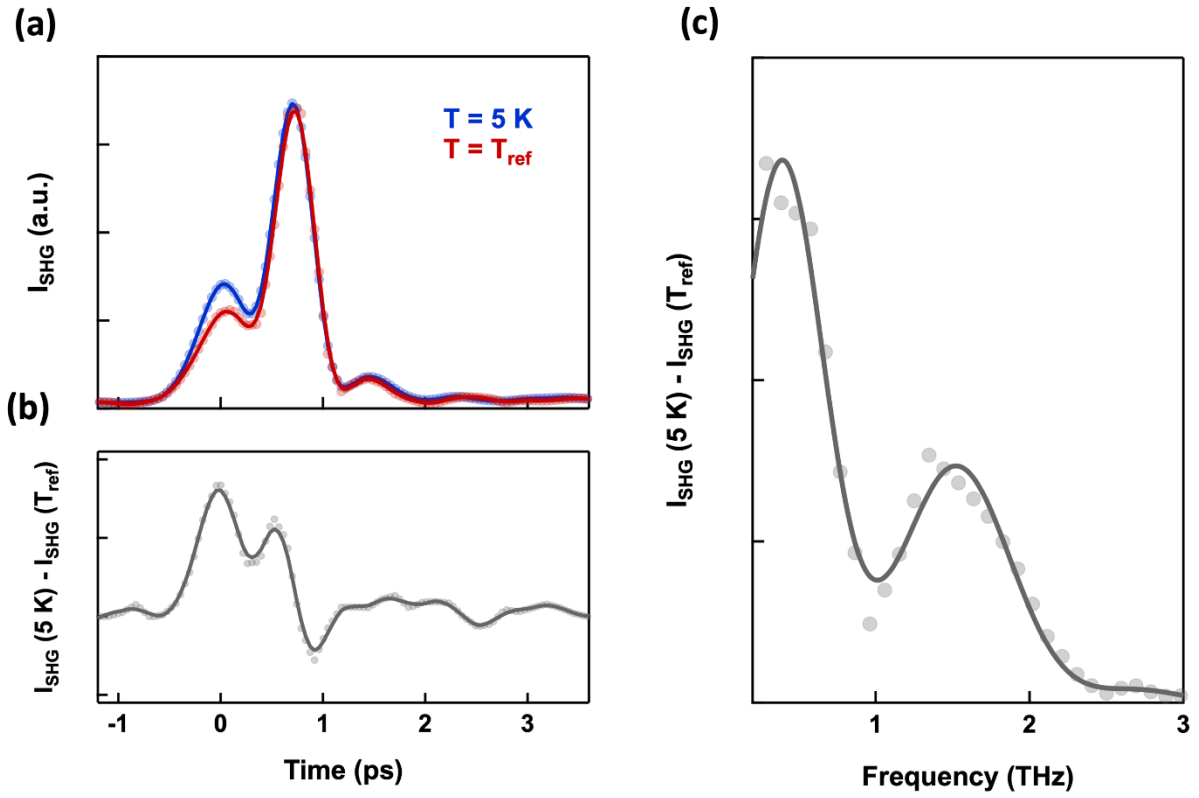

Figure 6-10: (a) Time-dependent Electric Field Induced Second Harmonic (EFISH) signal measured in $La_{1.905}Ba_{0.095}CuO_4$ at T = 5 K < T_C (blue) and at the reference temperature T_{ref} = 50 K for a THz peak electric field of ~160 kV/cm. (b) Normalized EFISH signal, obtained by subtracting the two curves in (a) in time domain. (c) Frequency-dependent normalized EFISH response, obtained by Fourier transforming the curve in (b).

In order to eliminate the effect of any slowly varying component in the signal unrelated to the pump-induced change in the sample, for instance the accumulation of a thin ice layer on the sample surface at low temperature, a special measuring procedure is employed as follows: 1) scans are acquired at one temperature over a period of time where the signal has not deteriorated considerably; 2) warm up the sample to room temperature to melt away any accumulated ice; 3) rapidly cool down to a different temperature; 4) repeat the first three steps for all temperature points of interest as one round of measurements; 5) repeat the first four steps multiple times to ensure reproducibility.

In Figure 6-10 (a), two typical time traces of the EFISH signal are plotted, one in the superconducting state of the sample and one in the normal state at a reference temperature, which is chosen for each sample to be above all relevant temperatures in that sample such that the signal is no longer temperature dependent, i.e. $T_{ref} = 50\ \mathrm{K} > T_C, T_{SO}, T_{CO}$ for LBCO 9.5% and at $T_{ref} = 70\ \mathrm{K} > T_C, T_{SO}, T_{CO}$ for LBCO 11.5%.

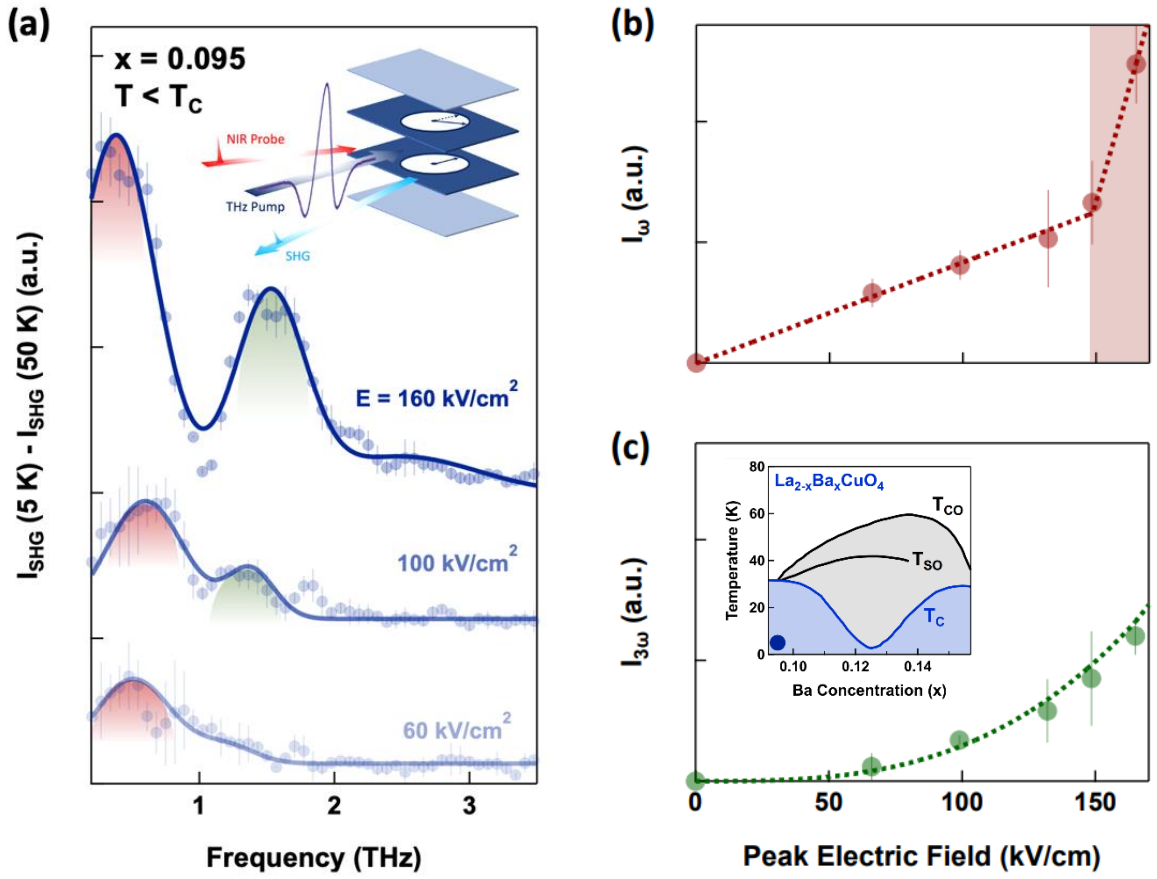

Figure 6-11: (a) Fourier transform of the second harmonic intensity measured in superconducting $La_{1.905}Ba_{0.095}CuO_4$ at T = 5 K < T_C for different THz peak driving fields (see legend), after subtraction of the same quantity measured at T > $T_C \simeq T_{SO} \simeq T_{CO}$. The spectra have been vertically offset maintaining their relative amplitude. Uncertainty bars are standard errors estimated from different measurement sets. The peaks at $\sim\omega_{drive}$ and $\sim 3\omega_{drive}$ are shaded in red and green, respectively, to recall the color code of panels (b) and (c). Inset: Schematic of the experimental geometry, in which a single cycle THz pulse polarized along the out-of-plane crystallographic c direction is shone onto the sample surface together with a near-IR probe pulse (also polarized along c). The radiation generated at the second harmonic of the probe is then detected. The clocks in the layers represent amplitude (diameter) and phase (hand angle) of the superconducting order parameter. (b) Peak electric field dependence of the $\sim\omega_{drive}$ spectral component. Error bars are extracted here from the multi-Gaussian fits in (a). Dashed lines are linear guides to the eye, while the red shading highlights the phase slip regime. (c) Same quantities as in (b), extracted for the $\sim 3\omega_{drive}$ component. Here the dashed lines are $\propto E^3$ fits. The vertical scales in (b) and (c) are mutually calibrated. Inset: Temperature-doping phase diagram of $La_{2-x}Ba_xCuO_4$, where the exact location of the investigated compounds is indicated by blue circles. Here, T_{CO}, T_{SO}, and T_C are the charge-order, spin-order, and superconducting transition temperature, respectively.

In this example, the time trace at $T_{ref} = 50$ K is subtracted from that at 5 K in order to eliminate the temperature independent background and isolate the contribution pertaining to the superconducting order, and the difference in plotted in Figure 6-10 (b). Next, this is Fourier transformed to obtain the frequency spectrum, shown in Figure 6-10 (c).

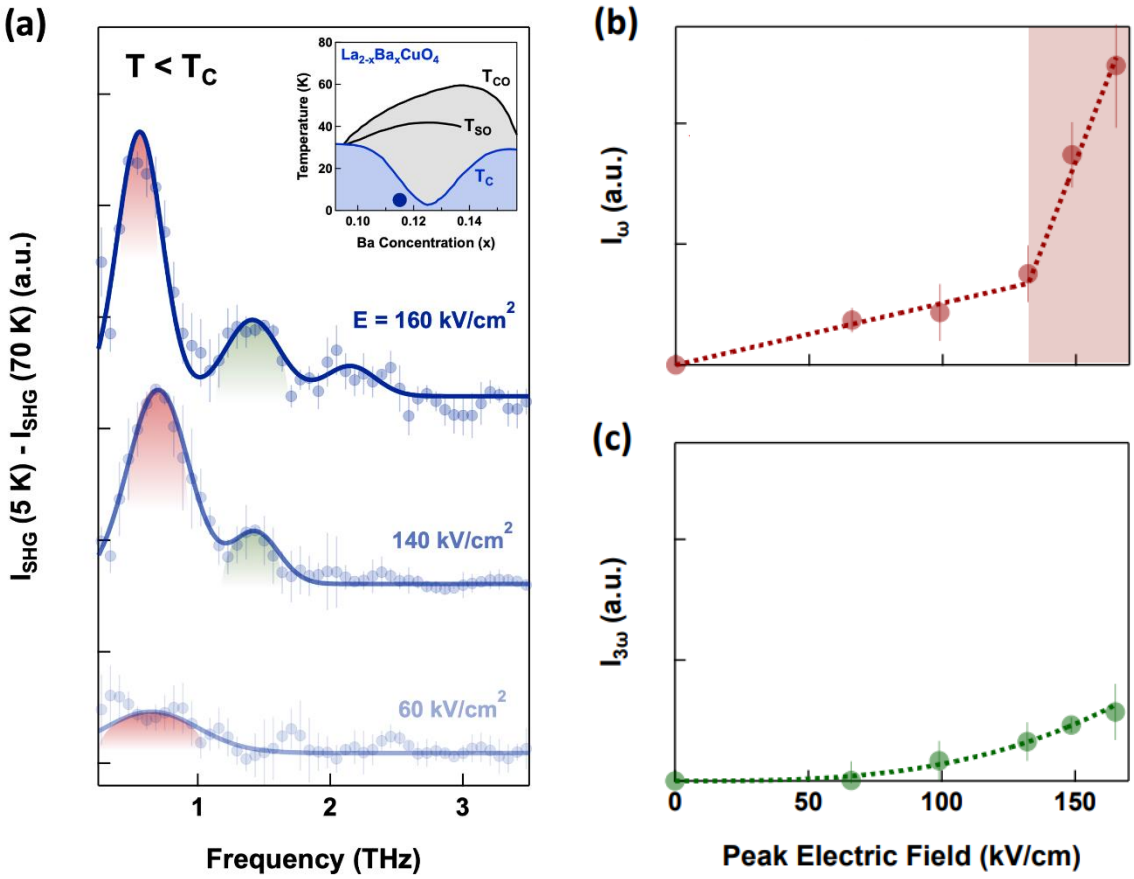

Figure 6-12: (a) Fourier transform of the second harmonic intensity measured in superconducting $La_{1.885}Ba_{0.115}CuO_4$ at T = 5 K < T_C for different THz peak driving fields, after subtraction of the same quantity measured at T > T_C, T_{SO}, T_{CO}. The spectra have been vertically offset maintaining their relative amplitude. Uncertainty bars are standard errors estimated from different measurement sets. The peaks at $\sim\omega_{drive}$ and $\sim 3\omega_{drive}$ are shaded in red and green, respectively, to recall the color code of panels (b) and (c). Inset: Temperature-doping phase diagram of $La_{2-x}Ba_xCuO_4$, where the exact location of the investigated compounds is indicated by blue circles. Here, T_{CO}, T_{SO}, and T_C are the charge-order, spin-order, and superconducting transition temperature, respectively. (b) Light red: Peak electric field dependence of the $\sim\omega_{drive}$ spectral component. Error bars are extracted here from the multi-Gaussian fits in (a). Dark red: Same quantity, measured in $La_{1.885}Ba_{0.115}CuO_4$ at T = 5 K < T_C, T_{SO}, T_{CO}. Dashed lines are linear guides to the eye, while the red shading highlights the phase slip regime. (c) Same quantities as in (b), extracted for the $\sim 3\omega_{drive}$ component. Here the dashed lines are $\propto E^3$ fits. The vertical scales in (b) and (c) are mutually calibrated.

In Figure 6-11 (a), the results of measurements as a function pump electric field strength following the same procedures as described above are shown. Two major components are observed: a large peak centred at ~0.5 THz (shaded red) and a smaller peak centred at ~1.5 THz (shaded green). The former corresponds to the fundamental frequency of the THz pump field $\omega_{drive} \simeq 0.5$ THz, while the latter appears only at high field strengths and is consistent with the third harmonic frequency $3\omega_{drive} \simeq 1.5$ THz. At the highest field $E_{peak} = 160$ kV/cm, a small contribution at $5\,\omega_{drive} \simeq 2.5$ THz can also be seen. The

frequencies of these contributions do not depend on E_{peak}, except for a small redshift of the fundamental peak at very high fields.

To obtain the magnitude of the fundamental and third harmonic components as a function of peak electric field, a multi-Gaussian fit is carried out for each measurement. The fitting function is a sum of three Gaussians and a constant offset, and from the fits the amplitude of each Gaussian term is extracted.

The interesting feature lies in the electric field dependence of different components in the EFISH signal. While the third harmonic contribution follows a power scaling as $\propto E_{peak}^3$ [see Figure 6-11 (c)], the fundamental peak follows a linear dependence for low fields but

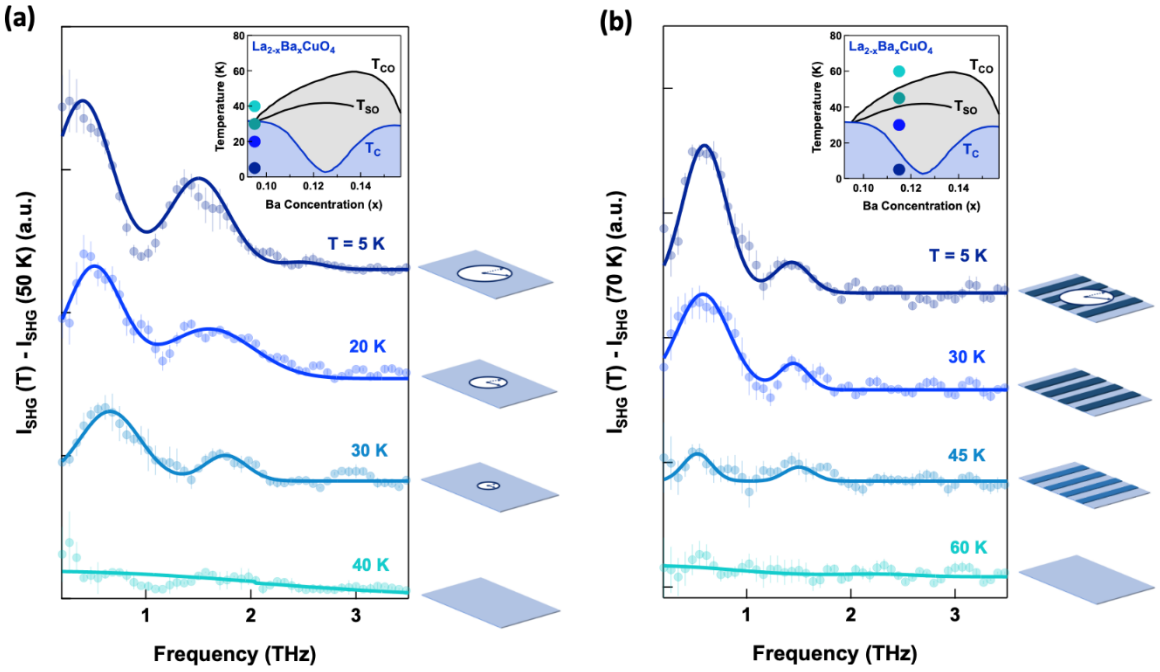

Figure 6-13: (a) Fourier transform of the second harmonic intensity measured in $La_{1.905}Ba_{0.095}CuO_4$ at different temperatures, for a peak THz field of ~160 kV/cm, after subtraction of the same quantity measured at T = 50 K > T_C. The spectra have been vertically offset maintaining their relative amplitude. Uncertainty bars are standard errors estimated from different measurement sets. Inset: Temperature-doping phase diagram of $La_{2-x}Ba_xCuO_4$, where the measured temperatures are indicated by circles (T_{CO}, T_{SO}, and T_C are the charge-order, spin-order, and superconducting transition temperature, respectively). The graphics on the right represent the progressive reduction of the amplitude of the superconducting order parameter (clock diameter) with increasing temperature and its disappearance above T_C. (b) Same quantity as in (a) measured in $La_{1.885}Ba_{0.115}CuO_4$ at different temperatures across T_C, T_{SO}, and T_{CO} for a ~160 kV/cm driving field. Normalization is done here by T = 70 K > T_C, T_{SO}, and T_{CO}. Inset: Temperature-doping phase diagram as in (a). The graphics on the right represent the disappearance of the macroscopic superconducting order parameter (clock) when crossing T_C, as well as the gradual fainting of the stripe order, which coexists with superconductivity at T < T_C and survives all the way up to T = T_{CO}.

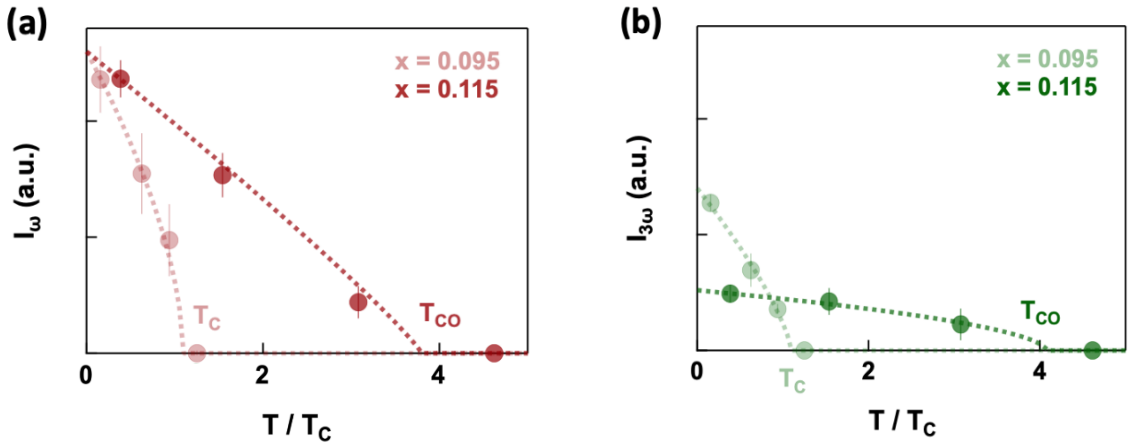

Figure 6-14: (a) Temperature dependence of the $\sim\omega_{drive}$ spectral component in the second harmonic intensity measured for both $La_{1.905}Ba_{0.095}CuO_4$ (light red) and $La_{1.885}Ba_{0.115}CuO_4$ (dark red), for a constant THz peak driving field of ~160 kV/cm. Error bars are extracted from multi-Gaussian fits to the experimental spectra in Figure 6-12, while dashed lines are mean field fits. The horizontal temperature axis has been normalized by the superconducting T_C of each compound. While for $La_{1.905}Ba_{0.095}CuO_4$ the response vanishes at $T_C = T_{CO} = 32$ K, in $La_{1.885}Ba_{0.115}CuO_4$ it persists well above $T_C = 13$ K, all the way up to $T_{CO} = 53$ K. (b) Same quantities as in (a), extracted for the $\sim 3\omega_{drive}$ component.

displays a dramatic jump around 150 kV/cm [see Figure 6-11 (b)]. This discontinuity in field scaling is reminiscent of that seen in the voltage drop simulation for a single Josephson junction discussed earlier in this chapter. Indeed, it is indicative of the occurrence of Josephson phase slips in the superconducting state of the sample, where the CuO_2 layers are coupled by coherent Josephson tunnelling and can be approximated as a large Josephson junction.

In the other doping, *x* = 11.5%, a similar effect is observed. As shown in Figure 6-12 (a), contributions at the fundamental frequency $\omega_{drive} \simeq 0.5$ THz, the third harmonic frequency $3\omega_{drive} \simeq 1.5$ THz, as well as possibly the fifth harmonic frequency $5\omega_{drive} \simeq 2.5$ THz (only at the highest field strength), are clearly visible. Furthermore, the scaling of amplitudes of the fundamental and third harmonic peaks with pump electric field shares a similar pattern as in the 9.5% doping: the fundamental displays a linear relation with peak field before a dramatic jump at high field strengths ($\geq$ 130 kV/cm), while the third harmonic follows a third power scaling with the peak THz field [see Figure 6-12 (b) and (c)]. Again, this behaviour is taken as a signature for the presence of a Josephson phase slip as seen in the other doping.

More interestingly, the temperature dependence of the EFISH signal diverges between the two dopings. For *x* = 9.5%, the two peak features in the Fourier spectrum reduces in magnitude as temperature rises and disappears when the superconducting $T_C \cong 32$ K is

crossed, as shown in Figure 6-13 (a). By contrast, for the *x* = 11.5% doping, the signal survives above $T_C \cong 13$ K all the way to roughly the charge order transition temperature $T_{co} \cong 53$ K, which is more than three times higher than T_C in this compound [see Figure 6-13 (b)]. As shown in Figure 6-14, this is quite reminiscent of the temperature dependence of third harmonic generation measured by nonlinear reflectivity in the same sample as discussed in Section 4.4.3 (Rajasekaran, Okamoto et al. 2018).

The presence of phase slips above T_C in the stripe phase of the 11.5% sample is further underscored by the electric field dependence of the EFISH signal at $T_c < T = 30\ \text{K} < T_{so}$. As

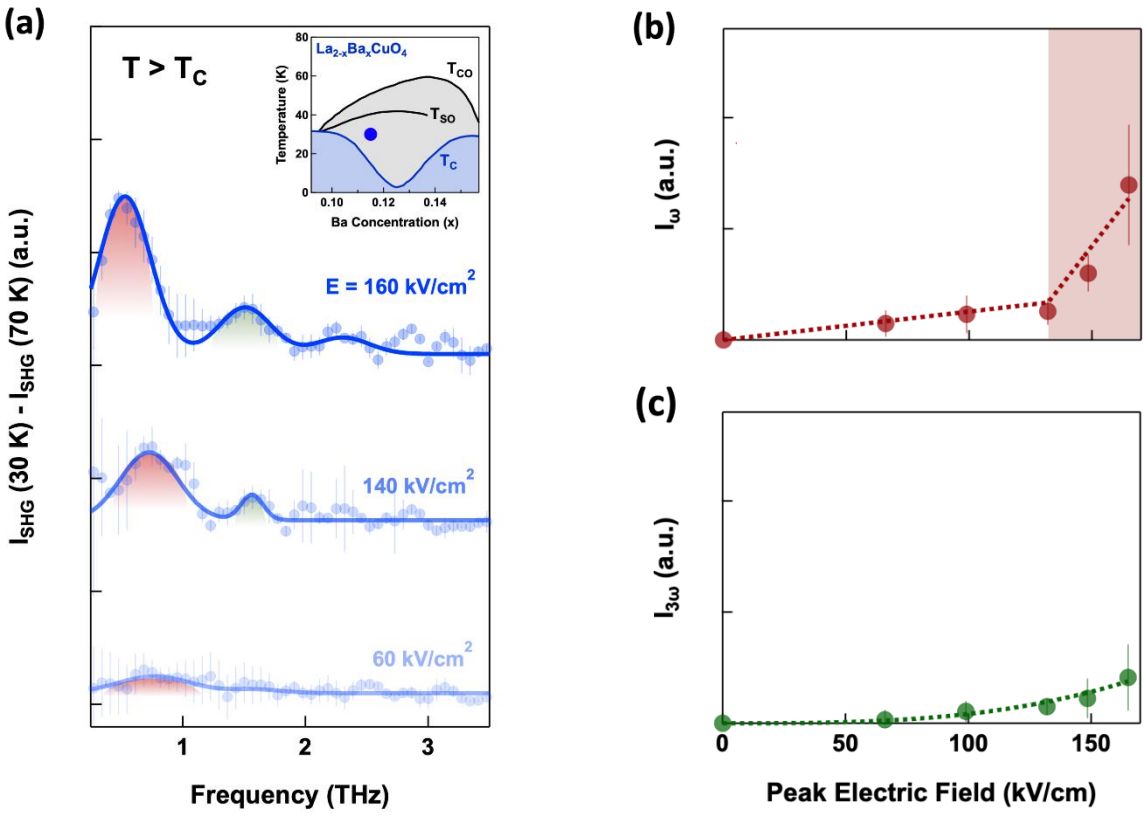

Figure 6-15: (a) Fourier transform of the second harmonic intensity measured in superconducting $La_{1.885}Ba_{0.115}CuO_4$ at T = 30 K > T_C for different THz peak driving fields, after subtraction of the same quantity measured at T > T_C, T_{SO}, T_{CO}. The spectra have been vertically offset maintaining their relative amplitude. Uncertainty bars are standard errors estimated from different measurement sets. The peaks at $\sim\omega_{drive}$ and $\sim 3\omega_{drive}$ are shaded in red and green, respectively, to recall the color code of panels (b) and (c). Inset: Temperature-doping phase diagram of $La_{2-x}Ba_xCuO_4$, where the exact location of the investigated compounds is indicated by blue circles. Here, T_{CO}, T_{SO}, and T_C are the charge-order, spin-order, and superconducting transition temperature, respectively. (b) Peak electric field dependence of the $\sim\omega_{drive}$ spectral component measured in $La_{1.885}Ba_{0.115}CuO_4$ at T_C < T = 30 K < T_{SO}, T_{CO}. Dashed lines are linear guides to the eye, while the red shading highlights the phase slip regime. (c) Same quantity as in (b), extracted for the $\sim 3\omega_{drive}$ component. Here the dashed lines are $\propto E^3$ fits. The vertical scales in (b) and (c) are mutually calibrated.

shown in Figure 6-15, the scaling of the amplitude of the fundamental peak in the frequency spectrum displays a very similar discontinuous jump when a certain threshold in pump field strength is crossed at ∼130 kV/cm, again suggestive of the same underlying origin of the voltage drop from Josephson phase slips. At almost three times T_C, tunnelling between Josephson coupled CuO_2 layers is no longer visible in linear THz spectroscopy measurements. Therefore, it should be surprising to see such a signal so closely resembling that in the superconducting state.

In light of the results of third harmonic generation by (Rajasekaran, Okamoto et al. 2018), the new observations can be interpreted as complementary evidence for interlayer coherence existing in the stripe phase as well as for pre-formed Cooper pairs that serve as tunnelling carriers. While the third harmonic generation can be explained by the nonlinear mixing of silent modes as discussed in Section 4.4.3, it is unclear that the model also accounts for the voltage drop as measured in this experiment. Although no comprehensive understanding has been formulated that reproduces the stripe phase response, and depinning and sliding of a charge density wave should be excluded as a possible mechanism, it is conceivable that fully activated Josephson tunnelling is a prerequisite of this response. Future theoretical and experimental effort should attempt to isolate the cause by studying different families of cuprate superconductors both in presence and absence of stripe orders.

7. Summary and outlook

This thesis is dedicated to the investigation of the emergence of superconducting behaviour from the normal state of $La_{2-x}Ba_xCuO_4$ in presence of the stripe order. Building upon previous experimental evidence suggestive of pre-existing superfluid inside the orthogonally aligned stripes, further studies are carried out to characterise the response of two dopings of particular interest under strong optical excitation.

At the beginning, a brief introduction to the phenomenon of superconductivity is given, covering the initial discovery followed up continual research identifying materials with ever increasing critical transition temperature. Then, early attempts at developing a theoretical model to describe the macroscopic phenomenology such as the London equations are discussed, and the ground-breaking BCS theory introduces the first microscopic model which provides a pairing mechanism for electrons to conduct without loss. Next, the so-called unconventional superconductivity bringing about unusually high T_C which the BCS theory cannot explain prompts a renewed drive to develop new understandings behind an ever-growing collection of compounds displaying superconducting properties in distinct ways. Further complicating the picture is the presence of a plethora of other ordered states commonly found in the phase diagram of unconventional superconductors, competing or coexisting with superconductivity in complex ways that may hold the key to a comprehensive theory. $La_{2-x}Ba_xCuO_4$ is one such system which provides a unique playground involving a combination of charge- and spin-ordered states to investigate their intricate interactions with superconductivity.

Then, a brief overview of several examples of optical control of superconductivity is given. Here, a common theme is the use of ultrafast laser pulses to perturb the cuprate superconductors both below and above T_C. Among different materials including LBCO and YBCO, enhanced coherence is detected in the superconducting state, but more interestingly, signatures of superconducting-like behaviour are also found in the normal state, often at

temperatures up to several times the equilibrium T_C. Some of these results can be understood through dynamic lattice distortions that favour superconductivity such as in YBCO, and others are consistent with the interpretation of the alleviation of suppression of superconducting coherence by competing orders such as in LBCO. They demonstrate the effectiveness of ultrafast optical excitation as a way of generating interesting dynamics and transient states inaccessible in equilibrium.

Subsequently, attention is turned to an introduction to the principles of the Josephson effect and the phenomenology of the Josephson junction, which serves as a basic building block for the c-axis electrodynamics of layered superconductors like the cuprates. When a Josephson junction is driven to large phase excursions, by an external current or electric field for example, nonlinear dynamics becomes pronounced in the optical response. A brief discussion of several experiments in cuprates is presented as examples of the nonlinear Josephson phase dynamics driven by intense THz radiation to different regimes. Moreover, these results highlight the utility of the sine-Gordon equation as a model for simulating the temporal and spatial evolution of the Josephson phase under strong excitation, as experimental data have been reproduced in good agreement by solving the sine-Gordon equation under different conditions.

In this context, the first experiment of this thesis focuses on characterising the transient superconducting state after photoexcitation in LBCO in presence of an external magnetic field. Previous experimental results suggest an intimate link between the stripe order found in this family of compounds and superconductivity, and the magnetic field provides a tuning knob to explore the nature of interaction between the two. Time-resolved pump-probe measurements point to a picture in which the light-induced superfluid stiffness along the c-axis is of a different origin from that of the equilibrium interlayer tunnelling. The much stronger pump-induced response from the doping with robust stripes is consistent with the pair-density-wave picture in which superconducting stripes frustrate tunnelling in equilibrium but can be excited by high-energy optical pulses to re-establish coherence across multiple unit cells. The role played by the magnetic field in strengthening the stripes further supports the observation that a more coherent superconducting state emerges from a stronger stripe order. The results can be interpreted as evidence for a fundamental difference between the homogenous condensate and a spatially modulated one.

The second experiment of this thesis builds on these ideas and takes one step further by considering an extreme case in which the Josephson phase is driven so far away from the initial equilibrium position that it is able to cross the potential barrier and slips to a different minimum in the washboard potential landscape. Again, this is predicted by the sine-Gordon equation by considering a long Josephson junction under excitation by an enormous electric field. However, the Josephson phase is not a directly measurable quantity, and hence a large voltage drop concomitant with the phase slip is identified as a signature which can be detected by the technique of Electric Field Induced Second Harmonic. Indeed, experimental data on two different dopings of LBCO in the superconducting state agree with the prediction by the sine-Gordon equation, but the persistence of a similar signal beyond the superconducting T_C into the stripe phase offers further evidence for the existence of pre-formed pairs and Josephson coupling between stripes in neighbouring CuO_2 planes. This result complements the previous observation of a gigantic THz third harmonic generation in the same material, ascribed to the mixing of coupled modes only visible in nonlinear response (Rajasekaran, Okamoto et al. 2018). Together, the data compels the development of a comprehensive model to account for observations consistent with Josephson tunnelling in the normal state in presence of the stripe order.

Based on results presented in this thesis, future endeavours should address other forms of charge ordering that compete or coexist with superconductivity, such as those found in $YBa_2Cu_3O_{6+\delta}$ (Chang, Blackburn et al. 2012, Ghiringhelli, Le Tacon et al. 2012). The same techniques have great potential for exploring other regions of the cuprate phase diagram, such as the pseudo-gap phase where optical data points to finite condensation without phase coherence (Kaiser, Hunt et al. 2014, von Hoegen, Fechner et al. 2019). The key to understanding the mechanism behind high-temperature superconductivity may very well lie in the other types of order appearing hand-in-hand with it.

Author Contributions

In the following, my contributions to the experiments presented in this thesis are summarised.

For the Magnetic field tuning of light-induced superconductivity in LBCO experiment presented in Chapter 4, the core concept was conceived by A. Cavalleri and D. Nicoletti. The preliminary optical setup was built by O. Mehio. The setup was modified and improved by myself together with S. Moore and A. Disa. The measurements were performed by myself under the guidance of D. Nicoletti. The experimental data was analysed by me and D. Nicoletti. The results are published in (Nicoletti, Fu et al. 2018).

For the Josephson phase slip in striped LBCO experiment presented in Chapter 6, the core concept was conceived by myself, A. Cavalleri, D. Nicoletti, A. von Hoegen, M. Först, and M. Buzzi. The experimental setup was designed and built by myself. The measurements were performed and the data collected by myself. The data was analysed by myself. The numerical sine-Gordon simulation was developed in MATLAB by myself with help from Michael Fechner. Extensive discussions were held among myself, D. Nicoletti, M. Fechner, and M. Buzzi. The results are published in (Fu, Nicoletti et al. 2021).

The LBCO samples used in both experiments were grown by G. Gu.

List of Publications

The results presented in this thesis are based on the following publications:

- **D. Fu**, D. Nicoletti, M. Fechner, M. Buzzi, G. D. Gu, A. Cavalleri, Terahertz Phase Slips in Striped $La_{2-x}Ba_xCuO_4$, *Physical Review B*, 05, L020502 (2022)
- D. Nicoletti, **D. Fu**, O. Mehio, S. Moore, A. S. Disa, G. D. Gu, and A. Cavalleri, Magnetic-Field Tuning of Light-Induced Superconductivity in Striped $La_{2-x}Ba_xCuO_4$, *Physical Review Letters*, 121, 267003 (2018)

I also contributed to work beyond the scope of this thesis:

- D. Nicoletti, E. Casandruc, **D. Fu**, P. Giraldo-Gallo, I. R. Fisher, and A. Cavalleri, Anomalous relaxation kinetics and charge-density-wave correlations in underdoped $BaPb_{1-x}Bi_xO_3$, *Proceedings of the National Academy of Sciences of the United States of America*, 114 (34) 9020-9025 (2017)

Appendix A. Optical properties of matter

In order to make use of light as a probe of material properties, it is imperative to first lay out in detail the principles governing the interaction between light and matter, from which the relation between characteristics of the electromagnetic waves and response functions of the material can be deduced. Propagation of light in presence of matter is described by Maxwell's equations, in c.g.s. units, as follows (Dressel and Grüner 2002):

$$\nabla \cdot \boldsymbol{D} = 0$$

$$\nabla \cdot \boldsymbol{B} = 0$$

$$\nabla \times \boldsymbol{E} = -\frac{1}{c}\frac{\partial \boldsymbol{B}}{\partial t}$$

$$\nabla \times \boldsymbol{H} = \frac{4\pi}{c}\boldsymbol{J}_{cond} + \frac{1}{c}\frac{\partial \boldsymbol{D}}{\partial t}$$

where $\boldsymbol{D}$ is the electric displacement, $\boldsymbol{B}$ the magnetic induction, $\boldsymbol{E}$ the electric field strength, $\boldsymbol{H}$ the magnetic field strength, and $\boldsymbol{J}_{cond}$ the conduction current arising from the motion of electrons under the influence of an electric field, in absence of any external charge or current added from the outside. The del operator ∇ acts with respect to $\boldsymbol{r}$.

Next, several material parameters need to be introduced, which relate the quantities above to each other:

$$\boldsymbol{J}_{cond} = \sigma_1 \boldsymbol{E}$$

$$\boldsymbol{D} = \varepsilon_1 \boldsymbol{E}$$

$$\boldsymbol{B} = \mu_1 \boldsymbol{H}$$

where σ_1 is the real part of conductivity, ε_1 the real part of dielectric function, and μ the permeability, ignoring dissipation for the time being. Substituting these into the Maxwell's equations above yields:

$$c\nabla \times H = 4\pi\sigma_1 E - i\omega\varepsilon_1 E = -i\omega\tilde{\varepsilon}E$$

where it is assumed that $\frac{\partial \boldsymbol{D}}{\partial t} = -i\omega\boldsymbol{D}$, and the complex dielectric function $\tilde{\varepsilon}$ is defined as

$$\tilde{\varepsilon} = \varepsilon_1 + i\frac{4\pi\sigma_1}{\omega} = \varepsilon_1 + i\varepsilon_2$$

where it is customary to denote the real and imaginary parts of $\tilde{\varepsilon}$ as ε_1 and ε_2.

In the same spirit, this can be rewritten as

$$\tilde{\varepsilon} = \frac{4\pi i}{\omega}(\sigma_1 + \frac{\omega}{4\pi i}\varepsilon_1) = \frac{4\pi i}{\omega}\tilde{\sigma}$$

where the complex conductivity $\tilde{\sigma}$ is defined as

$$\tilde{\sigma} = \sigma_1 + \frac{\omega}{4\pi i}\varepsilon_1 = \sigma_1 + i\sigma_2$$

Combining these expressions with the Maxwell's equations and using the vector identity,

$$\nabla \times (\nabla \times \boldsymbol{E}) = -\nabla^2 \boldsymbol{E} + \nabla(\nabla \cdot \boldsymbol{E})$$

one arrives at a wave equation for ***E***,

$$\nabla^2 \boldsymbol{E} = \frac{\mu_1\varepsilon_1}{c^2}\frac{\partial^2 \boldsymbol{E}}{\partial t^2} + \frac{4\pi\mu_1\sigma_1}{c^2}\frac{\partial \boldsymbol{E}}{\partial t}$$

where the first term on the right-hand side of the equation corresponds to the displacement current, and the second term the conduction current. The intuitive solution to the wave equation is an oscillatory travelling wave of the form

$$\boldsymbol{E} = \boldsymbol{E}_0 e^{i(\boldsymbol{K}\cdot\boldsymbol{r} - \omega t)}$$

where ***K*** is a complex propagation vector and ω is the frequency of the wave. Plugging this in yields a relation between ***K*** and ω, commonly known as the dispersion relation, as follows

$$-K^2 = -\frac{\varepsilon_1\mu_1\omega^2}{c^2} - \frac{4\pi i\sigma_1\mu_1\omega}{c^2}$$

Therefore, the expression for ***K*** is

$$\boldsymbol{K} = \frac{\omega}{c}\sqrt{\varepsilon_1\mu_1 + 4\pi i\frac{\sigma_1\mu_1}{\omega}}\,\hat{\boldsymbol{k}} = \frac{\omega}{c}\sqrt{\tilde{\varepsilon}\mu_1}\,\hat{\boldsymbol{k}}$$

where $\hat{\boldsymbol{k}}$ is a unit vector in the direction of $\boldsymbol{K}$, i.e. $\hat{\boldsymbol{k}} = \boldsymbol{K}/|\boldsymbol{K}|$.

Substituting this back into the original solution gives a plane wave of the form

$$\boldsymbol{E} = \boldsymbol{E}_0 e^{-i\omega t} e^{i\frac{\omega z}{c}\sqrt{\varepsilon_1\mu_1 + 4\pi i\frac{\mu_1\sigma_1}{\omega}}}$$

where *z* is assumed to be the direction of propagation. It is common to define, for convenience in describing propagation and dissipation of electromagnetic waves in media, the real refractive index *n* and the extinction coefficient *k*, which make up the complex refractive index $\widetilde{N}$, as follows

$$\widetilde{N} = \left(\varepsilon_1\mu_1 + 4\pi i\frac{\mu_1\sigma_1}{\omega}\right)^{\frac{1}{2}} = (\tilde{\varepsilon}\mu_1)^{\frac{1}{2}} = n + ik$$

Hence, the expressions for ***K*** and ***E*** become

$$\boldsymbol{K} = \frac{\omega}{c}\widetilde{N}\,\widehat{\boldsymbol{k}}$$

and

$$\boldsymbol{E} = \boldsymbol{E}_0 e^{-i\omega t} e^{i\frac{\omega z}{c}\widetilde{N}} = \boldsymbol{E}_0 e^{-i\omega t} e^{i\frac{\omega z}{c}(n+ik)}$$

It is clear that in a material with non-zero *k*, the amplitude of the wave decays exponentially over a characteristic distance *δ* given by

$$\delta = \frac{c}{\omega k}$$

where *δ* is called the optical skin depth.

Importantly, it should be stressed that all of the material parameters defined above are functions of frequency of the light wave ω. As a result, the choice of optical method of measurement becomes crucial, and THz time-domain spectroscopy is one such technique covering the key frequency range where many signatures of a superconducting state are found in the dielectric function and conductivity.

These parameters through other linked observables such as the complex coefficient of reflection are retrieved through electro-optic sampling (EOS), based on the Pockels effect, where both the amplitude and the phase of a coherent THz pulse can be measured simultaneously. This allows the precise determination of the complex refractive index of a material through a reflectivity measurement, which is governed by the Fresnel's law of reflection as follows.

Consider the propagation of a plane electromagnetic wave in vacuum, impinging on the surface of a medium with complex refractive index $\widetilde{N}$, with the electric field of the form

$$\boldsymbol{E_i} = \boldsymbol{E}_{0i} e^{i(\boldsymbol{q_i} \cdot \boldsymbol{r} - \omega t)}$$

where $\boldsymbol{q_i}$ is the incident wavevector. In the simplified case of normal incidence, it is unnecessary to separately consider components of the electric field parallel and perpendicular to the plane of incidence. Without loss of generality, it can be safely assumed that the wavevector $\boldsymbol{q_i}$, along the ***z*** direction, is perpendicular to the surface in the ***xy*** plane, and the electric field $\boldsymbol{E}_{0i}$ in the ***x*** direction, respectively.

The boundary condition dictates a continuity of the tangential components of ***E*** on either side of the interface. Thus, in the case of normal incidence, it can be simply written as

$$E_{0t} = E_{0i} + E_{0r}$$

where E_{0i}, E_{0t}, and E_{0t} are the amplitudes of the incident, reflected, and transmitted electric fields, respectively, all along the x direction. Hence, the Fresnel equation gives

$$\tilde{r} = \frac{E_{0r}}{E_{0i}} = \frac{1 - \widetilde{N}}{1 + \widetilde{N}}$$

where $\tilde{r}$ is the complex coefficient of reflection. Again, it should be noted that, both $\tilde{r}$ and $\widetilde{N}$ are frequency dependent. Since $\widetilde{N}$ can be complex, a relative phase might develop between the reflected field and the incident one, which is apparent if the above equation is rewritten as

$$\tilde{r}(\omega) = |\tilde{r}(\omega)| e^{i\delta(\omega)}$$

where $\delta(\omega)$ gives the frequency-dependent phase shift. In the case where the phase information of the incident and reflected electric fields is lost, for example when the detector is sensitive to only the intensity of the light, only the magnitude of the complex coefficient of reflection is retrieved, which is the reflectivity and is defined as

$$R = \frac{|E_{0r}|^2}{|E_{0i}|^2} = |\tilde{r}|^2 = \left| \frac{1 - \widetilde{N}}{1 + \widetilde{N}} \right|^2$$

As a result, in order to recover both the real and imaginary parts of the complex refractive index, the phase information of the electric fields is crucial. From there, the other

related material properties such as the frequency-dependent conductivity $\tilde{\sigma}(\omega)$ and dielectric function $\tilde{\varepsilon}(\omega)$ can be readily calculated.

The reflected probe field is measured at a range of temperatures as described above. The time traces are then Fourier transformed to obtain the complex frequency spectrum $\tilde{E}_r(\omega, T)$. Ideally, if the incident field $\tilde{E}_i(\omega, T)$ is also measured this way, it would be straightforward to calculate the material response functions $\widetilde{N}$, $\tilde{\sigma}(\omega)$, and $\tilde{\varepsilon}(\omega)$. However, in practice it is very challenging to measure the incident field in precisely the same configuration. An alternative is to rely on reference data measured in a different way. For example, at temperatures in the superconducting state, the reflectivity $R(\omega, T < T_C)$ can be calculated by

$$R(\omega, T < T_C) = \frac{\left|\tilde{E}_r(\omega, T < T_c)\right|^2}{\left|\tilde{E}_r(\omega, T \geq T_c)\right|^2} R(\omega, T \geq T_C)$$

where $R(\omega, T \geq T_C)$ is the reflectivity in the normal state, and is measured with Fourier-transform infrared spectroscopy (FTIR). While FTIR data has access to a wider range of measurement frequency through a combination of different sources and detectors, it is not sensitive to phase information, hence not allowing the precise determination of the complex coefficient of reflection $\tilde{r}$, without which one cannot calculate the three material response functions. Given $R = |\tilde{r}|^2$, a way to estimate the complex phase of $\tilde{r}$ is needed.

The Kramers-Kronig transformation provides a solution to this problem. Given the real part of a complex function over all frequency, the Kramers-Kronig transformation can be used to compute the imaginary part, or vice versa. In this case, since the amplitude of $\tilde{r}$ is known for a wide range of frequency, the Kramers-Kronig transformation can produce the complex phase of $\tilde{r}$, hence allowing complete evaluation of $\tilde{r}$ and the consequent calculation of other response functions of the material (Dressel and Grüner 2002).

Appendix B. Penetration depth mismatch in NIR-pump, THz-probe measurements

The electric field of the reflected probe pulse, measured both below and above T_C, undergoes Fourier transform to yield the complex-valued, frequency dependent $\tilde{E}_r(\omega, T)$. The equilibrium reflectivity in the superconducting state can then be determined as

$$R(\omega, T < T_C) = \frac{\left|\tilde{E}_r(\omega, T < T_c)\right|^2}{\left|\tilde{E}_r(\omega, T \geq T_c)\right|^2} R(\omega, T \geq T_C)$$

where $R(\omega, T \geq T_C)$ is the reflectivity in the normal state measured with Fourier-transform infrared spectroscopy on the same batch of samples, which is completely flat and featureless in the THz range. The reflectivity spectra for the 9.5% and 11.5% dopings are shown in Figure B-1. The reflectivity is then fit with a model describing the optical response of Josephson plasma (solid blue and green lines) and merged at 2.5 THz with broadband spectra from literature. This allows Kramers-Kronig transformation to be performed, producing full sets of equilibrium optical response functions, including complex conductivity $\tilde{\sigma}_0(\omega)$, complex

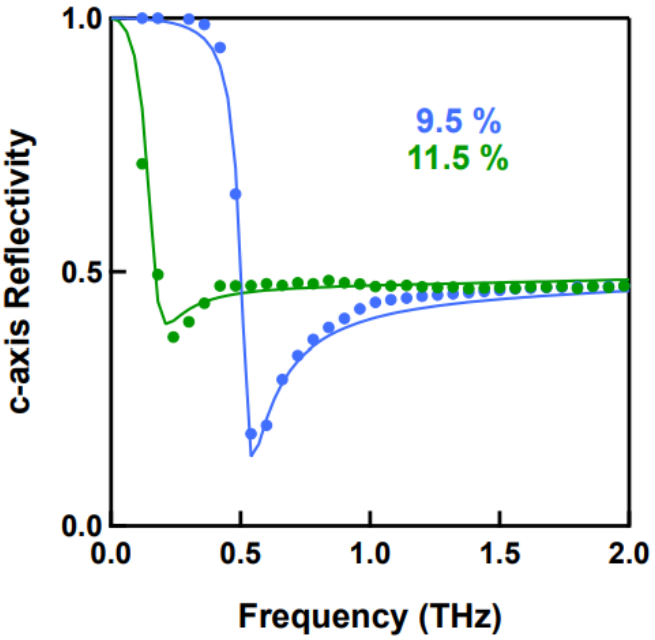

Figure B-1: Equilibrium c-axis reflectivity of LBCO measured with THz time-domain spectroscopy. Blue and green circles are experimental data taken at T = 5 K (no magnetic field) on the x = 9.5% and x = 11.5% sample, respectively. Fits with a model describing the optical response of a Josephson plasma are displayed as solid lines. From (Nicoletti, Fu et al. 2018).

dielectric function $\tilde{\varepsilon}_0(\omega)$, and complex refractive index $\tilde{N}_0(\omega)$, for all temperatures and magnetic fields investigated in the pump-probe measurements.

In the time-resolved pump-probe measurements, changes in c-axis optical properties are retrieved as a function of time delay between the NIR pump pulse and the THz probe pulse with a temporal resolution of ~350 fs. The pump-induced change in the electric field of the THz probe $\Delta E_r(t,\tau) = E_r^{pumped}(t,\tau) - E_r(t)$ is acquired at each time delay τ by filtering out the electro-optic sampling signal with a lock-in amplifier, triggered by modulation of the optical pump with a mechanical chopper. This measurement yields "pump on" minus "pump off" reflected electric field. Here, in order to account for possible average heating by the high energy pump beam on the sample and ensure that $\Delta E_r(t,\tau)$ is not a result of change in temperature, the "pump off" probe field $E_r(t)$ is determined with pump on but at negative delay, i.e. the pump arrives after the probe. The differential electric field $\Delta E_r(t,\tau)$ and the "equilibrium" field $E_r(t)$ are then independently Fourier transformed to obtain the complex-valued, frequency dependent $\Delta\tilde{E}_r(\omega,\tau)$ and $\tilde{E}_r(\omega)$.

It is worth mentioning that, due to the sensitive nature of the measurements to the phase of the electric field, the same measurements were repeated using two methods: (i) directly measure $\tilde{E}_r^{pumped}(\omega,\tau)$ and $\tilde{E}_r(\omega)$ without chopping the pump beam and then calculate $\Delta\tilde{E}_r(\omega,\tau) = \tilde{E}_r^{pumped}(\omega,\tau) - \tilde{E}_r(\omega)$; or alternatively (ii) acquire $\Delta\tilde{E}_r(\omega,\tau)$ and $\tilde{E}_r(\omega)$ simultaneously at each time delay τ by filtering the electro-optic sampling signals with two lock-in amplifiers. Method (i) does not require calibration of the absolute phase of the lock-in amplifier and eliminates phase errors in estimating optical properties, whereas method (ii) avoids the introduction of possible artefacts due to long term drifts and is particular useful when the measured electric field contains fast-varying frequencies. It has been verified that both methods yielded identical results.

Next, the transient complex coefficient of reflection after photo-excitation can be determined by

$$\frac{\Delta\tilde{E}_r(\omega,\tau)}{\tilde{E}_r(\omega)} = \frac{\tilde{r}(\omega,\tau) - \tilde{r}_0(\omega)}{\tilde{r}_0(\omega)}$$

where $\tilde{r}_0(\omega)$ is the complex coefficient of reflection at equilibrium, extracted from equilibrium optical properties, determined independently at the same temperature and magnetic field values as explained above.

In addition, the issue of penetration depth mismatch requires careful consideration. The raw light-induced reflectivity changes are only ~0.5-1% relative to the equilibrium value. They need to be reprocessed in order to take into account the mismatch between the penetration depth, $d(w) = \frac{c}{2\omega\, Im[\tilde{N}_0(\omega)]}$, of the THz probe and that of the NIR pump. At THz frequency, light penetrates roughly $d(\omega \approx 0.3 - 2.5\, THz) \approx 50 - 200$ µm, whereas in the near-IR, it is $d(\omega \approx 375\, THz) \approx 0.4$ µm. This is illustrated in Figure B-2.

This mismatch can be accounted for by modelling the response of the system as that of a homogeneously photo-excited layer of thickness $d \approx 0.4\ \mu m$ with the majority of the bulk beneath it staying unperturbed. Therefore, the complex coefficient of reflection of such a multilayer system can be expressed as

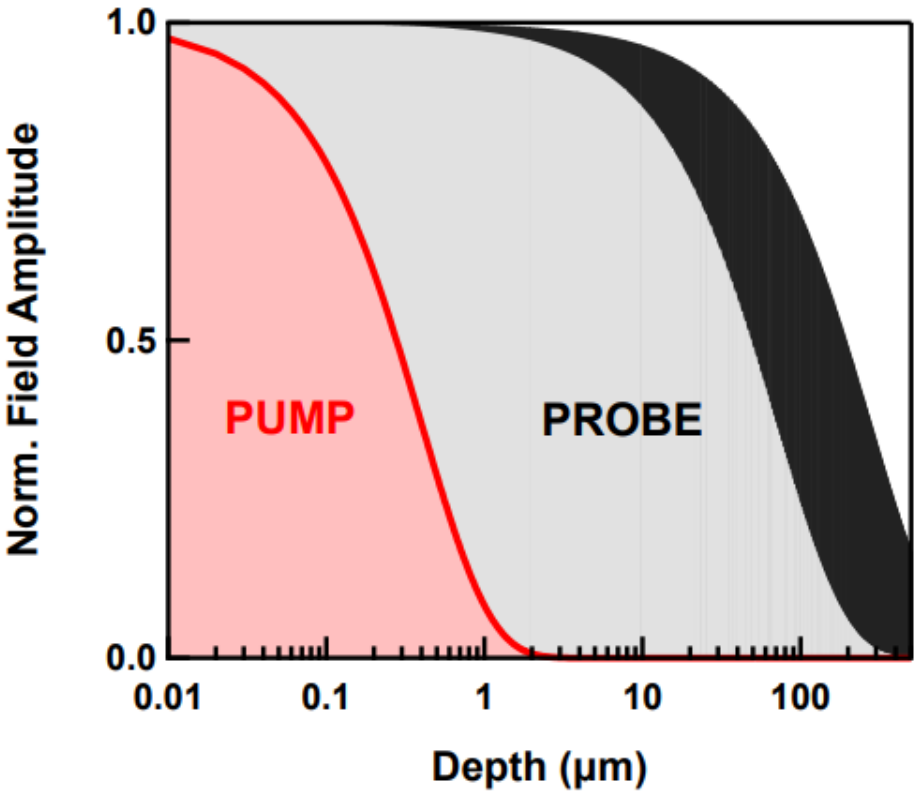

Figure B-2: Schematics of pump-probe penetration depth mismatch. The exponential decay of both pump (red) and probe (black) field profiles is displayed as a function of depth into the material. The black region includes all field decay profiles within the bandwidth of the probe pulse. From (Nicoletti, Fu et al. 2018).

$$\tilde{r}(\omega,\tau) = \frac{\tilde{r}_A(\omega,\tau) + \tilde{r}_B(\omega,\tau)e^{2i\delta(\omega,\tau)}}{1 + \tilde{r}_A(\omega,\tau)\tilde{r}_B(\omega,\tau)e^{2i\delta(\omega,\tau)}}$$

where $\tilde{r}_A(\omega,\tau)$ and $\tilde{r}_B(\omega,\tau)$ are the coefficients of reflection at the interfaces of vacuum/photo-excited layer and photo-excited layer/unperturbed bulk, respectively, and $\delta(\omega,\tau) = 2\pi d\widetilde{N}(\omega,\tau) \,/\, \lambda_0$ is the complex refractive index of the photo-excited layer and λ_0 is the probe wavelength (Dressel and Grüner 2002).

This equation can be solved numerically to yield $\widetilde{N}(\omega,\tau)$ from the experimentally determined $\tilde{r}(\omega,\tau)$. Then the complex conductivity for the homogenously excited volume can be retrieved by

$$\tilde{\sigma}(\omega,\tau) = \frac{\omega}{4\pi i}\left[\widetilde{N}(\omega,\tau)^2 - \varepsilon_\infty\right]$$

where $\varepsilon_\infty = 4.5$ is the high frequency limit dielectric function and a standard value for high-T_C cuprates (Marel, Molegraaf et al. 2003).

It is worth noting that the consistency of this multilayer model was checked against an alternative method, which treats the excited surface as a stack of thin layers with a homogeneous refractive index and describes the excitation profile with an exponential decay (Mitrano, Cantaluppi et al. 2016, Cantaluppi, Buzzi et al. 2018). Both methods produce very similar results.

The temporal resolution of the pump-probe signal is limited by the inverse bandwidth of the detected probe pulse, which is a convolution of the generated THz pulse and the detector response (electro-optic sampling crystal), and by the duration of the pump pulse, because the optical delay stages are operated according to (Kindt and Schmuttenmaer 1999). Note that the temporal resolution is independent of the duration of the THz probe pulse. For all measurements presented here, the temporal resolution is on the order of 350 fs. To put this into perspective, the pump-probe signal develops in ~1.5-2 ps, and the relaxation takes place within ~3-5 ps. Hence it can be assumed that any possible spectral deformation is negligible.

Appendix C. Sine-Gordon equation solver with finite difference method in MATLAB

```
%create grid for calculation
c = 299.792458;              %speed of light in um/ps
% c = 0.00299792458;             %speed of light in m/ps
courant = 0.1;

n = 100000;                   %time points
t_max = 400;                  %time max in ps
dt = t_max/(n-1);            %time spacing
i = 5001;                     %number of grid points
x_max = 5000;                 %max distance in um
dx = x_max/(i-1);            %grid spacing
% dx = dt*c/courant;
% dx = dt*100;
% x_max = (i-1)*dx;
x = linspace(0,x_max,i);
t = linspace(0,t_max,n);

%create grid for plotting
x_interv = 100;                %recording interval in space
t_interv = 20;               %recording interval in time
% xplot = linspace(0,x_max,((i-1)/x_interv+1));
xplot = [0:18 19:x_interv:(i-1)];
tplot = linspace(0,t_max,((n-1)/t_interv+1))-10;
dtplot = dt*t_interv;
f = (1/dtplot*(0:(n/t_interv/2))/(n/t_interv))';

%outer loop over parameter
for outer = [1]
R1 = double.empty;
R2 = double.empty;
R3 = double.empty;
R4 = double.empty;
R5 = double.empty;
R6 = double.empty;
R7 = double.empty;
R8 = double.empty;
R9 = double.empty;
Q1 = [];
Q2 = [];
Q3 = [];

%inner loop over parameter
for inner = [1]


    %material parameters
    epsilon = 25;                %epsilon r
    epsilon_normal = 30+1i*2;
    f_p = 0.53;                     %plasma frequency in THz
    w_p = f_p*2*pi;
    gamma = 0.7*f_p;              %damping coefficient
    gamma_normal = 5;
    %lambda_j = c/sqrt(epsilon)/w_j;              %plasma wavelength in um
```

```
    D = 10;                         %Distance between the planes in Angstroem
    flux_quantum = 206;             %flux quantum in kV/ps
    E0 = flux_quantum*f_p/D;        %E field normalisation constant so that A
has units kV/cm
    Y = -0;


    %external drive parameters
    A = inner*1;                     %amplitude in KV/cm
    w = (0.56)*2*pi;                %frequency in THz
    t_0 = 10;
    tau = 1;
    phase = 4.5;
%     F = A*exp(-(t-t_0).^2./(tau^2)).*sin(w*(t-t_0)+phase);
%     F = F+A/1000*(-1+2*rand(1,length(t)));
%     F = sin((0+0.5)*2*pi*t+phase).*(exp(-(0.5*2*pi*t-
15.7080).^2/(tau*1.5*3.1416^2))).*0.5.*(1+erf((0.5*2*pi*t-
15.7080)/8*6.2832));
%     F = A*F;%./min(F);
    envelope = exp(-(t-t_0).^2./(tau^2));
    F = 0.+1*A*sin(w*t+phase).*envelope;
%     double_pulse = F;
%     t_0 = 60;
%     A = 195;
%     envelop = exp(-(t-t_0).^2./(tau^2));
%     F = 0.+1*A*sin(w*t+phase).*envelop;
%     F = double_pulse + F;
%     F = A*ones(1,n);

    phi = zeros(i,3);
    V = zeros(i,3);
    Et_normal = zeros(i,3);
%     init_layers = 5;
%     init_displace = 4;
%     phi(2:init_layers+1,1) = -init_displace*pi;
    PG = [];
    PVG = [];
    EnG = [];
    E_in = [];


    %iterative algorithm
    for k=1:n-1

        %first space row
        %SC state boundary

        % original boundary coundtition only
        phi(1,3) = phi(1,2)+1*dt*(2*w_p/E0*F(k)+c/dx*(phi(2,2)-phi(1,2)));

        % original boundary condition plus SG
%         phi(1,3) = (2*phi(1,2)-
phi(1,1))/dt^2+(2*gamma+w_p)/2/dt*phi(1,1)-w_p^2*sin(phi(1,2))...
%             +c^2/epsilon/dx^2*(phi(3,2)-
2*phi(2,2)+phi(1,2))+c*2*w_p/1/dx*(phi(2,2)-phi(1,2))+2*2*w_p^2/E0*F(k);
%         phi(1,3) = (1/dt^2+(2*gamma+2*w_p)/2/dt)^(-1)*phi(1,3);

        % alternative boundary condition with d/dx only plus SG
%         phi(1,3) = (2*phi(1,2)-phi(1,1))/dt^2+(2*gamma)/2/dt*phi(1,1)-
w_p^2*sin(phi(1,2))...
```

```
%             +c^2/epsilon/dx^2*(phi(3,2)-
2*phi(2,2)+phi(1,2))+(c+c/sqrt(epsilon))*w_p/dx*(phi(2,2)-
phi(1,2))+2*w_p^2/E0*F(k);
%          phi(1,3) = (1/dt^2+(2*gamma)/2/dt)^(-1)*phi(1,3);

        % alternative boundary condition with d/dt only plus SG
%          phi(1,3) = (2*phi(1,2)-
phi(1,1))/dt^2+(2*gamma+(sqrt(epsilon)+1)*w_p)/2/dt*phi(1,1)-
w_p^2*sin(phi(1,2))...
%             +c^2/epsilon/dx^2*(phi(3,2)-
2*phi(2,2)+phi(1,2))+2*w_p^2/E0*F(k);
%          phi(1,3) = (1/dt^2+(2*gamma+(sqrt(epsilon)+1)*w_p)/2/dt)^(-
1)*phi(1,3);


        %normal state boundary
        Et_normal(1,3) = real(2/(1+sqrt(epsilon_normal))*F(k));



        %all other space rows
        %SC phase
        phi(2:i-1,3) = (2*phi(2:i-1,2)-phi(2:i-1,1))/dt^2+gamma*phi(2:i-
1,1)/dt...
            -w_p^2*sin(phi(2:i-1,2))+outer*c^2/epsilon*(phi(3:i,2)-
2*phi(2:i-1,2)+phi(1:i-2,2))/dx^2....
            +Y/2/dx*(phi(3:i,2)-phi(1:i-2,2));
        phi(2:i-1,3) = (1/dt^2+2*gamma/(2*dt))^(-1)*phi(2:i-1,3);

        %SC voltage
        V(1:i-1,3) = (phi(1:i-1,3)-phi(1:i-1,2))/dt*0.329;  %in mV (210610
changed from flux_quantum/2/pi;

        %normal state E field
        Et_normal(2:i-1,3) = (2*Et_normal(2:i-1,2)-Et_normal(2:i-
1,1))/dt^2+gamma_normal*Et_normal(2:i-1,1)/dt...
            +c^2/real(epsilon_normal)*(Et_normal(3:i,2)-2*Et_normal(2:i-
1,2)+Et_normal(1:i-2,2))/dx^2;
        Et_normal(2:i-1,3) = (1/dt^2+2*gamma_normal/(2*dt))^(-
1)*Et_normal(2:i-1,3);

        %save phi at specified space and time intervals

        if rem(k-1,t_interv)==0

            PG = [PG phi(xplot+1,3)];
            PVG = [PVG V(xplot+1,3)];
            EnG = [EnG Et_normal(xplot+1,3)];
            E_in = [E_in F(k)];
        end




    %
    %     G(1,k) = k;
    %     G(2,k) = phi(1,2);
    %     G(3,k) = phi(2,2);
    %     G(4,k) = 2*dt*2*w_p/E0*F(k);
    %     G(5,k) = 2*dt*c/dx*(phi(2,2)-phi(1,2));
```

```
%         if k > 1
%             return
%         end

        %shift time window
        phi(:,1) = phi(:,2);
        phi(:,2) = phi(:,3);
        Et_normal(:,1) = Et_normal(:,2);
        Et_normal(:,2) = Et_normal(:,3);



    end
xplot = xplot*dx;
depthP = size(PG);
% potential = (1-cos(PG))*w_p^2;
% kinetic = PVG.^2./2;

tau = 10;
envelope = exp(-(t-t_0).^2./(tau^2));
envelope_gate = envelope(1:t_interv:end);

%voltage difference
VdiffG = PVG - EnG*D;
surface = PVG(2,:) - EnG(2,:)*D;
gated_surface = envelope_gate.*surface;


%Load previous files
%{
close all
Q = (dlmread('Broad_A1p0_w500000000000p264159265358979.3_PhiData.dat'))';
E_in = Q(1,(length(tplot)+1):end);
P = Q(:,1:length(tplot));
tick = 1.0;
%}

%take slices at various depths
cut_0 = PG(1,:);
% cut_10 = PG((floor((length(xplot)-1)*0.01)),:);
% cut_20 = PG((floor((length(xplot)-1)*0.02)),:);
% cut_30 = PG((floor((length(xplot)-1)*0.03)),:);
% surface = P(1,:);  %Take phase in second layer on surface
% surf_avg = mean(surface,1);
voltage_0 = PVG(1,:).*envelope_gate;


% current = sin(surf_avg);
% current = (surface);              %I = Ic*sin(phi) approximated as I =
Ic*phi


%calculate transmitted and reflected fields
% E_trans = zeros(1,length(tplot));
% E_refl = zeros(1,length(tplot));
%{
surface_SC = PG(2,:);
for l=1:(length(surface_SC)-1)
```

```
%     E_trans(l+1) = cB0/w_j/sqrt(epsilon)*(surface(l+1) -
surface(l))/dtplot;
    E_trans(l+1) = E0/w_p*(surface_SC(l+1) - surface_SC(l))/dtplot;
    E_refl(l+1) = E_trans(l+1) - E_in(l+1);
end
E_tot_below = E_trans;

surface_normal = EnG(2,:);
for l=1:(length(surface_normal)-1)
    E_trans(l+1) = surface_normal(l);
    E_refl(l+1) = E_trans(l+1) - E_in(l+1);
end
E_tot_above = E_trans;
%}

%FFT
fft_0 = fft_amplitude(cut_0(1:376),dtplot);
fft_V0 = fft_amplitude(voltage_0,dtplot);
% fft_V0 = fft_amplitude(voltage_0(1:376),dtplot);
% fft_10 = fft_amplitude(cut_10,dtplot);
% fft_20 = fft_amplitude(cut_20,dtplot);
% fft_30 = fft_amplitude(cut_30,dtplot);
% fft_Ei = fft_amplitude(E_in,dtplot);
% fft_Er = fft_amplitude(E_refl,dtplot);
% fft_Et = fft_amplitude(E_trans,dtplot);
fft_VscG = fft_2d_row(PVG);
fft_VnG = fft_2d_row(EnG*D);
fft_VdiffG = fft_2d_row(VdiffG);
fft_ungated = fft_amplitude(surface,dtplot);
fft_gated = fft_amplitude(gated_surface,dtplot);

% Reflectivity = (fft_Er(:,2)./fft_Ei(:,2)).^2;
% Transmitivity = (fft_Et(:,2)./fft_Ei(:,2)).^2;

%find peak in spectrum
gate = 1;
if gate
    [peakVdiff, posVdiff] = max(fft_gated(:,2), [], 'linear');
else
    [peakVdiff, posVdiff] = max(fft_ungated(:,2), [], 'linear');
end


%plot 2D heat map
%{
plt = 0;
if plt

    figure
    imagesc(tplot,xplot,P)
    colormap default
    colorbar
    % caxis([-A A])
    % xlim([0 100])
    title(['Phase  dx=' num2str(dx)])
    xlabel('Time (ps)')
%     xlim([0 200])
    ylabel('Depth (um)')
%     ylim([0 1000])
%     caxis([-1*max(P,[],'all') 1*max(P,[],'all')])
end
```

```
%}

%for SC state
plt = 0;
if plt
    cMap = parula(256);
    dataMax = 0.02%2.2;
    dataMin = -0.015%-0.6;
    centerPoint = 0.002%0.709;
    scalingIntensity = 2%10;
    cs = 1:length(cMap);
    cs = cs - (centerPoint-dataMin)*length(cs)/(dataMax-dataMin);
    cs = scalingIntensity * cs/max(abs(cs));
    cs = sign(cs).* exp(abs(cs));
    cs = cs - min(cs);
    cs = cs*511/max(cs)+1;
    newMap = interp1(cs, cMap, 1:0.01:512);

    figure
    surf(tplot,xplot,PG/pi,'EdgeColor','none')
%     surf(tplot,xplot,P,'EdgeColor','none')
%     colormap(newMap)
    ax = gca;
    ax.FontSize = 12
    cb = colorbar;
    cb.Label.String = '$\varphi/\pi$';
    cb.Label.Interpreter = 'latex';
    cb.Label.FontSize = 20;
    cb.Label.FontWeight = 'bold';
    cb.Ticks = [-0.005, 0, 0.005 0.01];
    cb.FontSize = 12;
%     cb.TickLabels = {'-0.005\pi', '0', '0.005\pi', '0.01\pi'};
    view([0 90])
%     title(['Phase  dx=' num2str(dx)])
%     title('Phase excursion')
    xlabel('Time (ps)', 'fontsize', 15)
    ylabel('Depth (\mum)', 'fontsize', 15)
    xlim([-5 30])
    ylim([0 300])
    caxis([-0.012 0.015])
%     set(gca, 'XTickLabel', [])


end

%for potential energy
plt = 0;
if plt
    figure
    surf(tplot,xplot,potential,'EdgeColor','none')
    colormap default
    cb = colorbar;
    cb.Label.String = 'Potential energy';
    view([0 90])
    %     title(['Phase  dx=' num2str(dx)])
    title('Potential energy')
    xlabel('Time (ps)')
    ylabel('Depth (um)')
    xlim([5 30])
    ylim([0 1000])
end
```

```
%for kinetic energy
plt = 0;
if plt
    figure
    surf(tplot,xplot,kinetic,'EdgeColor','none')
    colormap default
    cb = colorbar;
    cb.Label.String = 'Kinetic energy';
    view([0 90])
    %     title(['Phase  dx=' num2str(dx)])
    title('Kinetic energy')
    xlabel('Time (ps)')
    ylabel('Depth (um)')
    xlim([5 30])
    ylim([0 1000])
end

%for voltage
plt = 0;
if plt
    cMap = parula(256);
    dataMax = 428;
    dataMin = -285;
    centerPoint = 60;
    scalingIntensity = 5;
    cs2 = 1:length(cMap);
    cs2 = cs2 - (centerPoint-dataMin)*length(cs2)/(dataMax-dataMin);
    cs2 = scalingIntensity * cs2/max(abs(cs2));
    cs2 = sign(cs2).* exp(abs(cs2));
    cs2 = cs2 - min(cs2);
    cs2 = cs2*511/max(cs2)+1;
    newMap = interp1(cs2, cMap, 1:0.1:512);

    figure
    surf(tplot,xplot,PVG,'EdgeColor','none')
%     colormap(newMap)
    cb = colorbar;
    cb.Label.String = 'Voltage (?V)';
    cb.Label.FontSize = 15;
    view([0 90])
%     title(['Phase  dx=' num2str(dx)])
%     title('SC state Voltage (?V)')
%     xlabel('Time (ps)')
    ylabel('Depth (um)')
    xlim([-5 15])
    ylim([0 300])
    caxis([-285 428])
    set(gca, 'XTickLabel', [])
end

%for normal state
plt = 0;
if plt

    figure
    surf(tplot,xplot,EnG*D,'EdgeColor','none')
    colormap default
    c = colorbar;
    c.Label.String = 'Voltage (?V)';
    view([0 90])
%     title(['Phase  dx=' num2str(dx)])
```

```
    title('Normal state Voltage (?V)')
    xlabel('Time (ps)')
    ylabel('Depth (um)')
    xlim([0 100])
    ylim([0 500])
%     caxis([-1 15+0.1])
end

%for voltage difference
plt = 0;
if plt

    figure
    surf(tplot,xplot,VdiffG,'EdgeColor','none')
    colormap default
    c = colorbar;
    c.Label.String = 'Voltage (?V)';
    view([0 90])
%     title(['Phase  dx=' num2str(dx)])
    title('Voltage difference (?V)')
    xlabel('Time (ps)')
    ylabel('Depth (um)')
    xlim([0 80])
    ylim([0 500])
%     caxis([-1 15+0.1])
end

%for Vdiff spectra
plt = 0;
if plt

    figure
    surf(f,xplot,fft_VdiffG,'EdgeColor','none')
    colormap default
    c = colorbar;
    c.Label.String = 'Voltage (?V)';
    view([0 90])
%     title(['Phase  dx=' num2str(dx)])
    title('Normal state Voltage (?V)')
    xlabel('Frequency (THz)')
    ylabel('Depth (um)')
    xlim([0 3])
    ylim([0 500])
%     caxis([-1 15+0.1])
end

%Plot slices
%{
figure
hold on
% plot(t,F)
plot(tplot,cut_0)
plot(tplot,cut_10)
plot(tplot,cut_20)
plot(tplot,cut_30)
plot(tplot,surf_avg)
% xlim([0 100])
xlabel('Time')
ylabel('Amplitude')
title('Line cuts')
legend('Surface','2%','4%','6%','emitting layer')
%}
```

```
%plot time traces
plt = 0;
if plt

    figure
    hold on
    plot(tplot,E_in,'k')
%     plot(tplot,E_trans)
    xlabel('Time (ps)', 'fontsize',15)
    ylabel('Electric field amplitude (kV/cm)')
    yyaxis right
    plot(tplot,PG(1,:)/pi,'-k')
%     plot(tplot,PG(2,:)/pi,'c')
    ylabel('Phase (pi)')


%     title('Incident field and phase')
%     title('Electric field and phase')
    legend('Incdient field','Phase')
%     legend('Incident field','1st layer', '2nd layer')
%     legend('Incident field','old 1st', 'old 2nd','new 1st','new 2nd')
    xlim([-5 15])
    ylim([-1 2.4])
end

%for voltages
plt = 0;
if plt

    figure
    hold on
%     plot(tplot,PG(1,:)/pi,'k')
%     plot(tplot,E_in)
    xlabel('Time (ps)')
%     ylabel('Phase (pi)')
%     yyaxis right
    plot(tplot,PVG(1,:),'-k')
%     plot(tplot,real(EnG(2,:))*D,'-r')
%     plot(tplot,surface,'-c')
    ylabel('Voltage (?V)')
%     title('Voltage')
%     legend('Incident field','SC state','Normal state','Difference')
    xlim([5 30])
    ylim([-285 460])

end

plt = 0;
if plt
    t_slice = 4101;
    figure
    hold on
    plot(xplot,PG(:,t_slice)/pi)
    xlabel('Depth (um)')
    ylabel('Phase (pi)')
    title(['Phase along cut in time dx=' num2str(dx)])
%     legend('Incident field','Transmitted field','Reflected field')
    xlim([0 300])
end
```

```
%plot spectra
plt = 0;
if plt
    figure
%     semilogy(f,fft_Et(:,2))
%     hold on
%     plot(f,fft_10(:,2))
%     plot(f,fft_20(:,2))
%     plot(f,fft_30(:,2))
%     plot(f,fft_Ei(:,2))
    semilogy(fft_0(:,1),fft_0(:,2))
    xlabel('Frequency (THz)')
    ylabel('Phase')
%     title('Line cuts')
%     legend({'Surface','1%','2%','3%','Incident'},'Location','northeast')
    % legend('Phase on surface','Incident field')
%     ax = gca;
%     ax.YGrid = 'off';
%     ax.XGrid = 'on';
    xlim([0. 3])
    % xticks(0:tick:6)
    ylim([0.0000005 2])
end

plt = 0;
if plt
    figure
%     plot(f,fft_VscG(2,:)/max(fft_VscG(2,:)))
    semilogy(fft_V0(:,1),fft_V0(:,2)/30.3263)
    hold on
%     plot(f,fft_VnG(2,:))
%     plot(f,fft_gated(:,2))
    xlabel('Frequency (THz)')
    ylabel('Voltage')
%     title('Voltages on surface')
%     legend({'SC state','Normal
state','Difference'},'Location','northeast')
    xlim([0. 3])
    ylim([0.00000001 2])
end

%plot normalised spectra and reflectivity
plt = 0;
if plt

    figure
    hold on
    plot(f,fft_Ei(:,2)/max(fft_Ei(:,2)))
    plot(f,fft_Et(:,2)/max(fft_Ei(:,2)))
    plot(f,fft_Er(:,2)/max(fft_Ei(:,2)))
    xlabel('frequency (THz)')
    ylabel('Amplitude')
    title('Reflectivity')

legend('Incident','Transmitted','Reflected','Reflectivity','Transmitivity')
    xlim([0.1 2])
    ylim([0 1])
end
```

```
%output files
tfile = ['quick_gam' erase(num2str(gamma/f_p),'.') '_'
erase(num2str(gamma_normal),'.')];
% mfile = [tfile '_A' num2str(inner) '.mat' ];
% mfile = ['dx' erase(num2str(dx),'.') '_init' num2str(init_layers) 'L'
num2str(init_displace) 'pi.mat'];
mfile = [tfile '_A' erase(num2str(inner), '.') '.mat' ];



% R1 = [R1 fft_Et(:,2)];
% R2 = [R2 Reflectivity];
% R3 = [R3 E2_tot_below'];
% R4 = [R4 difference'];
% R5 = [R5 A];
% R6 = [R6 diff_amp(:,2)];
if gate
    R7 = [R7 fft_gated(:,2)];
else
    R7 = [R7 fft_ungated(:,2)];
end

Q1 = [Q1 [A;max(abs(PG(2,:)/pi))]];
Q2 = [Q2 [A;peakVdiff]];
Q3 = [Q3 [A;f(posVdiff)]];

save(mfile);

if max(abs(PG(1,:)))/pi>1.99
    break
end

end

plt = 0;
if plt

    figure
    plot(Q1(1,:),Q1(2,:))
    ylabel('Phase in pi')
    ylim([0 2])
    hold on
    yyaxis right
    ylabel('Peak amplitude in FFT')
    plot(Q2(1,:),Q2(2,:))
    legend('phase','voltage difference peak')
    xlabel('Driving field')
    title('Peak amplitude in spectrum')

    figure
    plot(Q1(1,:),Q1(2,:))
    hold on
    ylabel('Phase')
    yyaxis right
    plot(Q3(1,:),Q3(2,:))
    ylabel('Frequency')
    xlabel('Driving field')
    legend('phase','voltage diff peak')
    title('Peak position')
```

```
end


% spectrafile = [tfile '_spectra.dat'];
% reffile = [tfile '_reflectivity.dat'];
% totfile = [tfile '_totfield.dat'];
% difffile = [tfile '_difference.dat'];
% ampfile = [tfile '_amplitudes.dat'];
% tdfile = [tfile '_pulse.dat'];
% diffampfile = [tfile '_diffamp.dat'];
maxPhase = [tfile '_maxPhase.dat'];
VdiffFD = [tfile '_VdiffFD.dat'];
Vdiffpeak = [tfile '_Vdiffpeak.dat'];


output = 0;
if output == 1

%     dlmwrite(spectrafile,[f R1]);
%     dlmwrite(reffile,[f R2]);
%     dlmwrite(totfile,[tplot' R3]);
%     dlmwrite(difffile,[tplot' R4]);
%     dlmwrite(ampfile,R5);
%     dlmwrite(tdfile,[tplot' E_in']);
%     dlmwrite(diffampfile,[f R6]);
dlmwrite(maxPhase,Q1');
dlmwrite(VdiffFD, [f R7]);
dlmwrite(Vdiffpeak, Q2');
end
fclose('all');

end
```

Bibliography

Abbamonte, P., A. Rusydi, S. Smadici, G. D. Gu, G. A. Sawatzky and D. L. Feng (2005). "Spatially modulated 'Mottness' in $La_{2-x}Ba_xCuO_4$." Nature Physics **1**(3): 155-158.

Abrikosov, A. A. (1957). "On the magnetic properties of superconductors of the second group." Sov. Phys. JETP **5**: 1174-1182.

Apostolov, S. S., Z. A. Maizelis, M. A. Sorokina, V. A. Yampol'skii and F. Nori (2010). "Self-induced tunable transparency in layered superconductors." Physical Review B **82**(14): 144521.

Axe, J. D., A. H. Moudden, D. Hohlwein, D. E. Cox, K. M. Mohanty, A. R. Moodenbaugh and Y. Xu (1989). "Structural phase transformations and superconductivity in $La_{2-x}Ba_xCuO_4$." Physical Review Letters **62**(23): 2751-2754.

Bardeen, J., L. N. Cooper and J. R. Schrieffer (1957). "Microscopic Theory of Superconductivity." Physical Review **106**(1): 162-164.

Bardeen, J. and D. Pines (1955). "Electron-Phonon Interaction in Metals." Physical Review **99**(4): 1140-1150.

Barišić, N., M. K. Chan, Y. Li, G. Yu, X. Zhao, M. Dressel, A. Smontara and M. Greven (2013). "Universal sheet resistance and revised phase diagram of the cuprate high-temperature superconductors." Proceedings of the National Academy of Sciences **110**(30): 12235.

Basov, D. N., R. D. Averitt, D. van der Marel, M. Dressel and K. Haule (2011). "Electrodynamics of correlated electron materials." Reviews of Modern Physics **83**(2): 471-541.

Bednorz, J., M. Takashige and K. Müller (1987). "Susceptibility measurements support high-T_c superconductivity in the Ba-La-Cu-O system." EPL (Europhysics Letters) **3**(3): 379.

Bednorz, J. G. and K. A. Müller (1986). "Possible highTc superconductivity in the Ba−La−Cu−O system." Zeitschrift für Physik B Condensed Matter **64**(2): 189-193.

Berg, E., E. Fradkin, E. A. Kim, S. A. Kivelson, V. Oganesyan, J. M. Tranquada and S. C. Zhang (2007). "Dynamical Layer Decoupling in a Stripe-Ordered High-T_c Superconductor." Physical Review Letters **99**(12): 127003.

Berg, E., E. Fradkin, S. A. Kivelson and J. M. Tranquada (2009). "Striped superconductors: how spin, charge and superconducting orders intertwine in the cuprates." New Journal of Physics **11**(11): 115004.

Bilbro, L. S., R. V. Aguilar, G. Logvenov, O. Pelleg, I. Božović and N. P. Armitage (2011). "Temporal correlations of superconductivity above the transition temperature in $La_{2-x}Sr_xCuO_4$ probed by terahertz spectroscopy." Nature Physics **7**(4): 298-302.

Bill, A., V. Z. Kresin and S. A. Wolf (1998). The Isotope Effect in Superconductors. Pair Correlations in Many-Fermion Systems. V. Z. Kresin. Boston, MA, Springer US**:** 25-55.

Bor, Z., B. Racz, G. Szabo, M. Hilbert and H. Hazim (1993). "Femtosecond pulse front tilt caused by angular dispersion." Optical Engineering **32**(10).

Budden, M., T. Gebert, M. Buzzi, G. Jotzu, E. Wang, T. Matsuyama, G. Meier, Y. Laplace, D. Pontiroli, M. Riccò, F. Schlawin, D. Jaksch and A. Cavalleri (2021). "Evidence for metastable photo-induced superconductivity in K_3C_{60}." Nature Physics **17**(5): 611-618.

Cantaluppi, A., M. Buzzi, G. Jotzu, D. Nicoletti, M. Mitrano, D. Pontiroli, M. Riccò, A. Perucchi, P. Di Pietro and A. Cavalleri (2018). "Pressure tuning of light-induced superconductivity in K_3C_{60}." Nature Physics **14**(8): 837-841.

Casandruc, E., D. Nicoletti, S. Rajasekaran, Y. Laplace, V. Khanna, G. D. Gu, J. P. Hill and A. Cavalleri (2015). "Wavelength-dependent optical enhancement of superconducting interlayer coupling in $La_{1.885}Ba_{0.115}CuO_4$." Physical Review B **91**(17): 174502.

Cavalleri, A. (2018). "Photo-induced superconductivity." Contemporary Physics **59**(1): 31-46.

Cavalleri, A., M. Rini, H. H. W. Chong, S. Fourmaux, T. E. Glover, P. A. Heimann, J. C. Kieffer and R. W. Schoenlein (2005). "Band-Selective Measurements of Electron Dynamics in VO_2 Using Femtosecond Near-Edge X-Ray Absorption." Physical Review Letters **95**(6): 067405.

Chakravarty, S., R. B. Laughlin, D. K. Morr and C. Nayak (2001). "Hidden order in the cuprates." Physical Review B **63**(9): 094503.

Chang, J., E. Blackburn, A. T. Holmes, N. B. Christensen, J. Larsen, J. Mesot, R. Liang, D. A. Bonn, W. N. Hardy, A. Watenphul, M. v. Zimmermann, E. M. Forgan and S. M. Hayden (2012). "Direct observation of competition between superconductivity and charge density wave order in $YBa_2Cu_3O_{6.67}$." Nature Physics **8**(12): 871-876.

Chang, J., Y. Sassa, S. Guerrero, M. Månsson, M. Shi, S. Pailhés, A. Bendounan, R. Mottl, T. Claesson, O. Tjernberg, L. Patthey, M. Ido, M. Oda, N. Momono, C. Mudry and J. Mesot (2008). "Electronic structure near the 1/8-anomaly in La-based cuprates." New Journal of Physics **10**(10): 103016.

Cooper, L. N. (1956). "Bound Electron Pairs in a Degenerate Fermi Gas." Physical Review **104**(4): 1189-1190.

Corson, J., R. Mallozzi, J. Orenstein, J. N. Eckstein and I. Bozovic (1999). "Vanishing of phase coherence in underdoped $Bi_2Sr_2CaCu_2O_{8+\delta}$." Nature **398**(6724): 221-223.

Damascelli, A., Z. Hussain and Z.-X. Shen (2003). "Angle-resolved photoemission studies of the cuprate superconductors." Reviews of Modern Physics **75**(2): 473-541.

de Launay, J. (1954). "The Isotope Effect in Superconductivity." Physical Review **93**(4): 661-665.

Dienst, A., E. Casandruc, D. Fausti, L. Zhang, M. Eckstein, M. Hoffmann, V. Khanna, N. Dean, M. Gensch, S. Winnerl, W. Seidel, S. Pyon, T. Takayama, H. Takagi and A. Cavalleri (2013). "Optical

excitation of Josephson plasma solitons in a cuprate superconductor." Nature Materials **12**(6): 535-541.

Ding, H., M. R. Norman, J. C. Campuzano, M. Randeria, A. F. Bellman, T. Yokoya, T. Takahashi, T. Mochiku and K. Kadowaki (1996). "Angle-resolved photoemission spectroscopy study of the superconducting gap anisotropy in $Bi_2Sr_2CaCu_2O_{8+x}$." Physical Review B **54**(14): R9678-R9681.

Doiron-Leyraud, N., O. Cyr-Choinière, S. Badoux, A. Ataei, C. Collignon, A. Gourgout, S. Dufour-Beauséjour, F. F. Tafti, F. Laliberté, M. E. Boulanger, M. Matusiak, D. Graf, M. Kim, J. S. Zhou, N. Momono, T. Kurosawa, H. Takagi and L. Taillefer (2017). "Pseudogap phase of cuprate superconductors confined by Fermi surface topology." Nature Communications **8**(1): 2044.

Dordevic, S., S. Komiya, Y. Ando, Y. Wang and D. Basov (2005). "Josephson vortex state across the phase diagram of $La_{2-x}Sr_xCuO_4$: A magneto-optics study." Physical Review B **71**(5): 054503.

Dressel, M. and G. Grüner (2002). Electrodynamics of Solids: Optical Properties of Electrons in Matter. Cambridge, Cambridge University Press.

Drozdov, A. P., M. I. Eremets, I. A. Troyan, V. Ksenofontov and S. I. Shylin (2015). "Conventional superconductivity at 203 kelvin at high pressures in the sulfur hydride system." Nature **525**(7567): 73-76.

Dubroka, A., M. Rössle, K. W. Kim, V. K. Malik, D. Munzar, D. N. Basov, A. A. Schafgans, S. J. Moon, C. T. Lin, D. Haug, V. Hinkov, B. Keimer, T. Wolf, J. G. Storey, J. L. Tallon and C. Bernhard (2011). "Evidence of a Precursor Superconducting Phase at Temperatures as High as 180 K in $RBa_2Cu_3O_{7-\delta}$ (R = Y, Gd, Eu) Superconducting Crystals from Infrared Spectroscopy." Physical Review Letters **106**(4): 047006.

Dunsiger, S. R., Y. Zhao, Z. Yamani, W. J. L. Buyers, H. A. Dabkowska and B. D. Gaulin (2008). "Incommensurate spin ordering and fluctuations in underdoped $La_{2-x}Ba_xCuO_4$." Physical Review B **77**(22): 224410.

Ehrke, H., R. I. Tobey, S. Wall, S. A. Cavill, M. Först, V. Khanna, T. Garl, N. Stojanovic, D. Prabhakaran, A. T. Boothroyd, M. Gensch, A. Mirone, P. Reutler, A. Revcolevschi, S. S. Dhesi and A. Cavalleri (2011). "Photoinduced Melting of Antiferromagnetic Order in $La_{0.5}Sr_{1.5}MnO_4$ Measured Using Ultrafast Resonant Soft X-Ray Diffraction." Physical Review Letters **106**(21): 217401.

Eichberger, M., H. Schäfer, M. Krumova, M. Beyer, J. Demsar, H. Berger, G. Moriena, G. Sciaini and R. J. D. Miller (2010). "Snapshots of cooperative atomic motions in the optical suppression of charge density waves." Nature **468**(7325): 799-802.

Emery, V. J. and S. A. Kivelson (1995). "Importance of phase fluctuations in superconductors with small superfluid density." Nature **374**(6521): 434-437.

Estève, D., J. M. Martinis, C. Urbina, M. H. Devoret, G. Collin, P. Monod, M. Ribault and A. Revcolevschi (1987). "Observation of the a.c. Josephson Effect Inside Copper-Oxide-Based Superconductors." Europhysics Letters (EPL) **3**(11): 1237-1242.

Fausti, D., R. I. Tobey, N. Dean, S. Kaiser, A. Dienst, M. C. Hoffmann, S. Pyon, T. Takayama, H. Takagi and A. Cavalleri (2011). "Light-Induced Superconductivity in a Stripe-Ordered Cuprate." Science **331**(6014): 189.

Fink, J., E. Schierle, E. Weschke, J. Geck, D. Hawthorn, V. Soltwisch, H. Wadati, H.-H. Wu, H. A. Dürr, N. Wizent, B. Büchner and G. A. Sawatzky (2009). "Charge ordering in $La_{1.8-x}Eu_{0.2}Sr_xCuO_4$ studied by resonant soft x-ray diffraction." Physical Review B **79**(10): 100502.

Först, M., A. Frano, S. Kaiser, R. Mankowsky, C. R. Hunt, J. J. Turner, G. L. Dakovski, M. P. Minitti, J. Robinson, T. Loew, M. Le Tacon, B. Keimer, J. P. Hill, A. Cavalleri and S. S. Dhesi (2014). "Femtosecond x rays link melting of charge-density wave correlations and light-enhanced coherent transport in $YBa_2Cu_3O_{6.6}$." Physical Review B **90**(18): 184514.

Först, M., R. Mankowsky and A. Cavalleri (2015). "Mode-Selective Control of the Crystal Lattice." Accounts of Chemical Research **48**(2): 380-387.

Först, M., C. Manzoni, S. Kaiser, Y. Tomioka, Y. Tokura, R. Merlin and A. Cavalleri (2011). "Nonlinear phononics as an ultrafast route to lattice control." Nature Physics **7**(11): 854-856.

Först, M., R. I. Tobey, H. Bromberger, S. B. Wilkins, V. Khanna, A. D. Caviglia, Y. D. Chuang, W. S. Lee, W. F. Schlotter, J. J. Turner, M. P. Minitti, O. Krupin, Z. J. Xu, J. S. Wen, G. D. Gu, S. S. Dhesi, A. Cavalleri and J. P. Hill (2014). "Melting of Charge Stripes in Vibrationally Driven $La_{1.875}Ba_{0.125}CuO_4$: Assessing the Respective Roles of Electronic and Lattice Order in Frustrated Superconductors." Physical Review Letters **112**(15): 157002.

Fradkin, E., S. A. Kivelson and J. M. Tranquada (2015). "Colloquium: Theory of intertwined orders in high temperature superconductors." Reviews of Modern Physics **87**(2): 457-482.

Fröhlich, H. (1950). "Theory of the Superconducting State. I. The Ground State at the Absolute Zero of Temperature." Physical Review **79**(5): 845-856.

Fu, D., D. Nicoletti, M. Fechner, M. Buzzi, G. Gu and A. Cavalleri (2021). "Terahertz phase slips in striped $La_{2-x}Ba_xCuO_4$." Physical Review B **105**(2): L020502.

Fujita, M., H. Goka, K. Yamada, J. M. Tranquada and L. P. Regnault (2004). "Stripe order, depinning, and fluctuations in $La_{1.875}Ba_{0.125}CuO_4$ and $La_{1.875}Ba_{0.075}Sr_{0.050}CuO_4$." Physical Review B **70**(10): 104517.

Fujita, M., H. Hiraka, M. Matsuda, M. Matsuura, J. M. Tranquada, S. Wakimoto, G. Xu and K. Yamada (2011). "Progress in Neutron Scattering Studies of Spin Excitations in High-T_c Cuprates." Journal of the Physical Society of Japan **81**(1): 011007.

Fujita, M., K. Yamada, H. Hiraka, P. M. Gehring, S. H. Lee, S. Wakimoto and G. Shirane (2002). "Static magnetic correlations near the insulating-superconducting phase boundary in $La_{2-x}Sr_xCuO_4$." Physical Review B **65**(6): 064505.

Fukuzumi, Y., K. Mizuhashi, K. Takenaka and S. Uchida (1996). "Universal Superconductor-Insulator Transition and T_c Depression in Zn-Substituted High-T_c Cuprates in the Underdoped Regime." Physical Review Letters **76**(4): 684-687.

Gammel, P. L., D. J. Bishop, G. J. Dolan, J. R. Kwo, C. A. Murray, L. F. Schneemeyer and J. V. Waszczak (1987). "Observation of Hexagonally Correlated Flux Quanta In $YBa_2Cu_3O_7$." Physical Review Letters **59**(22): 2592-2595.

Ghiringhelli, G., M. Le Tacon, M. Minola, S. Blanco-Canosa, C. Mazzoli, N. B. Brookes, G. M. De Luca, A. Frano, D. G. Hawthorn, F. He, T. Loew, M. M. Sala, D. C. Peets, M. Salluzzo, E. Schierle, R. Sutarto, G. A. Sawatzky, E. Weschke, B. Keimer and L. Braicovich (2012). "Long-Range Incommensurate Charge Fluctuations in $(Y,Nd)Ba_2Cu_3O_{6+x}$." Science **337**(6096): 821-825.

Ginzburg, V. and L. Landau (1950). "Theory of superconductivity." Zh. Eksp. Teor. Fiz.;(USSR) **20**(12).

Gomes, K. K., A. N. Pasupathy, A. Pushp, S. Ono, Y. Ando and A. Yazdani (2007). "Visualizing pair formation on the atomic scale in the high-Tc superconductor $Bi_2Sr_2CaCu_2O_{8+\delta}$." Nature **447**(7144): 569-572.

Gough, C. E., M. S. Colclough, E. M. Forgan, R. G. Jordan, M. Keene, C. M. Muirhead, A. I. M. Rae, N. Thomas, J. S. Abell and S. Sutton (1987). "Flux quantization in a high-Tc superconductor." Nature **326**(6116): 855-855.

Grafe, H. J., N. J. Curro, B. L. Young, A. Vyalikh, J. Vavilova, G. D. Gu, M. Hücker and B. Büchner (2010). "Charge order and low frequency spin dynamics in lanthanum cuprates revealed by Nuclear Magnetic Resonance." The European Physical Journal Special Topics **188**(1): 89-101.

Greene, R. L., P. R. Mandal, N. R. Poniatowski and T. Sarkar (2020). "The Strange Metal State of the Electron-Doped Cuprates." Annual Review of Condensed Matter Physics **11**(1): 213-229.

Hashimoto, M., I. M. Vishik, R.-H. He, T. P. Devereaux and Z.-X. Shen (2014). "Energy gaps in high-transition-temperature cuprate superconductors." Nature Physics **10**(7): 483-495.

Hayward Lauren, E., G. Hawthorn David, G. Melko Roger and S. Sachdev (2014). "Angular Fluctuations of a Multicomponent Order Describe the Pseudogap of $YBa_2Cu_3O_{6+x}$." Science **343**(6177): 1336-1339.

He, R.-H., K. Tanaka, S.-K. Mo, T. Sasagawa, M. Fujita, T. Adachi, N. Mannella, K. Yamada, Y. Koike, Z. Hussain and Z.-X. Shen (2009). "Energy gaps in the failed high-T_c superconductor $La_{1.875}Ba_{0.125}CuO_4$." Nature Physics **5**(2): 119-123.

Hebling, J., G. Almási, I. Z. Kozma and J. Kuhl (2002). "Velocity matching by pulse front tilting for large-area THz-pulse generation." Optics Express **10**(21): 1161-1166.

Hebling, J., K.-L. Yeh, M. C. Hoffmann, B. Bartal and K. A. Nelson (2008). "Generation of high-power terahertz pulses by tilted-pulse-front excitation and their application possibilities." Journal of the Optical Society of America B **25**(7): B6-B19.

Himeda, A., T. Kato and M. Ogata (2002). "Stripe States with Spatially Oscillating *d*-Wave Superconductivity in the Two-Dimensional *t-t'-J* Model." Physical Review Letters **88**(11): 117001.

Hirota, K. (2001). "Neutron scattering studies of Zn-doped $La_{2-x}Sr_xCuO_4$." Physica C: Superconductivity **357-360**: 61-68.

Hoevers, H., P. Van Bentum, L. Van De Leemput, H. Van Kempen, A. Schellingerhout and D. Van Der Marel (1988). "Determination of the energy gap in a thin $YBa_2Cu_3O_{7-x}$ film by Andreev reflection and by tunneling." Physica C: Superconductivity **152**(1): 105-110.

Homes, C. C., M. Hücker, Q. Li, Z. J. Xu, J. S. Wen, G. D. Gu and J. M. Tranquada (2012). "Determination of the optical properties of $La_{2-x}Ba_xCuO_4$ for several dopings, including the anomalous x = 1/8 phase." Physical Review B **85**(13): 134510.

Hu, W., S. Kaiser, D. Nicoletti, C. R. Hunt, I. Gierz, M. C. Hoffmann, M. Le Tacon, T. Loew, B. Keimer and A. Cavalleri (2014). "Optically enhanced coherent transport in $YBa_2Cu_3O_{6.5}$ by ultrafast redistribution of interlayer coupling." Nature Materials **13**(7): 705-711.

Hücker, M., M. v. Zimmermann, M. Debessai, J. S. Schilling, J. M. Tranquada and G. D. Gu (2010). "Spontaneous Symmetry Breaking by Charge Stripes in the High Pressure Phase of Superconducting $La_{1.875}Ba_{0.125}CuO_4$." Physical Review Letters **104**(5): 057004.

Hücker, M., M. v. Zimmermann, G. D. Gu, Z. J. Xu, J. S. Wen, G. Xu, H. J. Kang, A. Zheludev and J. M. Tranquada (2011). "Stripe order in superconducting $La_{2-x}Ba_xCuO_4$ ($0.095 \leq x \leq 0.155$)." Physical Review B **83**(10): 104506.

Hücker, M., M. v. Zimmermann, Z. J. Xu, J. S. Wen, G. D. Gu and J. M. Tranquada (2013). "Enhanced charge stripe order of superconducting $La_{2-x}Ba_xCuO_4$ in a magnetic field." Physical Review B **87**(1): 014501.

Hunt, C. R., D. Nicoletti, S. Kaiser, T. Takayama, H. Takagi and A. Cavalleri (2015). "Two distinct kinetic regimes for the relaxation of light-induced superconductivity in $La_{1.675}Eu_{0.2}Sr_{0.125}CuO_4$." Physical Review B **91**(2): 020505.

Ido, M., T. Kudo, N. Yamada, N. Momono, N. Abe, T. Nakano, C. Manabe and M. Oda (1996). "Pressure effect on anomalous suppression of T_c around x = 1/8 in $La_{2-x}Ba_xCuO_4$ and $La_{1.8-x}Nd_{0.2}Ba_xCuO_4$." JOURNAL OF LOW TEMPERATURE PHYSICS **105**(3-4): 311-316.

Josephson, B. D. (1962). "Possible new effects in superconductive tunnelling." Physics Letters **1**(7): 251-253.

Josephson, B. D. (1964). "Coupled Superconductors." Reviews of Modern Physics **36**(1): 216-220.

Kaiser, S., C. R. Hunt, D. Nicoletti, W. Hu, I. Gierz, H. Y. Liu, M. Le Tacon, T. Loew, D. Haug, B. Keimer and A. Cavalleri (2014). "Optically induced coherent transport far above T_c in underdoped $YBa_2Cu_3O_{6-\delta}$." Physical Review B **89**(18): 184516.

Kanigel, A., U. Chatterjee, M. Randeria, M. R. Norman, G. Koren, K. Kadowaki and J. C. Campuzano (2008). "Evidence for Pairing above the Transition Temperature of Cuprate Superconductors from the Electronic Dispersion in the Pseudogap Phase." Physical Review Letters **101**(13): 137002.

Katano, S., S. Funahashi, N. Môri, Y. Ueda and J. A. Fernandez-Baca (1993). "Pressure effects on the structural phase transitions and superconductivity of $La_{2-x}Ba_xCuO_4$ (x=0.125)." Physical Review B **48**(9): 6569-6574.

Keimer, B., S. A. Kivelson, M. R. Norman, S. Uchida and J. Zaanen (2015). "From quantum matter to high-temperature superconductivity in copper oxides." Nature **518**(7538): 179-186.

Khanna, V., R. Mankowsky, M. Petrich, H. Bromberger, S. A. Cavill, E. Möhr-Vorobeva, D. Nicoletti, Y. Laplace, G. D. Gu, J. P. Hill, M. Först, A. Cavalleri and S. S. Dhesi (2016). "Restoring interlayer Josephson coupling in $La_{1.885}Ba_{0.115}CuO_4$ by charge transfer melting of stripe order." Physical Review B **93**(22): 224522.

Kim, Y.-J., G. D. Gu, T. Gog and D. Casa (2008). "X-ray scattering study of charge density waves in $La_{2-x}Ba_xCuO_4$." Physical Review B **77**(6): 064520.

Kindt, J. T. and C. A. Schmuttenmaer (1999). "Theory for determination of the low-frequency time-dependent response function in liquids using time-resolved terahertz pulse spectroscopy." The Journal of Chemical Physics **110**(17): 8589-8596.

Kittel, C. (1976). "Introduction to solid state physics."

Kleiner, R., B. Aigner, B. Avenhaus, C. Kreuzer, P. Pospischil, F. Steinmeyer, P. Müller and K. Andres (1994). "Intrinsic Josephson effects in high-Tc single crystals." Physica B: Condensed Matter **194-196**: 1753-1754.

Kleiner, R., P. Müller, H. Kohlstedt, N. F. Pedersen and S. Sakai (1994). "Dynamic behavior of Josephson-coupled layered structures." Physical Review B **50**(6): 3942.

Koch, R. H., C. P. Umbach, G. J. Clark, P. Chaudhari and R. B. Laibowitz (1987). "Quantum interference devices made from superconducting oxide thin films." Applied Physics Letters **51**(3): 200-202.

Kofu, M., S. H. Lee, M. Fujita, H. J. Kang, H. Eisaki and K. Yamada (2009). "Hidden Quantum Spin-Gap State in the Static Stripe Phase of High-Temperature $La_{2-x}Sr_xCuO_4$ Superconductors." Physical Review Letters **102**(4): 047001.

Laplace, Y. and A. Cavalleri (2016). "Josephson plasmonics in layered superconductors." Advances in Physics: X **1**(3): 387-411.

Lawrence, W. E. and S. Doniach (1970). Proc. 12th Intl. Conf. Low Temp. Phys. (Kyoto, 1970), E. Kanda, ed. (Keigaku, Tokyo, 1971).

Lee, C. H., K. Yamada, H. Hiraka, C. R. Venkateswara Rao and Y. Endoh (2003). "Spin pseudogap in $La_{2-x}Sr_xCuO_4$ studied by neutron scattering." Physical Review B **67**(13): 134521.

Lee, P. A. (2014). "Amperean Pairing and the Pseudogap Phase of Cuprate Superconductors." Physical Review X **4**(3): 031017.

Lee, P. A., N. Nagaosa and X.-G. Wen (2006). "Doping a Mott insulator: Physics of high-temperature superconductivity." Reviews of Modern Physics **78**(1): 17-85.

Lee, Y. S., R. J. Birgeneau, M. A. Kastner, Y. Endoh, S. Wakimoto, K. Yamada, R. W. Erwin, S. H. Lee and G. Shirane (1999). "Neutron-scattering study of spin-density wave order in the superconducting state of excess-oxygen-doped La_2CuO_{4+y}." Physical Review B **60**(5): 3643-3654.

Li, Q., M. Hücker, G. D. Gu, A. M. Tsvelik and J. M. Tranquada (2007). "Two-Dimensional Superconducting Fluctuations in Stripe-Ordered $La_{1.875}Ba_{0.125}CuO_4$." Physical Review Letters **99**(6): 067001.

Liu, H. Y., I. Gierz, J. C. Petersen, S. Kaiser, A. Simoncig, A. L. Cavalieri, C. Cacho, I. C. E. Turcu, E. Springate, F. Frassetto, L. Poletto, S. S. Dhesi, Z. A. Xu, T. Cuk, R. Merlin and A. Cavalleri (2013). "Possible observation of parametrically amplified coherent phasons in $K_{0.3}MoO_3$ using time-resolved extreme-ultraviolet angle-resolved photoemission spectroscopy." Physical Review B **88**(4): 045104.

London, F. and H. London (1935). "The electromagnetic equations of the supraconductor." Proceedings of the Royal Society of London. Series A-Mathematical and Physical Sciences **149**(866): 71-88.

Lozano, P. M., G. D. Gu, J. M. Tranquada and Q. Li (2021). "Experimental evidence that zinc impurities pin pair-density-wave order in $La_{2-x}Ba_xCuO_4$." Physical Review B **103**(2): L020502.

Magnuson, M., T. Schmitt, V. N. Strocov, J. Schlappa, A. S. Kalabukhov and L. C. Duda (2014). "Self-doping processes between planes and chains in the metal-to-superconductor transition of $YBa_2Cu_3O_{6.9}$." Scientific Reports **4**(1): 7017.

Mankowsky, R., M. Först and A. Cavalleri (2016). "Non-equilibrium control of complex solids by nonlinear phononics." Reports on Progress in Physics **79**(6): 064503.

Mankowsky, R., M. Först, T. Loew, J. Porras, B. Keimer and A. Cavalleri (2015). "Coherent modulation of the $YBa_2Cu_3O_{6+\delta}$ atomic structure by displacive stimulated ionic Raman scattering." Physical Review B **91**(9): 094308.

Mankowsky, R., A. Subedi, M. Först, S. O. Mariager, M. Chollet, H. T. Lemke, J. S. Robinson, J. M. Glownia, M. P. Minitti, A. Frano, M. Fechner, N. A. Spaldin, T. Loew, B. Keimer, A. Georges and A. Cavalleri (2014). "Nonlinear lattice dynamics as a basis for enhanced superconductivity in $YBa_2Cu_3O_{6.5}$." Nature **516**(7529): 71-73.

Marel, D. v. d., H. J. A. Molegraaf, J. Zaanen, Z. Nussinov, F. Carbone, A. Damascelli, H. Eisaki, M. Greven, P. H. Kes and M. Li (2003). "Quantum critical behaviour in a high-T_c superconductor." Nature **425**(6955): 271-274.

Maxwell, E. (1950). "Isotope Effect in the Superconductivity of Mercury." Physical Review **78**(4): 477-477.

Meissner, W. and R. Ochsenfeld (1933). "Ein neuer Effekt bei Eintritt der Supraleitfähigkeit." Naturwissenschaften **21**(44): 787-788.

Mitrano, M., A. Cantaluppi, D. Nicoletti, S. Kaiser, A. Perucchi, S. Lupi, P. Di Pietro, D. Pontiroli, M. Riccò, S. R. Clark, D. Jaksch and A. Cavalleri (2016). "Possible light-induced superconductivity in K_3C_{60} at high temperature." Nature **530**(7591): 461-464.

Moler, K. A. (2010). "How the cuprates hid their stripes." Nature **468**(7324): 643-644.

Monthoux, P., A. V. Balatsky and D. Pines (1991). "Toward a theory of high-temperature superconductivity in the antiferromagnetically correlated cuprate oxides." Physical Review Letters **67**(24): 3448-3451.

Monthoux, P., A. V. Balatsky and D. Pines (1992). "Weak-coupling theory of high-temperature superconductivity in the antiferromagnetically correlated copper oxides." Physical Review B **46**(22): 14803-14817.

Monthoux, P. and D. Pines (1994). "Spin-fluctuation-induced superconductivity and normal-state properties of $YBa_2Cu_3O_7$." Physical Review B **49**(6): 4261-4278.

Monthoux, P. and D. J. Scalapino (1994). "Self-consistent d_x^2-y^2 pairing in a two-dimensional Hubbard model." Physical Review Letters **72**(12): 1874-1877.

Moodenbaugh, A. R., Y. Xu, M. Suenaga, T. J. Folkerts and R. N. Shelton (1988). "Superconducting properties of $La_{2-x}Ba_xCuO_4$." Physical Review B **38**(7): 4596-4600.

Nachumi, B., A. Keren, K. Kojima, M. Larkin, G. M. Luke, J. Merrin, O. Tchernyshöv, Y. J. Uemura, N. Ichikawa, M. Goto and S. Uchida (1996). "Muon Spin Relaxation Studies of Zn-Substitution Effects in High-T_c Cuprate Superconductors." Physical Review Letters **77**(27): 5421-5424.

Nakayama, K., T. Sato, Y. Sekiba, K. Terashima, P. Richard, T. Takahashi, K. Kudo, N. Okumura, T. Sasaki and N. Kobayashi (2009). "Evolution of a Pairing-Induced Pseudogap from the Superconducting Gap of $(Bi, Pb)_2Sr_2CuO_6$." Physical Review Letters **102**(22): 227006.

Nicoletti, D., E. Casandruc, Y. Laplace, V. Khanna, C. R. Hunt, S. Kaiser, S. S. Dhesi, G. D. Gu, J. P. Hill and A. Cavalleri (2014). "Optically induced superconductivity in striped $La_{2-x}Ba_xCuO_4$ by polarization-selective excitation in the near infrared." Physical Review B **90**(10): 100503.

Nicoletti, D. and A. Cavalleri (2016). "Nonlinear light–matter interaction at terahertz frequencies." Advances in Optics and Photonics **8**(3): 401-464.

Nicoletti, D., D. Fu, O. Mehio, S. Moore, A. S. Disa, G. D. Gu and A. Cavalleri (2018). "Magnetic-Field Tuning of Light-Induced Superconductivity in Striped $La_{2-x}Ba_xCuO_4$." Physical Review Letters **121**(26): 267003.

Onnes, H. K. (1911). Commun. Phys. Lab. Univ. Leiden. Suppl. 29.

Pavarini, E., I. Dasgupta, T. Saha-Dasgupta, O. Jepsen and O. K. Andersen (2001). "Band-Structure Trend in Hole-Doped Cuprates and Correlation with $T_{c\,max}$." Physical Review Letters **87**(4): 047003.

Petersen, J. C., S. Kaiser, N. Dean, A. Simoncig, H. Y. Liu, A. L. Cavalieri, C. Cacho, I. C. E. Turcu, E. Springate, F. Frassetto, L. Poletto, S. S. Dhesi, H. Berger and A. Cavalleri (2011). "Clocking the Melting Transition of Charge and Lattice Order in 1*T*-TaS_2 with Ultrafast Extreme-Ultraviolet Angle-Resolved Photoemission Spectroscopy." Physical Review Letters **107**(17): 177402.

Petit, S., A. H. Moudden, B. Hennion, A. Vietkin and A. Revcolevschi (1997). "Spin dynamics study of $La_{2-x}Sr_xCuO_4$ by inelastic neutron scattering." Physica B: Condensed Matter **234-236**: 800-802.

Polli, D., M. Rini, S. Wall, R. W. Schoenlein, Y. Tomioka, Y. Tokura, G. Cerullo and A. Cavalleri (2007). "Coherent orbital waves in the photo-induced insulator–metal dynamics of a magnetoresistive manganite." Nature Materials **6**(9): 643-647.

Rajasekaran, S., E. Casandruc, Y. Laplace, D. Nicoletti, G. D. Gu, S. R. Clark, D. Jaksch and A. Cavalleri (2016). "Parametric amplification of a superconducting plasma wave." Nature Physics **12**(11): 1012-1016.

Rajasekaran, S., J.-i. Okamoto, L. Mathey, M. Fechner, V. Thampy, G. D. Gu and A. Cavalleri (2018). "Probing optically silent superfluid stripes in cuprates." Science **359**(6375): 575-579.

Reynolds, C. A., B. Serin, W. H. Wright and L. B. Nesbitt (1950). "Superconductivity of Isotopes of Mercury." Physical Review **78**(4): 487-487.

Rohwer, T., S. Hellmann, M. Wiesenmayer, C. Sohrt, A. Stange, B. Slomski, A. Carr, Y. Liu, L. M. Avila, M. Kalläne, S. Mathias, L. Kipp, K. Rossnagel and M. Bauer (2011). "Collapse of long-range charge order tracked by time-resolved photoemission at high momenta." Nature **471**(7339): 490-493.

Sandu, V., E. Cimpoiasu, T. Katuwal, S. Li, M. B. Maple and C. C. Almasan (2004). "Evidence for Vortices in the Pseudogap Region of $Y_{1-x}Pr_xBa_2Cu_3O_7$ from Angular Magnetoresistivity Measurements." Physical Review Letters **93**(17): 177005.

Schafgans, A. A., A. D. LaForge, S. V. Dordevic, M. M. Qazilbash, W. J. Padilla, K. S. Burch, Z. Q. Li, S. Komiya, Y. Ando and D. N. Basov (2010). "Towards a Two-Dimensional Superconducting State of $La_{2-x}Sr_xCuO_4$ in a Moderate External Magnetic Field." Physical Review Letters **104**(15): 157002.

Schrieffer, J. R., X. G. Wen and S. C. Zhang (1989). "Dynamic spin fluctuations and the bag mechanism of high-T_c superconductivity." Physical Review B **39**(16): 11663-11679.

Schwartz, B. (2013). Superconductor Applications: SQUIDs and Machines, Springer US.

Shen, Z. X., D. S. Dessau, B. O. Wells, D. M. King, W. E. Spicer, A. J. Arko, D. Marshall, L. W. Lombardo, A. Kapitulnik, P. Dickinson, S. Doniach, J. DiCarlo, T. Loeser and C. H. Park (1993). "Anomalously large gap anisotropy in the a-b plane of $Bi_2Sr_2CaCu_2O_{8+\delta}$." Physical Review Letters **70**(10): 1553-1556.

Shi, Z., P. G. Baity, T. Sasagawa and D. Popović (2019). "Vortex phase diagram and the normal state of cuprates with charge and spin orders." Science Advances **6**(7): eaay8946.

Shi, Z., P. G. Baity, J. Terzic, T. Sasagawa and D. Popović (2020). "Pair density wave at high magnetic fields in cuprates with charge and spin orders." Nature Communications **11**(1): 3323.

Slezak, J. A., J. Lee, M. Wang, K. McElroy, K. Fujita, B. M. Andersen, P. J. Hirschfeld, H. Eisaki, S. Uchida and J. C. Davis (2008). "Imaging the impact on cuprate superconductivity of varying the interatomic distances within individual crystal unit cells." Proceedings of the National Academy of Sciences **105**(9): 3203.

Snider, E., N. Dasenbrock-Gammon, R. McBride, M. Debessai, H. Vindana, K. Vencatasamy, K. V. Lawler, A. Salamat and R. P. Dias (2020). "Room-temperature superconductivity in a carbonaceous sulfur hydride." Nature **586**(7829): 373-377.

Tajima, S., T. Noda, H. Eisaki and S. Uchida (2001). "c-Axis Optical Response in the Static Stripe Ordered Phase of the Cuprates." Physical Review Letters **86**(3): 500-503.

Terhune, R. W., P. D. Maker and C. M. Savage (1962). "Optical Harmonic Generation in Calcite." Physical Review Letters **8**(10): 404-406.

Timusk, T. and B. Statt (1999). "The pseudogap in high-temperature superconductors: an experimental survey." Reports on Progress in Physics **62**(1): 61-122.

Tinkham, M. (2004). Introduction to superconductivity, Courier Corporation.

Townsend, P. and J. Sutton (1962). "Investigation by Electron Tunneling of the Superconducting Energy Gaps in Nb, Ta, Sn, and Pb." Physical Review **128**(2): 591-595.

Tranquada, J. M. (2013). Spins, stripes, and superconductivity in hole-doped cuprates.

Tranquada, J. M., D. J. Buttrey, V. Sachan and J. E. Lorenzo (1994). "Simultaneous Ordering of Holes and Spins in $La_2NiO_{4.125}$." Physical Review Letters **73**(7): 1003-1006.

Tranquada, J. M., G. D. Gu, M. Hücker, Q. Jie, H. J. Kang, R. Klingeler, Q. Li, N. Tristan, J. S. Wen, G. Y. Xu, Z. J. Xu, J. Zhou and M. v. Zimmermann (2008). "Evidence for unusual superconducting correlations coexisting with stripe order in $La_{1.875}Ba_{0.125}CuO_4$." Physical Review B **78**(17): 174529.

Tranquada, J. M., B. J. Sternlieb, J. D. Axe, Y. Nakamura and S. Uchida (1995). "Evidence for stripe correlations of spins and holes in copper oxide superconductors." Nature **375**(6532): 561-563.

Uchida, S., T. Ido, H. Takagi, T. Arima, Y. Tokura and S. Tajima (1991). "Optical spectra of $La_{2-x}Sr_xCuO_4$: Effect of carrier doping on the electronic structure of the CuO_2 plane." Physical Review B **43**(10): 7942-7954.

Uykur, E., K. Tanaka, T. Masui, S. Miyasaka and S. Tajima (2014). "Persistence of the Superconducting Condensate Far above the Critical Temperature of $YBa_2(Cu, Zn)_3O_y$ Revealed by c-Axis Optical Conductivity Measurements for Several Zn Concentrations and Carrier Doping Levels." Physical Review Letters **112**(12): 127003.

Valla, T., A. V. Fedorov, J. Lee, J. C. Davis and G. D. Gu (2006). "The Ground State of the Pseudogap in Cuprate Superconductors." Science **314**(5807): 1914.

Van Delft, D. and P. Kes (2010). "The discovery of superconductivity." Physics Today **63**(9): 38-43.

van der Marel, D. and A. Tsvetkov (1996). "Transverse optical plasmons in layered superconductors." Czechoslovak Journal of Physics **46**(6): 3165-3168.

van der Marel, D. and A. A. Tsvetkov (2001). "Transverse-optical Josephson plasmons: Equations of motion." Physical Review B **64**(2): 024530.

Varma, C. M. (1999). "Pseudogap Phase and the Quantum-Critical Point in Copper-Oxide Metals." Physical Review Letters **83**(17): 3538-3541.

Vershinin, M., S. Misra, S. Ono, Y. Abe, Y. Ando and A. Yazdani (2004). "Local Ordering in the Pseudogap State of the High-T_c Superconductor $Bi_2Sr_2CaCu_2O_{8+\delta}$." Science **303**(5666): 1995-1998.

Vishik, I., W. Lee, F. Schmitt, B. Moritz, T. Sasagawa, S. Uchida, K. Fujita, S. Ishida, C. Zhang and T. Devereaux (2010). "Doping-dependent nodal fermi velocity of the high-temperature superconductor $Bi_2Sr_2CaCu_2O_{8+\delta}$ revealed using high-resolution angle-resolved photoemission spectroscopy." Physical review letters **104**(20): 207002.

von Hoegen, A., M. Fechner, M. Först, N. Taherian, E. Rowe, A. Ribak, J. Porras, B. Keimer, M. Michael, E. Demler and A. Cavalleri (2019) "Parametrically amplified phase-incoherent superconductivity in $YBa_2Cu_3O_{6+x}$." arXiv:1911.08284.

Weber, C., K. Haule and G. Kotliar (2010). "Apical oxygens and correlation strength in electron- and hole-doped copper oxides." Physical Review B **82**(12): 125107.

Wells, B. O., Z. X. Shen, D. S. Dessau, W. E. Spicer, D. B. Mitzi, L. Lombardo, A. Kapitulnik and A. J. Arko (1992). "Evidence for k-dependent, in-plane anisotropy of the superconducting gap in $Bi_2Sr_2CaCu_2O_{8+\delta}$." Physical Review B **46**(18): 11830-11834.

Wen, J., Q. Jie, Q. Li, M. Hücker, M. v. Zimmermann, S. J. Han, Z. Xu, D. K. Singh, R. M. Konik, L. Zhang, G. Gu and J. M. Tranquada (2012). "Uniaxial linear resistivity of superconducting $La_{1.905}Ba_{0.095}CuO_4$ induced by an external magnetic field." Physical Review B **85**(13): 134513.

Wen, J., Z. Xu, G. Xu, Q. Jie, M. Hücker, A. Zheludev, W. Tian, B. L. Winn, J. L. Zarestky, D. K. Singh, T. Hong, Q. Li, G. Gu and J. M. Tranquada (2012). "Probing the connections between superconductivity, stripe order, and structure in $La_{1.905}Ba_{0.095}Cu_{1-y}Zn_yO_4$." Physical Review B **85**(13): 134512.

Wesche, R. (2015). Physical properties of high-temperature superconductors, John Wiley & Sons.

Wu, T., H. Mayaffre, S. Krämer, M. Horvatić, C. Berthier, W. N. Hardy, R. Liang, D. A. Bonn and M.-H. Julien (2011). "Magnetic-field-induced charge-stripe order in the high-temperature superconductor $YBa_2Cu_3O_y$." Nature **477**(7363): 191-194.

Xu, Z. A., N. P. Ong, Y. Wang, T. Kakeshita and S. Uchida (2000). "Vortex-like excitations and the onset of superconducting phase fluctuation in underdoped $La_{2-x}Sr_xCuO_4$." Nature **406**(6795): 486-488.

Yang, H. B., J. D. Rameau, P. D. Johnson, T. Valla, A. Tsvelik and G. D. Gu (2008). "Emergence of preformed Cooper pairs from the doped Mott insulating state in $Bi_2Sr_2CaCu_2O_{8+\delta}$." Nature **456**(7218): 77-80.

Zaanen, J., G. A. Sawatzky and J. W. Allen (1985). "Band gaps and electronic structure of transition-metal compounds." Physical Review Letters **55**(4): 418-421.